Technische Universität München
TUM School of Natural Sciences

Towards Energy Saturation in Three-dimensional Simulations of Core-collapse Supernova Explosions

Daniel Kresse

Vollständiger Abdruck der von der TUM School of Natural Sciences der Technischen Universität München zur Erlangung des akademischen Grades eines

Doktors der Naturwissenschaften (Dr. rer. nat.)

genehmigten Dissertation.

Vorsitz:		Prof. Dr. Lothar Oberauer
Prüfer*innen der Dissertation:	1.	Prof. Dr. Hans-Thomas Janka
	2.	Prof. Dr. Alejandro Ibarra

Die Dissertation wurde am 03.05.2023 bei der Technischen Universität München eingereicht und durch die TUM School of Natural Sciences am 19.06.2023 angenommen.

Contents

1 Introduction

Core-collapse supernovae (CCSNe) are among the brightest and most energetic events in the Universe. They mark the violent, explosive deaths of massive stars and give birth to neutron stars and black holes, the most exotic compact objects known. Besides their relevance for regulating galactic dynamics and star formation processes, CCSNe are major sites of chemical element formation. Understanding the explosion mechanism of massive stars is therefore crucial for better defining the role of supernovae in the cosmic cycle of matter.

After almost a century of intense research, the question of how CCSNe explode is still not finally answered and remains one of the most long-standing riddles of stellar astrophysics. Thanks to the remarkable progress of theoretical and numerical modeling during the last decades, the "delayed neutrino-driven mechanism" has meanwhile been established as the most promising and widely accepted paradigm for CCSNe. However, one critical problem remains to be solved: namely, the question of whether neutrino-driven CCSNe can reach explosion energies in the range of commonly observed values of around ∼0.5–1 bethe (1 B = 10^{51} erg = 10^{44} J). This thesis addresses this question by performing long-time, three-dimensional (3D) hydrodynamics simulations, including a newly developed, computationally efficient scheme for neutrino effects. We show that energy saturation at the typical values of ∼0.5–1 B can be achieved in self-consistent 3D models of neutrino-driven CCSNe on relevant timescales of several seconds.

In this introductory chapter, we first provide a brief and general description of CCSNe (Section 1.1), followed by an extended summary of the neutrino-driven explosion mechanism and the most relevant physical processes involved (Section 1.2); in Section 1.3, we provide a short overview of important observational implications; Section 1.4 discusses the current status and open questions of the numerical modeling of CCSNe; in Section 1.5, we present the goals and outline of this thesis.

1.1. Core-collapse Supernovae

Only two years after the discovery of the neutron (Chadwick, 1932) in the first half of the 20th century, Baade & Zwicky (1934a,b,c) proposed that stars could end their lives in a catastrophic collapse to compact objects "consisting mainly of neutrons," which they termed "neutron stars" (NSs). They argued that such events could give rise to bright "supernovae" (SNe; a name that has also been coined by Baade and

Zwicky), observable in nearby and distant galaxies. Almost a century later, these visionary ideas still define the essence of our modern understanding of CCSNe.

Today, we distinguish between two major classes of SN explosions: In contrast to the thermonuclear explosions of white dwarfs (WDs) as Type Ia SNe (e.g., Hillebrandt & Niemeyer, 2000; Hillebrandt et al., 2013), CCSNe are the explosions of massive stars with at least nine times the mass of our Sun, which develop iron cores at the end of their lives. When such an iron core becomes gravitationally unstable and collapses to an NS (with a radius of only $\sim$10 km), an enormous amount of gravitational binding energy is released (some 10^{53} erg), carried away predominantly in the form of neutrinos. Due to their purely weakly interacting nature, most neutrinos escape the system freely. Nevertheless, a powerful explosion can be triggered if only a tiny fraction (less than 1%) of the emitted neutrino radiation gets reabsorbed in the star's infalling shells. Yet, it remained an open question whether this mechanism is sufficient to explain the majority of observed CCSNe with typical values of the explosion energy (i.e., thermal plus kinetic energy of the expanding SN debris) of around $\sim$0.5–1 B (e.g., Kasen & Woosley, 2009; Pejcha & Prieto, 2015b; Martinez et al., 2022). We will return to this question in the course of this thesis.

Due to the immense brightness of SN explosions, which can outshine their host galaxies for weeks, astronomers had already observed them in ancient history long before modern instruments such as telescopes became available (Clark & Stephenson, 1977). However, SNe that are close enough to be spotted with the naked eye are rare: Galactic CCSNe are expected to occur only around 1–3 times per century (Diehl et al., 2006; Ikeda et al., 2007; Agafonova et al., 2015). The latest CCSN that went off in the immediate "neighborhood" of our Galaxy was SN 1987A, the explosion of the blue supergiant star Sanduleak -69° 202 (Walborn et al., 1987) in the Large Magellanic Cloud. This event truly revolutionized the field of SN research. It allowed for the first, and so far only, detection of SN neutrinos in a roughly 10-second long burst (Bionta et al., 1987; Hirata et al., 1987; Alexeyev et al., 1988), which provided the first-ever direct evidence for the formation of an NS during an SN explosion.[1] Moreover, SN 1987A showed clear signs of pronounced explosion asymmetries and a highly anisotropic, radially mixed mass distribution of chemical elements in the SN ejecta (e.g., Woosley et al., 1988; Arnett et al., 1989; Haas et al., 1990; McCray, 1993; Utrobin et al., 2015, 2019, 2021), pointing to the intrinsically multi-dimensional nature of CCSN explosions.

Even though the basic picture of CCSNe as the explosions of massive stars, associated with the gravitational collapse of their iron cores to compact NSs, did not change since its initial proposition in the 1930s, the exact mechanism for powering CCSNe remained unclear for many decades.

[1] Very recently, high-resolution ALMA images revealed an excess infrared emission from a hot dust "blob" at around the expected position of the compact remnant of SN 1987A (Cigan et al., 2019), which indeed seems to hint at the thermal emission of a young and cooling NS (Page et al., 2020).

1.2. The Neutrino-driven Explosion Mechanism

Today, almost a century after the visionary ideas of Baade & Zwicky (1934a,b), the so-called "delayed neutrino-driven explosion mechanism" (Colgate & White, 1966; Arnett, 1966; Bethe & Wilson, 1985) has been established as the most promising and widely accepted theoretical framework to explain the CCSN explosions of massive stars (at least, for the majority of cases). For an overview of alternative explosion mechanisms discussed in the scientific community, see, e.g., the review by Janka (2012). In the following, we summarize the most relevant physical processes on the way to a neutrino-driven CCSN explosion. For more details, we refer to dedicated review articles in the literature (e.g., Bethe, 1990; Mezzacappa, 2005; Kotake et al., 2006; Janka, 2012, 2017a; Burrows, 2013; Janka et al., 2016; Müller, 2020; Burrows & Vartanyan, 2021).

1.2.1. Gravitational Collapse

When a massive star with an initial mass larger than around nine solar masses ($M_\odot$) approaches the end of its life, it consists of concentric shells of successively heavier chemical elements towards the center (i.e., it has an "onion-shell-like" structure).[2] These shells contain the "ashes" of a long series of nuclear burning stages that took place during the star's lifetime (from hydrogen burning on the main sequence all the way to the burning of silicon to iron-group elements). Once the star has developed a core consisting mainly of iron, nuclear fusion in this central region stops because iron possesses the highest binding energy per nucleon and further nuclear reactions would not result in a net energy generation. Yet, the (WD-like) inert iron core, which is stabilized primarily by electron-degeneracy pressure, continues to grow in mass due to ongoing silicon shell burning in the surrounding layers.

As the iron core approaches the Chandrasekhar mass limit (Chandrasekhar, 1931, 1935), it becomes gravitationally unstable and collapses as a consequence of the partial photodissociation of iron-group nuclei to α particles and free nucleons, as well as due to electron captures on nuclei and free protons. Electron neutrinos, which can escape freely from the star's central regions, carry away energy and lepton number, leading to a "neutronization" and "deleptonization" of the dynamically collapsing core. However, once the densities exceed values of around $10^{12}\,\mathrm{g\,cm^{-3}}$, neutrinos are effectively trapped in the core as their diffusion timescale becomes longer than the free-fall timescale. The subsequent collapse of the inner core proceeds adiabatically and homologously at subsonic velocities while the outer core falls inwards at supersonic speed.

[2] As a side note, we already want to mention here that convective shell burning can lead to significant deviations from a perfectly spherical structure; see the discussion in Section 3.1.

1.2.2. Core Bounce and Shock Formation

When the densities in the collapsing core exceed the nuclear saturation density ($\sim 2.7 \times 10^{14}\,\mathrm{g\,cm^{-3}}$), the repulsive nuclear forces lead to a sudden stiffening of the equation of state and the collapse stops abruptly. The inner core overshoots its new equilibrium state and rebounds (in what is referred to as the "core bounce"). This launches pressure waves that propagate outwards and steepen into a shock front when they hit the supersonically infalling matter of the outer core.

Nevertheless, already a few milliseconds after the core bounce, the shock loses its power because of the photodisintegration of iron-group nuclei, which consumes an energy of $\mathcal{O}(10^{51})\,\mathrm{erg}$ per $0.1\,\mathrm{M_\odot}$ of swept-up matter. Moreover, as the densities in the postshock layer fall below the threshold for neutrino trapping ($\sim 10^{12}\,\mathrm{g\,cm^{-3}}$), a luminous burst of electron neutrinos is emitted and extracts additional energy, which reduces the pressure behind the shock. As a consequence, the shock stalls at a radius of ~100–200 km, which is still well inside the iron core, and turns into an accretion shock with postshock velocities pointing inwards. The infalling pre-shock matter that is accreted through the shock gets decelerated and is then advected towards the hot "proto-neutron star" (PNS) that has formed in the center.

1.2.3. Onset of the Explosion

Neutrino Heating and Shock Revival. Reviving the stalled accretion shock and thus triggering an explosion requires a mechanism that deposits enough energy behind the shock to overcome the enormous ram pressure of the still-infalling outer shells. Colgate & White (1966) and Arnett (1966) were the first to speculate that neutrinos could be responsible for tapping the reservoir of gravitational binding energy stored in the hot PNS and transferring some fraction of this energy to the (more loosely bound) surrounding layers. Based on these pioneering ideas and grounded on results from numerical simulations by Wilson (1985) in spherical symmetry (1D), Bethe & Wilson (1985) proposed the "delayed neutrino-driven mechanism,"[3] which has meanwhile been established as the most promising and widely accepted paradigm for the explosions of massive stars.

In Figure 1.1, we provide a sketch illustrating this mechanism's basic working principle. The huge amount of gravitational binding energy (several $10^{53}\,\mathrm{erg}$), which is released during the collapse of the star's iron core and transiently stored in the nascent, hot and inflated PNS as thermal energy, slowly leaks out in the form of intense neutrino radiation. Due to their purely weakly interacting nature, most neutrinos leave the star without hindrance. However, a small fraction of the radiated (electron-type) neutrinos and antineutrinos get reabsorbed and deposit energy in

[3] Here, "delayed" means that the explosions do not happen instantaneously (as was previously suggested by the so-called "prompt bounce-shock mechanism") but on a typical timescale of some hundred milliseconds.

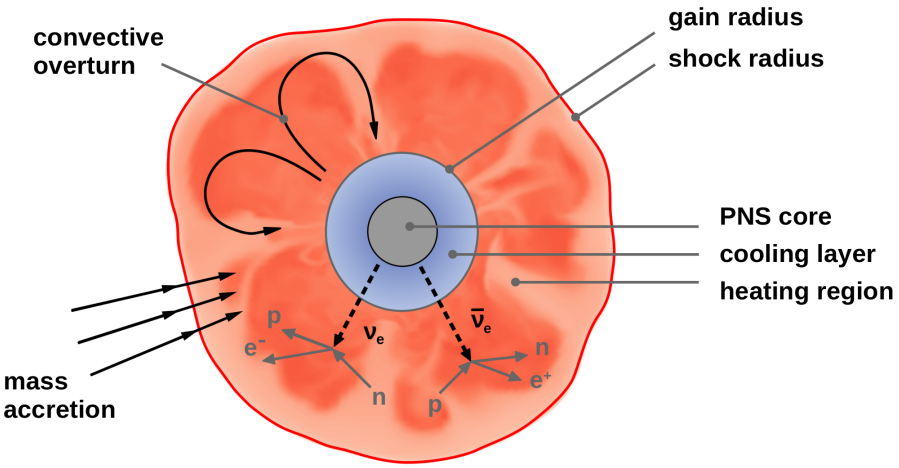

Figure 1.1.: Schematic picture of the delayed neutrino-driven explosion mechanism for CCSNe. The gravitational binding energy of the collapsed iron core is transiently stored in a hot and initially inflated PNS, which contracts and cools via intense neutrino emission over timescales of $\mathcal{O}$(seconds). A small fraction of the escaping neutrino radiation is reabsorbed in the gain layer behind the stalled accretion shock, mainly via the charged-current beta reactions of Equations (1.1) and (1.2). The gain radius separates regions of net neutrino cooling and net neutrino heating. Nonradial fluid instabilities such as convective overturn (or the standing accretion shock instability; see main text) stir the medium in the postshock layer, supporting the neutrino-heating mechanism. Runaway shock expansion sets in once the thermal (and turbulent) pressure behind the shock overcomes the ram pressure of the supersonically infalling pre-shock layer. Figure adapted from Janka (2001) and Melson (2016).

the layer behind the stalled accretion shock, mainly via the reactions (e.g., Bethe & Wilson, 1985; Janka, 2001):

$$\nu_{\mathrm{e}} + \mathrm{n} \longleftrightarrow \mathrm{p} + \mathrm{e}^{-} \,, \tag{1.1}$$

$$\bar{\nu}_{\mathrm{e}} + \mathrm{p} \longleftrightarrow \mathrm{n} + \mathrm{e}^{+} \,. \tag{1.2}$$

Because the neutrino energy-deposition (i.e., heating) rate depends on the neutrino fluxes, it scales approximately with the inverse radius squared, i.e., according to $\propto r^{-2}$. In contrast, neutrino cooling, which proceeds mainly via the back reactions of Equations (1.1) and (1.2), scales with the sixth power of the local matter temperature and therefore drops roughly as r^{-6} (see Janka, 2001). This implies that neutrino heating balances neutrino cooling at a certain radius (commonly referred to as the "gain radius"; Bethe & Wilson, 1985), within which the stellar fluid is effectively cooled, while matter in the layer between the gain radius and the shock front (i.e., in

the so-called "gain layer") experiences net heating.[4]

Runaway shock expansion finally sets in once the neutrino-energy deposition in the gain layer has increased the pressure behind the shock to sufficiently high values such that it exceeds the pre-shock ram pressure of the infalling outer shells. Burrows & Goshy (1993) have coined this condition in terms of a "critical luminosity" that is needed for shock revival given a certain mass-accretion rate.[5] According to the results from numerical simulations, runaway shock expansion typically sets in around the time when the Si/Si+O composition shell interface falls through the stagnant accretion shock (i.e., a few hundred milliseconds after the core bounce), as this coincides with a sudden drop of the density and thus of the pre-shock ram pressure (see, e.g., the discussions in Section 3.2).

Role of Hydrodynamic Instabilities. After the first multi-dimensional CCSN simulations (in axial symmetry, i.e., in "2D") became possible with the advent of more modern computers and the ongoing development of sophisticated numerical codes in the 1990s, it has soon become clear that nonradial hydrodynamic fluid instabilities play an essential role in the mechanism of neutrino-driven explosions (see, e.g., Herant et al., 1994; Burrows et al., 1995; Janka & Müller, 1996). These findings agreed with the growing observational evidence that CCSNe are intrinsically multi-dimensional phenomena (see, e.g., Section 1.1).

Because neutrino heating is strongest at the bottom of the gain layer and drops like r^{-2} towards larger radii, it creates a negative entropy gradient. For this reason, the postshock layer becomes unstable to violent, large-scale convective overturn, which carries hot, neutrino-heated matter (in mushroom-like, buoyant high-entropy plumes) to the region behind the stagnant shock. Simultaneously, colder gas from further outside is channeled inward close to the gain radius, where it can absorb neutrino energy most efficiently, subsequently being re-ejected. More detailed discussions on neutrino-driven convection and its aiding effects for shock revival can be found, e.g., in the works by Herant et al. (1994); Burrows et al. (1995); Janka & Müller (1996); Fryer & Warren (2002); Foglizzo et al. (2006); Murphy et al. (2013); Abdikamalov et al. (2015); Couch & Ott (2015); Radice et al. (2016).

Moreover, a large-scale (low-mode) oscillatory instability of the shock front, the so-called "standing accretion shock instability" (SASI; Blondin et al., 2003; Blondin & Mezzacappa, 2007; Iwakami et al., 2008) can develop in the postshock layer, leading to violent sloshing and spiral motions of the shock surface. The growth of

[4] On a much lower level (of only a few percent), also the energy transfer by scattering reactions contributes to the neutrino heating. In this context, we also want to mention that the cooling of the PNS's high-density core proceeds via the diffusive emission of neutrinos and antineutrinos of all flavors produced by various interaction processes; see Table 2.1 in Section 2.1.2. For a dedicated review on SN neutrino emission, we refer to, e.g., Janka (2017b).

[5] The "critical luminosity condition" of Burrows & Goshy (1993) has recently been generalized based on results from multi-dimensional simulations; see, e.g., Summa et al. (2016, 2018).

this instability can be explained by an "advective–acoustic cycle," which describes the coupling between acoustic waves that emerge at the PNS surface and vorticity perturbations that are generated at the shock front and advected with the fluid flow (Foglizzo et al., 2007; Scheck et al., 2008; Guilet & Foglizzo, 2012; Foglizzo et al., 2015). Secondary, "parasitic" (Kelvin-Helmholtz and Rayleigh-Taylor) instabilities grow at shear interfaces in the wake of the SASI (Guilet et al., 2010).

Both fluid instabilities, postshock convection and the SASI, support the neutrino-driven mechanism by pushing the shock front to larger radii and thus increasing the volume (and mass) of the gain layer (see, e.g., Marek & Janka, 2009; Hanke et al., 2013; Ott et al., 2013; Fernández, 2015; O'Connor & Couch, 2018a). Nonradial fluid flows also lead to a prolonged dwell time of matter in the heating region compared to the spherically symmetric case. Moreover, multi-dimensional, "chaotic" mass motions generate turbulent pressure that gives additional support to the stalled shock (e.g., Murphy et al., 2013; Couch & Ott, 2015; Müller & Janka, 2015; Radice et al., 2016; Mabanta & Murphy, 2018).

In the context of fluid instabilities, we want to briefly mention that convective overturn also takes place inside the nascent, hot PNS because of unstable lepton-number and entropy gradients (e.g., Burrows, 1987; Keil et al., 1996; Dessart et al., 2006; Nagakura et al., 2020). This drives a faster cooling and, thus, contraction of the PNS's high-density core and consequently boosts the neutrino emission (see, e.g., the review by Mirizzi et al., 2016, on SN neutrino emission). Moreover, PNS convection can lead to a global, hemispheric anisotropy of the neutrino emission, namely the so-called "lepton-number emission self-sustained asymmetry" (LESA; Tamborra et al., 2014a; Glas et al., 2019a), which can have important consequences for the NS recoil ("kick") velocities as well as for the neutron-to-proton ratio in the SN ejecta (see Section 3.6.1 and Appendix A).

1.2.4. Long-time Development of the Explosion

After an explosion has been launched successfully by neutrino heating, the outwards-moving shock front is still deep inside the dying star, with massive and yet gravitationally bound layers of the stellar envelope lying on top. Before the first electromagnetic radiation of the SN can escape the star, these overlying shells need to be traversed by the shock wave. Although the shock propagates with velocities of up to a few percent of the speed of light, it can take hours (or, in extreme cases, even days) until it breaks out from the stellar surface because the radii of red-supergiant progenitor stars with extended hydrogen envelopes reach up to 10^8–10^9 km.[6]

At the time of shock revival (i.e., typically a few hundred milliseconds after the

[6] In the case of hydrogen-stripped pre-SN stars, which may be a common outcome of binary stellar evolution (e.g., Podsiadlowski et al., 2004; Schneider et al., 2015, 2021; Woosley, 2019; Laplace et al., 2020, 2021), shock breakout occurs on much shorter timescales of $\mathcal{O}$(minutes) because the helium cores of massive stars have typical radii of "only" $\sim 10^6$–10^7 km.

core bounce), the "diagnostic explosion energy," which describes the total energy of unbound postshock matter (see Equation (3.9) in Chapter 3), has only begun to rise steeply. However, when considering the negative binding energy of the overlying stellar shells, the emergent explosion's net energy is still negative (or close to zero) at this early stage. As we will show in this thesis, the explosion energy of a CCSN, i.e., the total (internal plus kinetic) energy of the SN ejecta, builds up only over typical timescales of seconds through continued energy deposition by neutrino heating. This gradual rise of the explosion energy is enabled by ongoing and persistent accretion downflows of relatively cold matter to the region of strongest neutrino heating close to the PNS, simultaneously to the outflow of neutrino-heated high-entropy plumes. Moreover, the formation of heavy chemical elements, such as radioactive nickel, which is tightly coupled to the growth of the explosion energy, lasts for several seconds. Furthermore, also the properties of the newborn NSs, such as their kick velocities and spin periods, develop over (at least) similarly long timescales of $\mathcal{O}(10)$ seconds (barring possible late-time effects due to fallback accretion, which can carry mass, momentum, and angular momentum to the remnant NS).

1.3. Observational Implications

Eventually, observational evidence will be needed to assess the viability of the neutrino-driven explosion mechanism. Theoretical CCSN models should therefore aim at predicting and explaining directly measurable explosion properties.

In particular, the measurements of neutrinos and gravitational waves from a future galactic SN will allow for direct exploration of the physical processes *during the explosion onset* at the deep interior of a dying star, from where no electromagnetic radiation can escape. After the first (and so far only) detection of SN neutrinos for the case of SN 1987A (with rather low event statistics of only two dozen counts; Bionta et al., 1987; Hirata et al., 1987; Alexeyev et al., 1988), modern large-volume underground neutrino detectors (e.g., Ikeda et al., 2007; Abbasi et al., 2011; An et al., 2016) and (laser-interferometric) gravitational-wave observatories (e.g., Abbott et al., 2020) will yield a wealth of data from high-precision measurements of neutrinos and gravitational waves for the fortunate case of the next galactic CCSN. Nevertheless, such nearby events are rare (e.g., Diehl et al., 2006). In the meantime, a first detection of the diffuse supernova neutrino background (DSNB; i.e., the relic neutrino emission from past CCSNe) may be able to yield information on the entire population of stellar core-collapse events (see, e.g., Kresse et al., 2021, and references therein). Yet, accumulating DSNB event statistics will only be slow and take several years (see, e.g., Sawatzki et al., 2021, Figure 11).

Complementary to the measurement of neutrinos and gravitational waves, valuable insights on the *explosion development over longer timescales* (which is the focus of this thesis) can meanwhile be gained by studying the electromagnetic emission from CCSNe and their remnants. Due to the immense brightness of SN explosions, their spectra and light curves (i.e., apparent or absolute magnitude as a function

of time) can be measured in different wavelength bands with modern ground- and space-based telescopes out to far distances for hundreds to even thousands of cases per year. Because the electromagnetic emission of an SN is heavily influenced by the stellar envelope (and in some cases also by the presence of circumstellar matter), the inference of explosion properties is less direct than in the case of neutrinos or gravitational waves. Nevertheless, SN light curves and spectra carry information on various explosion properties, such as the mass of radioactive nickel synthesized during the explosion (which can be deduced from the tail of the bolometric light curve; e.g., Nadyozhin, 1994; Hamuy, 2003; Pejcha & Prieto, 2015b; Nakar et al., 2016), or the explosion energy and ejecta mass (which determine the luminosity and duration of the light-curve plateau of hydrogen-rich Type IIP SNe; e.g., Arnett, 1980; Popov, 1993; Kasen & Woosley, 2009; Dessart et al., 2010; Pejcha & Prieto, 2015a; Sukhbold et al., 2016; Goldberg et al., 2019; Martinez et al., 2020, 2022; Kozyreva et al., 2022).[7]

Observed SN spectra (e.g., Pastorello et al., 2004; Spiro et al., 2014; Smartt et al., 2015), which feature Doppler-broadened emission and absorption lines of different chemical elements, can be employed to estimate (photospheric) expansion velocities (e.g., using P-Cygni line profiles during the first ∼100 days after explosion, i.e., during the plateau phase of Type IIP SNe; see Dessart & Hillier, 2005). At even later times, a few months to a few years after the explosion, when the expanding SN ejecta have become optically thin, nebular-phase spectroscopy (e.g., Dessart & Hillier, 2011; Jerkstrand et al., 2012, 2014, 2018) can yield constraints on the masses and expansion velocities of individual elements in the innermost SN debris. Moreover, spectropolarimetric observations of SNe can reveal intrinsic explosion asphericities (see, e.g., Wang & Wheeler, 2008; Nagao et al., 2019, 2021; Vasylyev et al., 2023).

Supplementary to the observation of SN explosions themselves, also the study of their compact and gaseous remnants (decades to centuries later) can provide indirect constraints on the explosion mechanism. Because the driving "engine" of a neutrino-driven CCSN is tightly linked to the formation and cooling of an NS, measuring the birth properties of NSs is particularly relevant, such as their masses (e.g., Thorsett & Chakrabarty, 1999; Kiziltan et al., 2013; Özel & Freire, 2016), radii (e.g., Özel & Freire, 2016; Miller et al., 2019; Riley et al., 2019, 2021; Raaijmakers et al., 2021), spin periods (e.g., Kaspi & Helfand, 2002), and kick velocities (Hobbs et al., 2005; Katsuda et al., 2018). Moreover, observations of the anisotropic element distributions in gaseous SN remnants can provide evidence for intrinsic explosion asymmetries

[7] Dessart & Hillier (2019) and Goldberg & Bildsten (2020) pointed out that the light curve and line velocities of an observed SN can be matched equally well by synthetic models with very different input parameters (i.e., values of the ejecta mass, the explosion energy, and the progenitor radius). This degeneracy can be lifted, e.g., by pre-explosion progenitor-radius measurements or by independent constraints of the explosion energy and nickel mass (however, see also Martinez et al., 2020).

that stem from the dynamical evolution during the first seconds. Examples of well-studied, nearby CCSN remnants are, e.g., the Crab Nebula (Hester, 2008; Smith, 2013; Tominaga et al., 2013; Yang & Chevalier, 2015), Cassiopeia A (e.g., Hwang et al., 2004; Grefenstette et al., 2014), or Puppis A (Winkler & Kirshner, 1985; Petre et al., 1996; Mayer et al., 2020, 2022). In this thesis, based on our 3D CCSN models, we aim to predict some of the observationally accessible explosion properties mentioned above (see Section 1.5).

1.4. Numerical Modeling

Due to the high complexity and non-linear nature of CCSN explosions, numerical simulations are indispensable to better understand the physical processes that take place at the core of these explosive stellar-death events.

Numerical modeling of CCSNe dates back to the 1960s and has continuously been refined since then (e.g., Colgate & White, 1966; Arnett, 1966, 1977; Bethe et al., 1979; Hillebrandt & Müller, 1981; Wilson, 1985; Bethe & Wilson, 1985; Bruenn, 1986; Burrows & Lattimer, 1986). Although progenitor stars at the low-mass end of CCSNe (i.e., with initial masses between roughly 9 and 10 $M_\odot$) turned out to explode rather easily in numerical models even under the assumption of spherical symmetry (e.g., Kitaura et al., 2006; Janka et al., 2008; Fischer et al., 2010), the first multi-dimensional simulations in 2D revealed that nonradial mass motions and hydrodynamic instabilities play a pivotal role in aiding successful shock revival in numerical models of neutrino-driven explosions, especially for more massive stars (see, e.g., Herant et al., 1994; Burrows et al., 1995; Janka & Müller, 1996). Nevertheless, 2D simulations suffer from artifacts such as an unrealistic, torus-like flow geometry (e.g., Couch & O'Connor, 2014) and an inverse turbulent energy cascade to the largest (instead of the smallest) spatial scales (Kraichnan, 1967). Therefore, full-3D simulations are needed to reliably model the CCSN phenomenon.

1.4.1. Status of Three-dimensional Modeling

With the advent of modern, powerful supercomputers as well as due to the ongoing development of sophisticated neutrino-hydrodynamics simulation codes (e.g., Rampp & Janka, 2002; Liebendörfer et al., 2004; Buras et al., 2006b; Müller et al., 2010; Takiwaki et al., 2012; Just et al., 2015; O'Connor, 2015; Kuroda et al., 2016b; O'Connor & Couch, 2018b; Skinner et al., 2019; Bruenn et al., 2020), 3D modeling of CCSNe has meanwhile become a feasible, though still challenging task. Over the past two decades, considerable progress has been achieved through ongoing simulation efforts by different research groups.

After the first successful CCSN simulations in full 3D with simplified, gray neutrino transport and smoothed-particle hydrodynamics (SPH) by Fryer & Warren (2002, 2004) and 3D models with neutrino leakage schemes (e.g., Ott et al., 2013; Couch & O'Connor, 2014) or parameterized, local neutrino source terms (e.g., Nordhaus et al.,

2010b; Hanke et al., 2012; Burrows et al., 2012; Dolence et al., 2013; Murphy et al., 2013; Couch, 2013), successful neutrino-driven explosions have also been obtained for a growing number of modern, fully self-consistent, grid-based 3D hydrodynamics simulations with detailed, energy-dependent neutrino transport (e.g., Takiwaki et al., 2012, 2014; Lentz et al., 2015; Melson et al., 2015a,b; Roberts et al., 2016; Müller et al., 2017, 2019; Ott et al., 2018; Summa et al., 2018; Glas et al., 2019b; Vartanyan et al., 2019b; Burrows et al., 2019, 2020; Bollig et al., 2021). Those works have convincingly shown that CCSN explosions can be initiated by neutrino-energy deposition, assisted by large-scale hydrodynamic instabilities such as turbulent convection or the SASI, thus demonstrating the viability of the neutrino-driven mechanism in principle.

Numerous studies have, in much detail, investigated the evolution during the first few hundred milliseconds on the way towards successful shock revival, approaching the multi-faceted CCSN problem from different perspectives and investigating possibly relevant, still missing physical ingredients. In this regard, e.g., the impact of progenitor rotation has been studied (Fryer & Warren, 2004; Kuroda et al., 2014; Nakamura et al., 2014; Takiwaki et al., 2016; Summa et al., 2018; Powell & Müller, 2020); the presence of magnetic fields, either for rapidly rotating stars in the context of magneto-rotational SNe (Mösta et al., 2014; Kuroda et al., 2020; Obergaulinger & Aloy, 2021; Bugli et al., 2021), or for slowly- and non-rotating progenitors (Müller & Varma, 2020; Matsumoto et al., 2022; Varma et al., 2023); the aiding effects of progenitor perturbations from convective shell burning prior to core collapse (e.g., Couch & Ott, 2013; Müller & Janka, 2015; Müller et al., 2017, 2019; Bollig et al., 2021; Vartanyan et al., 2022); as well as uncertainties related to the employed microphysics (e.g., Melson et al., 2015a; Bollig et al., 2017; Yasin et al., 2020) or the numerical grid resolution (e.g., Abdikamalov et al., 2015; Radice et al., 2015, 2016; Nagakura et al., 2019; Melson et al., 2020). Beyond that, 3D CCSN models have been used to predict the measurable signals of neutrinos (e.g., Tamborra et al., 2013, 2014b; Takiwaki & Kotake, 2018; Walk et al., 2019, 2020; Vartanyan et al., 2019a) and gravitational waves (e.g., Kuroda et al., 2016a; Andresen et al., 2017, 2021; Vartanyan & Burrows, 2020; Powell & Müller, 2019, 2022). For more details on the status of 3D CCSN modeling, we refer to dedicated review articles, e.g., by Janka et al. (2016); Müller (2016, 2020); Burrows & Vartanyan (2021).

1.4.2. Open Questions

Despite the remarkable progress in the understanding of CCSN explosions that has been achieved by modern 3D neutrino-hydrodynamics simulations, the question remained whether the neutrino-driven mechanism can explain the properties of observed CCSNe (such as explosion energies, NS kick velocities, or the abundances and morphologies of chemical elements in the SN ejecta). Concerns were expressed that numerical models of neutrino-driven explosions might generally be under-energetic compared to observations (e.g., Papish et al., 2015; Murphy et al., 2019). Moreover, some authors have argued that self-consistent CCSN models may underproduce

radioactive ^{56}Ni compared to observations, which was coined the "nickel mass problem" (e.g., Suwa et al., 2019; Sawada & Suwa, 2023). However, due to the high computational demands of full-physics simulations with detailed neutrino transport, most 3D CCSN models to date have been evolved only until shortly after the onset of runaway shock expansion (i.e., typically until less than a second after core bounce). At this time, the explosion energy just begins to rise steeply, with values still far below the observationally inferred explosion energies of typically ∼0.5–1 B (Kasen & Woosley, 2009; Pejcha & Prieto, 2015b; Martinez et al., 2022). Only for stars near the low-mass end of CCSN progenitors (e.g., Kitaura et al., 2006; Melson et al., 2015b; Stockinger et al., 2020) or for ultra-stripped SNe (e.g., Müller et al., 2019), which exhibit steeply declining density profiles outside of their degenerate cores and thus explode readily and with fast shock expansion, such short timescales of less than 1 s may be sufficient to achieve converged explosion properties. For more massive progenitors with flatter density profiles and consequently higher mass-accretion rates, much longer evolution times (of several seconds) are needed for a saturation of the explosion energy, heavy-element nucleosynthesis yields, and NS properties (see, e.g., the long-time 2D simulations by Müller, 2015; Bruenn et al., 2016; Nakamura et al., 2019; Burrows & Vartanyan, 2021; Witt et al., 2021; Bruenn et al., 2023; or the 3D model by Müller et al., 2017).[8]

1.5. Goals and Outline of this Thesis

In the work at hand, we aim to close this gap between the early phase of shock revival and the fully developed explosion stage of neutrino-driven CCSNe. For the first time, we evolve a set of self-consistently exploded 3D SN models from the onset of the explosion over several seconds until energy saturation is reached asymptotically. For this purpose, we developed a computationally efficient scheme that accounts for the most crucial neutrino effects in an approximative manner, thus replacing the expensive neutrino transport calculations. This novel treatment — termed Nemesis (which stands for **N**eutrino-**E**xtrapolation **M**ethod for **E**fficient **SI**mulations of **S**upernova explosions) — comprises, in particular, the energy transfer of neutrinos to the stellar medium, which can drive persistent neutrino-heated outflows and can, therefore, fuel the continuous rise of the explosion energy and the growth of significant, large-scale explosion asymmetries. Moreover, the Nemesis scheme includes an approximate description of the electron-lepton-number changes by neutrino emission and absorption, which determine the electron fraction and, thus, the chemical composition of the SN ejecta.

[8] Further exceptions may arise in the rare case of rapidly rotating, strongly magnetized stars that explode in magneto-rotational SNe with relatively quick energy saturation (e.g., Obergaulinger & Aloy, 2021). Nevertheless, most CCSN progenitors can be expected to have only moderately rotating cores at the time of gravitational collapse due to efficient angular-momentum transport during the stellar evolution (e.g., Heger et al., 2005).

Our novel neutrino treatment, which we couple to full-3D stellar hydrodynamics, allows us to follow up the explosions from a set of previously computed, self-consistent 3D CCSN simulations with full, energy-dependent neutrino transport (Melson et al., 2015a,b, 2020; Summa et al., 2018; Bollig et al., 2021) and to extend their evolution until several seconds after the core bounce with an acceptable investment of computational resources. The basic idea of our approach is to adopt the neutrino (energy and lepton-number) source terms at the end of the full-transport 3D models and to smoothly extrapolate their time evolution through an analytical rescaling and transformation procedure based on local gas quantities and guided by time-dependent neutrino inputs from corresponding 1D PNS cooling simulations. In this way, we ensure that neutrino effects are included until late times when the central PNS has cooled down considerably, and the neutrino emission has declined to an insignificant level.

The following key scientific questions shall be addressed in the context of this thesis by performing a suite of seven long-time 3D hydrodynamics simulations with our new Nemesis scheme, extending the evolution of previous, fully self-consistent CCSN models with detailed neutrino transport:

- What are the terminal values of the explosion energy that can be reached in self-consistent models of neutrino-driven CCSNe? And on which timescales do the explosion energies saturate to their final values?

- What are the nucleosynthetic conditions for the formation of heavy chemical elements in the neutrino-processed ejecta? How does the proton-to-neutron ratio in the innermost SN ejecta evolve over time, and how does it vary spatially? How much radioactive ^{56}Ni is synthesized during the explosions?

- What are the properties of the newborn NSs, such as their masses, natal recoil kicks, and spin periods? How long does it take until the NSs get accelerated to their final kick velocities? And how large is the impact of anisotropic neutrino emission on the NS kick acceleration, as opposed to the hydrodynamic effects related to asymmetric mass ejection?

The thesis is organized as follows. In Chapter 2, we first describe the numerical methods used in this work. We introduce the fundamental equations of stellar hydrodynamics and neutrino transport as solved in the Prometheus-Vertex code (Section 2.1), provide a detailed discussion of our newly implemented Nemesis scheme (Section 2.2), and briefly comment on the performance and scaling efficiency of our numerical code (Section 2.3). In Chapter 3, we present the results of our 3D CCSN simulations. After a brief discussion of the employed stellar progenitor models (Section 3.1), we first summarize the main outcomes of the previously computed explosion models by Melson et al. (2015a,b, 2020), Summa et al. (2018), and Bollig et al. (2021) with full-fledged neutrino transport (Section 3.2), which are the starting points of our long-time 3D hydrodynamics simulations with the Nemesis treatment.

The main results of these (long-time) extension models are then discussed in Section 3.3, where we return to the guiding question of this thesis, namely whether neutrino-driven CCSN models can reach the typical explosion energies of observed SNe. More details on the growth of the explosion energy are provided in Section 3.4. Section 3.5 gives a brief overview of the nucleosynthesis yields of our models. The NS properties (i.e., kick velocities and spin periods) of our models are discussed in Section 3.6. We conclude with a summary of our most important results and a brief outlook in Chapter 4. Supplementary material can be found in Appendix A.

Some of the results discussed in this thesis have already been published in the works by Stockinger et al. (2020) and Bollig et al. (2021). We adopt some content from these two publications in this thesis, yet only the author's contributions are taken. Corresponding remarks are given at the beginnings of each section where this applies. Moreover, large parts of this thesis serve as input for forthcoming papers (Kresse et al., in preparation; Janka & Kresse, in preparation).

2
Numerical Methods

Modeling neutrino-driven CCSN explosions requires sophisticated tools to solve the complex interplay of stellar hydrodynamics and neutrino physics. In this chapter, we first describe the radiation hydrodynamics code Prometheus-Vertex (Section 2.1), which has been used by the Garching group over the past years to simulate a growing set of self-consistent 3D CCSN models, providing the initial conditions for the extension runs to later times simulated for this thesis. In Section 2.2, we then provide a detailed discussion of our newly developed Nemesis neutrino treatment, which enables us to perform 3D simulations with neutrino physics over timescales of several seconds until saturation of the explosion energy is reached asymptotically. In Section 2.3, we briefly comment on the performance and scaling efficiency of our simulation code.

Throughout this thesis, we use bold symbols to indicate vector-valued quantities, e.g., $\boldsymbol{v}$, while we write their absolute values in non-bold notation, i.e., v. If not stated otherwise, we employ spherical coordinates (r, θ, ϕ), with r denoting the radius, θ the polar angle, and ϕ the azimuthal angle.

2.1. The Prometheus-Vertex Code

For all models discussed in this thesis, the early evolutionary phases during the first ∼1–2 seconds — i.e., from core collapse and bounce through shock formation and shock stagnation to the eventual shock revival by neutrino heating — have been simulated with the radiation hydrodynamics code Prometheus-Vertex, which has been initially developed by Rampp & Janka (2002) for spherically symmetric (1D) SN simulations. The code has later been extended for multidimensional setups (in axial symmetry, i.e., 2D) by Buras et al. (2006b) and for application in full 3D geometry by Hanke (2014). In its latest version, it employs an axis-free overset Yin-Yang grid (as implemented by Melson, 2016), includes an effective general-relativistic gravitational potential (Marek et al., 2006, "Case A"), and has recently been updated and improved significantly concerning the employed microphysics as well as computational efficiency by Bollig (2018).

Prometheus-Vertex couples the time-explicit, Newtonian finite-volume hydrodynamics code Prometheus (Fryxell et al., 1989; Keil, 1997; Kifonidis et al., 2003) with the fully time-implicit neutrino transport module Vertex, which solves the two-moment equations with Boltzmann closure by means of the "variable Eddington

factor" method of Rampp & Janka (2002), using the "ray-by-ray plus" approximation of Buras et al. (2006b), including the most modern set of neutrino interactions. In the following, we will describe these two computational modules in some more detail, together with the fundamental equations of stellar hydrodynamics and neutrino radiative transfer.

2.1.1. Hydrodynamics

In good approximation, stellar matter can be regarded as an ideal fluid because the effects of viscosity and heat conduction are typically small in astrophysical flows and can thus be neglected (e.g., Müller, 1998; Abdikamalov et al., 2015).[9] The dynamics of the stellar plasma are therefore governed by the inviscid and compressible Euler equations (instead of the viscous and compressible Navier-Stokes equations), which are conservation laws for mass, momentum, and energy. In non-relativistic formulation, the equations read:

$$\frac{\partial \rho}{\partial t} + \nabla \cdot (\rho\, \boldsymbol{v}) = 0\,, \tag{2.1}$$

$$\frac{\partial}{\partial t}(\rho\, \boldsymbol{v}) + \nabla \cdot (\rho\, \boldsymbol{v} \otimes \boldsymbol{v}) + \nabla P = -\rho \nabla \Phi + \boldsymbol{Q}_{\mathbf{M}}\,, \tag{2.2}$$

$$\frac{\partial}{\partial t}(\rho\varepsilon) + \nabla \cdot ((\rho\varepsilon + P)\, \boldsymbol{v}) = -\rho\, \boldsymbol{v} \cdot \nabla \Phi + Q_{\mathrm{E}} + \boldsymbol{v} \cdot \boldsymbol{Q}_{\mathbf{M}}\,, \tag{2.3}$$

where $\rho = n_{\mathrm{B}} m_{\mathrm{u}}$ is the (baryonic) mass density, with n_{B} being the baryon number density and $m_{\mathrm{u}} = 1.66 \times 10^{-24}$ g the atomic mass unit; $\boldsymbol{v}$ is the fluid velocity, P the (isotropic) gas pressure, $\varepsilon = e + \boldsymbol{v} \cdot \boldsymbol{v}/2$ the specific total (i.e., internal plus kinetic) energy,[10] and Φ the gravitational potential of the fluid. The source terms, $\boldsymbol{Q}_{\mathbf{M}}$ and Q_{E}, incorporate the effects of momentum transfer and energy exchange by neutrino interactions (see Section 2.1.2). The symbol "$\otimes$" denotes the outer product (i.e., $\boldsymbol{a} \otimes \boldsymbol{b} = \boldsymbol{a}\, \boldsymbol{b}^{\intercal}$). All quantities in Equations (2.1)–(2.3) are functions of space (described by a position vector, $\boldsymbol{r}$, which is typically given in terms of spherical coordinates (r, θ, ϕ); see Section 2.1.3) and time, t.

The set of hydrodynamic equations is closed by an "equation of state" (EoS), which relates the gas pressure to the density and the specific internal energy (or temperature, T). Because, in general, the EoS also depends on the composition of

[9] Note, however, that every numerical method exhibits an intrinsic, finite numerical viscosity due to (unavoidable) discretization errors. The magnitude of the numerical viscosity depends on the employed numerical scheme, the resolution of the computational grid, and also on the properties of the flow itself (see, e.g., Abdikamalov et al., 2015; Melson et al., 2020).

[10] The internal energy density, ρe, is defined such that the "relativistic" energy density, $\rho_{\mathrm{tot}} c^2 = \rho(c^2 + e)$, includes the baryonic rest-mass energy density, $\rho_0 c^2 = n_{\mathrm{B}} \bar{m}_{\mathrm{B}} c^2$, where $\bar{m}_{\mathrm{B}}$ is the mean baryonic mass (which depends on the nuclear composition of the matter). This implies that ρe contains a "normalization" $\propto n_{\mathrm{B}}(\bar{m}_{\mathrm{B}} - m_{\mathrm{u}})c^2$.

the stellar fluid, the abundances of individual nuclear species need to be tracked by additional conservation equations:

$$\frac{\partial}{\partial t}(\rho X_i) + \nabla \cdot (\rho X_i \, \boldsymbol{v}) = R_i \,, \tag{2.4}$$

where X_i denotes the mass fraction of an individual nuclear species, $i = 1, ..., N_{\mathrm{nuc}}$, which satisfies $\sum_{i=1}^{N_{\mathrm{nuc}}} X_i = 1$. The mass fractions are defined according to $X_i := A_i n_i / n_{\mathrm{B}}$, where A_i and n_i are the atomic mass number and the number density of the nuclear species i. The source term R_i on the right-hand side of Equation (2.4) accounts for changes of the chemical composition due to nuclear reactions.

At sufficiently high temperatures, the stellar matter reaches nuclear statistical equilibrium (NSE), i.e., nuclear reactions proceed rapidly enough (compared to hydrodynamic timescales) such that reactive equilibrium is established. In this case, the thermodynamic state is fully determined by the density, the temperature, and the electron fraction, Y_{e}, which is defined as $Y_{\mathrm{e}} := (n_{\mathrm{e}^-} - n_{\mathrm{e}^+})/n_{\mathrm{B}}$, with n_{e^-} and n_{e^+} being the number densities of electrons and positrons, respectively. In NSE, the nuclear composition, $X_i = X_i(\rho, T, Y_{\mathrm{e}})$, can be computed from the Saha equations (see, e.g., Shapiro & Teukolsky 1983). In analogy to Equation (2.4), an additional advection equation needs to be solved also for the electron fraction:

$$\frac{\partial}{\partial t}(\rho Y_{\mathrm{e}}) + \nabla \cdot (\rho Y_{\mathrm{e}} \, \boldsymbol{v}) = Q_{\mathrm{N}} \,, \tag{2.5}$$

where Q_{N} denotes the source term for the change of the net electron number density due to the emission and absorption of electron-type neutrinos and antineutrinos (see Section 2.1.2).

Numerical Implementation

For numerical integration of Equations (2.1)–(2.5), we employ the Newtonian finite-volume hydrodynamics code Prometheus, which was developed by Fryxell et al. (1989) and later refined for application in supernova simulations by Keil (1997) and Kifonidis et al. (2003). It is based on a dimensionally split, time-explicit implementation of the piecewise parabolic method (PPM) of Colella & Woodward (1984), which is a conservative, Godunov-type scheme with third-order spatial and second-order temporal accuracy that employs an exact Riemann solver. In the vicinity of strong shocks, it switches from the original PPM solver to the (more diffusive) HLLE solver of Einfeldt (1988) to avoid the "odd-even decoupling" phenomenon (see, e.g., Quirk 1994; Kifonidis et al. 2003). The code is, therefore, capable of following flow discontinuities, such as shocks or boundary layers between shells of different chemical compositions, with high precision. The advection of individual nuclear species is, in regions where NSE does not hold, treated by the consistent multifluid advection (CMA) scheme of Plewa & Müller (1999). The computational time step of the hydrodynamics solver is constrained by the Courant–Friedrichs–Lewy (CFL)

condition (Courant et al., 1928), which depends on the local fluid velocity and the local sound speed as well as on the size of the numerical grid cells (see Section 2.1.3). Due to its high computational efficiency and numerical accuracy, the PROMETHEUS code is ideally suited for tackling the complex and intrinsically multi-dimensional problem of supernova explosions. It is the computational backbone of all simulations discussed in this thesis.

Treatment of Gravity

Even though PROMETHEUS is a purely Newtonian hydrodynamics code, it can take into account general relativistic effects in an approximate manner by employing an "effective gravitational potential" that mimics the deeper gravitational well as described by general relativity compared to the case of Newtonian gravity. Such an effective relativistic gravitational potential can be deduced from the Tolman-Oppenheimer-Volkoff (TOV) equation for hydrostatic equilibrium (see Rampp & Janka, 2002, Section 3.7). For the simulations discussed in this work, we employ the widely used modified TOV potential according to "Case A" of Marek et al. (2006) and assume spherical symmetry, i.e., $\Phi(\boldsymbol{r}, t) = \Phi(r, t)$, which is reasonably well justified because the gravitational field is dominated by the almost spherical mass distribution of the central PNS. The effective gravitational potential is given by

$$\Phi(r) = -G \int_r^\infty \mathrm{d}r' \frac{1}{r'^2} \left(m_{\mathrm{TOV}} + \frac{4\pi r'^3 (P + P_\nu)}{c^2} \right) \frac{1}{\Gamma^2} \left(\frac{\rho_{\mathrm{tot}} c^2 + P}{\rho c^2} \right) , \tag{2.6}$$

where G is the gravitational constant, c is the speed of light, r is the radius, P_ν is the neutrino pressure (see Section 2.1.2), and $\rho_{\mathrm{tot}} c^2 = \rho(c^2 + e)$ is the total ("relativistic") energy density of the fluid (i.e., the sum of internal and rest-mass energy densities; see footnote 10). The modified ("effective") TOV mass is computed according to

$$m_{\mathrm{TOV}}(r) = 4\pi \int_0^r \mathrm{d}r'\, r'^2 \left(\rho_{\mathrm{tot}} + \frac{\mathcal{E}_\nu}{c^2} + \frac{v F_\nu}{c^4 \Gamma} \right) \Gamma \, , \tag{2.7}$$

with $\mathcal{E}_\nu$ and F_ν being the neutrino energy density and neutrino energy flux, respectively (see Section 2.1.2), and v the fluid velocity in the radial direction. The metric function is defined as

$$\Gamma = \sqrt{1 + \frac{v^2}{c^2} - \frac{2G m_{\mathrm{TOV}}}{r' c^2}} \, . \tag{2.8}$$

All quantities entering Equations (2.6)–(2.8) are spherically averaged. The additional factor Γ in the integrand of Equation (2.7), which is not present in the standard TOV equations, corresponds to the (empirical) modification according to "Case A" of Marek et al. (2006). It reduces the TOV mass compared to its original definition as proposed by Rampp & Janka (2002), yielding a good agreement with full general relativistic simulations (see, e.g., Liebendörfer et al. 2005; Müller et al. 2010; da Silva

Schneider et al. 2020).

While we use a spherically symmetric, effective gravitational potential, another common approach in multi-dimensional simulations of CCSNe is to solve the Poisson equation for the Newtonian gravitational potential, $\nabla^2\Phi = 4\pi G\rho$, through a multipole expansion (see, e.g., Müller & Steinmetz 1995; Buras et al. 2006b; Couch et al. 2013; Almanstötter et al. 2018; Müller & Chan 2019) and to replace the monopole contribution by an effective TOV potential (as Equation (2.6) above), while leaving higher-order multipoles unchanged (e.g., Buras et al. 2006b; Marek et al. 2006). However, for models where the gravitational potential is dominated by the almost spherical (non-rotating or only moderately rotating) PNS, a 1D effective gravitational potential is sufficient and saves unnecessary computational overhead.

Equation of State

The closure relation for the set of fluid equations is given by an equation of state (EoS), which expresses the pressure as a function of the independent thermodynamic variables, i.e., $P = P(\rho, T, Y_\mathrm{e})$ if NSE holds, or $P = P(\rho, T, Y_\mathrm{e}, \{X_i\}_{i=1,\ldots,N_\mathrm{nuc}})$ otherwise. It needs to be provided for density-temperature regimes spanning from supranuclear densities (i.e., $\rho \sim 10^{15}\,\mathrm{g\,cm^{-3}}$) and temperatures of $T \gtrsim 10^{11}\,\mathrm{K}$ in the nascent PNS, down to much lower densities of $\rho \lesssim 10^{3}\,\mathrm{g\,cm^{-3}}$ and more moderate temperatures of $T \lesssim 10^{8}\,\mathrm{K}$ in the stellar envelope. To accommodate this wide range of conditions relevant to SN physics, we divide the EoS into a "low-density" and a "high-density" regime, which are separated by a threshold density, ρ_EoS (of typically $10^{11}\,\mathrm{g\,cm^{-3}}$).[11]

At low densities, i.e., for $\rho < \rho_\mathrm{EoS}$, we employ the EoS of Janka (1999), which treats the stellar matter as a mixture of ideal Boltzmann gases of nucleons and nuclei (using a tabulated NSE composition), plus ideal Fermi gases of arbitrarily degenerate and relativistic electrons and positrons, plus photons, and including a Coulomb lattice correction. In the high-density regime (i.e., for $\rho > \rho_\mathrm{EoS}$), we employ the widely used, pre-calculated, and tabulated mean-field EoS of Lattimer & Swesty (1991) for hot and dense matter, with an incompressibility modulus of bulk nuclear matter of $K = 220\,\mathrm{MeV}$ (in the following, referred to as "LS220"). This EoS is based on a compressible liquid-drop model and considers free nucleons, α particles, and one representative heavy nucleus (with, in general, a non-integer mass number). The LS220 EoS, which has been used previously by, e.g., Hanke et al. (2013); Tamborra et al. (2014a); Lentz et al. (2015); Abdikamalov et al. (2015); Müller (2015); Roberts et al. (2016); Summa et al. (2016); Radice et al. (2017), can support NSs up to a maximum (gravitational) mass of $\sim 2\,\mathrm{M_\odot}$, in rough agreement with the most massive observed pulsars (Demorest et al., 2010; Antoniadis et al., 2013; Cromartie et al.,

[11] For the collapse phase (i.e., before the core bounce), we use a lower threshold density of around 10^{7}–$10^{8}\,\mathrm{g\,cm^{-3}}$, while $\rho_\mathrm{EoS} = 10^{11}\,\mathrm{g\,cm^{-3}}$ is the standard choice for the entire post-bounce evolution of our models.

2020; Romani et al., 2021, 2022).

We want to add a somewhat technical remark: To avoid the total ("relativistic") energy density of the fluid being dominated by its rest-mass contribution, which would increase the risk of introducing numerical errors in our EoS interpolation routines, we re-normalize the energy as suggested by Lattimer & Swesty (1991). Accordingly, we subtract the term $(m_{\mathrm{n}}c^2 - 8.8\,\mathrm{MeV}) \cdot n_{\mathrm{B}} \approx 930.9\,\mathrm{MeV} \cdot n_{\mathrm{B}}$ from the total energy density, where m_{n} is the neutron rest mass and the value of 8.8 MeV is roughly equal to the binding energy per nucleon of iron.

Even though a thorough investigation of uncertainties related to the (still incompletely known) high-density EoS of nuclear matter is beyond the scope of this thesis, we still want to point out that meanwhile, a growing number of more modern, tabulated EoSs has become available, which are consistent with experimental data from heavy-ion collisions and are suitable for application in CCSN (and binary NS merger) simulations. Examples are the DD2 EoS (Typel et al., 2010; Hempel & Schaffner-Bielich, 2010), the SFHo and SFHx EoSs by Steiner et al. (2013), or the APR EoS of Schneider et al. (2019). For a detailed discussion on the EoS of dense matter, we refer, e.g., to the review article by Oertel et al. (2017).

Nuclear Reactions

Changes in the chemical composition through nuclear burning, photo-disintegration reactions, and recombination of free nucleons and α particles to heavy nuclei are approximately taken into account in our SN simulations.

Above a critical threshold temperature for NSE (typically $\sim$0.5 MeV), the nuclear composition is fully determined by the current thermodynamic state and is therefore given by the EoS. Once the temperatures in the expanding and cooling SN ejecta drop below this threshold temperature, the nuclear composition freezes out. We then map the NSE composition — under the constraint of charge neutrality and baryon number conservation — to a predefined, discrete set of nuclei, $\{(A_i, Z_i)\}_{i=1,\ldots,N_{\mathrm{nuc}}}$, consisting of neutrons, protons, α particles, and some suitably chosen heavy nuclei with atomic mass and charge numbers A_i and Z_i (for details, see Appendix B of Rampp & Janka 2002). In our standard setup, we consider $N_{\mathrm{nuc}} = 23$ nuclear species, whose advection with the fluid flow is followed via the CMA scheme of Plewa & Müller (1999), as mentioned above.

In the non-NSE regime, the most relevant nuclear reactions — i.e., silicon burning, carbon burning, and the burning of oxygen, neon, and magnesium to silicon — are modeled through the "flashing" treatment of Rampp & Janka (2002, Appendix B.2), which assumes that the conversions happen instantaneously at certain threshold temperatures characteristic of the considered reactions (see Hix & Thielemann, 1999a; Mezzacappa et al., 2001; Woosley et al., 2002). This assumption is well justified because the timescales of nuclear burning are short compared to hydrodynamic timescales. The adequate changes of the mass fractions X_i (and number densities n_i) of the individual nuclear species are taken into account in the fluid equations via the source term R_i on the right-hand side of Equation (2.4). Because

we define the specific internal energy to include nuclear rest-mass contributions (see footnote 10), the conversion between nuclear binding energy and thermal energy (and the corresponding adjustment of the fluid temperature) is automatically taken into account by our EoS. For this reason, no additional source term for nuclear energy generation (or consumption) appears in the energy conservation equation, i.e., Equation (2.3).

For one of our explosion models discussed in Chapter 3 (i.e., model s18.88), we substituted the flashing treatment of Rampp & Janka (2002) with a 23-species α-chain reaction network based on the nuclear burning network `XNet`[12] of Hix & Thielemann (1999b), which has recently been implemented in the Prometheus-Vertex code in an optimized version; see Bollig et al. (2021).

2.1.2. Neutrino Transport

In contrast to all other constituents of the stellar plasma, neutrinos are purely weakly interacting particles. Their mean free paths are much larger than the typical scales of macroscopic variations in the system. Consequently, neutrinos do not reach equilibrium with the surrounding matter (except at the extraordinarily high densities inside the PNS core regions). Therefore, neutrinos cannot be regarded as another fluid component, but a detailed radiation transport equation needs to be solved instead. In this subsection, we describe the essentials of neutrino radiative transfer and provide a brief overview of the neutrino transport module Vertex of the Prometheus-Vertex code. For details, we refer to the literature (e.g., Rampp 2000; Rampp & Janka 2002; Buras et al. 2006b).

The Boltzmann Transport Equation

The neutrino radiation field at a spatial position $\boldsymbol{r}$ for a single neutrino species $\nu \in \{\nu_\mathrm{e}, \bar{\nu}_\mathrm{e}, \nu_x\}$, with ν_x denoting a representative "heavy-lepton neutrino" $\{\nu_\mu, \bar{\nu}_\mu, \nu_\tau, \bar{\nu}_\tau\}$,[13] is commonly described by the dimensionless one-particle phase-space distribution function, $f(\boldsymbol{r}, \boldsymbol{p}, t)$, or, equivalently, by the specific ("monochromatic," i.e., energy-dependent) intensity, $\mathcal{I}$, which is related to f by:

$$\mathcal{I}(\boldsymbol{r}, \hat{\boldsymbol{n}}, \epsilon, t) = \frac{\epsilon^3}{h^3 c^2} f(\boldsymbol{r}, \hat{\boldsymbol{n}}, \epsilon, t)\,. \tag{2.9}$$

[12] https://github.com/starkiller-astro/XNet

[13] In most CCSN simulations to date, the four heavy-lepton (anti-)neutrinos, ν_μ, $\bar{\nu}_\mu$, ν_τ, and $\bar{\nu}_\tau$, are treated equally and commonly denoted by a placeholder ν_x. Such an approximation is motivated by the large masses of muons and tau leptons (0.1 GeV/c^2 and 1.8 GeV/c^2, respectively), which suppress their (abundant) formation at the temperatures typical for SN matter (implying small chemical potentials, $\mu_{\nu_\mu} \simeq \mu_{\nu_\tau} \simeq 0$). However, recently it has been shown that muon creation can have a non-negligible impact on the cooling and contraction behavior of PNSs (see, e.g., Bollig et al. 2017; Bollig 2018; Fischer et al. 2020). Note that, for reasons of clarity, we mostly omit the indices for the individual neutrino species in this section.

Here, $\hat{\boldsymbol{n}} = \boldsymbol{p}/p$ denotes the direction of neutrino propagation (which is inclined relative to $\boldsymbol{r}$ by an angle ϑ), $\boldsymbol{p}$ is the neutrino momentum, and $\epsilon = pc$ its energy (assuming neutrinos to be massless particles);[14] t is the time, h the Planck constant, and c the speed of light. The quantity $\mathcal{I}(\boldsymbol{r}, \hat{\boldsymbol{n}}, \epsilon, t) \cdot \cos\vartheta \, \mathrm{d}A \, \mathrm{d}\Omega \, \mathrm{d}\epsilon \, \mathrm{d}t$ can be understood as the amount of radiation energy in the energy interval $[\epsilon, \epsilon + \mathrm{d}\epsilon]$ that streams per unit time $\mathrm{d}t$ through the surface element $\mathrm{d}A$ with normal vector $\hat{\boldsymbol{r}} = \boldsymbol{r}/r$ into the solid angle $\mathrm{d}\Omega$ around $\hat{\boldsymbol{n}}$. The time evolution of the specific intensity is governed by the Boltzmann transport equation,

$$\frac{1}{c}\frac{\partial \mathcal{I}}{\partial t} + \hat{\boldsymbol{n}} \cdot \nabla \mathcal{I} = C(\mathcal{I}) \,. \tag{2.10}$$

Here, the so-called "collision integral," $C(\mathcal{I})$, encapsulates the neutrino interactions with the stellar matter (as well as neutrino-neutrino reactions). It contains source terms associated with neutrino emission processes, sink terms corresponding to neutrino absorption, and terms for redistributing neutrinos in energy-momentum space due to scattering reactions (out of and into the direction of propagation). Table 2.1 provides an overview of all neutrino interactions that are included in the code version of PROMETHEUS-VERTEX as employed for the models discussed in this thesis.

Angular-moment Scheme

Because the collision term $C(\mathcal{I})$ depends not only on the specific intensity, $\mathcal{I}$, but also on momentum-space integrals of $\mathcal{I}$ (possibly for multiple neutrino species), the Boltzmann transport equation is, in fact, an integro-differential equation, which makes it particularly difficult to tackle numerically. Moreover, solving the Boltzmann equation is a seven-dimensional problem, as the specific radiation intensity depends on three spatial coordinates, three momentum components, and time. Therefore, approximations are necessary to achieve numerical convergence with an acceptable amount of computing resources.

A widely used strategy to reduce the dimensionality of the problem is to express the specific intensity in terms of angular moments, which are defined as

$$\mathcal{I}^{(k)}(\boldsymbol{r}, \epsilon, t) = \frac{1}{4\pi} \int \mathrm{d}\Omega \, (\underbrace{\hat{\boldsymbol{n}} \otimes \hat{\boldsymbol{n}} \otimes \ldots \otimes \hat{\boldsymbol{n}}}_{\text{k times}}) \, \mathcal{I}(\boldsymbol{r}, \hat{\boldsymbol{n}}, \epsilon, t) \,, \tag{2.11}$$

where $k = 0, 1, \ldots$ runs up to some arbitrarily chosen order, and $\mathrm{d}\Omega$ denotes the solid angle in momentum space. Instead of the full Boltzmann transport equation (which would be recovered in the limit $k \to \infty$), a set of truncated moment equations is solved, typically for the zeroth and first angular moments, while a closure relation

[14] The assumption of effectively massless neutrinos (propagating with the speed of light) is well justified because of their small masses ($\lesssim$1 eV; Aker et al. 2019).

Table 2.1.: Overview of all neutrino interactions included in the code version of Prometheus-Vertex as employed for the models discussed in this thesis, with corresponding references to the literature.

Reaction			References
$\nu\,\mathrm{e}^{\pm}$	$\rightleftharpoons$	$\nu\,\mathrm{e}^{\pm}$	Mezzacappa & Bruenn (1993a); Cernohorsky (1994)
$\nu\,A_Z$	$\rightleftharpoons$	$\nu\,A_Z$	Horowitz (1997); Bruenn & Mezzacappa (1997) Langanke et al. (2008)
$\nu\,\mathrm{N}$	$\rightleftharpoons$	$\nu\,\mathrm{N}$	Burrows & Sawyer (1998); Horowitz et al. (2017)
$\bar{\nu}_\mathrm{e}\,\mathrm{p}$	$\rightleftharpoons$	$\mathrm{e}^+\,\mathrm{n}$	Burrows & Sawyer (1999)
$\nu_\mathrm{e}\,\mathrm{n}$	$\rightleftharpoons$	$\mathrm{e}^-\,\mathrm{p}$	Burrows & Sawyer (1999)
$\nu_\mathrm{e}\,A_{Z-1}$	$\rightleftharpoons$	$\mathrm{e}^-\,A_Z$	Bruenn (1985); Mezzacappa & Bruenn (1993b) Langanke et al. (2003)
$\nu\,\bar{\nu}$	$\rightleftharpoons$	$\mathrm{e}^-\,\mathrm{e}^+$	Bruenn (1985); Pons et al. (1998)
$\nu\,\bar{\nu}\,\mathrm{N}\,\mathrm{N}$	$\rightleftharpoons$	$\mathrm{N}\,\mathrm{N}$	Hannestad & Raffelt (1998)
$\nu_{\mu,\tau}\,\bar{\nu}_{\mu,\tau}$	$\rightleftharpoons$	$\nu_\mathrm{e}\,\bar{\nu}_\mathrm{e}$	Buras et al. (2003)
$\nu_{\mu,\tau}\,\nu_\mathrm{e}$	$\rightleftharpoons$	$\nu_{\mu,\tau}\,\nu_\mathrm{e}$	Buras et al. (2003)
$\bar{\nu}_{\mu,\tau}\,\bar{\nu}_\mathrm{e}$	$\rightleftharpoons$	$\bar{\nu}_{\mu,\tau}\,\bar{\nu}_\mathrm{e}$	Buras et al. (2003)

Note. Here, ν and $\bar{\nu}$ are placeholders for neutrinos and antineutrinos of any flavor, $A_Z := (A, Z)$ is a short notation for an atomic nucleus with mass number A and charge number Z, and $\mathrm{N} \in \{\mathrm{p}, \mathrm{n}\}$ denotes a free nucleon (i.e., a proton or neutron). Details on the numerical implementation of the reaction rates for the listed neutrino interactions can be found in Rampp & Janka (2002); Buras et al. (2003, 2006b). Note that the most recent version of the Prometheus-Vertex code is capable of full six-species neutrino transport and also includes muonic neutrino interactions; see Bollig et al. (2017); Bollig (2018).

gives the higher moments; see below. We refrain from providing expressions for the moment equations here and refer the interested reader to Rampp & Janka (2002, Equations (7) and (8)) for the spherically symmetric case and to Appendix B of Buras et al. (2006b) for the full-3D moment equations.

The "Ray-by-ray plus" Approach

In the Prometheus-Vertex code, the dimensionality of the problem is further reduced through the so-called "ray-by-ray" approximation (Rampp & Janka, 2002; Buras et al., 2006b), where the specific intensity is assumed to be axially symmetric around the radial direction. Under this assumption, the lateral and azimuthal fluxes vanish, and the full neutrino transport problem decouples into a system of individual, effectively 1D problems along "radial rays" in each angular direction, which allows for excellent parallel computing efficiency. In the framework of the ray-by-ray approach,

the angular moments of Equation (2.11) simplify to

$$\mathcal{I}^{(k)}(\boldsymbol{r},\epsilon,t) = \frac{1}{2}\int_{-1}^{1} \mathrm{d}\mu\, \mu^k \mathcal{I}(\boldsymbol{r},\mu,\epsilon,t)\,, \tag{2.12}$$

where $\mu := \cos\vartheta = \hat{\boldsymbol{r}}\cdot\hat{\boldsymbol{n}}$ is the cosine of the angle between the radial direction and the neutrino momentum vector. Based on the angular moments of the specific intensity, we define the following energy-integrated quantities:

$$\mathcal{N}_\nu(\boldsymbol{r},t) = \frac{2\pi}{c}\int_0^\infty \mathrm{d}\epsilon\, \epsilon^{-1}\int_{-1}^{1} \mathrm{d}\mu\, \mathcal{I}(\boldsymbol{r},\mu,\epsilon,t)\,, \tag{2.13}$$

$$\mathcal{E}_\nu(\boldsymbol{r},t) = \frac{2\pi}{c}\int_0^\infty \mathrm{d}\epsilon \int_{-1}^{1} \mathrm{d}\mu\, \mathcal{I}(\boldsymbol{r},\mu,\epsilon,t)\,, \tag{2.14}$$

$$F_\nu(\boldsymbol{r},t) = 2\pi\int_0^\infty \mathrm{d}\epsilon \int_{-1}^{1} \mathrm{d}\mu\, \mu\, \mathcal{I}(\boldsymbol{r},\mu,\epsilon,t)\,, \tag{2.15}$$

$$P_\nu(\boldsymbol{r},t) = \frac{2\pi}{c}\int_0^\infty \mathrm{d}\epsilon \int_{-1}^{1} \mathrm{d}\mu\, \mu^2\, \mathcal{I}(\boldsymbol{r},\mu,\epsilon,t)\,, \tag{2.16}$$

which denote the neutrino number density, the neutrino energy density, the neutrino energy flux density (pointing in the radial direction), and the radial (i.e., rr) component of the neutrino pressure tensor, respectively. By integration over the solid angle in position space, we further define the neutrino luminosity $L_\nu(r,t)$ and the neutrino mean energy $E_\nu(r,t)$ for a given radius r and time t:

$$L_\nu(r,t) = r^2 \int \mathrm{d}\Omega\, F_\nu(\boldsymbol{r},t)\,, \tag{2.17}$$

$$E_\nu(r,t) = \frac{1}{4\pi}\int \mathrm{d}\Omega\, \frac{\mathcal{E}_\nu(\boldsymbol{r},t)}{\mathcal{N}_\nu(\boldsymbol{r},t)}\,. \tag{2.18}$$

The Vertex neutrino transport module solves the two lowest-order moment equations in a "mixed-frame approach," where all physical quantities are measured in the comoving (Lagrangian) fluid frame of reference, whereas the spatial coordinates (r,θ,ϕ) are defined in the (Eulerian) lab frame. The transformation of the moment equations into the fluid frame introduces additional terms accounting for relativistic Doppler effects and advective transport, which are treated accurately to $\mathcal{O}(v/c)$ of the local fluid velocity v. According to the "ray-by-ray plus" approach of Buras et al. (2006b), this also includes terms for the nonradial (i.e., lateral and azimuthal) advection of neutrinos with the fluid, which leads to an angular coupling of neighboring transport rays. Moreover, in the optically thick regime (inside the high-density PNS core, at densities larger than $10^{12}\,\mathrm{g\,cm^{-3}}$), also nonradial neutrino-momentum transfer to the stellar medium is approximately taken into account. Detailed tests in a recent study by Glas et al. (2019b) have shown that ray-by-ray-plus neutrino-transport calculations yield results in good agreement with fully multidimensional two-moment schemes.

Variable Eddington Factor Method

Because the lowest-order moment equations (for the specific neutrino energy density $\propto \mathcal{I}^{(0)}$ and the specific neutrino energy flux $\propto \mathcal{I}^{(1)}$) also include higher angular moments (i.e., the second and third moments, $\mathcal{I}^{(2)}$ and $\mathcal{I}^{(3)}$), the truncated system of equations needs to be supplemented by adequate closure relations. In the VERTEX transport module, this is done in the framework of the variable Eddington factor method, where the higher moments are given by $\mathcal{I}^{(2)} = f_2 \cdot \mathcal{I}^{(0)}$ and $\mathcal{I}^{(3)} = f_3 \cdot \mathcal{I}^{(0)}$. The eponymous "variable Eddington factors," f_2 and f_3, are computed from the formal solution of a simplified ("model") Boltzmann equation in an iterative procedure, using the tangent-ray discretization described in Mihalas & Mihalas (1984) and Rampp & Janka (2002).

One clear advantage of the VERTEX neutrino transport compared to other methods employed in the SN community — besides its most complete set of neutrino interaction processes — is that the (variable Eddington factor) Boltzmann closure retains the linear nature of the coupled set of neutrino energy and momentum equations. It, therefore, avoids shortcomings of the commonly used algebraic (non-linear) M1 closure; see, e.g., the beam-crossing problem (Foucart et al., 2015; Foucart, 2018).

Coupling to the Hydrodynamics

The neutrino source terms that appear on the right-hand sides of the hydrodynamics equations for energy, momentum, and electron-lepton number conservation (i.e., Equations (2.3), (2.2), and (2.5)), describing the coupling of the neutrino radiation field with the stellar fluid, are computed according to:

$$Q_{\mathrm{E}}(\boldsymbol{r},t) = -4\pi \int_0^\infty \mathrm{d}\epsilon \sum_\nu C_\nu^{(0)}(\boldsymbol{r},\epsilon,t)\,, \tag{2.19}$$

$$\boldsymbol{Q}_{\mathrm{M}}(\boldsymbol{r},t) = -\frac{4\pi}{c} \int_0^\infty \mathrm{d}\epsilon \sum_\nu \boldsymbol{C}_\nu^{(\mathbf{1})}(\boldsymbol{r},\epsilon,t)\,, \tag{2.20}$$

where the sums run over all six neutrino species. Since changes in the electron-lepton number can only be caused by the emission and absorption of electron-type neutrinos and antineutrinos, the source term for Y_{e} is instead given by:

$$Q_{\mathrm{N}}(\boldsymbol{r},t) = -4\pi\, m_{\mathrm{B}} \int_0^\infty \mathrm{d}\epsilon\, \epsilon^{-1} \left[C_{\nu_{\mathrm{e}}}^{(0)}(\boldsymbol{r},\epsilon,t) - C_{\bar{\nu}_{\mathrm{e}}}^{(0)}(\boldsymbol{r},\epsilon,t)\right]. \tag{2.21}$$

The zeroth and first angular moments of the collision integral, $C_\nu^{(0)}$ and $\boldsymbol{C}_\nu^{(\mathbf{1})}$, are computed in analogy to the definition of the angular moments of the specific intensity in Equation (2.11):

$$C_\nu^{(0)}(\boldsymbol{r},\epsilon,t) := \frac{1}{4\pi} \int \mathrm{d}\Omega\, C_\nu(\boldsymbol{r},\hat{\boldsymbol{n}},\epsilon,t) \tag{2.22}$$

$$\boldsymbol{C}_\nu^{(\mathbf{1})}(\boldsymbol{r},\epsilon,t) := \frac{1}{4\pi} \int \mathrm{d}\Omega\, \hat{\boldsymbol{n}}\, C_\nu(\boldsymbol{r},\hat{\boldsymbol{n}},\epsilon,t) \tag{2.23}$$

Note that, in the regime of neutrino trapping (at densities larger than $10^{12}\,\mathrm{g\,cm^{-3}}$), the neutrino-momentum source term of Equation (2.20) also includes contributions from neutrino pressure gradients in nonradial (i.e., lateral and azimuthal) directions in the ray-by-ray-plus approach and is therefore a vector-valued quantity.

The neutrino source terms, as given by Equations (2.19)–(2.21), are included in the hydrodynamics solver in an "operator-split" manner, i.e., the neutrino transport and the hydrodynamics equations are solved in two independent, sequentially computed steps. While the hydrodynamic time step is restricted by the CFL criterion (see Section 2.1.1), our fully implicit neutrino-transport solver allows for typically much larger time steps. Therefore, several substeps of the hydrodynamics calculations are generally performed during one (computationally more expensive) neutrino-transport step; for the details, see Rampp & Janka (2002, Section 3.6.1). More information on the coupling of the neutrino transport with the hydrodynamics and on technical aspects regarding the numerical implementation in the Prometheus-Vertex code can be found in Rampp (2000), Rampp & Janka (2002), Buras et al. (2006b), and also Hanke (2014) for the full 3D case.

2.1.3. Computational Grids

The equations of hydrodynamics and neutrino radiative transfer, as described in Subsections 2.1.1 and 2.1.2, are formulated in terms of *continuous* quantities. To be able to solve these equations numerically, all quantities need to be *discretized* on a suitable computational grid. Because CCSNe are — barring the strong asymmetries that develop during the explosion — spherical events to first order, Prometheus-Vertex employs numerical grids that are based on spherical coordinates (r, θ, ϕ); namely the conventional spherical polar grid or, more recently, an axis-free overset Yin-Yang grid, as first introduced by Kageyama & Sato (2004). We briefly describe these two grid configurations below.

In contrast to Cartesian grids, spherical grids preserve spherical symmetry accurately without imposing artificial perturbations on radial flows and are therefore well-suited to describe, particularly, the regions in and around the almost spherical PNS at the grid center. For this same reason, we need to introduce small perturbations "by hand" to seed the growth of nonradial fluid flows in our 3D simulations in the case of starting from spherically symmetric initial conditions (typically, this is done by imposing random cell-to-cell perturbations in the density or radial velocity with an amplitude of 0.1% shortly after core bounce; however, see Section 3.1 for the use of more realistic 3D pre-collapse initial conditions).

To accommodate the vastly different spatial scales of relevance (ranging from $\mathcal{O}(10)$ meters at the PNS surface to thousands of kilometers in the SN envelope), we employ a non-equidistant (logarithmically spaced) radial grid that is gradually refined throughout a simulation to adequately resolve the steepening density gradients at the edge of the cooling and contracting PNS. The computational grid extends to a maximum radius of several ten thousand kilometers, where we employ an inflow

boundary condition for the hydrodynamics (with a constant mass inflow rate) and a free outflow condition for neutrinos.[15] Once the expanding SN shock reaches close to this outer boundary, we expand the radial grid to even larger radii (typically ∼100,000 km after an evolution period of a few seconds).

Spherical Polar Grid

For one of our models discussed in this thesis, namely model s20, a conventional spherical polar grid was employed for the early evolution period with full Vertex neutrino transport; see Melson et al. (2015a). In the left panel of Figure 2.1, we provide a schematic sketch of the corresponding arrangement of the angular zones, with uniform angular resolution in both polar and azimuthal directions. Note, however, that we only show an exemplary grid with a resolution of 7.5° for illustration. In contrast, the actual simulation of model s20 has been carried out with a uniform angular resolution of 2°. The angular domain covers the entire sphere, i.e., $0 \leqslant \theta \leqslant \pi$ in polar direction and $0 \leqslant \phi \leqslant 2\pi$ in azimuthal direction. At the grid axis (i.e., at $\theta = 0$ and $\theta = \pi$), we impose reflecting boundary conditions, whereas periodic boundaries are employed in azimuthal direction at $\phi = 0$ and $\phi = 2\pi$. As noted above, we use a logarithmically spaced grid in the radial direction, $0 \leqslant r \leqslant r_{\mathrm{max}}$, with an inflow boundary condition at r_{max} (and a reflecting boundary at the coordinate origin). The spherical polar grid has been employed in several simulations with the Prometheus-Vertex code (e.g., Hanke et al., 2012, 2013; Tamborra et al., 2014a; Melson et al., 2015a).

Known drawbacks of the spherical polar grid are its singularities at the poles and the correspondingly small, wedge-shaped cells around the grid axis (see Figure 2.1), which dictate the CFL time step for a given radius (unless the fluid velocities are overly high elsewhere). Moreover, the polar axis is a potential source of numerical artifacts because the smaller grid zones near the poles also lead to a reduced numerical viscosity compared to regions of lower latitudes. This can have the consequence that postshock instabilities (like convection or the SASI) develop faster along the poles compared to the equator (e.g., Kane et al., 2000; Hanke et al., 2012; Müller, 2015; Melson et al., 2020). These shortcomings of the spherical polar grid can be overcome by utilizing a so-called Yin-Yang grid.

Yin-Yang Grid

Most of the models discussed in this thesis have been simulated on an axis-free overset Yin-Yang grid, which was first proposed by Kageyama & Sato (2004) in the context of geophysical applications and later implemented in the Prometheus-Vertex

[15] We note in passing that the two computational modules of our simulation code, the Prometheus hydrodynamics solver and the Vertex neutrino-transport module, do not only employ different computational time steps (as mentioned above). They also allow for choosing different spatial grids; see Rampp & Janka (2002, Section 3.6.2) for more details.

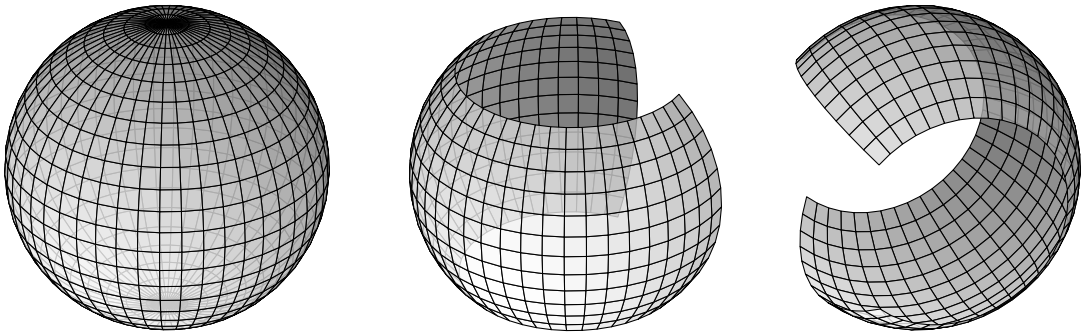

Figure 2.1.: Schematic picture of the computational grids as employed in PROMETHEUS-VERTEX. *Left:* Spherical polar grid. *Center/right:* "Yin" and "Yang" grid patches of an axis-free overset Yin-Yang grid. Note that, for illustration, we only show grid configurations with an angular resolution of 7.5°. In contrast, our simulations are computed on grids with typically 2° resolution (see Chapter 3 for the detailed specifications of our models).

code by Melson (2016), guided by the work of Wongwathanarat et al. (2010a). This multi-patch grid consists of two identical, partly overlapping low-latitude subsets of the spherical polar grid (with $\pi/4 \leqslant \theta \leqslant 3\pi/4$ and $-3\pi/4 \leqslant \phi \leqslant 3\pi/4$) that are rotated against each other. The two grid patches, schematically illustrated in the center and right panels of Figure 2.1, are denoted as "Yin" and "Yang." The transformation between the reference frames of the two individual component grids is most conveniently expressed in terms of Cartesian coordinates of the Yin and Yang systems:

$$\begin{pmatrix} x_{\mathrm{yin}} \\ y_{\mathrm{yin}} \\ z_{\mathrm{yin}} \end{pmatrix} = \begin{pmatrix} -1 & 0 & 0 \\ 0 & 0 & 1 \\ 0 & 1 & 0 \end{pmatrix} \begin{pmatrix} x_{\mathrm{yang}} \\ y_{\mathrm{yang}} \\ z_{\mathrm{yang}} \end{pmatrix} . \tag{2.24}$$

The (local) Cartesian coordinates are related to the spherical coordinates of the Yin and Yang frames in the usual way, i.e., $x_{\mathrm{y}} = r \sin\theta_{\mathrm{y}} \cos\phi_{\mathrm{y}}$, $y_{\mathrm{y}} = r \sin\theta_{\mathrm{y}} \sin\phi_{\mathrm{y}}$, and $z_{\mathrm{y}} = r \cos\theta_{\mathrm{y}}$, where "y" is a placeholder for Yin and Yang. The radius coordinate r is common for both grid patches. Details on the numerical implementation of the Yin-Yang grid and more subtle issues, such as the treatment of the overlap regions and surface integrals, can be found in the literature (see, e.g., Kageyama & Sato, 2004; Peng et al., 2006; Wongwathanarat et al., 2010a; Melson, 2016).

Since the Yin-Yang grid covers the full-4π solid angle of the entire sphere with cells of roughly equal size (and approximately rectangular shape), it circumvents the aforementioned disadvantages of the spherical polar grid and, thus, allows for an increased CFL time step for a given radius and angular resolution. At the same time, grid-induced artifacts can be reduced to a much lower level. Another example of a spherical multi-patch grid employed in astrophysical simulations is the so-called "cubed sphere" grid (with six component meshes), as introduced by Ronchi et al.

(1996). This composite grid comes without significant overlap regions (except for the boundary lines between the individual component blocks) and can, therefore, largely avoid the interpolation between grid patches, which is necessary for overlapping multi-patch grids such as the Yin-Yang grid.

SMR Grid – Angular Resolution

While for most of our simulations, we employ a Yin-Yang grid with a uniform angular resolution of 2°, in one case (for model s9.0), we additionally used a newly implemented static mesh refinement (SMR) grid (Melson, 2016; Melson et al., 2020), where the standard angular resolution of 2° was stepwise increased to 1° (at the gain radius) and 0.5° (outside of a fixed radius of 160 km) to compensate for the diverging nature of the spherical grid.[16] This allows for enhanced angular resolution in the neutrino-heated postshock region, which is most prone to fluid instabilities and turbulent convection. On the downside, the SMR grid turned out to be unfavorable for shock expansion in marginally exploding cases at the borderline between successful SNe and failed explosions (see model s20 in Melson et al., 2020). This effect could be traced back to the conversion of nonradial kinetic energy to internal energy in flows crossing an SMR resolution interface (from a finer to a coarser resolved layer), which reduces the turbulent pressure support behind the shock (for an in-depth discussion, see Melson et al., 2020).

In this context, we want to point out that our standard choice of the (uniform) angular resolution of 2°, as used for most of our models, is a compromise between numerical accuracy and computational feasibility. Certainly, an even higher angular resolution (of around 1° or below) would be desirable to better resolve the development of hydrodynamic flow instabilities (such as Kelvin-Helmholtz and Rayleigh-Taylor instabilities; see, e.g., Guilet et al., 2010) and the turbulent energy cascade to the smallest scales (Kolmogorov, 1941); see, e.g., Abdikamalov et al. (2015); Radice et al. (2015, 2016); Nagakura et al. (2019).[17] However, the detailed resolution study by Melson et al. (2020) suggests that the overall post-bounce dynamics seem to converge at an angular resolution of around 1°, with results from 2° simulations not being far off. Therefore, our standard 2° setup should be able to capture the overall explosion dynamics sufficiently well while keeping the computational costs at a feasible level.

[16] Note that in our SMR procedure, we only refine the spatial grid for the hydrodynamics calculations, while the angular resolution of the neutrino-transport grid (which can be chosen independently from the hydrodynamics grid; see footnote 15) remains unchanged. Such an approach is justified because the neutrino optical depths in the refinement layers are comparatively small, and neutrinos couple only loosely to the stellar fluid in those regions.

[17] As was pointed out by Melson et al. (2020, Appendix B), the effects of neutrino viscosity (at high densities inside the PNS core; e.g., van den Horn & van Weert, 1984; Burrows & Lattimer, 1988) and of neutrino drag (in the gain region; cf. Guilet et al., 2015) become comparable to the effects of numerical viscosity when increasing the resolution beyond 1°–2°. These non-ideal effects should hence be considered in high-resolution simulations of neutrino-driven CCSN explosions.

We should note that, in the work by Melson et al. (2020), small-amplitude (0.1%), random cell-to-cell perturbations were imposed to break spherical symmetry of the employed 1D initial conditions, as noted above. More recently, Bollig et al. (2021) compared full-physics Prometheus-Vertex simulations with 1°, 2°, and 4° that were all based on more realistic initial conditions from a 3D progenitor model with large-scale, large-amplitude pre-collapse perturbations in the oxygen shell (Yadav et al., 2020). They found a very similar evolution of the average shock radius for all three models, basically independent of the employed angular grid resolution (see their Figure A1). The results of Bollig et al. (2021), therefore, suggest that the growth conditions for postshock convection (and hence the susceptibility to shock revival) are dominated by the presence of strong pre-collapse perturbations rather than by the angular resolution of the computational grid (for more details, see Sections 3.1 and 3.2).

Spherical Inner Core – 1D Convection Treatment

Because of the r^2 dependence of the surface elements in spherical grid configurations, the cell widths in lateral and azimuthal directions converge towards the coordinate singularity at the origin (at $r = 0$). To avoid an overly restrictive CFL time-step constraint at the grid center, we thus treat the innermost zones of the computational domain in spherical symmetry (1D). This is well justified for the inner core regions of a PNS, which barely deviate from spherically symmetric conditions as long as they are convectively stable. At early times (during the first few hundred milliseconds after the bounce), PNS convection occurs only at radii larger than roughly 10 km (see, e.g., Nagakura et al., 2020). Yet, the bottom of the PNS convection layer moves inward over time. For this reason, we typically employ "1D cores" of only 1–3 km in radius, and only in one case (for model s20) we took a larger radius of 10 km (see Chapter 3).

For our long-time simulations until several seconds after bounce with the Nemesis neutrino treatment (see Section 2.2), we instead use a 1D core that extends to the time-dependent radius where the (angle-averaged) density falls below a value of $5 \times 10^{12}\,\mathrm{g\,cm^{-3}}$, thus covering the convectively unstable layer inside the PNS. To still account for the effects of PNS convection in an approximative manner, we employ a mixing-length treatment as described in Hüdepohl (2014) and Mirizzi et al. (2016). This mixing-length approach for PNS convection is also applied to the 1D long-time PNS cooling simulations that are used as input for our 3D simulations with the Nemesis scheme, which we will describe in detail in the following section.

2.2. The Nemesis Scheme

In full-physics, neutrino hydrodynamics simulations with the PROMETHEUS-VERTEX code, the neutrino-transport module VERTEX (see Section 2.1.2) is coupled to the PROMETHEUS hydrodynamics code (see Section 2.1.1) via source terms for energy, electron-lepton number, and momentum. However, because of the immense computational costs of detailed neutrino-transport calculations, long-time 3D simulations over timescales of several seconds — which are necessary to achieve saturation of the explosion properties — are currently not feasible. To advance CCSN models from the phase of shock revival by neutrino heating to the fully developed explosion stage, we thus need to replace VERTEX with a computationally less demanding scheme that is still able to approximately capture the most relevant neutrino effects — namely, the cooling of the PNS's surface layer and the heating of matter in the surrounding gain region, as well as the net change of the electron number density due to neutrino emission and absorption. In this section, we describe the NEMESIS neutrino scheme that we have developed for this study, building upon the initial ideas and implementation by Janka et al. (2017).[18]

The basic idea of this simplified and computationally efficient approach is to take the energy and electron-lepton-number source terms at the end of a CCSN simulation with full VERTEX neutrino transport, as given by Equations (2.19) and (2.21), and to smoothly extrapolate their time evolution by means of analytical scaling relations (Janka, 2001). The scaling of the source terms is based on local gas quantities and the time evolution of the luminosities and mean energies of electron neutrinos and antineutrinos, which we adopt from suitable 1D PNS cooling simulations. In this section, we use angle brackets "$\langle ... \rangle$" to indicate spherical averages.

2.2.1. Source Term for Energy

The energy source term, Q_{E}, that appears on the right-hand side of Equation (2.3) describes the net energy exchange of the neutrino radiation field with the stellar fluid. Inside the nascent, hot PNS and close to its surface layers, the emission of neutrinos (and antineutrinos) carries away energy, while, at larger radii, (anti)neutrinos deposit net energy through absorption and scattering reactions, with the dominant energy-exchanging processes being the charged-current beta reactions of Equations (1.1) and (1.2); see, e.g., Bethe & Wilson (1985); Janka (2001). As illustrated in the left panel of Figure 2.2, the gain radius, R_{gain}, separates these two regimes of net cooling and net heating. In full-physics simulations with multi-dimensional neutrino transport, the gain radius is generally a function of the angular direction, $R_{\mathrm{gain}} = R_{\mathrm{gain}}(\theta, \phi)$.

[18] NEMESIS is short for **N**eutrino-**E**xtrapolation **M**ethod for **E**fficient **SI**mulations of **S**upernova explosions. An early version of this scheme, as applied to the explosions of two low-mass (∼9–10 $\mathrm{M}_\odot$) progenitors, has already been described in Appendix E of Stockinger et al. (2020). Some content from this publication is adopted here, yet only the author's contributions are taken.

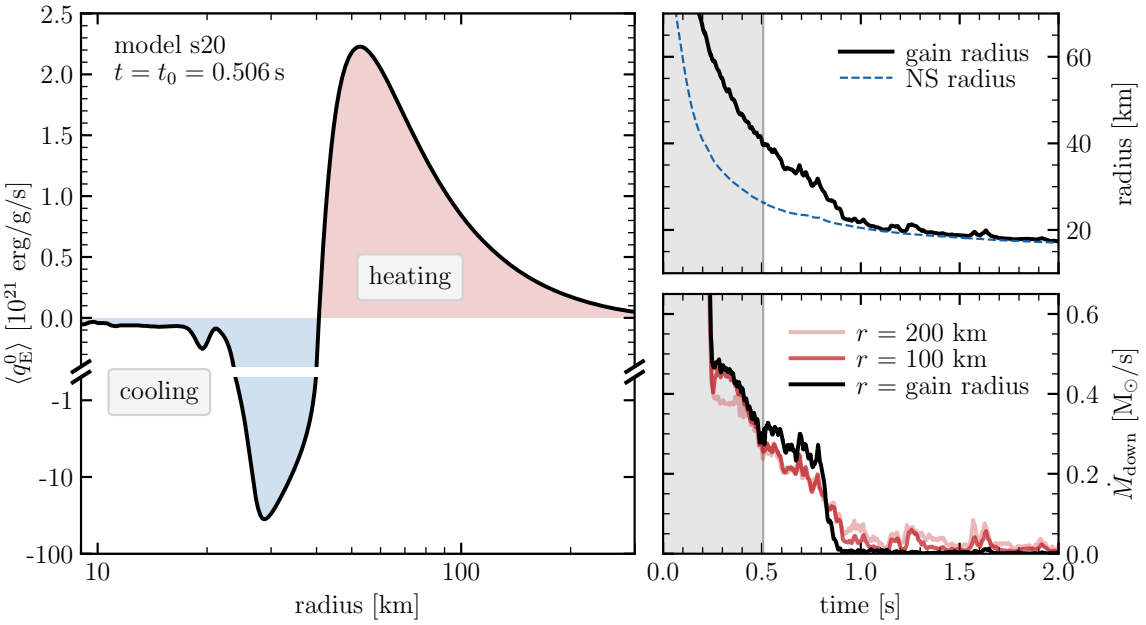

Figure 2.2.: Schematic picture of neutrino heating and cooling regions, taking the exemplary case of model s20 (see Chapter 3 for more details). *Left:* Radial profile of the angle-averaged specific energy source term, $\langle q_\mathrm{E}^0 \rangle := \langle Q_\mathrm{E}(t_0)/\rho(t_0) \rangle$, at the time t_0 when we switch off the VERTEX neutrino transport. Regions of net heating (i.e., $Q_\mathrm{E} > 0$) and net cooling (i.e., $Q_\mathrm{E} < 0$) are indicated by red and blue shading, respectively. *Upper right:* Time evolution of the gain radius, R_gain (black solid line), which separates the regions of cooling ($r < R_\mathrm{gain}$) and heating ($r > R_\mathrm{gain}$). It follows the contraction of the NS radius (blue dashed line). *Lower right:* Time evolution of the mass-accretion rate of downflows (i.e., $v_r < 0$), evaluated at a fixed radius of 200 km, 100 km, and at the time-dependent gain radius (light red, dark red, and black lines, respectively). The gray vertical bands in the right panels mark the evolution period with full neutrino transport.

However, for our NEMESIS treatment, it is sufficient to assume a spherically symmetric gain radius, which we define as the zero-crossing of the angle-averaged specific net heating/cooling rate, i.e., $\langle Q_\mathrm{E}/\rho \rangle_{r=R_\mathrm{gain}} = 0$.

Within our NEMESIS approach, we divide Q_E into separate expressions for heating in the gain layer and cooling below the gain radius:

$$Q_\mathrm{E}(\boldsymbol{r}, t) = \begin{cases} Q_\mathrm{E}^+(\boldsymbol{r}, t) \geqslant 0, & \text{i.e., } \textbf{heating}, \text{ if } r \geqslant R_\mathrm{gain}(t)\,, \\ Q_\mathrm{E}^-(\boldsymbol{r}, t) < 0, & \text{i.e., } \textbf{cooling}, \text{ if } r < R_\mathrm{gain}(t)\,. \end{cases} \tag{2.25}$$

Because we do not solve the neutrino-transport equations in our NEMESIS scheme, we need to prescribe the evolution of the gain radius for the time after VERTEX has been switched off. Hence, we employ the following empirical expression, which couples the time evolution of the gain radius to the contraction of the PNS radius,

$R_{\mathrm{NS}}(t)$, taking into account an inflated accretion-mantle layer that vanishes in the limit of ceased mass accretion onto the PNS:

$$R_{\mathrm{gain}}(t) = \left[\left(\frac{R_{\mathrm{gain}}(t_0)}{R_{\mathrm{NS}}(t_0)} - 1.01\right)\frac{\dot{M}_{\mathrm{down}}(t)}{\dot{M}_{\mathrm{down}}(t_0)} + 1.01\right] \cdot R_{\mathrm{NS}}(t)\,, \tag{2.26}$$

where $R_{\mathrm{gain}}(t_0)$ and $R_{\mathrm{NS}}(t_0)$ are the gain radius and the PNS radius at the time t_0 when we switch off the VERTEX neutrino transport and replace it with the NEMESIS scheme; $\dot{M}_{\mathrm{down}}(t)$ is the time-dependent mass-accretion rate, evaluated at a fixed radius of 100 km and for downflows (i.e., fluid elements with negative radial velocity, $v_r < 0$) only (see Equation (3.2) in Chapter 3); and the constant of 1.01 controls the asymptotic behavior of $R_{\mathrm{gain}}(t) \to 1.01 \cdot R_{\mathrm{NS}}(t)$ in the limit of $\dot{M}_{\mathrm{down}} \to 0$. This specific value of 1.01 is empirically motivated by the late-time evolution of the gain radius in spherically symmetric CCSN simulations with full neutrino transport. The PNS radius, R_{NS}, is defined as the radius where the angle-averaged density equals a value of $10^{11}\,\mathrm{g\,cm^{-3}}$.

The gain radius, as given by Equation (2.26), ties in seamlessly with $R_{\mathrm{gain}}(t)$ during the evolution period $t < t_0$ that has been computed with full neutrino transport (see upper right panel of Figure 2.2 for the exemplary case of model s20, which will be discussed in more detail in Chapter 3). Note that, to prevent feedback-coupling effects, we do not evaluate the mass-accretion rate of downflows, $\dot{M}_{\mathrm{down}}$, in Equation (2.26) at the time-dependent gain radius but instead at a fixed radius of 100 km, which leads to a smooth transition of $R_{\mathrm{gain}}(t)$ at the time t_0. In any case, the overall behavior of the mass-accretion rate as a function of time is largely insensitive to the exact radius of evaluation, as can be seen in the lower right panel of Figure 2.2.

Neutrino Heating

In the gain layer (i.e., for $r \geqslant R_{\mathrm{gain}}(t)$), we apply the following expression for the net neutrino energy-deposition rate per volume:

$$Q^{+}_{\mathrm{E}}(\boldsymbol{r}, t) = \left\langle q^{0}_{\mathrm{E}} \right\rangle (x^{+}_{\mathrm{E}}) \cdot \rho(\boldsymbol{r}, t) \left(\frac{R_{\mathrm{gain}}(t_0)}{R_{\mathrm{gain}}(t)}\right)^{2} \cdot \zeta_L(t) \cdot \zeta_E(t)\,, \tag{2.27}$$

where $\langle q^{0}_{\mathrm{E}} \rangle := \langle Q_{\mathrm{E}}(t_0)/\rho(t_0) \rangle$ is the angle-averaged specific net heating rate at the time t_0 when we switch our neutrino treatments, $\rho(\boldsymbol{r}, t)$ is the local mass density, and $\zeta_L(t)$ and $\zeta_E(t)$ are time-dependent scaling factors (see Equations (2.28) and (2.30)). This functional ansatz is motivated by the rough scaling of the ν_{e} and $\bar{\nu}_{\mathrm{e}}$ absorption rates with the density of a gas of free nucleons (see Janka, 2001). $\langle q^{0}_{\mathrm{E}} \rangle$ is smoothed by time-averaging over the last few milliseconds of the evolution with detailed neutrino transport and tabulated as a function of the relative radius coordinate x^{+}_{E}, defined as $x^{+}_{\mathrm{E}} := r(t)/R_{\mathrm{gain}}(t) = r(t_0)/R_{\mathrm{gain}}(t_0)$. In this way, we contract the radial heating profile according to the time evolution of the gain radius as given by Equation (2.26). The factor $[R_{\mathrm{gain}}(t_0)/R_{\mathrm{gain}}(t)]^2$ results from the transformation responsible for the

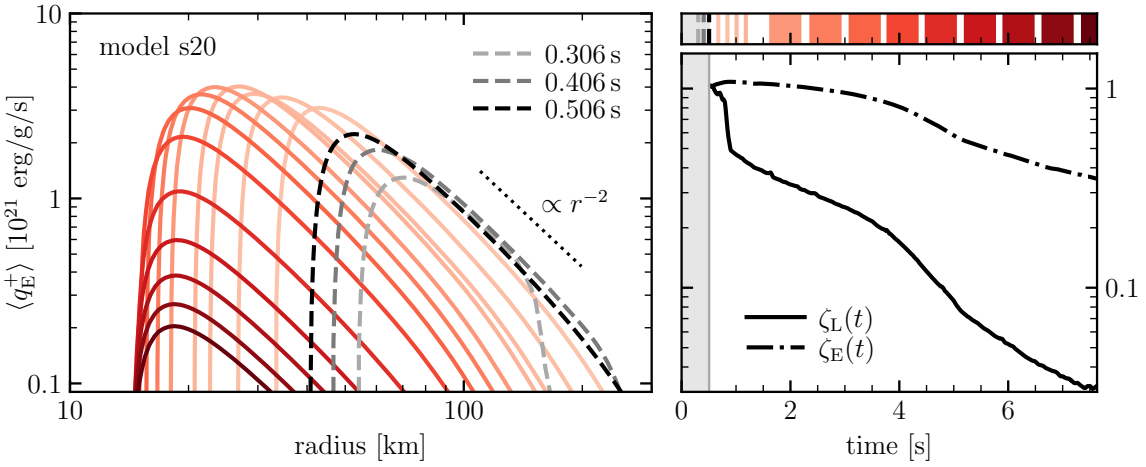

Figure 2.3.: Time evolution of the neutrino-heating source term for the exemplary case of model s20 (see Chapter 3 for more details on the model). *Left:* Radial profiles of the angle-averaged specific net heating rate, $\langle q_E^+ \rangle = \langle Q_E^+/\rho \rangle$, at three different times $t \leqslant t_0$ during and at the end of the evolution with full Vertex neutrino transport (gray and black dashed lines) and at various times $t > t_0$ during the evolution with our Nemesis neutrino treatment (red solid lines; see color legend in the upper right). The dotted line indicates the r^{-2} scaling. Note that the "knees" visible in the early-time (i.e., 0.306 s and 0.406 s) heating profiles at radii of ∼150 km and ∼250 km roughly coincide with the spherically averaged shock positions at those times. *Right:* Time evolution of the scaling factors $\zeta_L(t)$ and $\zeta_E(t)$. The sudden drop of $\zeta_L(t)$ at around 0.8–0.9 s after bounce is caused by the steep decline of the mass-accretion rate at this time (see lower right panel of Figure 2.2 and Equation (2.28)). The curves are smoothed by running averages of 50 ms. The gray vertical band marks the evolution period with full neutrino transport.

inward shift of the heating profile and ensures that $q_E^+ := (Q_E^+/\rho)$ drops like r^{-2} at large radii (see left panel of Figure 2.3 for the time evolution of the angle-averaged specific net heating rate, $\langle q_E^+ \rangle$, for the exemplary case of model s20; more details on this model will be provided in Chapter 3).

The dependence of the heating rate on the time-dependent neutrino emission properties is captured by the scaling factors $\zeta_L(t)$ and $\zeta_E(t)$ (see right panel of Figure 2.3), which are based on inputs from corresponding 1D PNS cooling simulations with full Vertex neutrino transport, including a mixing-length treatment for PNS convection. The factor $\zeta_L(t)$ encapsulates the time evolution of the ν_e and $\bar{\nu}_e$ luminosities, $L_{\nu_e}(t)$ and $L_{\bar{\nu}_e}(t)$, which can be written as the sum of an accretion and a core component (e.g., Fischer et al. 2009; Müller & Janka 2014; Hüdepohl 2014):

$$\zeta_L(t) = \underbrace{\frac{M_{\rm NS}(t)\dot{M}_{\rm down}(t)/R_{\rm NS}(t)}{M_{\rm NS}(t_0)\dot{M}_{\rm down}(t_0)/R_{\rm NS}(t_0)} \cdot \xi^0_{\rm acc}}_{\text{accretion component}} + \underbrace{\frac{L^{\rm 1D}_{\nu_e}(t) + L^{\rm 1D}_{\bar{\nu}_e}(t)}{L^{\rm 1D}_{\nu_e}(t_0) + L^{\rm 1D}_{\bar{\nu}_e}(t_0)} \cdot (1 - \xi^0_{\rm acc})}_{\text{core component}} . \quad (2.28)$$

The first term accounts for the emission of ν_e and $\bar{\nu}_\mathrm{e}$ from the inflated PNS mantle layer, which is fed by continued mass accretion. The associated release of gravitational energy is proportional to the (baryonic) NS mass, $M_\mathrm{NS}(t)$, to the mass-accretion rate, $\dot{M}_\mathrm{down}(t)$, of downflows ($v_r < 0$), and to the inverse of the NS radius, $R_\mathrm{NS}(t)^{-1}$. Here, we evaluate $\dot{M}_\mathrm{down}$ at the time-dependent gain radius, $R_\mathrm{gain}(t)$. The constant factor ξ^0_acc denotes the fraction of the accretion luminosities of ν_e and $\bar{\nu}_\mathrm{e}$ compared to their total luminosities at the time t_0, which can be derived from the time evolution of the neutrino signal during the last ∼100 ms of the 3D simulation with full neutrino transport (see discussion below).

The second term on the right-hand side of Equation (2.28) describes the time evolution of the diffusive emission of ν_e and $\bar{\nu}_\mathrm{e}$ from the dense PNS core regions. For this core component, we employ the time-dependent neutrino luminosities, $L^\mathrm{1D}_{\nu_\mathrm{e}}(t)$ and $L^\mathrm{1D}_{\bar{\nu}_\mathrm{e}}(t)$, from a corresponding 1D long-time PNS cooling simulation with Prometheus-Vertex (Bollig, 2022), extracted at a radius of 400 km. Such neutrino signals from 1D models are well suited for describing the core emission because, in spherically-symmetric simulations, mass accretion onto the PNS ends shortly after shock revival (as simultaneous outflows and downdrafts are prevented by the 1D geometry), and the neutrino emission is core-dominated already early on.

The fraction of the accretion luminosity relative to the total luminosity, $\xi^{0,\nu_i}_\mathrm{acc} = L^\mathrm{acc}_{\nu_i}(t_0)/L_{\nu_i}(t_0)$, of an individual neutrino species ν_i at the time t_0 can be obtained approximately from comparing the time-dependent neutrino luminosity $L_{\nu_i}(t)$, as given from the 3D simulation with full Vertex neutrino transport, over a time span of ∼100 ms (prior to t_0) with a function of the form

$$L_{\nu_i}(t) = L_{\nu_i}(t_0)\cdot\left[\frac{M_\mathrm{NS}(t)\dot{M}_\mathrm{down}(t)/R_\mathrm{NS}(t)}{M_\mathrm{NS}(t_0)\dot{M}_\mathrm{down}(t_0)/R_\mathrm{NS}(t_0)}\cdot\xi^{0,\nu_i}_\mathrm{acc} + \frac{L_\mathrm{core}(t)}{L_\mathrm{core}(t_0)}\cdot\left(1-\xi^{0,\nu_i}_\mathrm{acc}\right)\right]. \quad (2.29)$$

Here, the time evolution of the (a priori not known) core luminosity, $L_\mathrm{core}(t)/L_\mathrm{core}(t_0)$, can be approximated by an analytical power-law expression of the form $(t/t_0)^{-\alpha}$ with $\alpha \sim 0.5$ (or equally well by an exponential of the form $\exp[-(t-t_0)/\tau]$, with a typical cooling timescale $\tau \sim$ 1–2 s). We note that the exact time evolution of the core component is irrelevant in our estimation of $\xi^{0,\nu_i}_\mathrm{acc}$ because the core emission does not change significantly during the short considered time interval of ∼100 ms. The time dependence of the neutrino signal during this short period is, instead, driven mainly by the time-dependent mass-accretion rate, while the core emission acts almost as a constant "floor value." All other quantities in Equation (2.29) being given from the 3D model, the factor $\xi^{0,\nu_i}_\mathrm{acc}$ is then the only free parameter and can be obtained approximately from a comparison of Equation (2.29) with the luminosity from the 3D simulation with Prometheus-Vertex. For the exemplary case of model s20, as shown in Figures 2.2 and 2.3, this procedure yields a combined value for ν_e and $\bar{\nu}_\mathrm{e}$ of $\xi^0_\mathrm{acc} = (\xi^{0,\nu_\mathrm{e}}_\mathrm{acc} + \xi^{0,\bar{\nu}_\mathrm{e}}_\mathrm{acc})/2 \simeq 0.38$, which is, then, entering in the description of the scaling factor $\zeta_L(t)$ in Equation (2.28).

Because the cross sections for ν_e and $\bar{\nu}_\mathrm{e}$ absorption via inverse beta decay (i.e., Equations (1.1) and (1.2)) depend, to leading order, on the mean squared neutrino energies, we scale the heating rate in Equation (2.27) with the additional factor $\zeta_E(t)$, which is defined as:

$$\zeta_E(t) = \left(\frac{E^{1\mathrm{D}}_{\nu_\mathrm{e}}(t) + E^{1\mathrm{D}}_{\bar{\nu}_\mathrm{e}}(t)}{E^{1\mathrm{D}}_{\nu_\mathrm{e}}(t_0) + E^{1\mathrm{D}}_{\bar{\nu}_\mathrm{e}}(t_0)} \right)^2 \left(\frac{M_\mathrm{NS}(t)}{M_\mathrm{NS}(t_0)} \right)^2 . \tag{2.30}$$

Here, $E^{1\mathrm{D}}_{\nu_\mathrm{e}}(t)$ and $E^{1\mathrm{D}}_{\bar{\nu}_\mathrm{e}}(t)$ are the time-dependent ν_e and $\bar{\nu}_\mathrm{e}$ mean energies from the corresponding 1D full-transport simulation, evaluated at a radius of 400 km. The scaling with the PNS mass, $M_\mathrm{NS}(t)$, is guided by the findings of Müller & Janka (2014) and shall account for possible differences in the time evolution of the PNS mass in our 1D and 3D models. Nevertheless, this mass dependence of $\zeta_E(t)$ is only weak because $M_\mathrm{NS}(t)$ has almost converged to its final value by the time t_0.

Neutrino Cooling

Below the gain radius, the emission of neutrinos and antineutrinos leads to a net cooling of the stellar plasma. We should mention that an adequate treatment of this highly complex transition regime from neutrino trapping in the optically thick high-density core of the PNS to semi-transparency in its surface layers (and eventual free-streaming at large radii) is specifically delicate and should ideally be tackled by means of detailed neutrino-transport calculations. Because, as mentioned above, such a full-physics treatment over periods of $\mathcal{O}(10)$ seconds is computationally not feasible in 3D simulations, we rely on a more pragmatic approach. Here, we hence distinguish between two separate regions and write the energy-loss rate per volume as

$$Q^-_\mathrm{E}(\boldsymbol{r}, t) = \begin{cases} Q^-_\mathrm{E,m}(\boldsymbol{r}, t), & \text{if } R_\mathrm{core}(t) \leqslant r < R_\mathrm{gain}(t)\,, \\ Q^-_\mathrm{E,c}(\boldsymbol{r}, t), & \text{if } R_\mathrm{core}(t) > r\,, \end{cases} \tag{2.31}$$

where $Q^-_\mathrm{E,m}$ denotes the source term for neutrino cooling in the PNS's inflated mantle layer (i.e., for $R_\mathrm{core} \leqslant r < R_\mathrm{gain}$) and $Q^-_\mathrm{E,c}$ describes the cooling of the high-density PNS core ($r < R_\mathrm{core}$), which we define as the region where the angle-averaged mass density is larger than a threshold value of $5 \times 10^{12}\,\mathrm{g\,cm^{-3}}$.

In the PNS mantle, where the neutrino optical depths are moderate compared to the deeper core regions and where neutrinos leak out more efficiently than being (re-)absorbed, we employ the following expression for the net neutrino-cooling rate:

$$Q^-_\mathrm{E,m}(\boldsymbol{r}, t) = \left\langle \frac{q^0_\mathrm{E}}{T_0^6} \right\rangle (x^-_\mathrm{E,m}) \cdot \rho(\boldsymbol{r}, t) T(\boldsymbol{r}, t)^6 \cdot \underbrace{\frac{M_\mathrm{NS}(t)\dot{M}_\mathrm{down}(t)/R_\mathrm{NS}(t)}{M_\mathrm{NS}(t_0)\dot{M}_\mathrm{down}(t_0)/R_\mathrm{NS}(t_0)}}_{\propto \text{ accretion luminosity}} . \tag{2.32}$$

Here, q^0_E and T_0 are the specific net cooling rate and the local fluid temperature at the time t_0 when we switch off the Vertex neutrino transport and replace it with our

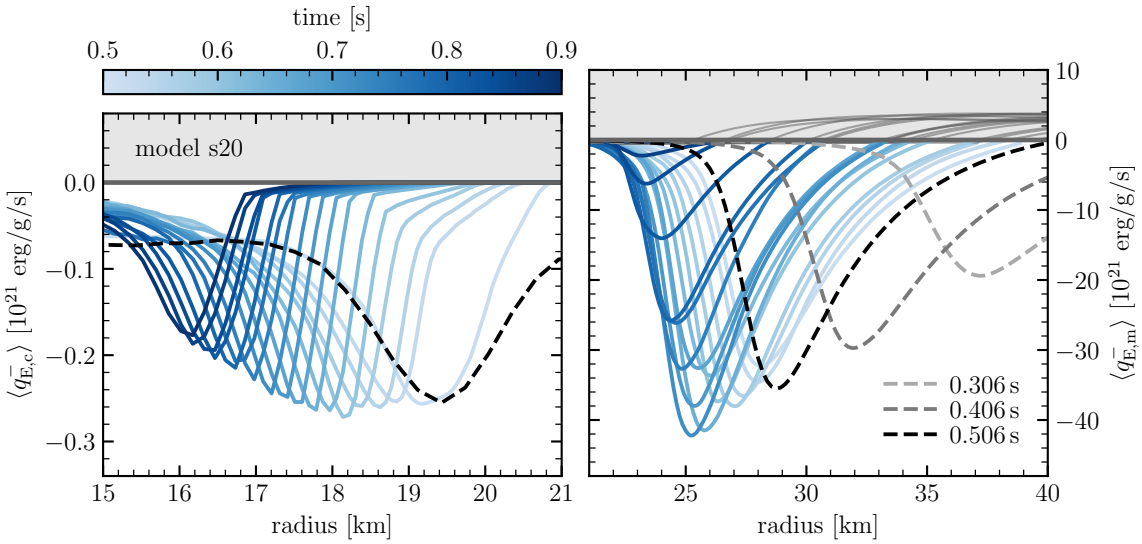

Figure 2.4.: Time evolution of the (angle-averaged) neutrino-cooling source term for the exemplary model s20 (see Chapter 3 for more details on the model). *Left:* Radial profiles of the specific cooling rate inside the PNS's high-density core, $\langle q^-_{\mathrm{E,c}}\rangle = \langle Q^-_{\mathrm{E,c}}/\rho\rangle$. *Right:* Radial profiles of the specific cooling rate in the PNS's accretion mantle, $\langle q^-_{\mathrm{E,m}}\rangle = \langle Q^-_{\mathrm{E,m}}/\rho\rangle$. Note the largely different scales of the two panels. The profiles are shown for the time $t_0 = 0.506$ s (after bounce) when we switch off the Vertex neutrino transport (black dashed line) and for the first ∼400 ms of the evolution with the Nemesis treatment with a spacing of ∼25 ms (blue solid lines; see color legend in the upper left). In the right panel we further show the profiles for two more times during the full-transport evolution (gray dashed lines). The gray shaded horizontal bands indicate the domain of neutrino heating (i.e., $Q_{\mathrm{E}} > 0$ for $r > R_{\mathrm{gain}}(t)$; see Figure 2.3). At around 0.9 s when mass accretion onto the PNS has basically ceased (see lower right panel of Figure 2.2), neutrino cooling in the mantle layer becomes insignificant. Nonetheless, the PNS core continues to cool via neutrino diffusion also at later times, resulting in an ongoing contraction of the PNS (see Figure 2.5).

Nemesis scheme. Like the angle-averaged specific heating rate $\langle q^0_{\mathrm{E}}\rangle$ on the right-hand side of Equation (2.27), we also smoothen the (spherically-averaged) radial profile of $\langle q^0_{\mathrm{E}}/T_0^6\rangle$ by time-averaging over the last few milliseconds of the evolution with full neutrino transport and tabulate it as a function of a relative radius coordinate, $x^-_{\mathrm{E,m}}$, which we define as:

$$x^-_{\mathrm{E,m}} = \begin{cases} \dfrac{r - R_{\mathrm{NS}}(t)}{R_{\mathrm{gain}}(t) - R_{\mathrm{NS}}(t)}, & \text{if } R_{\mathrm{NS}}(t) \leqslant r < R_{\mathrm{gain}}(t)\,, \\ \dfrac{r - R_{\mathrm{core}}(t)}{R_{\mathrm{NS}}(t) - R_{\mathrm{core}}(t)}, & \text{if } R_{\mathrm{core}}(t) \leqslant r < R_{\mathrm{NS}}(t)\,. \end{cases} \tag{2.33}$$

Splitting the PNS mantel layer into regions outside and inside the time-dependent

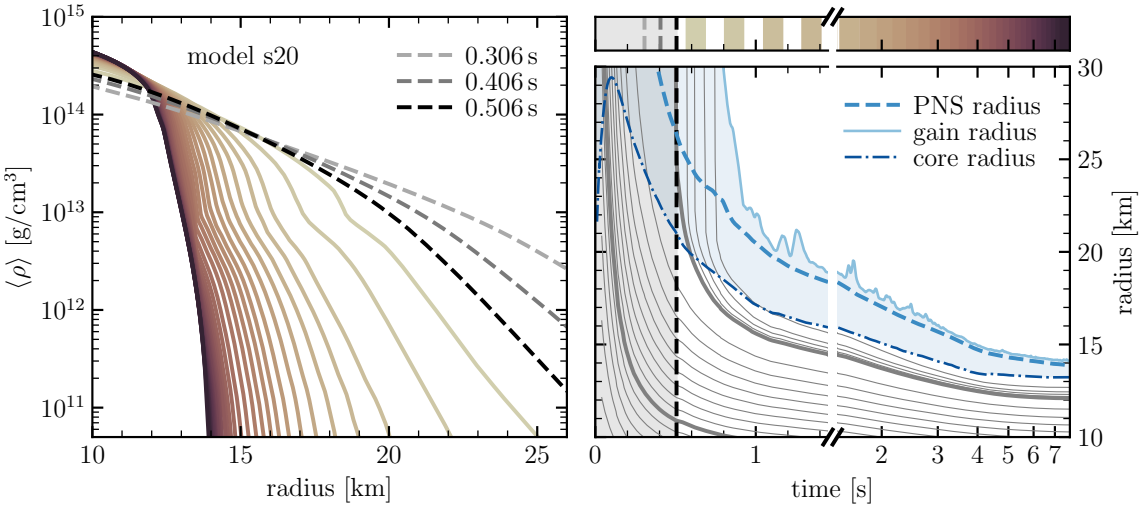

Figure 2.5.: Time evolution of the PNS contraction for the exemplary case of model s20 (see Chapter 3 for more details). *Left:* Radial profiles of the angle-averaged baryonic mass density, $\langle\rho\rangle$, at three times during and at the end of the evolution with full VERTEX neutrino transport (gray and black dashed lines) and during the long-time evolution with the NEMESIS treatment (brown lines; see color legend in the upper right of the figure). *Right:* Time evolution of the PNS radius ($R_{\rm NS}(t)$; dashed blue line), the gain radius ($R_{\rm gain}(t)$; solid blue line), and the PNS core radius ($R_{\rm core}(t)$; dash-dotted blue line). The gray lines indicate mass shells (i.e., radii corresponding to specific values of the enclosed baryonic mass) with a spacing of $0.1\,{\rm M}_\odot$. The bold gray lines mark the mass coordinates of $1.0\,{\rm M}_\odot$ and $1.9\,{\rm M}_\odot$. For enclosed masses larger than $1.9\,{\rm M}_\odot$, the mass shells have a spacing of $0.01\,{\rm M}_\odot$. The final baryonic PNS mass (at a post-bounce time of 8 seconds) is $1.949\,{\rm M}_\odot$. All curves are smoothed by running averages of 30 ms. The gray vertical band marks the evolution period with full neutrino transport.

PNS radius, $R_{\rm NS}(t)$, turned out to be necessary to adequately control the inward shift and transformation of the initial cooling profile at the time t_0 and to thus ensure a continuous contraction behavior of the PNS surface layers.

The scaling of the cooling rate in Equation (2.32) with the local matter density and the sixth power of the local temperature is motivated by the density and temperature dependence of the electron and positron capture rates on nucleons in the limit of vanishing electron degeneracy (Janka, 2001). The last factor in Equation (2.32) is proportional to the accretion component of the neutrino luminosity, associated with the emission from matter downdrafts reaching close to the PNS. It ensures that cooling in the mantle layer is down-regulated once mass accretion onto the PNS abates (see right panel of Figure 2.4). As in Equation (2.28), the mass-accretion rate of downflows, $\dot{M}_{\rm down}$, is evaluated at the time-dependent gain radius.

In the PNS's high-density core, our cooling prescription of Equation (2.32), which is based on a pure emission model, is not applicable anymore because dense-medium

effects become relevant, and the neutrino radiation field is strongly coupled to the stellar fluid by abundant emission, scattering, and re-absorption processes. To describe the cooling of the PNS core regions (at radii $r < R_{\rm core}$), we thus take a different approach and employ the time-dependent specific cooling rate, $q_{\rm E}^{\rm 1D} = (Q_{\rm E}^{\rm 1D}/\rho^{\rm 1D})$, from the same 1D full-transport model that is also used to compute the scaling factors ζ_L and ζ_E of Equations (2.28) and (2.30). The net cooling rate per volume in the PNS core is then given by:

$$Q_{\rm E,c}^{-}(\boldsymbol{r},t) = q_{\rm E}^{\rm 1D}(\rho,t)\cdot\rho(\boldsymbol{r},t)\,, \tag{2.34}$$

where $q_{\rm E}^{\rm 1D}$ is tabulated for every time, t, as a function of density, ρ, and then interpolated to the time-dependent local density, $\rho(\boldsymbol{r},t)$, of the 3D Nemesis model. During a transition period of ∼30 ms, we smoothly switch from the initial cooling profile at the end of the full-transport 3D simulation (i.e., at the time t_0) to the time-dependent cooling profile of the 1D model (see left panel of Figure 2.4).

Our approach ensures a smooth and continuous contraction of the PNS interior and its surface layers, as shown in Figure 2.5 for the exemplary case of model s20. To further relax the computational time-step constraint for the long-time evolution with the Nemesis neutrino treatment, we increase the size of the spherical inner core at a post-bounce time of ∼800 ms (i.e., after a transition phase of ∼300 ms) from $r = 10$ km to $r = R_{\rm core}(t)$ and employ a mixing-length treatment for PNS convection (Hüdepohl, 2014; Mirizzi et al., 2016) within the 1D domain; see Section 2.1.3. Moreover, we slightly reduce the radial resolution inside the PNS core. On the other hand, the radial grid is continuously refined in regions close to the PNS surface during the entire long-time evolution to adequately resolve the steepening density gradient at the edge of the cooling and contracting PNS.

2.2.2. Source Term for Electron Number

The emission and absorption of electron-type neutrinos and antineutrinos does not only affect the energy content of the stellar fluid, it also changes the net electron-lepton number density of the plasma. This effect is encapsulated in the source term $Q_{\rm N}$, which appears on the right-hand side of the advection equation for the electron fraction $Y_{\rm e}$ (i.e., Equation (2.5)). In analogy to our description of the energy source term $Q_{\rm E}$, we also divide $Q_{\rm N}$ into separate expressions for the net gain of electron number at large radii and the net deleptonization of the fluid in proximity to the PNS:

$$Q_{\rm N}(\boldsymbol{r},t) = \begin{cases} Q_{\rm N}^{+}(\boldsymbol{r},t) \geqslant 0, & \text{i.e., } \textbf{leptonization}\text{, if } r \geqslant R_{\rm gain}^{Y_{\rm e}}(t)\,, \\ Q_{\rm N}^{-}(\boldsymbol{r},t) < 0, & \text{i.e., } \textbf{deleptonization}\text{, if } r < R_{\rm gain}^{Y_{\rm e}}(t)\,, \end{cases} \tag{2.35}$$

where $R_{\rm gain}^{Y_{\rm e}}(t)$ denotes the (time-dependent) radius above which neutrino reactions with the stellar matter lead to a net rise of the electron fraction $Y_{\rm e}$ ("leptonization") and below which the matter loses net electron-lepton number ("deleptonization").

We couple the time evolution of this radius, $R^{Y_\mathrm{e}}_\mathrm{gain}(t)$, to the time-dependent gain radius, $R_\mathrm{gain}(t)$, according to

$$R^{Y_\mathrm{e}}_\mathrm{gain}(t) = R^{Y_\mathrm{e}}_\mathrm{gain}(t_0) \cdot \frac{R_\mathrm{gain}(t)}{R_\mathrm{gain}(t_0)}\,, \tag{2.36}$$

where $R^{Y_\mathrm{e}}_\mathrm{gain}(t_0)$ is defined as the radius where the angle-averaged specific electron-lepton-number source term from the full-transport simulation at the time t_0, $\langle q^0_\mathrm{N}\rangle := \langle Q_\mathrm{N}(t_0)/\rho(t_0)\rangle$, crosses zero. Usually, this radius is close to but not exactly the same as the position of the (energy) gain radius, $R_\mathrm{gain}(t_0)$. In the case of our exemplary s20 model (as shown in Figures 2.2–2.5), the ratio $R^{Y_\mathrm{e}}_\mathrm{gain}(t_0)/R_\mathrm{gain}(t_0)$ has a value of approximately 1.176.

Leptonization

In analogy to Equation (2.27) for neutrino heating in the gain layer, we employ the following expression for the rise of the net electron number density of the stellar fluid through neutrino-matter interactions:

$$Q^+_\mathrm{N}(\boldsymbol{r},t) = \left\langle q^0_\mathrm{N}\right\rangle\!(x^+_\mathrm{N}) \cdot \rho(\boldsymbol{r},t) \left(\frac{R_\mathrm{gain}(t_0)}{R_\mathrm{gain}(t)}\right)^2 \cdot \zeta_L(t) \cdot \zeta_E(t) \cdot \zeta_{Y_\mathrm{e}}(\boldsymbol{r},t)\,. \tag{2.37}$$

Here, we assume the same scaling with the local fluid density, $\rho(\boldsymbol{r},t)$, the inverse of the gain radius squared, $R_\mathrm{gain}(t)^{-2}$, and the factors $\zeta_L(t)$ and $\zeta_E(t)$, as we also do in case of Equation (2.27). The initial (angle-averaged) specific source term profile $\langle q^0_\mathrm{N}\rangle$, extracted at the end of the 3D simulation with full Vertex neutrino transport, is tabulated as a function of the coordinate $x^+_\mathrm{N} := r(t)/R^{Y_\mathrm{e}}_\mathrm{gain}(t) = r(t_0)/R^{Y_\mathrm{e}}_\mathrm{gain}(t_0)$ and smoothed by time-averaging over an interval of a few milliseconds. The additional scaling factor, $\zeta_{Y_\mathrm{e}}(\boldsymbol{r},t)$, that appears on the right-hand side of Equation (2.37) is defined as:

$$\zeta_{Y_\mathrm{e}}(\boldsymbol{r},t) = \max\left\{0, \min\left\{1, \frac{1.1\,Y^\mathrm{eq}_\mathrm{e}(t) - Y_\mathrm{e}(\boldsymbol{r},t)}{0.1\,Y^\mathrm{eq}_\mathrm{e}(t)}\right\}\right\}\,. \tag{2.38}$$

It shall ensure that Y_e in the SN ejecta is limited by its kinetic equilibrium value, Y^eq_e, which is approached when ν_e absorption on neutrons is balanced by $\bar{\nu}_\mathrm{e}$ absorption on protons (Qian & Woosley, 1996; McLaughlin et al., 1996), i.e.:

$$\begin{aligned}\frac{\mathrm{d}Y_\mathrm{e}}{\mathrm{d}t} &\simeq (\lambda_{\nu_\mathrm{e}} + \lambda_{\mathrm{e}^+})Y_\mathrm{n} - (\lambda_{\bar{\nu}_\mathrm{e}} + \lambda_{\mathrm{e}^-})Y_\mathrm{p} \\ &\simeq \lambda_{\nu_\mathrm{e}}(1 - Y_\mathrm{e}) - \lambda_{\bar{\nu}_\mathrm{e}} Y_\mathrm{e} \\ &\simeq 0\,,\end{aligned} \tag{2.39}$$

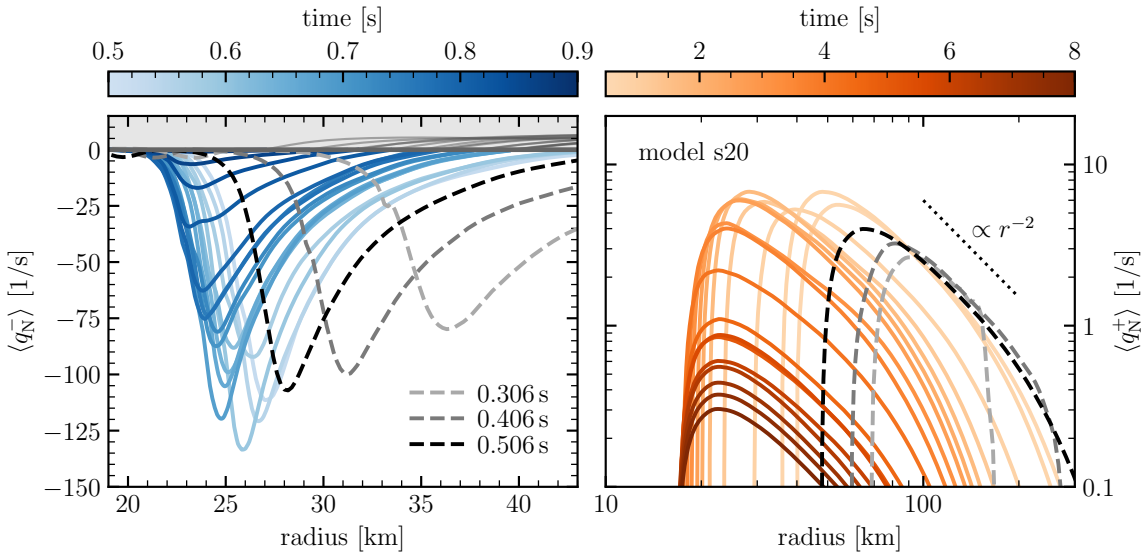

Figure 2.6.: Time evolution of the angle-averaged, specific electron-lepton number source term, $\langle q_N \rangle = \langle Q_N/\rho \rangle$, for the exemplary case of model s20 (see Chapter 3 for more details on the model). *Left:* Radial profiles of the specific deleptonization rate, $\langle q_N^- \rangle = \langle Q_N^-/\rho \rangle < 0$, in the PNS's mantle layer at three different times $t \leqslant t_0$ during and at the end of the evolution with full Vertex neutrino transport (gray and black dashed lines) and during the first ∼400 ms of the evolution with the Nemesis treatment (blue solid lines). *Right:* Radial profiles of the specific leptonization rate, $\langle q_N^+ \rangle = \langle Q_N^+/\rho \rangle > 0$, at radii $r > R_{\mathrm{gain}}^{Y_e}$ for the same times of the full-transport evolution as in the left panel (gray and black dashed lines) and at various times $t > t_0$ during the entire long-time evolution with the Nemesis scheme (orange lines). The dotted line indicates the r^{-2} scaling. Note that the "knees" visible in the early-time (i.e., 0.306 s and 0.406 s) profiles of $\langle q_N^+ \rangle$ at ∼150 km and ∼250 km roughly coincide with the spherically averaged shock radii at those times.

where λ_{ν_e}, $\lambda_{\bar{\nu}_e}$, λ_{e^-}, and λ_{e^+} are the rates for ν_e, $\bar{\nu}_e$, electron, and positron captures on free nucleons, i.e., the forward and reverse reactions of Equations (1.1) and (1.2), and $Y_n := n_n/n_B$ and $Y_p := n_p/n_B$ are the number fractions of neutrons and protons (with corresponding number densities n_n and n_p). Here, it was assumed that $\lambda_{e^+} = \lambda_{e^-} = 0$ and that the stellar matter in the neutrino-heating layer is, essentially, made up of free nucleons, which is a good approximation considering the high temperatures in the regions close to the PNS. Then, charge neutrality yields $Y_n = (1 - Y_e)$ and $Y_p = Y_e$, such that the kinetic equilibrium value of Y_e is given by

$$Y_e^{\mathrm{eq}}(t) = \left[1 + \lambda_{\bar{\nu}_e}(t)/\lambda_{\nu_e}(t)\right]^{-1} . \tag{2.40}$$

For the ν_e and $\bar{\nu}_e$ capture rates, we employ Equations (5)–(8) of Pllumbi et al. (2015), which include correction terms associated with the nucleon recoils and with weak magnetism (Horowitz & Li, 1999; Horowitz, 2002). These equations are evaluated

using the time-dependent neutrino emission quantities from the same 1D PNS cooling simulation with VERTEX neutrino transport and mixing-length convection as employed for the computation of the scaling factors $\zeta_L(t)$ and $\zeta_E(t)$.

In the right panel of Figure 2.6, we show the time evolution of the angle-averaged, specific rate of change of the electron-lepton number, $\langle q_{\rm N}^{+}\rangle = \langle Q_{\rm N}^{+}/\rho\rangle$, as a function of radius, $r > R_{\rm gain}^{Y_{\rm e}}$, for the exemplary case of model s20 (see Chapter 3 for more details on the model). At large radii, the radial profile of $\langle q_{\rm N}^{+}\rangle$ drops roughly like r^{-2} (as does the specific neutrino net heating rate $\langle q_{\rm E}^{+}\rangle$; cf. Figure 2.3).

Deleptonization

Accretion streams that penetrate the cooling layer around the PNS, instead, lose net electron-lepton number, associated with an excess of the $\nu_{\rm e}$ number emission compared to that of $\bar{\nu}_{\rm e}$, which goes in hand with a "neutronization" of the fluid (i.e., the net conversion of protons to neutrons via electron capture reactions).[19] We describe the deleptonization of matter in the PNS mantle layer similarly to our cooling expression of Equation (2.32). Based on the specific lepton-number source term, $q_{\rm N}^{0}$, the temperature, T_0, and the electron fraction, $Y_{\rm e}^{0}$, at the time t_0 when we switch off the VERTEX neutrino transport, we write $Q_{\rm N}^{-} = Q_{\rm N,m}^{-}$, with:

$$Q_{\rm N,m}^{-}(\boldsymbol{r},t) = \left\langle \frac{q_{\rm N}^{0}}{T_0^{5}} \right\rangle (x_{\rm N,m}^{-}) \cdot \rho(\boldsymbol{r},t) T(\boldsymbol{r},t)^{5} \cdot \frac{Y_{\rm e}(\boldsymbol{r},t)}{\langle Y_{\rm e}^{0}\rangle (x_{\rm N,m}^{-})} \cdot \underbrace{\frac{M_{\rm NS}(t)\dot{M}_{\rm down}(t)/R_{\rm NS}(t)}{M_{\rm NS}(t_0)\dot{M}_{\rm down}(t_0)/R_{\rm NS}(t_0)}}_{\propto \text{ accretion luminosity}} . \tag{2.41}$$

Once again, the angle-averaged initial radial profiles, $\langle q_{\rm N}^{0}/T_0^{5}\rangle$ and $\langle Y_{\rm e}^{0}\rangle$, are smoothed by time-averaging over the last few milliseconds of the evolution with full neutrino transport and tabulated as a function of the relative radius coordinate $x_{\rm N,m}^{-}$, which is defined by Equation (2.33), except that $R_{\rm gain}(t)$ is replaced by $R_{\rm gain}^{Y_{\rm e}}(t)$. Inside the PNS's high-density core (i.e., for $r < R_{\rm core}$) and in regions where $Y_{\rm e} < 0.05$, we do not apply Equation (2.41) and instead set $Q_{\rm N}^{-} = 0$. This simplification does not have a relevant impact on the dynamical evolution of our long-time NEMESIS models (as we are not aiming at a detailed description of the PNS interior but rather at capturing the most crucial neutrino effects on the SN explosion).

[19] Note that the $\nu_{\rm e}$ and $\bar{\nu}_{\rm e}$ luminosities are, in fact, very similar in magnitude, but the energy spectrum of $\bar{\nu}_{\rm e}$ is getting increasingly harder compared to the one of $\nu_{\rm e}$, as a consequence of the decreasing proton abundance and therefore reduced absorption opacity of $\bar{\nu}_{\rm e}$, which moves the $\bar{\nu}_{\rm e}$ neutrinosphere (i.e., the region where $\bar{\nu}_{\rm e}$ roughly decouple from the medium and start leaking out) deeper inwards (to higher temperatures). Accordingly, the $\bar{\nu}_{\rm e}$ number fluxes ($\propto L_{\bar{\nu}_{\rm e}}/E_{\bar{\nu}_{\rm e}}$) are smaller compared to those of $\nu_{\rm e}$ despite similar luminosities ($L_{\nu_{\rm e}} \approx L_{\bar{\nu}_{\rm e}}$); see, e.g., Mirizzi et al. (2016); Janka (2017b).

In the left panel of Figure 2.6, we show the time evolution of the specific deleptonization rate, $\langle q_{\rm N}^- \rangle = \langle Q_{\rm N}^-/\rho \rangle < 0$, inside the PNS's inflated accretion mantle as a function of radius. At $\sim$0.9 s after the bounce, when the mass-accretion rate of downflows has declined to an insignificant level (see lower right panel of Figure 2.2), the deleptonization of matter in the PNS's surface layer basically stops (see the dependence of $Q_{\rm N,m}^-$ on $\dot{M}_{\rm down}$ in Equation (2.41)).

2.2.3. Neutrino Pressure Correction

Switching off the neutrino transport would also lead to a sudden drop of pressure support in the high-density regime if the contributions of neutrinos to the total pressure were ignored. To ensure hydrostatic equilibrium and thus to avoid unphysical artifacts such as PNS oscillations, we replace the neutrino-momentum source term, $\boldsymbol{Q}_{\rm M}$, in the hydrodynamics equations by an adequate neutrino-pressure contribution that is added to the gas pressure. Assuming that neutrinos are in local chemical equilibrium with the stellar matter at sufficiently high densities, we can employ the following analytic expression for a relativistic Fermi gas of one individual neutrino species with chemical potential μ (see, e.g., Bludman & van Riper 1978):

$$\begin{aligned} P'_\nu(\eta) &= \frac{1}{3}\frac{4\pi}{(hc)^3}\int_0^\infty \frac{\epsilon^3 {\rm d}\epsilon}{1+\exp[(\epsilon-\mu)/k_{\rm B}T]} \\ &= \frac{4\pi(k_{\rm B}T)^4}{3(hc)^3}\underbrace{\int_0^\infty \frac{x^3 {\rm d}x}{1+\exp(x-\eta)}}_{\equiv\, 6\,\cdot\, F_3(\eta)}\,, \end{aligned} \tag{2.42}$$

where $\eta := \mu/(k_{\rm B}T)$ denotes the neutrino degeneracy parameter, T the local fluid temperature, ϵ the neutrino energy, and $x := \epsilon/(k_{\rm B}T)$. Here, we have also introduced the Fermi integral of order n, which is defined as

$$F_n(\eta) = \frac{1}{\Gamma(n+1)}\int_0^\infty \frac{x^n {\rm d}x}{1+\exp(x-\eta)}\,, \tag{2.43}$$

where Γ indicates the Gamma function, with $\Gamma(3+1) = 3! = 6$. The total neutrino pressure (in thermal equilibrium) is then given as a sum of the contributions from all six neutrino species (i.e., $\nu_{\rm e}$, $\bar{\nu}_{\rm e}$, and the four heavy-lepton neutrinos, ν_μ, $\bar{\nu}_\mu$, ν_τ, and $\bar{\nu}_\tau$, which are commonly denoted as ν_x; see footnote 13 in Section 2.1.2):

$$\begin{aligned} P_\nu^{\rm eq} &= P'_\nu(\eta_{\nu_{\rm e}}) + P'_\nu(\eta_{\bar{\nu}_{\rm e}}) + 4\cdot P'_\nu(\eta_{\nu_x}) \\ &= \frac{4\pi(k_{\rm B}T)^4}{3(hc)^3}\cdot 6\cdot\left[F_3(\eta_{\nu_{\rm e}}) + F_3(-\eta_{\nu_{\rm e}}) + 4\cdot F_3(0)\right] \\ &= \frac{4\pi(k_{\rm B}T)^4}{3(hc)^3}\cdot\left[\frac{21\pi^4}{60} + \frac{1}{2}\eta_{\nu_{\rm e}}^2\left(\pi^2 + \frac{1}{2}\eta_{\nu_{\rm e}}^2\right)\right]\,, \end{aligned} \tag{2.44}$$

Here, we made use of the fact that the chemical potentials of electron neutrinos and antineutrinos in beta equilibrium are equal but opposite, i.e., $\mu_{\bar{\nu}_\mathrm{e}} = -\mu_{\nu_\mathrm{e}}$, with $\mu_{\nu_\mathrm{e}} = \mu_\mathrm{p} - \mu_\mathrm{n} + \mu_\mathrm{e}$ (where μ_p, μ_n, and μ_e are the chemical potentials of protons, neutrons, and electrons, respectively), and $\mu_{\nu_x} = 0$. In the last line of Equation (2.44), we have used the exact relation $F_3(\eta) + F_3(-\eta) = 7\pi^2/360 + \pi^2\eta^2/12 + \eta^4/24$ (and $2 \cdot F_3(0) = 7\pi^2/360$); see, e.g., Van Halen & Pulfrey (1985).

Since the assumption of local chemical equilibrium does not hold in regions of low matter densities, i.e., close to and outside of the neutrinospheres, from where neutrinos start to free-stream, we describe the neutrino pressure in the entire computational domain according to

$$P_\nu(\boldsymbol{r}, t) = P_\nu^\mathrm{eq}(\boldsymbol{r}, t) \cdot \zeta_P(\rho)\,, \tag{2.45}$$

with

$$\zeta_P(\rho) = \left\langle \frac{P_\nu^\mathrm{tr}(t_0)}{P_\nu^\mathrm{eq}(t_0)} \right\rangle(\rho) \cdot \min\left\{1, \frac{\rho(\boldsymbol{r}, t)}{10^{13}\,\mathrm{g\,cm^{-3}}}\right\}\,, \tag{2.46}$$

where the density-dependent factor $\zeta_P(\rho)$ accounts for a gradual reduction of the neutrino pressure with decreasing density (for densities lower than $10^{13}\,\mathrm{g\,cm^{-3}}$). At the high densities inside the PNS core, this factor also corrects for a possible small mismatch of the analytic equilibrium pressure of Equation (2.44) and the numerically computed neutrino pressure, P_ν^tr, as given by our neutrino-transport solver Vertex (see Section 2.1.2 and Equation (2.16) there):

$$\begin{aligned} P_\nu^\mathrm{tr}(\boldsymbol{r}, t) &= \frac{2\pi}{c} \sum_{\nu_i} \int_0^\infty \mathrm{d}\epsilon \int_{-1}^1 \mathrm{d}\mu\, \mu^2\, \mathcal{I}_{\nu_i}(\boldsymbol{r}, \mu, \epsilon, t) \\ &= \frac{4\pi}{c} \sum_{\nu_i} \int_0^\infty \mathrm{d}\epsilon\, \mathcal{I}_{\nu_i}^{(0)}(\boldsymbol{r}, \epsilon, t) \cdot \max\left\{\frac{1}{3}, f_{2,\nu_i}(\boldsymbol{r}, \epsilon, t)\right\}\,, \end{aligned} \tag{2.47}$$

with $\mathcal{I}_{\nu_i}$, $\mathcal{I}_{\nu_i}^{(0)}$, and f_{2,ν_i} being the specific intensity for the neutrino species ν_i, its zeroth angular moment, and the corresponding variable Eddington factor (for the second moment), respectively (see Section 2.1.2 for more details). Again, the sum runs over all six neutrino species. In Equation (2.46), the full-transport neutrino pressure, P_ν^tr, and the analytical equilibrium neutrino pressure, P_ν^eq, are evaluated at time t_0 when our neutrino treatments are switched. The ratio of the two pressure terms is then averaged over all angular directions and tabulated as a function of the matter density ρ.

In our long-time simulations with the Nemesis treatment, the neutrino pressure contribution of Equation (2.45) is added to the gas pressure in the hydrodynamics equations for momentum and energy conservation (i.e., in Equations (2.2) and (2.3)). Moreover, with the same prescription, we also include the neutrino pressure and energy contributions to the general relativistic corrections in the effective gravitational potential of Marek et al. (2006, "Case A"), i.e., P_ν in Equation (2.6) and $\mathcal{E}_\nu/c^2 = 3P_\nu/c^2$ in Equation (2.7), which holds for an ideal relativistic Fermi gas. The term $vF_\nu/(c^4\Gamma)$ in Equation (2.7) is neglected since $vF_\nu/c^2 \ll \mathcal{E}_\nu$ at the high densities inside the PNS. Again, this treatment minimizes numerical noise and allows for a

mostly transient-free and smooth transition when our approximate NEMESIS neutrino scheme replaces the VERTEX transport.

2.3. Code Performance and Scaling Efficiency

Performing full-3D simulations of CCSN explosions remains a major challenge even if the computationally most expensive neutrino transport is replaced by a more simplified neutrino treatment (as described in Section 2.2): Adequately resolving the relevant length scales of the problem, which range from $\mathcal{O}(10)$ meters to thousands of kilometers (see Section 2.1.3), requires an enormous number of spatial grid zones (typically more than 10 million for an angular resolution of 2°). On top of that, high sound speeds and fluid velocities (of up to some 10% of the speed of light) in combination with the small radial grid zones at the PNS surface severely constrain the CFL time step (to typical values of around 10^{-8}–10^{-6} seconds). This implies that millions of computational steps must be performed per model (for an evolution period of a few seconds), which can only be achieved by running massively parallel and highly efficient simulation codes on the most powerful supercomputers.

The neutrino radiation-hydrodynamics code PROMETHEUS-VERTEX (Section 2.1; Fryxell et al., 1989; Rampp & Janka, 2002; Buras et al., 2003) as developed and continuously refined by the Max-Planck CCSN group around Thomas Janka has been the production tool in numerous Tier-0/Tier-1 high-performance computing (HPC) projects since 2013, supported by grants of the European PRACE initiative,[20] the German GAUSS program,[21] as well as by local grants of the Leibniz Supercomputing Centre (LRZ).[22] The code's excellent performance and scaling efficiency has been described previously, e.g., in the works by Marek et al. (2014) and Melson (2016). Here, we only briefly reiterate the overall parallelization strategy and comment on the scaling behavior of the PROMETHEUS hydrodynamics solver coupled to our newly implemented NEMESIS neutrino scheme (Section 2.2).

Our simulation code employs a hybrid MPI/OpenMP parallelization strategy where the computational domain gets decomposed into angular blocks via MPI with direct next-neighbor communication. The individual angles are then distributed by an intra-block OpenMP parallelization scheme. To keep next-neighbor MPI communication at a minimal level, our domain decomposition routines optimize the load balancing with angular blocks preferably symmetric in polar and azimuthal angles. This strategy ensures an excellent strong-scaling behavior up to several thousand compute cores for the typical problem size of our considered models. Moreover, the code version applied in this work has been updated and optimized for use on the

[20] https://prace-ri.eu/
[21] https://www.gauss-centre.eu/
[22] https://www.lrz.de/english/

Table 2.2.: Strong-scaling behavior of the PROMETHEUS code with the NEMESIS neutrino treatment (in a full production setup) on SuperMUC-NG at LRZ.[23]

# of Nodes	# of Cores	Relative Speedup	Scaling Efficiency
10	480	1.00	100.0%
25	1,200	2.97	118.7%
35	1,680	4.25	121.5%
50	2,400	6.40	128.0%
175	8,400	17.31	98.9%
350	16,800	22.79	65.1%
700	33,600	32.99	47.1%

Note. These strong-scaling tests were performed with a problem size of $N_r \times N_\theta \times N_\phi \times 2 = 730 \times 56 \times 150 \times 2$ zones, where N_r, N_θ, and N_ϕ denote the grid extensions in radial, lateral, and azimuthal directions, and the factor of 2 indicates the two grid patches of the Yin-Yang grid (see Section 2.1.3). This grid configuration corresponds to a typical setup used in our production runs. The relative speedup is normalized to 10 nodes of SuperMUC-NG, which are each consisting of 48 compute cores.

SuperMUC-NG system[23] at LRZ by introducing rigorous AVX-512 vectorization (Bollig et al., 2021; Bollig, 2022).

Table 2.2 and Figure 2.7 show the results of our detailed scaling tests on SuperMUC-NG, which we could use for the long-time simulations of the models discussed in this thesis. Our tests of the strong-scaling behavior are based on a complete model with the full implementation of all physical processes and numerical techniques that we also use in our production runs. The measured scaling efficiency on SuperMUC-NG is, therefore, directly applicable to the long-time 3D simulations carried out in the context of this thesis (see Chapter 3).

We note in passing that the PROMETHEUS-VERTEX code with full energy-dependent ray-by-ray-plus neutrino transport shows an almost perfect scaling up to even more than 100,000 cores (see Marek et al., 2014; Melson, 2016). The fact that our code setup with the NEMESIS neutrino treatment (instead of the full neutrino transport) starts to deviate from the ideal (i.e., linear) scaling already at a smaller number of compute cores (at around ∼10,000 cores; see Figure 2.7) can be understood based on the much reduced computational costs of our effectively pure-hydrodynamics calculations with only negligible overhead due to the NEMESIS neutrino scheme. The

[23] https://doku.lrz.de/display/PUBLIC/SuperMUC-NG

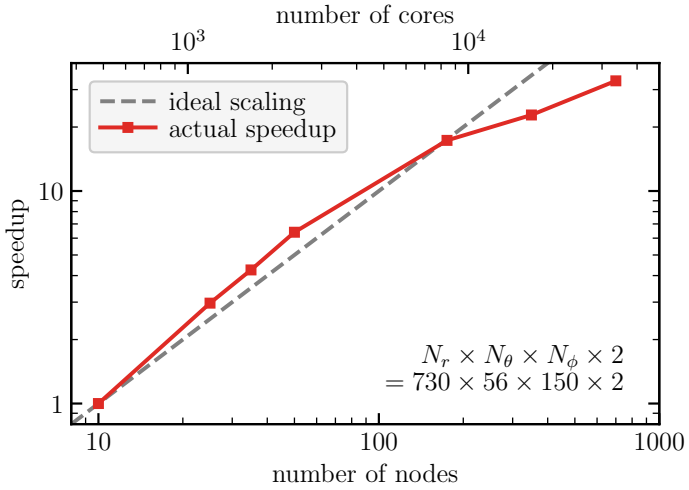

Figure 2.7.: Strong-scaling behavior of the PROMETHEUS code with the NEMESIS neutrino treatment (in a full production setup) on SuperMUC-NG at LRZ. The shown code scaling results (*red squares*) have been obtained for a problem size of $N_r \times N_\theta \times N_\phi \times 2 = 730 \times 56 \times 150 \times 2$ zones, which corresponds to a typical grid configuration as used in our production runs with Yin-Yang grid (see Section 2.1.3). The relative speedup is normalized to 10 compute nodes of SuperMUC-NG, each consisting of 48 cores. Note that our simulation code scales nearly perfectly up to roughly 10,000 compute cores and deviates from the (ideal) linear scaling (*gray dashed line*) only for even larger numbers of cores. For our production runs, we typically employ 42–175 nodes (i.e., 2,016–8,400 cores), depending on the specific model under consideration and the exact grid configuration.

bottleneck associated with frequent MPI communication thus begins to dominate the computation load per task already at a smaller number of compute nodes. Moreover, the hydrodynamics calculations do not profit from the (implicitly parallel) ray-by-ray approach employed in the VERTEX transport module.

3

Core-collapse Supernova Simulations

This chapter presents the results of our long-time 3D hydrodynamics simulations of neutrino-driven CCSN explosions from the early phase of shock revival until the fully developed explosion stage several seconds later. In Section 3.1, we first describe the stellar progenitor models used as initial conditions for our simulations. In Section 3.2, we briefly summarize the main outcomes of the self-consistent PROMETHEUS-VERTEX simulations with full-fledged neutrino transport by Melson et al. (2015a,b, 2020), Summa et al. (2018), and Bollig et al. (2021), which are the starting points of our long-time 3D hydrodynamics simulations with the NEMESIS scheme. The main results of these extension models are discussed in Section 3.3, where we provide a detailed overview of the model setups and neutrino signals that enter these simulations, describe the dynamical evolution of the models, and return to the question whether neutrino-driven CCSN models can reach the typical explosion energies of observed SNe. More details on the growth of the explosion energy are provided in Section 3.4. Section 3.5 gives a brief overview of the nucleosynthesis yields of our models. The NS properties (i.e., kick velocities and spin periods) of our models are discussed in Section 3.6.

3.1. Progenitor Models

For our 3D CCSN simulations, we rely on initial conditions in the form of pre-SN progenitor models (provided to us by external collaborators; e.g., Woosley & Heger, 2015). These progenitor models result from stellar evolution calculations over the entire lifetimes of massive stars, from the hydrogen-burning zero-age main sequence (ZAMS) until the eventual onset of iron core collapse. All pre-SN models considered in this work are based on spherically symmetric (i.e., 1D), single-star stellar evolution simulations with the KEPLER code (Weaver et al., 1978; Heger & Woosley, 2010), yet for one model (for model s18.88) the final minutes previous to core collapse were modeled in full 3D geometry.

Because of the long stellar lifetimes that need to be covered (typically millions of years in the case of massive stars), complete stellar evolution calculations can only be achieved in 1D. Nevertheless, in recent years there has been a growing interest in the multi-dimensional nature of convective shell burning during the final evolutionary stages before gravitational core collapse (e.g., Arnett & Meakin, 2011; Couch et al., 2015; Müller et al., 2016; Yoshida et al., 2019; Yadav et al., 2020; Fields

Table 3.1.: Progenitor models employed as initial conditions for the CCSN simulations discussed in this thesis, with references to the literature.

Model	M_{ZAMS}[a] [$\mathrm{M}_\odot$]	Z[b] [$Z_\odot$]	$\xi_{1.5}$[c]	$\xi_{1.75}$[c]	$\xi_{2.0}$[c]	$\xi_{2.5}$[c]	3D[d]	Rot.[e]	Ref.[f]
s9.0	9.0	1	0.00523	0.00007	0.00005	0.00004	no	no	[1]
z9.6	9.6	0	0.00023	0.00011	0.00009	0.00008	no	no	[2]
m15	15.0	1	0.84573	0.28952	0.17206	0.10602	no	yes	[3]
s18.88	18.88	1	0.99174	0.77953	0.47325	0.28335	yes	no	[4]
s20	20.0	1	0.99743	0.76953	0.46949	0.28462	no	no	[5]

[a] ZAMS mass (in units of solar masses). [b] Metallicity (in terms of the solar metallicity, $Z_\odot$; Lodders, 2003; Asplund et al., 2009). [c] Pre-collapse compactness parameter ξ_M (O'Connor & Ott, 2011), for $M = \{1.5, 1.75, 2.0, 2.5\}\,\mathrm{M}_\odot$, see Equation (3.1). [d] 3D (pre-SN) initial conditions: For model s18.88, the final seven minutes of convective oxygen shell burning before core collapse have been simulated in 3D (see main text). [e] Progenitor model with rotation: The rotating m15 model (more precisely, model m15u6 from https://2sn.org/stellarevolution/magnet/) has been evolved with angular-momentum transport by magnetic fields; see main text for more details. [f] References: [1] Woosley & Heger (2015), [2] Heger (2012), [3] Heger et al. (2005), [4] Yadav et al. (2020), [5] Woosley & Heger (2007).

& Couch, 2021; Fields, 2022; McNeill & Müller, 2022; Varma & Müller, 2021). The works by Couch & Ott (2013) and Müller & Janka (2015) have shown that the presence of large-scale pre-collapse perturbations in the convectively burning silicon and oxygen shells can foster the growth of nonradial instabilities in the postshock layer, thus facilitating explosions (see, e.g., Müller et al., 2017, 2019; Bollig et al., 2021; Vartanyan et al., 2022).

Table 3.1 provides an overview of all progenitor models considered in this work. At the lower mass end of iron-core SN progenitors, we use two models with ZAMS masses of $9.0\,\mathrm{M}_\odot$ and $9.6\,\mathrm{M}_\odot$, namely the solar-metallicity progenitor s9.0 from Woosley & Heger (2015) and the zero-metallicity progenitor z9.6 from Heger (2012). Both (non-rotating) models have already been studied extensively in the literature. The s9.0 model has been employed, e.g., in the 2D simulations by Radice et al. (2017) and Just et al. (2018), as well as in the 3D simulations by Glas et al. (2019b) and Melson et al. (2020). The z9.6 model has been studied previously in 1D (e.g., Mirizzi et al., 2016), in 2D (e.g., Janka et al., 2012; Müller et al., 2013), and in 3D (e.g., Melson et al., 2015b; Müller et al., 2019; Stockinger et al., 2020; Sandoval et al., 2021). Both progenitors, the s9.0 and the z9.6 models, have been shown to explode rather readily in numerical simulations because of their steeply declining density profiles outside of the iron core (see Figure 3.1). This characteristic becomes apparent also from the small values of the (pre-collapse) compactness parameter (O'Connor & Ott, 2011),

which is defined as:

$$\xi_M = \frac{M/\mathrm{M}_\odot}{r(M)/1000\,\mathrm{km}}\,. \tag{3.1}$$

Yet, the main focus of this thesis is on the explosions of more massive (solar-metallicity) progenitors with ZAMS masses of $15.0\,\mathrm{M}_\odot$, $18.88\,\mathrm{M}_\odot$, and $20.0\,\mathrm{M}_\odot$, namely model m15 from Heger et al. (2005), model s18.88 from Yadav et al. (2020), and model s20 from Woosley & Heger (2007). The (intermediate-mass) m15 model (more precisely, model m15u6 from https://2sn.org/stellarevolution/magnet/) has been evolved with the effects of differential rotation, including angular momentum transport by magnetic fields. The evolution of this model had been started with an initial equatorial rotation velocity of $300\,\mathrm{km\,s^{-1}}$ on the ZAMS, leading to a relatively moderate final pre-collapse angular rotation rate of $\sim 10^{-3}\,\mathrm{rad\,s^{-1}}$ at the Si/Si+O composition shell interface (Heger et al., 2005).[24] However, as this model did not yield a successful explosion in the self-consistent 3D CCSN simulations by Summa et al. (2018), these authors also studied a modified version of this progenitor model with an artificially enhanced rotation rate (roughly 300 times faster than the original model from the stellar evolution calculation; case "artrot" in Figure 1 of Summa et al., 2018). The same rotation profile had been used previously in the studies by Müller et al. (2004), Buras et al. (2006a), and Marek & Janka (2009). Our simulations of the $15\,\mathrm{M}_\odot$ progenitor discussed below are based on the fast-rotating "artrot" 3D model of Summa et al. (2018).

For the s18.88 progenitor model of Yadav et al. (2020), the traditionally used assumption of a 1D stellar structure as the initial condition for CCSN simulations has been dropped and replaced by more realistic, self-consistent initial conditions as generated by 3D simulations of the final seven minutes of convective oxygen-shell burning before stellar core collapse.[25] The 3D model by Yadav et al. (2020) showed a violent oxygen-neon shell merger prior to the collapse of the iron core and developed large-scale convective perturbations (in density, velocity, and chemical composition) of considerable amplitude, aiding a successful and energetic explosion (see Section 3.2 and Bollig et al., 2021).

Lastly, we consider the heavily used s20 pre-SN model from Woosley & Heger (2007), a non-rotating, solar-metallicity progenitor star ranging at the borderline between successful and failed explosions. It has been employed in numerous 2D simulations by different groups (e.g., Bruenn et al., 2013, 2016; Dolence et al., 2015; Pan

[24] The work by Heger et al. (2005) suggests that the cores of typical (single-star) CCSN progenitors do not rotate with high rotation rates at the end of their lives because of angular momentum transport by magnetic fields, which is in line with the relatively modest spin periods observed for young pulsars (Kaspi & Helfand, 2002; Ott et al., 2006); cf. Cantiello et al. (2014) for a discussion of angular-momentum transport in the cores of evolved low-mass stars.

[25] The 1D stellar evolution calculations of this progenitor model until seven minutes before core collapse (i.e., until the start of the 3D simulation of convective shell burning) have been carried out following the procedure as detailed in Müller et al. (2016, Section 2.1).

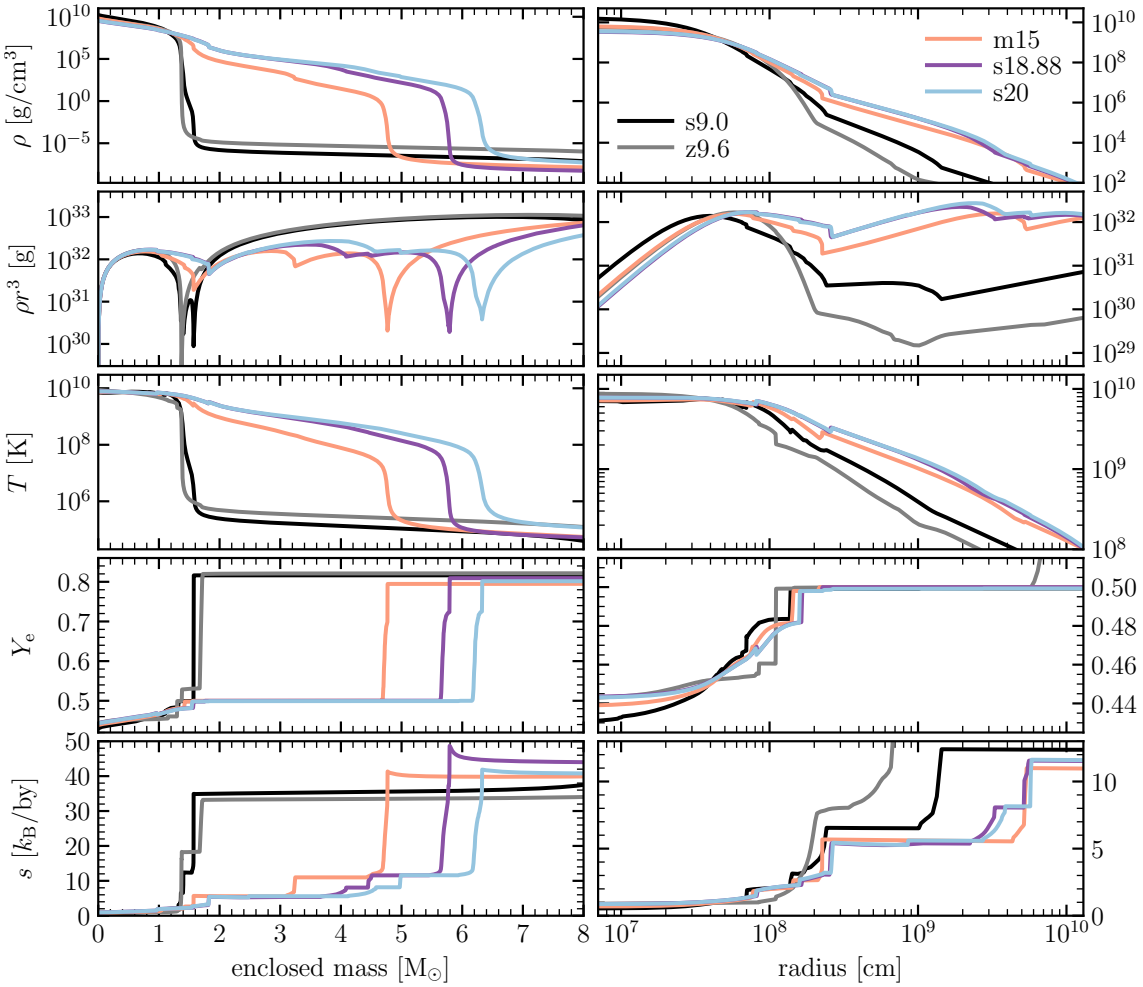

Figure 3.1.: Overview of pre-collapse progenitor structures for the models considered in this work (see Table 3.1). From top to bottom, profiles of the density, the density times the radius cubed, the temperature, the electron fraction, and the specific entropy (i.e., the entropy per baryon) are shown as functions of the enclosed mass (*left panels*) and the radius (*right panels*). Note the different axis scales in the left and right panels.

et al., 2016; Skinner et al., 2016; Suwa et al., 2016; Summa et al., 2016; Bollig et al., 2017; Kotake et al., 2018; O'Connor & Couch, 2018b; Just et al., 2018; Vartanyan et al., 2018) and also in various 3D simulations (e.g., Melson et al., 2015a, 2020; Ott et al., 2018; Glas et al., 2019b). Both the s18.88 and the s20 progenitor models have comparatively shallow density profiles in the layers around the iron core and exhibit correspondingly large values of the pre-collapse compactness parameter (see Table 3.1). This has the important consequence of high mass-accretion rates onto the stagnant shock and into the region close to the central PNS during the first seconds of the explosions, as will be discussed in more depth in the following sections.

Figure 3.1 provides an overview of the pre-SN structures of all five progenitor models considered in this thesis. We show the radial profiles of the matter density, ρ, the density times the radius cubed, ρr^3, the temperature, T, the electron fraction, Y_e, and the specific entropy, s. Note that all five progenitor stars have largely different pre-collapse structures, which strongly affect the characteristics of the subsequent SNe, such as the explosion energy, the development of explosion asymmetries, or the mixing of heavy chemical elements from the stellar core into the star's envelope (see the following sections). For example, in regions where the gradient of ρr^3 is positive, deceleration of the outgoing SN shock can be expected, whereas negative gradients of ρr^3 cause shock acceleration (Sedov, 1959). Near the composition shell interfaces, this can lead to the formation of dense shells (with density inversions) that are prone to Rayleigh-Taylor or Richtmyer-Meshkov instabilities (see, e.g., Wongwathanarat et al., 2015; Stockinger et al., 2020). Moreover, the progenitor structures also determine the observable neutrino signals, the SN light curves and spectra, the nucleosynthetic yields, as well as the masses, recoil kicks, and spins of the remnant neutron stars. It is, therefore, essential to account for the diversity of initial conditions by exploring larger samples of pre-SN stars. Our study only marks a first step in this direction. and should be augmented by a growing number of self-consistent SN models in the future, also considering progenitors from binary stellar evolution calculations (e.g., Podsiadlowski et al., 2004; Schneider et al., 2015, 2021; Woosley, 2019; Laplace et al., 2020, 2021).

3.2. Onset of the Explosions

Over the past years, the set of fully self-consistent 3D CCSN models simulated with the Prometheus-Vertex code has been growing steadily (see Hanke et al., 2013; Tamborra et al., 2013, 2014a,b; Melson et al., 2015a,b, 2020; Summa et al., 2018; Walk et al., 2020; Bollig et al., 2021). Because of the high computational costs of detailed neutrino-transport calculations, most of these models were evolved only until far less than a second after bounce. At this early stage, the characteristic explosion properties, such as the explosion energy and the PNS recoil kick velocity, only start to build up, which is why we extend the models until later times by means of our newly developed Nemesis neutrino scheme. In this section, we briefly summarize the setups and main results of the full-transport simulations by Melson et al. (2015a,b, 2020), Summa et al. (2018), and Bollig et al. (2021), which are the starting points of the long-time Nemesis extension models simulated in the context of this thesis (and discussed in Section 3.3).

3.2.1. Simulation Setups

In Table 3.2, we provide an overview of the model specifications for the five full-transport Prometheus-Vertex 3D simulations considered in this work, with references to the publications where the models have been presented first. All simulations were

Table 3.2.: Model specifications of the full-transport 3D simulations discussed in this thesis, with references to the corresponding publications.

Model	Grid[a]	$\Delta\theta$[b]	R_{1D}[c]	N_ϵ[d]	Burning[e]	Reference
s9.0	YY	SMR	1.6 km	12	Flashing	Melson et al. (2020)
z9.6	YY	2°	1.6 km	12	Flashing	Melson et al. (2015b)
m15	YY	2°	1.6 km	12	Flashing	Summa et al. (2018)
s18.88	YY	2°	1.6 km*	15	Network	Bollig et al. (2021)
s20	SP	2°	10 km	12	Flashing	Melson et al. (2015a)

[(a)] Computational grid: Yin-Yang (YY) or spherical polar (SP); see Section 2.1.3. [(b)] Angular grid resolution: 2° (uniformly) or SMR grid with stepwise increased angular resolution (2° inside the gain radius, 1° between the gain radius and a fixed radius of 160 km, and 0.5° outside of 160 km). [(c)] Radius of the spherical (1D) inner core. [(*)] For model s18.88, the radius of the 1D core was increased from 1.6 km to 3 km at ∼1 s after bounce. [(d)] Number of geometrically spaced neutrino energy bins (covering 0–380 MeV). [(e)] Treatment of nuclear burning: Flashing scheme (Rampp & Janka, 2002, Appendix B.2) or α-chain reaction network (Hix & Thielemann, 1999b; Bollig et al., 2021).

All models: Three-flavor, ray-by-ray-plus neutrino transport (with the full set of neutrino interactions listed in Table 2.1); LS220 high-density EoS; 23 nuclear species; gravitational potential according to Marek et al. (2006, "Case A"); gradually refined radial grid with a terminal resolution of $\Delta r/r \sim 0.001$–0.005 at the PNS surface.

carried out with three-flavor, energy-dependent, ray-by-ray-plus neutrino transport, including the complete set of neutrino interactions and microphysics described in Section 2.1.2 (see Table 2.1). The neutrino spectrum was discretized using 12–15 geometrically spaced energy bins with an upper bound of 380 MeV.

All models were computed with the LS220 nuclear EoS (Lattimer & Swesty, 1991) and an effective 1D gravitational potential according to Marek et al. (2006, "Case A"). Nuclear burning was treated approximately through the flashing scheme of Rampp & Janka (2002) or, for model s18.88, by means of a newly implemented α-chain reaction network (Bollig et al., 2021), including 23 nuclear species. In the regime of NSE, i.e., above a critical threshold temperature, T_{NSE}, the nuclear composition was given by the EoS. For model s18.88, a threshold value of $T_{\mathrm{NSE}} = 0.689$ MeV was taken, whereas all other models employed $T_{\mathrm{NSE}} = 0.5$ MeV. Albeit, in the case of models s9.0 and m15, this standard value of 0.5 MeV was taken only for infalling matter, whereas a lower value of $T_{\mathrm{NSE}} = 0.343$ MeV was assumed for neutrino-heated, high-entropy outflows to facilitate nucleon recombination to α particles and heavy nuclei. For more details, we refer to Section 2.1.

One of the full-transport 3D simulations, namely model s20, was computed on a spherical polar grid. All other models, in contrast, were simulated on an axis-free overset Yin-Yang grid (see Section 2.1.3). Our standard choice of the (uniform)

angular grid resolution of 2° was replaced for model s9.0 by an SMR grid, where the angular resolution of 2° was stepwise increased to 1° (at the gain radius) and 0.5° (outside of a fixed radius of 160 km). In all simulations, the innermost volume of the PNS (i.e., $r \leqslant R_{1D}$, with $R_{1D} = 1.6$–10 km; see Table 3.2) was treated in spherical symmetry to relax the CFL time-step constraint at the grid center.

The pre-bounce collapse phase of all models was computed on a Lagrangian (i.e., moving) radial grid, whereas an Eulerian (i.e., fixed), non-equidistant radial grid with initially 400–550 logarithmically spaced zones was employed for the post-bounce evolution, covering the stars innermost $(1$–$6)\times10^9$ cm with a resolution of $\Delta r/r \leqslant 0.028$ everywhere. To properly resolve the steepening density gradient at the surface of the contracting PNS, the radial grid was gradually refined throughout a simulation, typically reaching ∼600–700 zones and a resolution of $\Delta r/r \sim 0.001$–0.005 around the location of the gain radius at the end of the evolution period with full neutrino transport.

For all models that were started from 1D initial conditions (see Section 3.1), spherical symmetry was broken by imposing random cell-to-cell seed perturbations of 0.1% in density or radial velocity (in the entire computational domain) at 10 ms after bounce. As noted above, the s18.88 model is instead based on more realistic initial conditions as provided from 3D simulations of the last seven minutes of convective shell burning (Yadav et al., 2020), providing self-consistent (large-scale and large-amplitude) perturbations in density, velocity and chemical composition.

Because of the high computational costs of simulations with full neutrino transport, the 3D Prometheus-Vertex models were typically evolved only until post-bounce times of ∼0.5 s. However, the most recent of all models discussed in this thesis, namely model s18.88, has been simulated until 1.675 s after bounce, which became possible due to a significant acceleration of the simulation code compared to previously employed code versions (Bollig et al., 2021). The final evolution times of all models with full neutrino transport are provided below in Table 3.5. If not stated otherwise, all times given in this work are post-bounce times, i.e., measured relative to the time of the core bounce.

3.2.2. Early-time Explosion Dynamics

In Figure 3.2, we provide an overview of some key quantities that illustrate the evolution during the first ∼0.5 s of the explosions for all five 3D models with full neutrino transport, as discussed in the publications listed in Table 3.2. We show the mass-accretion rates of downflows at 400 km, the angle-averaged shock radii, the baryonic and gravitational PNS masses, and the PNS radii and PNS core radii. Here, the mass-accretion rate of downflows is defined as the surface integral of the density, ρ, times the radial velocity, v_r, over a sphere of given radius r,

$$\dot{M}_{\mathrm{down}}(r) = -r^2 \int_{4\pi} \mathrm{d}\Omega\, \rho\, v_r\, \Theta(-v_r)\,, \tag{3.2}$$

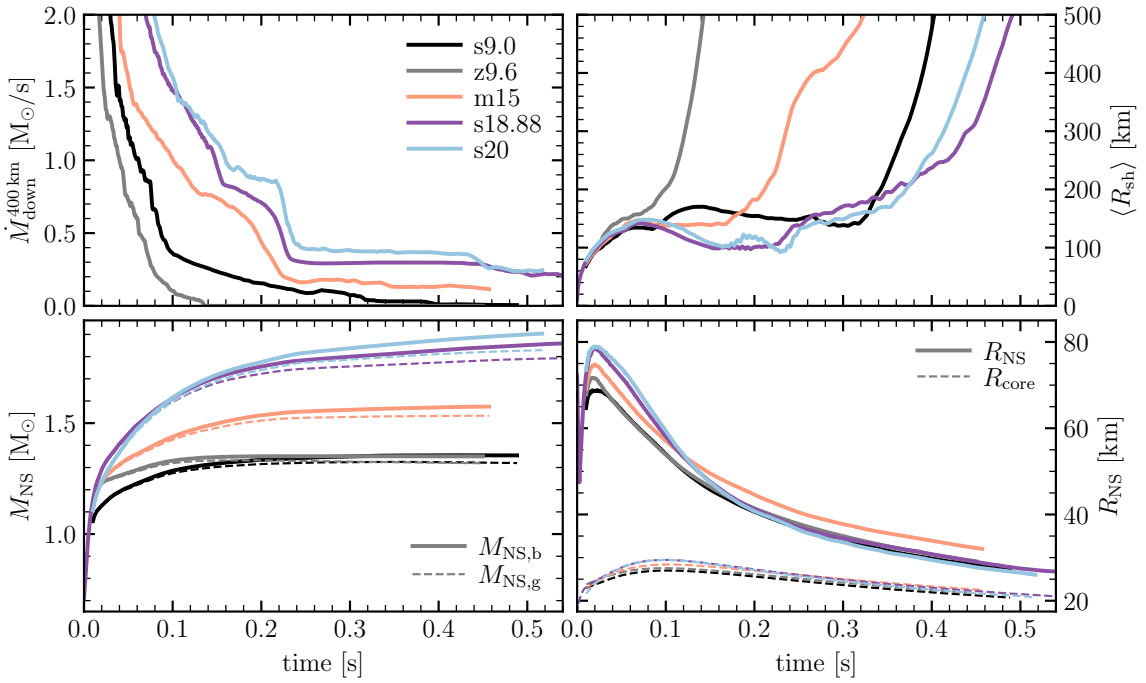

Figure 3.2.: Time evolution of the mass-accretion rate of downflows (evaluated at 400 km; *top left*), the angle-averaged shock radius (*top right*), the baryonic and gravitational PNS mass (*bottom left*), and the PNS radius and the PNS core radius (*bottom right*) for the full-transport 3D Prometheus-Vertex models considered in this work (see Table 3.2). Note that we only show the initial 0.54 s, while model s18.88 was computed with full neutrino transport until ∼1.7 s after bounce (see Figure 3.10 for the whole evolution).

where $\Theta(x)$ is the Heaviside step function. The time-dependent PNS radius, $R_{\mathrm{NS}}(t)$, and PNS core radius, $R_{\mathrm{core}}(t)$, are defined as the radii where the angle-averaged density equals $10^{11}\,\mathrm{g\,cm^{-3}}$ and $5 \times 10^{12}\,\mathrm{g\,cm^{-3}}$, respectively. The baryonic mass of the PNS, $M_{\mathrm{NS,b}}(t)$, is obtained by integrating ρ over the volume inside the PNS radius; its gravitational mass, $M_{\mathrm{NS,g}}(t)$, is related to the baryonic mass by subtracting the mass equivalent corresponding to the energy loss through neutrino emission:

$$M_{\mathrm{NS,g}}(t) = M_{\mathrm{NS,b}}(t) - \frac{1}{c^2} \int_0^t L_\nu^{\mathrm{tot}}(t')\,\mathrm{d}t' \tag{3.3}$$

Here, $L_\nu^{\mathrm{tot}}(t)$ denotes the time-dependent, total neutrino luminosity (i.e., the sum of the luminosities of all six neutrino species; see Equation (2.17)), and c is the speed of light.[26] The time evolution of the neutrino luminosities of the individual species is

[26] In fact, the time integral also includes a small contribution from $t' < 0$, i.e., from the (pre-bounce) collapse phase, when the ν_{e} luminosity is already non-zero because of electron captures on nuclei and free protons.

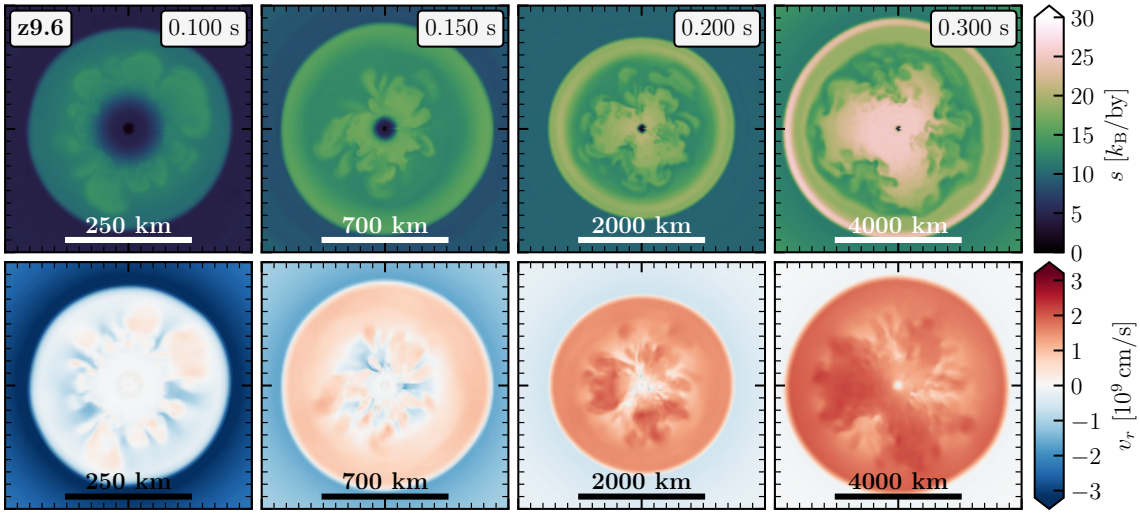

Figure 3.3.: Cross-sectional cuts in the x–z plane of model z9.6 with full neutrino transport (Melson et al., 2015b) at 100, 150, 200, and 300 ms after bounce, showing the specific entropy (i.e., entropy per baryon; *top row*) and the radial velocity (*bottom row*). Note the changing length scales of the plots.

shown below in Figure 3.9. In the following, we briefly summarize the dynamical evolution of all five full-transport models during the first few hundred milliseconds after the bounce. For more details, we refer to the references given in Table 3.2.

Models z9.6 and s9.0

The two low-mass models z9.6 and s9.0 (Melson et al., 2015b, 2020) clearly differ from the more massive progenitors in the sense that they are characterized by steep density profiles outside of their iron cores, as is evident also from their small values of the pre-collapse compactness parameter (see Table 3.1). Consequently, the mass-accretion rate drops quickly during the first ∼100 ms after the bounce, which in turn leads to a comparatively low ram pressure onto the transiently stalled shock front. The z9.6 and s9.0 models, therefore, explode robustly in numerical simulations (cf. Glas et al., 2019b; Müller et al., 2019; Sandoval et al., 2021). At the same time, the low mass-accretion rates result in relatively low-mass NSs (∼1.3–1.4 $M_\odot$; Table 3.5), low neutrino luminosities and mean energies (Figure 3.9), and relatively small values of the explosion energy, as will be discussed in more detail below (see Sections 3.3.3 and 3.4).

In particular, the z9.6 model is a pretty exceptional case among the iron-core progenitors of Table 3.1, as it closely resembles the structure of stars with degenerate oxygen-neon-magnesium cores (and very dilute outer stellar shells) that explode as electron-capture SNe (ECSNe; see, e.g. Kitaura et al., 2006; Janka et al., 2008; Fischer et al., 2010; Gessner & Janka, 2018; Stockinger et al., 2020). Therefore, explosions like the one of model z9.6 are sometimes called "ECSN-like" in the literature. As seen in the upper right panel of Figure 3.2, its evolution is characterized by a very short

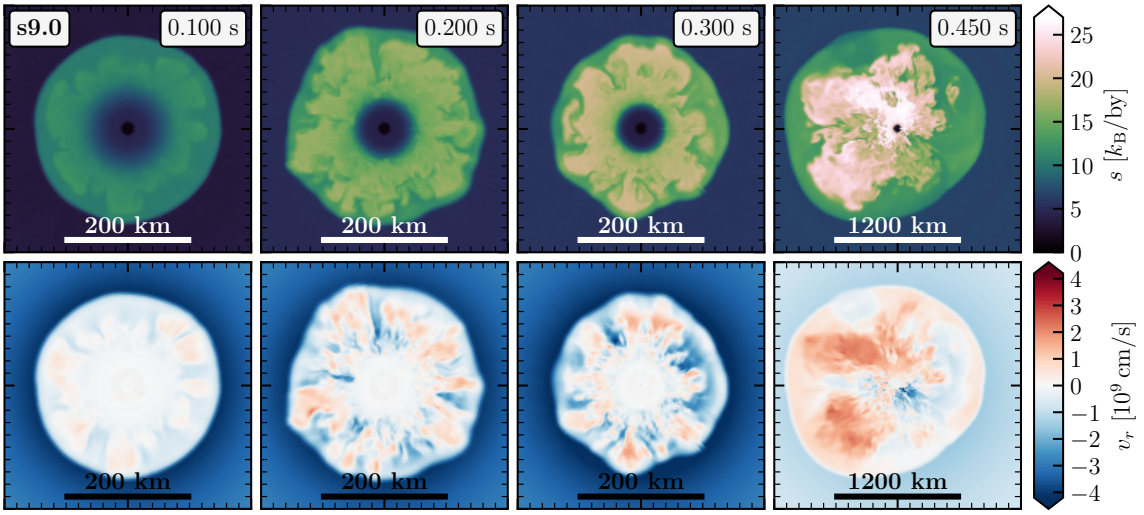

Figure 3.4.: Cross-sectional cuts in the x–z plane of model s9.0 with full neutrino transport (Melson et al., 2020) at 100, 200, 300, and 450 ms after bounce, showing the specific entropy (i.e., entropy per baryon; *top row*) and the radial velocity (*bottom row*). Note the changing length scales of the plots.

period of shock stagnation of only a few tens of milliseconds, followed by an early onset of runaway shock expansion (around 100 ms after the bounce). The explosion is almost spherical, with only a relatively small degree of nonradial asymmetries (see Figure 3.3). In fact, the z9.6 model explodes self-consistently even in 1D CCSN simulations, though at a somewhat later time (at ∼300 ms) compared to the 3D case, which experiences an additional boost by neutrino-driven turbulent convection (Melson et al., 2015b).

Likewise, the s9.0 model is highly susceptible to explosion. However, the mass-accretion rate does not drop to as low vales as in the case of model z9.6 (see upper left panel of Figure 3.2). Consequently, the shock stagnates at the typical radius of ∼100–200 km and is revived by neutrino-heating only with the arrival of the Si/O composition interface at around 320 ms after bounce (reaching 400 km at 390 ms). This leaves enough time for the development of significant nonradial asymmetries, as seen clearly in Figure 3.4. The model does not show any signs of SASI activity. However, large-scale convective plumes develop in the neutrino-heated postshock flow, deforming the shock front visibly (as in CCSN simulations of the same progenitor model by Glas et al., 2019b). At the end of the full-transport simulation, accretion streams are still piercing through to the innermost regions around the central PNS. As was shown in the resolution study by Melson et al. (2020), the explosion properties of the s9.0 model are nearly unaffected by changes in the angular resolution, with only minor differences between the high-resolution SMR case (discussed here) and a simulation of the same model with a reduced angular resolution of 3.5°. This result agrees with the findings of Glas et al. (2019b).

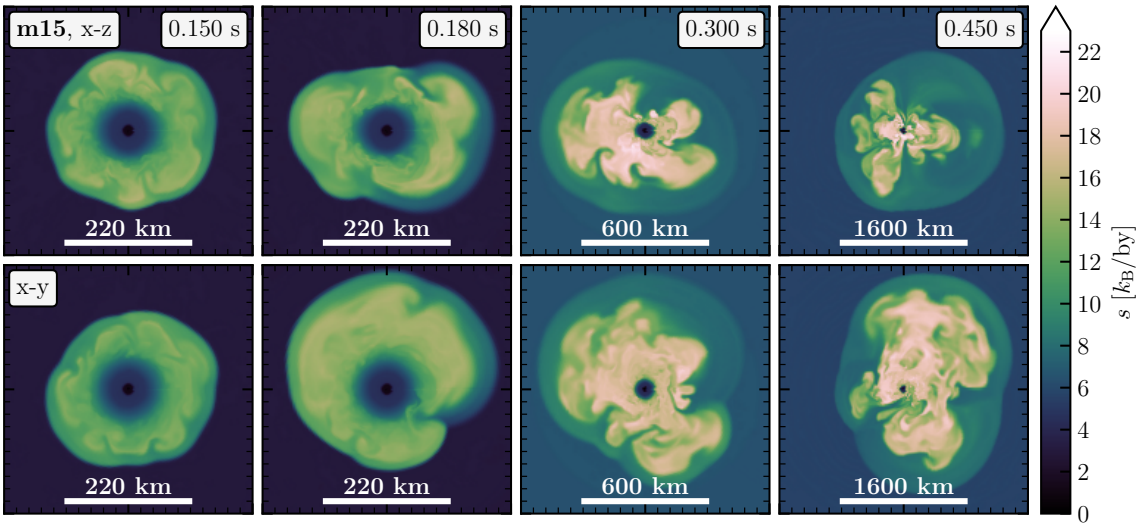

Figure 3.5.: Cross-sectional cuts in the x–z plane (*top row*) and x–y plane (*bottom row*) of model m15 with full neutrino transport (Summa et al., 2018) at 150, 180, 300, and 450 ms after bounce, showing the specific entropy (i.e., entropy per baryon). The z-axis coincides with the rotation axis of the model. Note the changing length scales of the plots.

Model m15

Among all CCSN simulations discussed in this work, the intermediate-mass model m15 (Summa et al., 2018) is the only one that is based on a (fairly rapidly, differentially) rotating progenitor star. Up to 10 ms after the core bounce, it was simulated in 2D (on a spherical polar grid), and only afterward was it mapped to the 3D Yin-Yang grid. This approach did not affect the later evolution of the model because relevant 3D effects emerged only after ∼100 ms. Otherwise, the model was computed with the standard setup as employed for the other full-transport simulations (see Section 3.2.1).

The m15 model explodes relatively fast and in a highly oblate fashion due to the aid of a powerful SASI spiral mode. Shock expansion (in the equatorial plane) sets in only ∼200 ms after the bounce, even before the Si/Si+O interface falls through the shock front (Summa et al., 2018). Although rotational effects lead to a more extended and cooler PNS compared to the non-rotating models (see lower right panel of Figure 3.2) and thus to reduced neutrino luminosities and mean energies (Figure 3.9), the spiral SASI pushes the shock outward and therefore increases the volume and mass of the gain layer. This allows for an efficient neutrino-energy deposition, overcompensating the rotationally reduced neutrino emission. Moreover, the SASI spiral motions store gravitational energy of the accretion flow in kinetic energy of rotation (cf. Blondin & Mezzacappa, 2007; Fernández, 2015; Kazeroni et al., 2016). In Figure 3.5, we provide snapshots of model m15 at four different times, showing cross-sectional cuts of the specific entropy in the x-z plane (including the

rotation axis; upper panels) and in the x-y plane (perpendicular to the rotation axis; lower panels). The oblate deformation and the spiral flow pattern are clearly visible in the plots (especially at 180 ms and 300 ms). At the end of the evolution with full neutrino transport, accretion of low-entropy matter towards the PNS continues along the poles and from the negative y-direction (see snapshot at 450 ms).

We note that rapid core rotation is not expected for most CCSN progenitors (see footnote 24 in Section 3.1). The fast-rotating "artrot" model of Summa et al. (2018), therefore, cannot be regarded as a representative CCSN model but instead serves as a test case to study the impact of rotation on the explosion dynamics. For a small subset of all SN progenitors that have even more rapidly rotating cores, explosions can be triggered by the growth of a corotational ("low-T/W") instability, which manifests itself in a powerful one-armed (open) spiral wave (e.g., Takiwaki et al., 2016; Kazeroni et al., 2017); and, in the presence of magnetic fields, additional fluid instabilities such as the magneto-rotational instability (e.g., Balbus & Hawley, 1991; Obergaulinger et al., 2009) can arise, which can give support to magneto-rotational SNe (e.g., Mösta et al., 2014; Kuroda et al., 2020; Obergaulinger & Aloy, 2021; Bugli et al., 2021). Yet, we point out again that such extreme cases are expected only for a small subset of the entire CCSN population, while most massive stars are assumed to have only moderately rotating cores.

Model s18.88

The critical aspect that differentiates model s18.88 (Bollig et al., 2021) from all other full-transport simulations discussed in this work is the presence of large-scale progenitor perturbations of significant amplitude, which were obtained self-consistently from 3D simulations of the last seven minutes of convective oxygen shell burning prior to core collapse (see Yadav et al., 2020, and Section 3.1), in contrast to the otherwise employed 1D initial conditions. As can be seen in Figure 3.2, the s18.88 model is characterized by a high mass-accretion rate (of more than one solar mass per second during the first ∼150 ms after bounce) and a correspondingly massive PNS (∼1.9 $M_\odot$; see Table 3.5). The SN shock reaches an early maximum at ∼70 ms and contracts quickly afterward, followed by a phase of weak SASI activity during ∼150–230 ms (see the first three panels in Figure 3.6).

The situation changes drastically with the arrival of the (washed out) Si/Si+O interface at around 200 ms, which coincides with a (somewhat smooth) drop of the mass-accretion rate (see Figure 3.2): The infall of large-scale, nonradial progenitor asymmetries, as faintly visible in Figure 3.6 (snapshots at 220–240 ms), triggers the development of vigorous postshock convection, which pushes the shock outwards to larger radii and, eventually, facilitates the onset of runaway shock expansion at around 400 ms after bounce. The aiding effects of pre-collapse perturbation on the growth of postshock instabilities and, thus, on successful shock revival have been discussed in the works by Couch & Ott (2013) and Müller & Janka (2015). Interestingly, the density perturbations in the infalling progenitor shells also cause anisotropies of the pre-shock ram pressure. Because the shock expands fastest in directions of lower ram

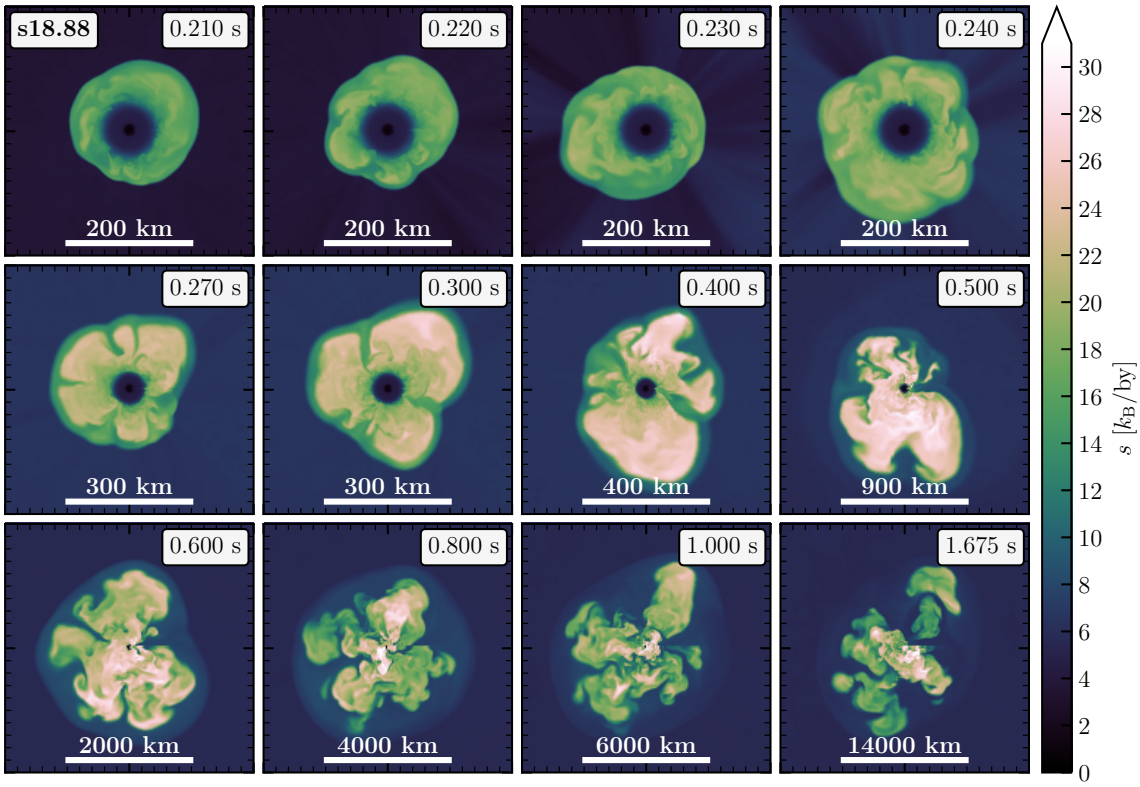

Figure 3.6.: Snapshots of model s18.88 with full neutrino transport (Bollig et al., 2021), showing cross-sectional cuts of the specific entropy (i.e., entropy per baryon) in the x–y plane. Note the changing length scales of the plots.

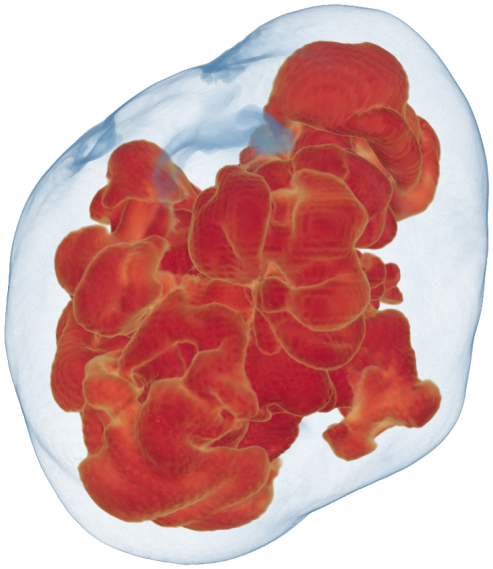

Figure 3.7.: 3D volume-rendering of the s18.88 model at 1.675 s after bounce (i.e., at the end of the evolution with full neutrino transport), showing the geometry of neutrino-heated high-entropy plumes (*red structures*) and the deformed SN shock (*bluish surface*), viewed from the positive z-axis (cf. Figure 3.6). This figure is adapted from Bollig et al. (2021).

pressure, the progenitor asymmetries, therefore, also determine the overall explosion morphology (see, e.g., the discussions in Section 4.5 of Müller, 2020, and Section 3.2 of Bollig et al., 2021).

At the end of the simulation with full neutrino transport (see last snapshot at 1.675 s in Figure 3.6 and the 3D rendering in Figure 3.7), the explosion is well on its way, and the average shock radius has reached ∼10,000 km already. At this stage, mass accretion into the central volume around the nascent PNS continues in narrow funnels (at a still significant rate), which feeds the steady rise of the explosion energy, as we will elaborate in Sections 3.3.3 and 3.4. The complete time evolution of the quantities shown in Figure 3.2 is provided below in Figure 3.10.

Even though our discussion of the s18.88 model in this work is focused on the simulation with the setup as described in Section 3.2.1, we want to mention briefly that Bollig et al. (2021) studied explosions of the s18.88 progenitor for a large set of configurations and input physics. Besides investigating the effect of 3D initial conditions compared to employing a 1D progenitor model, they also varied the angular resolution of their computational grid, used different nuclear equations of state (namely, the LS220 EoS of Lattimer & Swesty, 1991, and the SFHo EoS of Steiner et al., 2013), and employed full six-species neutrino transport including muon physics in some of their simulations. They found that the growth of postshock instabilities is dominated by the presence (or absence) of large-scale, large-amplitude progenitor perturbations rather than by the angular grid resolution (see Section 2.1.3); the inclusion of muons revealed a similar effect as the usage of a softer EoS, in particular a faster PNS contraction, leading to higher temperatures at the neutrino sphere, harder neutrino spectra, and higher neutrino luminosities, and thus to more favorable conditions for explosion (cf. Bollig et al., 2017; Fischer et al., 2020; Yasin et al., 2020).

Model s20

The model s20 (Melson et al., 2015a) ranges at the borderline between successful and failed explosions (see, e.g., Ott et al., 2018; Glas et al., 2019b; Melson et al., 2020). Whether the stalled shock of a CCSN can get revived successfully depends also on still incompletely known details of neutrino-matter interactions. In this regard, Melson et al. (2015a) investigated the effect of considering strangeness corrections to the nucleon spin. In their study, the neutral-current scattering opacity of neutrons was reduced by adding a moderate strange-quark contribution of $g_{\mathrm{a}}^{\mathrm{s}} = -0.2$ to the axial-vector coupling constant ($g_{\mathrm{a}} \approx 1.26$).[27] This results in faster cooling and contraction of the PNS, in higher luminosities and mean energies of all neutrino species, and, consequently, in an enhanced energy-deposition rate in the gain layer,

[27] This value was purposely chosen somewhat larger than the theoretically and experimentally estimated value of $g_{\mathrm{a}}^{\mathrm{s}} \sim -0.1$ (Ellis & Karliner, 1996; Airapetian et al., 2007; COMPASS Collaboration et al., 2007) to explore the possible effect on the neutrino-driven explosion mechanism within the range of microphysical uncertainties.

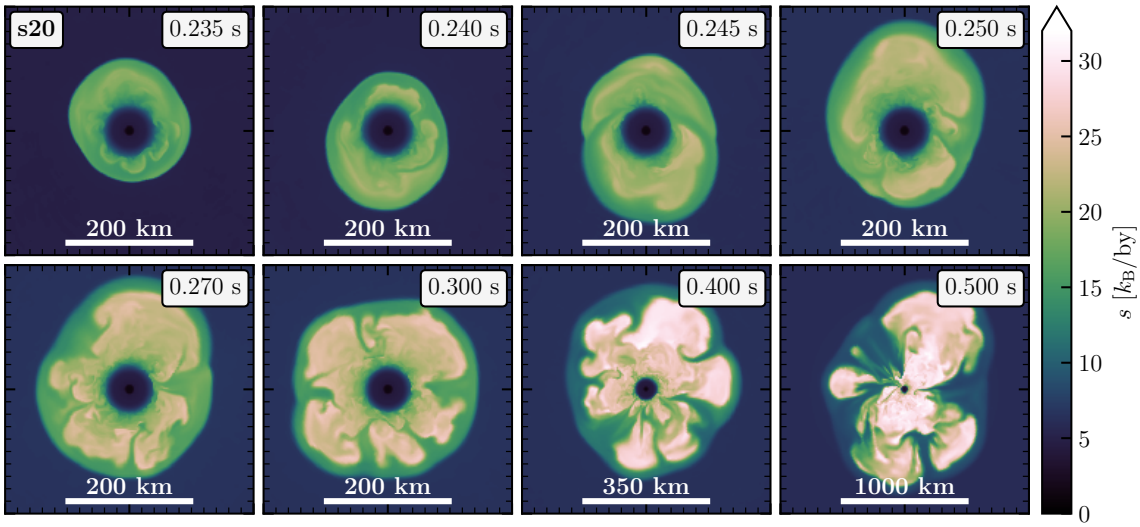

Figure 3.8.: Snapshots of model s20 with full neutrino transport (Melson et al., 2015a), showing cross-sectional cuts of the specific entropy (i.e., entropy per baryon) in the x–y plane. Note the changing length scales of the plots.

similarly as in the case of a soft nuclear EoS (e.g., Marek & Janka, 2009; Suwa et al., 2013; Yasin et al., 2020) or for models including muons (e.g., Bollig et al., 2017; Fischer et al., 2020; Bollig et al., 2021). This moderate change of the microphysics was sufficient to foster a successful explosion. In contrast, a model of the same s20 progenitor but without strangeness contributions to the neutrino-nucleon scattering opacities (i.e., $g_a^s = 0$) did not explode in the study by Melson et al. (2015a).

Similarly to model s18.88, the s20 model is characterized by a high mass-accretion rate and a large PNS mass ($\sim$1.9 $M_\odot$; Figure 3.2 and Table 3.5), which is evident from the similar progenitor structures of the two models and the almost equal values of the pre-collapse compactness parameter (Table 3.1). Nevertheless, after the passage of the Si/O composition interface (at $\sim$230 ms), the mass-accretion rate of downflows at 400 km levels off at a somewhat higher value of $\sim$0.4 $M_\odot\,s^{-1}$ for the s20 model (compared to $\sim$0.3 $M_\odot\,s^{-1}$ in the case of model s18.88). Between $\sim$150 ms and $\sim$270 ms, the postshock dynamics of the s20 model are dominated by strong SASI sloshing motions (see upper panels in Figure 3.8). Later, in contrast, neutrino-driven convection takes over as the dominant fluid instability in the gain layer (see, e.g., the snapshot at 300 ms). The shock accelerates outwards at around 350 ms, exceeding 400 km at 439 ms after the bounce (see Table 3.5).

The large PNS mass, combined with the high mass-accretion rate and consequently high neutrino luminosities and mean energies (see Section 3.3.2), lead to an early and rapid increase of the energy that is deposited and stored in the expanding SN ejecta. However, at the time when the PROMETHEUS-VERTEX simulation by Melson et al. (2015a) had to be stopped because of the high computational costs of the detailed neutrino transport (i.e., at $\sim$0.5 s after the bounce), the explosion energy had only begun to rise steeply. Actually, the total energy budget of the emergent

SN, also accounting for the (negative) binding energy of the stellar matter ahead of the shock, is still below zero at this early time. Much longer evolution times are required to achieve saturation of the explosion energy, which is why we extend the set of self-consistently exploded PROMETHEUS-VERTEX models until several seconds after the bounce using our newly developed NEMESIS neutrino scheme (Section 2.2). In the following section, we will describe the long-time evolution of these extension runs until late times that were carried out for this thesis.

3.3. Long-time Development of the Explosions

In this section, we present our long-time 3D NEMESIS simulations, which smoothly continue the evolution of the full-transport PROMETHEUS-VERTEX models discussed in the previous section (Section 3.2). The computationally most expensive neutrino transport was switched off in these extension runs and replaced by our newly developed NEMESIS neutrino scheme (Section 2.2). This allowed us to follow the evolution of the models until the convergence of the explosion energy several seconds after the bounce. The results discussed in this section have already been published partly by Stockinger et al. (2020) and Bollig et al. (2021).[28]

3.3.1. Simulation Setups

In total, we simulated seven long-time 3D models with our NEMESIS scheme, continuing the evolution of the five full-transport simulations discussed in Section 3.2. For the m15 and s20 models, we each computed two different versions with slightly modified input physics, as we will elaborate below. Table 3.3 provides an overview of the setups for all seven long-time explosion models with the NEMESIS neutrino treatment. All of these simulations were computed on an axis-free overset Yin-Yang grid with an angular resolution of 2°. As discussed in Section 2.1.3, this choice of angular resolution is an acceptable compromise between numerical convergence and computational practicality. The (logarithmically spaced) radial grid was successively extended to several ten thousand kilometers to be able to follow the expansion of the SN shock. To relax the CFL time-step constraint, the size of the spherical inner core was increased for our long-time NEMESIS simulations to the values given in Table 3.3. Moreover, we slightly coarsened the radial grid resolution inside the 1D computational domain. On the other hand, a fine radial resolution (of $\Delta r/r \sim 0.001$–0.005) was maintained around the PNS surface to adequately resolve the steep density gradient in this region.

The long-time extension models discussed in this section were computed employing different versions of our NEMESIS treatment with varying degrees of sophistication.

[28] Some content from these two publications is adopted here in this section, yet only the author's contributions are taken.

Table 3.3.: Model specifications of the NEMESIS simulations.

Model	Grid[a]	1D Core[b]	Version[c]	Reference
s9.0	YY (2°)	10 km	v1.1.1	Stockinger et al. (2020)
z9.6	YY (2°)	10 km	v1.1.0	Stockinger et al. (2020)
m15	YY (2°)	15 km	v1.0.0	Kresse et al. (in prep.)
m15e	YY (2°)	17 km	v1.0.e	Kresse et al. (in prep.)
s18.88	YY (2°)	3×10^{13} g/cm^3	v1.1.1	Bollig et al. (2021)
s20	YY (2°)	5×10^{12} g/cm^3	v2.0.0	Kresse et al. (in prep.)
s20e	YY (2°)	5×10^{12} g/cm^3	v2.0.e	Kresse et al. (in prep.)

[a] Yin-Yang (YY) grid with uniform 2° angular resolution. [b] Radius of the spherical inner core. For models s18.88, s20, and s20e, the 1D core was instead determined by a threshold value of the angle-averaged mass density (yielding a time-dependent radius between ∼21 and ∼13 km). [c] Version of the NEMESIS scheme (see main text for the details).

The basic approach as applied in versions v1.0 and v1.1 has been presented in Appendix E of Stockinger et al. (2020), while the most recent version of our NEMESIS scheme (version v2.0), with a revised treatment of the neutrino effects in the cooling layer, is described in much detail in Section 2.2 of this thesis. In the following, we provide a short overview of the main features that discriminate the different versions:

v1.0 This initial version of our NEMESIS neutrino scheme uses the approach as described in Stockinger et al. (2020, Appendix E), with the exception that the contraction of the gain radius according to their Equation (E8), i.e., Equation (2.26) in this thesis, is not yet considered. Instead, the gain radius is kept constant over time, i.e., $R_{\mathrm{gain}}(t) = R_{\mathrm{gain}}(t_0)$. Moreover, the neutrino pressure correction, as described in Section 2.2.3 (cf. Stockinger et al., 2020, Section E2), is not yet included, which leads to a transient phase of PNS oscillations when the neutrino treatments are switched and the PNS interior settles to a new equilibrium state. Nevertheless, these transient oscillations did not have a relevant impact on the overall evolution of the explosion models. Lastly, in version v1.0 of the NEMESIS scheme, the factor f_{Y_e} that appears in Equation (E6) of Stockinger et al. (2020), which limits Y_e by its kinetic equilibrium value from the high side, is set to one for $v_r \geqslant 0$ (i.e., their Equation (E7a); cf. Equation (2.38) in this thesis). However, because of the coexistence of outflows (with $\mathrm{d}Y_\mathrm{e}/\mathrm{d}t > 0$) and downflows (with $\mathrm{d}Y_\mathrm{e}/\mathrm{d}t < 0$), the electron fraction of the SN ejecta remains fairly close to 0.5, anyway.

v1.1 This version of the NEMESIS scheme has been employed for the long-time extension runs of models s9.0, z9.6, and s18.88, as presented in Stockinger et al. (2020) and Bollig et al. (2021). It considers the time-dependent evolution of the gain radius according to Equation (2.26) and, thus, accounts for an inward shift

of the radial profiles of the neutrino heating and cooling rates (as well as of the Y_e source term). Beyond that, it includes the neutrino pressure correction in the high-density regime (Section 2.2.3) as well as, since version v1.1.1, the control factor f_{Y_e} according to Equation (E7) of Stockinger et al. (2020).

v2.0 This latest and most sophisticated version of the NEMESIS scheme, as detailed in Section 2.2, includes an updated and improved treatment of the neutrino effects in the cooling layer around the PNS (with separate methods for the PNS's core and mantle regions and a better controlled inward shift and transformation of the cooling and Y_e source terms). This new prescription cured earlier problems related to runaway cooling that occurred either at late times in the deep interior of the PNS or in the case of massive accretion streams penetrating the cooling layer (see below). Moreover, in version v2.0, we explicitly consider an accretion component of the neutrino luminosity (see Equations (2.28), (2.32), and (2.41)). This is relevant for models whose neutrino emission is not yet core-dominated at the times t_0 when the neutrino treatments are switched (i.e., for models with $\xi^0_{\rm acc} \gg 0$, as in the case of model s20).

As pointed out in Appendix E of Stockinger et al. (2020), the cooling prescription in our early versions of the NEMESIS scheme lacked a self-regulating mechanism to avoid runaway cooling. The inward shift and transformation of the initial profile of the energy source term (at time t_0) to smaller radii, in combination with the density and temperature scaling via Equations (E1) and (E5) of Stockinger et al. (2020), turned out to be problematic, as it can lead to overestimated cooling in the PNS's interior or its surface layers and thus to an accelerated PNS contraction. While such artifacts can be suppressed through an optical-depth-dependent exponential damping term, if they occur in the deep interior of the PNS, this strategy turned out to be ineffective in curing runaway cooling in the PNS's mantle layer (with relatively low optical depths).

In the models z9.6 and s9.0, the cooling treatment according to version v1.1 of our NEMESIS scheme worked well and ensured a smooth and continuous contraction of the PNS. Nevertheless, in the case of model s9.0, we encountered the mentioned issues with runaway cooling in a thin shell in the deep interior of the PNS. We, therefore, switched off the anyway low energy and lepton-number loss rates at $\sim$1 s after bounce and continued the simulation with gain-layer heating only. Since the PNS radius at that time had decreased to 20 km already (see Figure 3.10), and its further contraction was only slow, we could not witness any transient or discontinuous behavior as a consequence of our measure. Similarly, for model s18.88, we turned off the energy and lepton-number loss terms at $\sim$1.7 s, when the PNS had already contracted to a radius of $\sim$18 km, to circumvent the problem of runaway cooling in the PNS's surface layer. Yet, we are confident that this simplification did not significantly impact the overall explosion dynamics of the model. To ensure that neutrino heating at the bottom of the SN ejecta was not underestimated in the case of switched-off PNS cooling (and thus halted PNS contraction), the heating

and lepton-number source terms were scaled with the factor $f_{\rm NS}$ (Equation (E9) of Stockinger et al., 2020), accounting for the subsequent shallow PNS contraction seen in the guiding 1D PNS cooling simulations.

In the latest implementation of our NEMESIS scheme, i.e., for version v2.0, the above-mentioned issues with runaway cooling have been cured. The key improvements of the new cooling treatment compared to earlier versions are a more precisely controlled inward shift of the energy and lepton-number source terms, as well as separate prescriptions of cooling in the optically thick high-density core of the PNS and its semi-transparent surface layers (see detailed discussions in Section 2.2). These improvements allow us to handle neutrino cooling even in cases with ongoing substantial mass accretion and, consequently, high energy-loss rates in the inflated PNS mantle, as is the case for model s20 (see Figure 2.4). With our updated NEMESIS treatment (v2.0), we can, therefore, adequately capture the contraction of the PNS also at phases after the detailed neutrino transport has been switched off and replaced by the NEMESIS scheme (see, e.g., Figure 2.5).

Models with enhanced heating. For the models m15 and s20, we computed the long-time evolution each in two different realizations (with slightly modified input physics) to investigate the effect of an enhanced neutrino-heating rate on the development of the explosion. As opposed to version v1.0.0 of our NEMESIS scheme, which was used for the long-time evolution of the m15 model in the "standard case," model m15e was simulated with the code version **v1.0.e**, where we did not scale the source terms $Q^{+}_{\rm E}$ and $Q^{+}_{\rm N}$ (see Equations (2.27) and (2.37) in Section 2.2) with the time-dependent neutrino luminosities and mean energies from the guiding 1D PNS-cooling simulation, but instead assumed $L^{\rm 1D}_{\nu_{\rm e},\bar{\nu}_{\rm e}}(t) = L^{\rm 1D}_{\nu_{\rm e},\bar{\nu}_{\rm e}}(t_0)$ and $E^{\rm 1D}_{\nu_{\rm e},\bar{\nu}_{\rm e}}(t) = E^{\rm 1D}_{\nu_{\rm e},\bar{\nu}_{\rm e}}(t_0)$, thus maintaining a higher neutrino-heating rate.

For the s20 model, whose long-time evolution was computed with version v2.0.0 of the NEMESIS scheme (see Section 2.2), we additionally considered a second realization, namely model s20e, for which we employed a modified treatment of neutrino cooling (and deleptonization) in the PNS mantle layer (**v2.0.e**). Here, we did not use Equations (2.32) and (2.41) for the time evolution of the energy- and $Y_{\rm e}$-loss terms but instead adopted the time-dependent, adequately rescaled and transformed, specific cooling and deleptonization rates from the guiding 1D simulation:

$$Q^{-}_{\rm E,m}(\boldsymbol{r},t) = q^{\rm 1D}_{\rm E,rs}(x^{-}_{\rm E,m},t)\cdot\rho(\boldsymbol{r},t)\,, \tag{3.4}$$

$$Q^{-}_{\rm N,m}(\boldsymbol{r},t) = q^{\rm 1D}_{\rm N,rs}(x^{-}_{\rm N,m},t)\cdot\rho(\boldsymbol{r},t)\,, \tag{3.5}$$

where $q^{\rm 1D}_{\rm E,rs}$ and $q^{\rm 1D}_{\rm N,rs}$ are the specific net energy-loss and deleptonization rates from the 1D model, albeit rescaled to continuously match the corresponding profiles of the full-transport 3D simulation (for the definitions of $x^{-}_{\rm E,m}$ and $x^{-}_{\rm N,m}$, see Section 2.2). This approach leads to a faster decline of neutrino cooling in the PNS mantel layer and, thus, to an increased net energy input for model s20e compared to model s20 (with the standard treatment as per v2.0.0 of our NEMESIS scheme). In Section 3.3.3,

we will discuss the dynamical consequences of the enhanced heating for the models m15e and s20e, compared to their respective counterparts, m15 and s20.

As for the initial full-transport simulations discussed in Section 3.2, the evolution of all seven long-time NEMESIS extension models was computed with an effective 1D gravitational potential according to Marek et al. (2006, "Case A"), with the LS220 high-density EoS (Lattimer & Swesty, 1991), and considering 23 nuclear species. Burning was treated through the flashing scheme of Rampp & Janka (2002, Appendix B.2), except for model s18.88, whose evolution was continued with an α-chain reaction network (Hix & Thielemann, 1999b; Bollig et al., 2021) for a short transition period of 110 ms (after switching the neutrino treatments at the time t_0) and only later on with the flashing scheme. For all simulations with the NEMESIS neutrino treatment, NSE was assumed at temperatures above 0.5 MeV for infalling matter and above 0.343 MeV for neutrino-heated high-entropy outflows. The initial and final evolution times, t_0 and t_f, of all NEMESIS models are provided below in Table 3.5.

3.3.2. Neutrino Signals

Before discussing the dynamical evolution of our long-time 3D CCSN simulations with the NEMESIS neutrino scheme, we first provide an overview of the neutrino signals that enter into our approximative description of the neutrino effects. As discussed in Section 2.2, the luminosities and mean energies of electron neutrinos and antineutrinos control the time evolution of the neutrino heating and leptonization rates via the scaling factors ζ_L and ζ_E of Equations (2.28) and (2.30), respectively. Moreover, the energy emission of all six neutrino species determines the evolution of the gravitational PNS mass (see Equation (3.3)).

Because we do not solve the neutrino-transport problem self-consistently in our NEMESIS approach, we need to prescribe the time evolution of the neutrino luminosities and neutrino mean energies for our 3D extension runs (from the times t_0 when the neutrino methods are switched until several seconds after bounce). For this purpose, we employ inputs from corresponding long-time 1D PNS cooling simulations with PROMETHEUS-VERTEX, including a mixing-length treatment for PNS convection. We express the time-dependent neutrino luminosity of an individual neutrino species $\nu_i \in \{\nu_\mathrm{e}, \bar{\nu}_\mathrm{e}, \nu_x\}$ for $t > t_0$ according to

$$L_{\nu_i}(t) = L_{\nu_i}(t_0) \cdot \left[\frac{M_\mathrm{NS}(t)\dot{M}_\mathrm{down}(t)/R_\mathrm{NS}(t)}{M_\mathrm{NS}(t_0)\dot{M}_\mathrm{down}(t_0)/R_\mathrm{NS}(t_0)} \cdot \xi_\mathrm{acc}^{0,\nu_i} + \frac{L_{\nu_i}^\mathrm{1D}(t)}{L_{\nu_i}^\mathrm{1D}(t_0)} \cdot \left(1 - \xi_\mathrm{acc}^{0,\nu_i}\right) \right], \quad (3.6)$$

i.e., as the sum of an accretion and a core component (e.g., Fischer et al., 2009; Müller & Janka, 2014). The time-dependent neutrino mean energy is described according to

$$E_{\nu_i}(t) = E_{\nu_i}(t_0) \cdot \frac{E_{\nu_i}^\mathrm{1D}(t)}{E_{\nu_i}^\mathrm{1D}(t_0)} \cdot \frac{M_\mathrm{NS}(t)}{M_\mathrm{NS}(t_0)} \,. \quad (3.7)$$

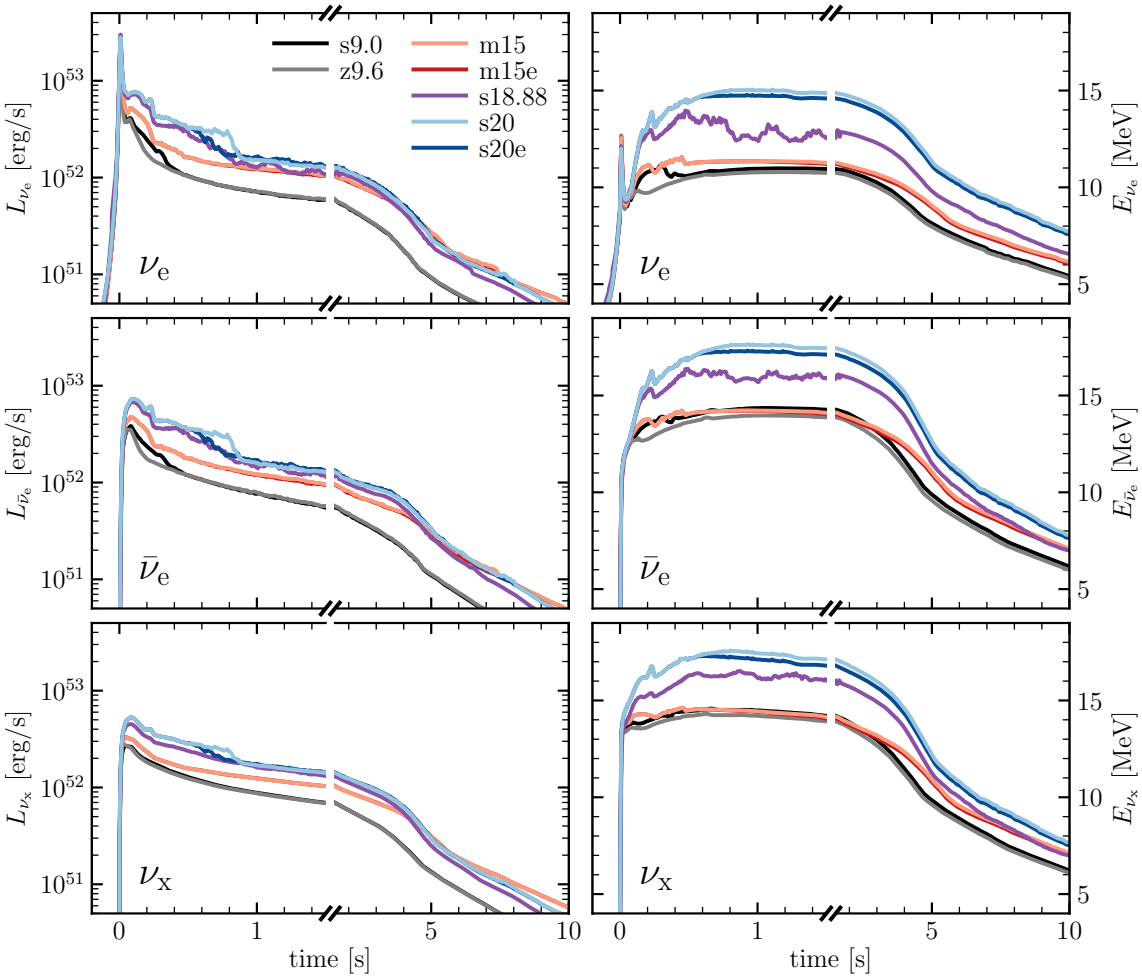

Figure 3.9.: Time evolution of the neutrino luminosities (*left panels*) and neutrino mean energies (*right panels*) of electron neutrinos, electron antineutrinos, and a representative species of heavy-lepton (anti)neutrinos (from *top* to *bottom*), evaluated at a radius of 400 km for a lab-frame observer at a large distance (i.e., gravitationally redshifted to infinity). We show both the self-consistently obtained neutrino signals from the full-transport 3D simulations and their extensions to later times according to Equations (3.6) and (3.7), which are employed as input for the long-time 3D simulations with the Nemesis treatment. Note that, for optimal visibility, the time axes are split into two parts with differing scales.

In these expressions, $L_{\nu_i}(t_0)$ and $E_{\nu_i}(t_0)$ are the neutrino luminosities and mean energies at the end of the full-transport 3D simulations, as self-consistently obtained from the Vertex transport solver via Equations (2.17) and (2.18), and $L^{1D}_{\nu_i}(t)$ and $E^{1D}_{\nu_i}(t)$ are the corresponding analogs from the associated 1D models. The (baryonic) PNS mass, $M_{NS}(t)$, the mass-accretion rate, $\dot{M}_{down}(t)$, and the PNS radius, $R_{NS}(t)$, are taken from the 3D hydrodynamical evolution of our long-time Nemesis models. The mass-accretion rate of downflows is evaluated at the time-dependent gain radius

(see Section 2.2 for more details).

The factor $\xi_{\mathrm{acc}}^{0,\nu_i}$ denotes the fraction of the accretion luminosity relative to the total luminosity for neutrino species ν_i at the end of the full-transport 3D evolution. In the models s9.0, z9.6, and s18.88, the neutrino emission is already dominated by the diffusive component from the PNS core at the time t_0, whereas the contribution from the PNS's accretion mantle has declined to an insignificant level already (i.e., $\xi_{\mathrm{acc}}^{0,\nu_i} \approx 0$), either because of low mass-accretion rates (in the case of models s9.0 and z9.6) or because the neutrino transport is switched off only at a relatively late time (in the case of model s18.88, with $t_0 = 1.675\,\mathrm{s}$). For the models m15 and m15e, we use the heavy-lepton neutrino luminosity at the time t_0 as a proxy for the PNS's core luminosity of all species at this time (i.e., $\xi_{\mathrm{acc}}^{0,\nu_i} = [L_{\nu_i}(t_0) - L_{\nu_x}(t_0)]/L_{\nu_i}(t_0)$; cf. Hüdepohl, 2014; Müller & Janka, 2014). This yields $\xi_{\mathrm{acc}}^{0,\nu_\mathrm{e}} \approx \xi_{\mathrm{acc}}^{0,\bar{\nu}_\mathrm{e}} \approx 0.10$ and $\xi_{\mathrm{acc}}^{0,\nu_x} = 0$. In the case of the $20\,\mathrm{M}_\odot$ progenitor, which has the highest mass-accretion rate among all models discussed (see Figure 3.2), the ν_x luminosity still shows a non-vanishing accretion component at the time $t_0 = 0.506\,\mathrm{s}$. Therefore, we obtain the factors $\xi_{\mathrm{acc}}^{0,\nu_i}$ for all three neutrino species, ν_e, $\bar{\nu}_\mathrm{e}$, and ν_x, from a two-component fit of the luminosities (i.e., as the sum of an accretion and a core component) during the last $\sim$100 ms of the full-transport 3D simulation, as described in Section 2.2.1 (see Equation (2.29)). This procedure yields $\xi_{\mathrm{acc}}^{0,\nu_\mathrm{e}} \approx 0.42$, $\xi_{\mathrm{acc}}^{0,\bar{\nu}_\mathrm{e}} \approx 0.34$, and $\xi_{\mathrm{acc}}^{0,\nu_\mathrm{e}} \approx 0.20$ for the neutrino luminosities of the models s20 and s20e.

The scaling of the neutrino mean energies with the PNS mass in Equation (3.7) is guided by the findings of Müller & Janka (2014). It shall account for possible (minor) differences in the mass evolution of the long-time 3D models and the associated 1D PNS cooling simulations. Regardless, the PNS mass has practically reached its final value by the time t_0, when the neutrino treatments are switched (see lower left panel of Figure 3.2). Therefore, the scaling of the neutrino mean energies with the PNS mass has only a subsidiary effect on the time evolution of the neutrino signal.

In Figure 3.9, we provide an overview of the neutrino luminosities and neutrino mean energies of ν_e, $\bar{\nu}_\mathrm{e}$, and ν_x for all of our long-time 3D CCSN models discussed in this thesis. We show both the self-consistently computed neutrino signals during the evolution phase with full Vertex neutrino transport and their extensions to late times, as obtained by Equations (3.6) and (3.7). During the first second, clear imprints of the progenitor-specific mass-accretion rate are visible in the neutrino signals, especially for electron-type neutrinos and antineutrinos, and most prominently for the most massive models (cf. Figures 3.2 and 3.10). At later times, i.e., during the PNS cooling phase, the evolution of the neutrino luminosities and mean energies becomes more similar among the different models.

To back up the long-time neutrino signals, as shown in Figure 3.9 and employed in our Nemesis approach, we cross-check the values of the total radiated neutrino energy, $E_{\nu,\mathrm{tot}}^{\infty} = \int_0^\infty L_\nu^{\mathrm{tot}}(t')\,\mathrm{d}t'$, of all six species (i.e., ν_e, $\bar{\nu}_\mathrm{e}$, and $4 \times \nu_x$) by comparing them to the available budget of the NS gravitational binding energy (BE) as estimated from an analytic, radius-dependent (approximate) fit formula of Lattimer & Prakash

Table 3.4.: Neutrino energetics and NS masses.

Model	t_f	$E^\mathrm{f}_{\nu,\mathrm{tot}}$	$E^\infty_{\nu,\mathrm{tot}}$	$M^\mathrm{f}_\mathrm{NS,b}$	$M^\mathrm{f}_\mathrm{NS,g}$	$M^\infty_\mathrm{NS,g}$	$M^{11}_\mathrm{NS,g}$	$M^{12}_\mathrm{NS,g}$	$M^{13}_\mathrm{NS,g}$
	[s]	[10^{53} erg]				[$\mathrm{M}_\odot$]			
s9.0	3.936	1.773	2.055	1.355	1.255	1.240	1.223	1.233	1.242
z9.6	1.450	1.086	2.016	1.350	1.290	1.237	1.220	1.230	1.238
m15	7.433	3.166	3.376	1.605	1.427	1.416	1.424	1.437	1.449
m15e	8.002	3.184	3.357	1.583	1.405	1.396	1.407	1.420	1.431
s18.88	8.360	3.943	4.035	1.878	1.657	1.652	1.636	1.653	1.668
s20	8.038	4.492	4.627	1.949	1.698	1.690	1.690	1.708	1.724
s20e	7.978	4.453	4.591	1.912	1.663	1.655	1.662	1.680	1.695

Note: t_f is the final simulation time of the evolution period with the NEMESIS neutrino scheme, measured relative to the time of core bounce; $E^\mathrm{f}_{\nu,\mathrm{tot}}$ is the total neutrino energy that is radiated away (in all six neutrino species, i.e., ν_e, $\bar{\nu}_\mathrm{e}$, and $4 \times \nu_x$) until the time t_f, computed as time-integral of the total neutrino luminosity (given from the full-transport 3D model at times $t \leqslant t_0$ and according to Equation (3.6) for $t > t_0$); $E^\infty_{\nu,\mathrm{tot}}$ is the total radiated neutrino energy computed in the same way but in the limit $t \to \infty$; $M^\mathrm{f}_\mathrm{NS,b}$, $M^\mathrm{f}_\mathrm{NS,g}$, and $M^\infty_\mathrm{NS,g}$ are the final baryonic NS mass, the final gravitational NS mass (according to Equation (3.3)), and the gravitational NS mass for $t \to \infty$, respectively; $M^{11}_\mathrm{NS,g}$, $M^{12}_\mathrm{NS,g}$, and $M^{13}_\mathrm{NS,g}$ are the gravitational NS masses according to the analytic, radius-dependent fit formula of Lattimer & Prakash (2001) for the NS gravitational binding energy (i.e., Equation (3.8)), assuming a final NS radius of 11 km, 12 km and 13 km, respectively.

(2001, their Equation (36)):

$$\frac{\mathrm{BE}/c^2}{M_\mathrm{NS,g}} \simeq \frac{0.6\beta}{1 - 0.5\beta} \,, \tag{3.8}$$

with $\mathrm{BE}/c^2 \equiv M_\mathrm{NS,b} - M_\mathrm{NS,g}$ and the dimensionless parameter $\beta \equiv GM_\mathrm{NS,g}/R_\mathrm{NS}c^2$. This expression connects the PNS's baryonic mass, $M_\mathrm{NS,b}$, with its gravitating mass, $M_\mathrm{NS,g}$, assuming a particular value of the final (cold) NS radius R_NS. In Table 3.4, we provide the total radiated neutrino energies and the (baryonic and gravitational) PNS masses at the end of our 3D NEMESIS simulations (i.e., at the post-bounce times t_f) as well as in the limit $t \to \infty$, together with estimates of the final (cold) NS gravitational masses as obtained from Equation (3.8) assuming final NS radii of 11 km, 12 km, and 13 km. This range of values is motivated by the most recent constraints of the NS radius through gravitational-wave and kilonova observations from binary NS mergers (e.g., Abbott et al., 2017; Bauswein et al., 2017) and NS radius measurements by NICER (e.g., Miller et al., 2019; Riley et al., 2019, 2021; Raaijmakers et al., 2021). The comparison in Table 3.4 reveals an excellent agreement of the gravitational NS masses as obtained via Equation (3.3) and the analytic estimates based on the

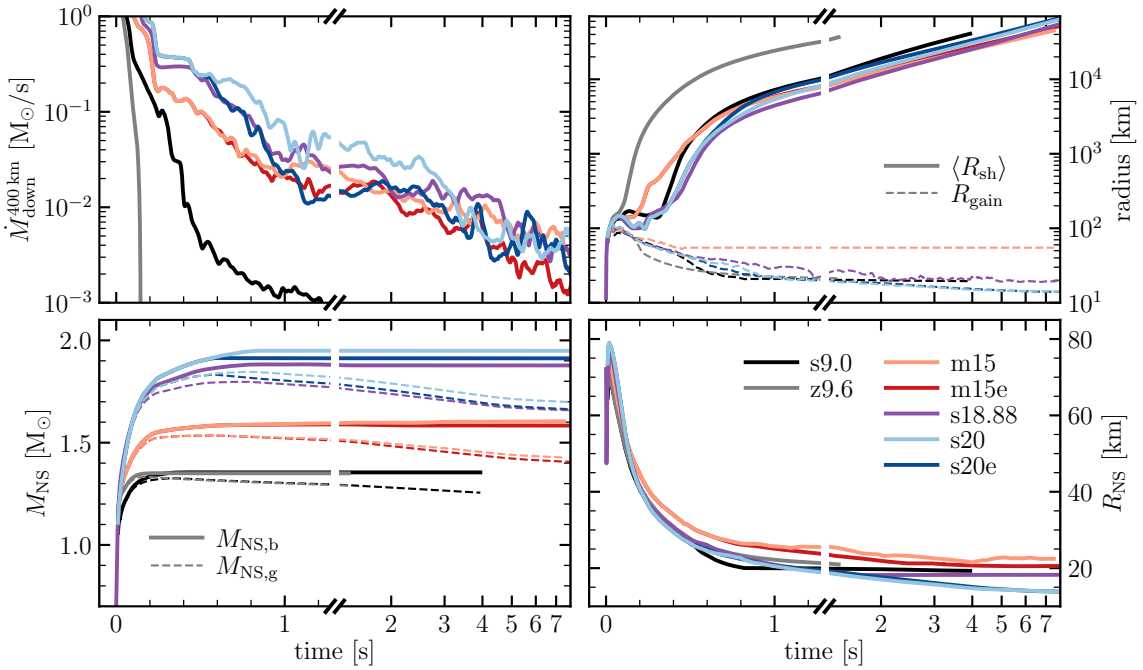

Figure 3.10.: Time evolution of the mass-accretion rate of downflows (evaluated at 400 km; *top left*), the angle-averaged shock radius and the gain radius (*top right*), the baryonic and gravitational PNS mass (*bottom left*), and the PNS radius (*bottom right*) for all long-time 3D models considered in this work. We show both the early evolution of the models, which was computed with full neutrino transport (cf. Figure 3.2), and the late evolution, which was simulated with the Nemesis neutrino scheme (see Table 3.3). Note that the time axes are split into two parts for better visibility, with a linear scale until roughly 1.3 s and a logarithmic scale until ∼8 s after the bounce.

radius-dependent formula by Lattimer & Prakash (2001) on the order of 1% (within the uncertainties of the still unknown radius of cold NSs), therefore providing a strong backup for our (empirically constructed) neutrino signals.

3.3.3. Long-time Explosion Dynamics

In Figure 3.10, we show the time evolution of the progenitor-dependent mass-accretion rate of downflows (evaluated at 400 km), the angle-averaged shock radius, the gain radius, the baryonic and gravitational PNS mass, and the PNS radius for all of our long-time 3D CCSN models, from the early phase of shock revival until several seconds after core bounce. Note that the time axes in the figure are split for optimal visibility. The simulations with the Nemesis neutrino scheme smoothly extend the evolution of the full-transport explosion models (cf. Figure 3.2 for the early phase until ∼0.5 s after bounce).

The critical quantity that determines the dynamical evolution of the explosion models during the first seconds after the onset of runaway shock expansion is the

Table 3.5.: Overview of explosion properties.

Model	$t_{\rm exp}$ [s]	t_0 [s]	$t_{\rm f}$ [s]	$M^{\rm f}_{\rm NS,b}$ [$M_\odot$]	$M^{\rm f}_{\rm NS,g}$ [$M_\odot$]	$\langle R^{\rm f}_{\rm sh}\rangle$ [km]	$\langle v^{\rm f}_{\rm sh}\rangle$ [km/s]	$E^{\rm diag}_{\rm exp}$ [B]	$E^{\rm OB-}_{\rm exp}$ [B]
s9.0	0.390	0.488	3.936	1.355	1.255	40,916	10,796	0.054	0.052
z9.6	0.134	0.450	1.450	1.350	1.290	36,770	27,519	0.086	0.086
m15	0.267	0.457	7.433	1.605	1.427	45,127	5,958	0.332	0.281
m15e	0.267	0.457	8.002	1.583	1.405	53,409	6,878	0.436	0.394
s18.88	0.469	1.675	8.360	1.878	1.657	59,722	8,028	1.000	0.938
s20	0.439	0.506	8.038	1.949	1.698	66,103	8,841	1.229	1.157
s20e	0.439	0.506	7.978	1.912	1.663	68,013	8,816	1.431	1.361

Note: $t_{\rm exp}$ is the explosion time, defined as the time when the angle-averaged shock radius crosses 400 km; t_0 is the time when the detailed VERTEX neutrino transport is switched off and replaced by the NEMESIS scheme; $t_{\rm f}$ is the final evolution time; $M^{\rm f}_{\rm NS,b}$ and $M^{\rm f}_{\rm NS,g}$ are the final baryonic and gravitational PNS masses (i.e., at the time $t_{\rm f}$); $\langle R^{\rm f}_{\rm sh}\rangle$ and $\langle v^{\rm f}_{\rm sh}\rangle$ are the final angle-averaged shock radius and shock velocity; $E^{\rm diag}_{\rm exp}$ and $E^{\rm OB-}_{\rm exp}$ are the final diagnostic explosion energy and the final explosion energy without overburden. All times are measured relative to the time of core bounce.

amount of matter that is channeled from large radii towards the central, neutrino-emitting and cooling PNS, i.e., the mass-accretion rate of downflows, as displayed in the upper left panel of Figure 3.10. The presence of long-lasting, significant matter downdrafts (with several $10^{-2}\,M_\odot$/s until a few seconds after the bounce) differentiates the $15\,M_\odot$, $18.88\,M_\odot$, and $20\,M_\odot$ stars from the two low-mass s9.0 and z9.6 models. As we will show below, this continued mass accretion, in combination with the ongoing, intense neutrino emission from the PNS (see Section 3.3.2), allows for a steady rise of the energy that is deposited and stored in the SN ejecta.

When our NEMESIS simulations were stopped, the angle-averaged shock radii had reached several ten thousand kilometers, with final shock velocities ranging from $\sim 6 \times 10^3$ km/s to $\sim 3 \times 10^4$ km/s (see Table 3.5). As described in Section 3.3.1, the gain radius was kept constant for the models m15 and m15e during the evolution period with the NEMESIS scheme (which leads to a somewhat reduced neutrino-heating rate in the gain layer; see discussion in Section 3.4). In all other models, the gain radius follows the contraction of the PNS radius according to Equation (2.26). Note that our improved treatment of PNS cooling, as implemented in the latest version of our NEMESIS scheme (v2.0; see Section 3.3.1), enabled us to properly follow the contraction of the PNS until late times to radii below 15 km for models s20 and s20e. In contrast, our other models have slightly larger final PNS radii of around 20 km (see lower right panel of Figure 3.10). After less than one second, the baryonic PNS masses of all models have essentially leveled off to their final values (as provided in Tables 3.4 and 3.5), signaling that most of the accreted matter gets re-ejected as a consequence of ongoing neutrino heating during the subsequent evolution (see the

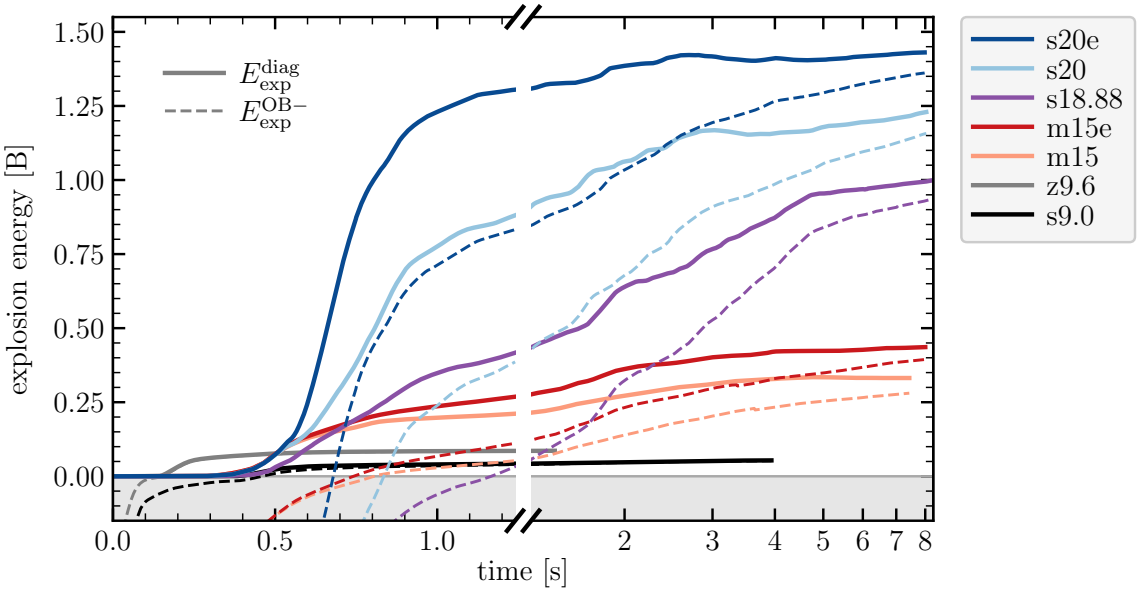

Figure 3.11.: Time evolution of the diagnostic explosion energy and the explosion energy without overburden for all long-time 3D models considered in this work. We show both the early evolution of the models, which was computed with full neutrino transport (see Section 3.2), and the late evolution, which was simulated with the Nemesis scheme (see Table 3.3). Note that the time axis is split into two parts for better visibility, with a linear scale until roughly 1.3 s and a logarithmic scale until ∼8 s after bounce. The final explosion energies at the end of the simulations are provided in Table 3.5.

more detailed discussion in Section 3.4).

This continued heating and re-ejection of matter that is accreted to the central regions around the neutrino-emitting PNS fuels the continuous growth of the explosion energy (Figure 3.11). As an estimate of the energy stored in the expanding SN ejecta, one commonly uses the "diagnostic" explosion energy,

$$E_{\rm exp}^{\rm diag} = \int_{r<R_{\rm sh}} {\rm d}V\, \rho \varepsilon_{\rm tot} \Theta(\varepsilon_{\rm tot})\,, \tag{3.9}$$

which is computed as the volume integral of the density ρ times the total (i.e., internal plus kinetic plus gravitational) specific energy, $\varepsilon_{\rm tot} = e + v^2/2 + \Phi$, over the postshock layer ($r < R_{\rm sh}$), considering fluid cells where this energy is positive (i.e., for unbound matter). Here, the specific internal energy, e, does not include any rest-mass contributions. $\Theta(x)$ denotes the Heaviside step function, and $\Phi(r) = -Gm(r)/r$ is the (Newtonian) gravitational potential, computed for a given mass shell at radius r from the enclosed gravitating mass $m(r)$, which takes into account the mass-loss equivalent of the neutrino energy emission (cf. Equation (3.3)). Because the unbound SN ejecta typically have large distances from the central PNS (i.e., several hundreds to thousands of kilometers), the approximation of Newtonian gravity is

sufficiently accurate, and general relativistic corrections can safely be ignored. Note that, following Buras et al. (2006a,b), we only consider the enclosed mass inside a given radius r for the computation of the gravitational potential $\Phi(r)$ and disregard the contribution from matter at larger radii to adequately account for the fact that the stellar gas constitutes a self-gravitating system (see, e.g., discussion in Section 4.1 of Müller et al., 2017).

Since the diagnostic explosion energy does not account for the (negative) binding energy of the stellar matter ahead of the shock, we also provide the explosion energy without the "overburden" of the overlying shells. It is computed according to

$$E_{\rm exp}^{\rm OB-} = E_{\rm exp}^{\rm diag} + \underbrace{\int_{r>R_{\rm sh}} {\rm d}V\, \rho\varepsilon_{\rm tot}}_{\text{"overburden" } (<0)} , \tag{3.10}$$

where the total specific energy $\varepsilon_{\rm tot}$ is defined as before. In Figure 3.11, we provide an overview of the explosion energies (diagnostic and without overburden) as functions of time after core bounce for all of our long-time 3D CCSN simulations.

The two low-mass models, s9.0 and z9.6, show an early saturation of the explosion energy at relatively small values of less than 0.1 B (see Table 3.5). As a consequence of fast shock expansion combined with the comparatively low densities in the dilute outer stellar shells of the progenitor stars (see Section 3.1), the overburden shrinks to an insignificant level after less than a second for these two models. In contrast, the explosion energies of the more massive models m15, m15e, s18.88, s20, and s20e (with much higher mass-accretion rates) grow over significantly longer timescales of several seconds (in agreement with previous results from, e.g., the long-time 2D simulations by Müller, 2015; Bruenn et al., 2016; Nakamura et al., 2019; Burrows & Vartanyan, 2021; Bruenn et al., 2023, or the 3D model by Müller et al., 2017). The net energy budget of the emergent explosions of our 15 $\rm M_\odot$, 18.88 $\rm M_\odot$, and 20 $\rm M_\odot$ models is still negative during the first few hundred milliseconds. It becomes positive only at ∼0.7–1.2 s after the bounce when the continued neutrino radiation from the central PNS has deposited enough energy in the SN ejecta to exceed the negative overburden energy of the outer shells. Energy saturation is approached asymptotically towards the end of our simulations at ∼7–8 s when the neutrino emission from the cooling PNS fades eventually (see Section 3.3.2).

Most remarkably, our models reach final explosion energies of up to more than 1 B, in agreement with the typical values measured for observed CCSNe (e.g., Kasen & Woosley, 2009; Pejcha & Prieto, 2015b; Martinez et al., 2022). Even though the outwards propagating blast waves are still deep inside the stellar interiors at the end of our simulations, the explosion energies without overburden have nearly converged with the diagnostic energies (see Figure 3.11 and Table 3.5) because the extended envelopes are only loosely bound (i.e., contribute little to the total overburden). A more detailed analysis of the energy growth and saturation will be presented in Section 3.4. In the following, we discuss the dynamical evolution of all seven long-time explosion models.

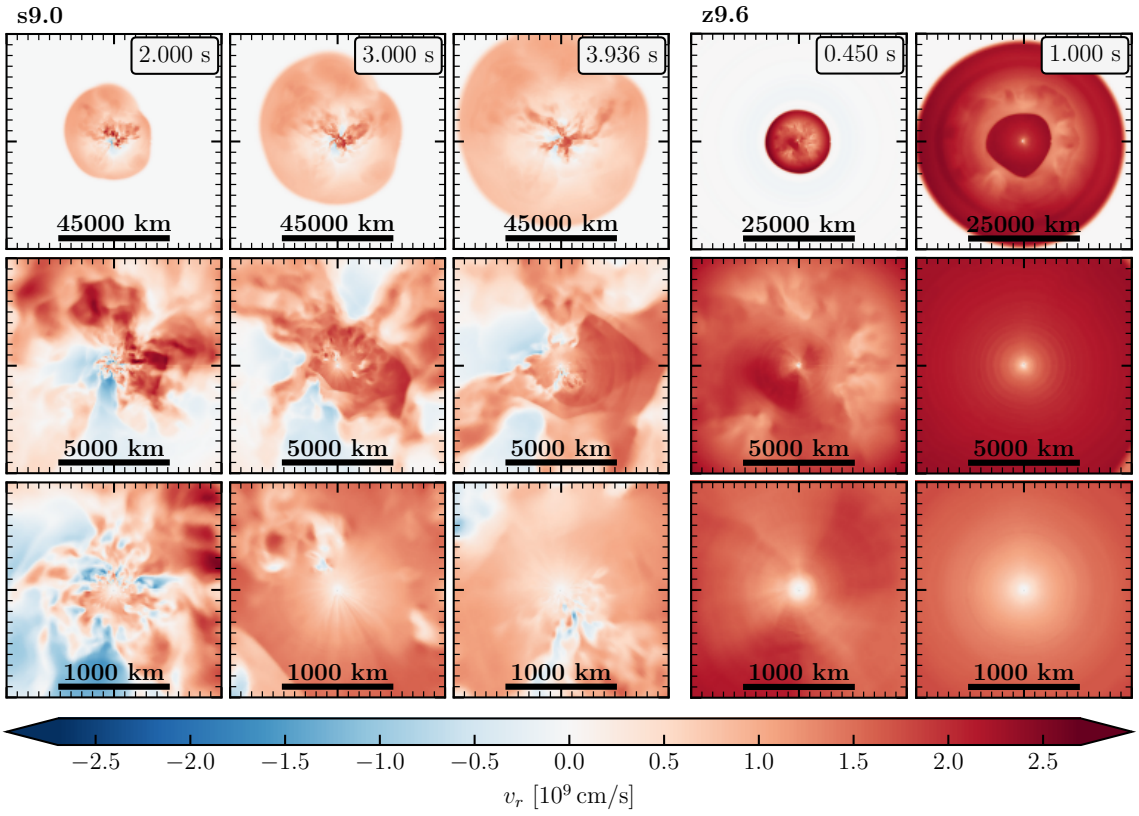

Figure 3.12.: Exemplary snapshots of the models s9.0 (*left panels*) and z9.6 (*right panels*) at different times during the evolution with the Nemesis neutrino scheme, showing cross-sectional cuts of the radial velocity in the x-z plane. From top to bottom, we show magnifications of successively deeper regions around the central PNS (note the decreasing length scales). The post-bounce times of the snapshots are indicated in each column's top panel.

Models z9.6 and s9.0

As noted above, the two low-mass models, z9.6 and s9.0, are characterized by fast declining mass-accretion rates (as a consequence of the steep density gradients outside of their iron cores) and, therefore, have small PNS masses and correspondingly low neutrino luminosities. Both models explode with low energies of less than 0.1 B (i.e., 0.086 B and 0.052 B, respectively; see Table 3.5). These values are in good agreement with the explosion energies inferred for the Crab SN (SN 1054; Yang & Chevalier, 2015) or for more recently observed low-luminosity Type IIP SNe (e.g., SN 2005cs or SN 2020cxd; Valerin et al., 2022; Kozyreva et al., 2022).

In Figure 3.12, we visualize the overall flow morphology of the two low-mass models by cross-sectional cuts showing the radial gas velocity. Model z9.6 explodes in an essentially spherical manner with only a small degree of nonradial asymmetries (see right panels of Figure 3.12), very similar to the explosion models of ECSNe (e.g., Radice et al., 2017; Gessner & Janka, 2018; Stockinger et al., 2020). The shock wave

expands rapidly in this model, reaching ∼10,000 km after only half a second. Because of the low densities in the dilute outer stellar shells and the high velocities of the expanding postshock flow, mass accretion onto the central PNS stops soon after shock revival (see Figure 3.10 and snapshot at 0.45 s in Figure 3.12). In contrast, model s9.0 has a slightly less steep density profile outside its iron core (Figure 3.1), leading to a somewhat more slowly subsiding mass-accretion rate. Relatively cold stellar matter is channeled from large radii towards the central volume around the PNS in persistent accretion downdrafts over several seconds (see left panels of Figure 3.12; e.g., snapshot at 2.0 s). The interplay of continued accretion of cold matter and the simultaneous re-ejection of neutrino-heated outflows shapes the highly asymmetric morphology of the inner SN ejecta, leaving an imprint also on the late-time spatial distribution of heavy chemical elements that are synthesized during the explosion (such as, e.g., radioactive ^{56}Ni; see Section 3.5 and Stockinger et al., 2020).

Such accretion downflows do not exist in the model z9.6 (except for the convective mass motions during the first ∼200 ms after bounce, as visible in Figure 3.3). Instead, the z9.6 model quickly develops a neutrino-driven wind, which is a low-density outflow of matter that is lifted off from the surface of the hot and neutrino-emitting PNS and blown outwards in an essentially spherically symmetric manner (e.g., Duncan et al., 1986; Qian & Woosley, 1996). Neutrino-driven winds have been investigated in several previous 1D and 2D simulations (e.g., Burrows et al., 1995; Janka & Müller, 1996; Scheck et al., 2006; Arcones et al., 2007, 2008) and have been discussed in the literature as possible sites for r-process (i.e., rapid neutron-capture) nucleosynthesis (e.g., Takahashi et al., 1994; Otsuki et al., 2000; Wanajo et al., 2002; Wanajo, 2007; Nevins & Roberts, 2023). The snapshot of model z9.6 at 1.0 s in Figure 3.12 clearly shows the nearly isotropic outflow that fills the inner volume ($r \lesssim 6{,}000$ km) around the PNS. At the location where this (supersonic) wind collides with the more slowly expanding inner ejecta, a wind-termination shock is formed (e.g., Arcones et al., 2007; Arcones & Janka, 2011; see the sharp discontinuity visible in Figure 3.12 at a radius of ∼6,000–8,000 km for model z9.6 at 1.0 s; more details on the neutrino-driven wind of this model can be found in Stockinger et al., 2020).

For model s9.0, on the other hand, it turned out (somewhat surprisingly) that a strong neutrino-driven wind does not develop, in stark contrast to model z9.6. Even though the accretion downflows gradually lose their strength after a few seconds and neutrino-heated, outwards moving gas begins to fill the innermost volume around the PNS (i.e., possibly signaling the onset of a weak wind; see, e.g., the snapshot at 3.0 s in Figure 3.12), cold gas nevertheless continues to fall back into the gravitational well of the PNS in narrow streams, even several seconds after the onset of the explosion (see, e.g., the snapshot at ∼3.9 s in Figure 3.12). However, because the densities in the expanding postshock flow have already decreased to small values, these late-time accretion downdrafts carry little mass and thus contribute only on a subordinate level to the growth of the explosion energy (Section 3.4) and to the hydrodynamic recoil kick acceleration of the PNS (Section 3.6).

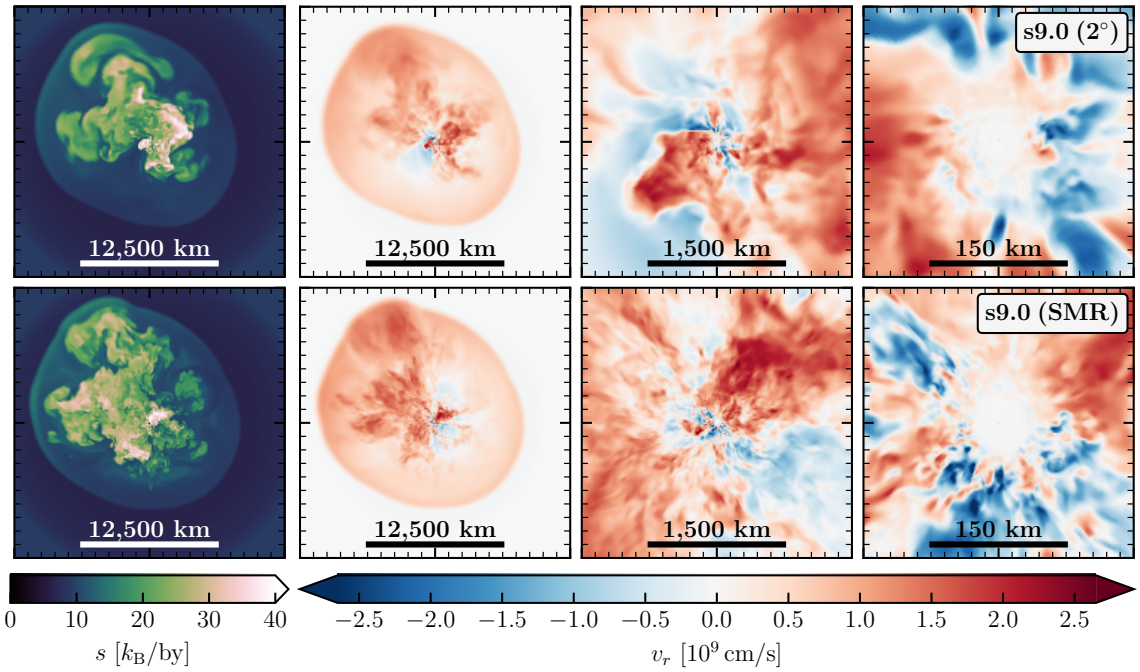

Figure 3.13.: Flow dynamics of model s9.0 with 2° angular resolution (*upper row*) compared to the same model computed on an SMR grid with stepwise increased angular resolution (2° inside the gain radius, 1° between the gain radius and a fixed radius of 160 km, and 0.5° outside of 160 km; *lower row*) at ∼1.2 s after core bounce. The panels show the specific entropy (i.e., entropy per baryon; *left*) and the radial velocity (*right*) in cross-sectional cuts in the x-y plane. The length scales are indicated by scale bars.

Since the PNS's neutrino emission has declined significantly by the end of our simulation (at ∼4 s after bounce; see Figure 3.9), we do not expect a powerful neutrino-driven wind to develop at later times for model s9.0. Instead, we hypothesize that the early phase of neutrino heating smoothly transitions into a subsequent episode of fallback accretion of matter that does not get gravitationally unbound in the explosion, with possibly important implications for the spin of the remnant NS (see, e.g., Stockinger et al., 2020; Janka et al., 2022).

High-resolution Simulation of Model s9.0

To investigate how much the overall explosion morphology depends on the angular resolution of the computational grid, we simulated the s9.0 Nemesis model, additionally to our standard setup with uniform 2° angular resolution (as discussed above), also on an SMR grid, i.e., with the same angular resolution of up to 0.5° as for the early, full-transport evolution of the s9.0 model (see Melson et al., 2020, and Section 3.2.1). Because of the enormous computational costs of high-resolution 3D simulations, we evolved the s9.0 model on the SMR grid only for an evolution period of ∼700 ms with our Nemesis scheme, i.e., until ∼1.2 s after bounce. In

Figure 3.13, we provide snapshots of the two s9.0 models at this time, comparing the flow morphology obtained in the simulation with 2° angular resolution (upper panels) with the one from the high-resolution simulation on the SMR grid (lower panels). As expected, the better-resolved model shows a more fragmented flow pattern, in contrast to more coherent (in- and outflow) structures in the 2° simulation. This difference can be understood because of a smaller numerical viscosity in the case of finer spatial resolution (e.g., Abdikamalov et al., 2015; Melson et al., 2020). Furthermore, the two models display stochastic variations due to the chaotic mass motions in the turbulent, neutrino-heated gain layer. Despite these differences, the overall explosion morphologies of the two models agree very well, with large-scale (buoyant) high-entropy plumes of similar extent and shape, deforming the shock front notably. On smaller scales, both models are characterized by the coexistence of neutrino-heated outflows and accretion downdrafts that reach close to the immediate surroundings of the PNS, irrespective of the angular grid resolution.

Models m15 and m15e

Our two intermediate-mass, rotating $15\,M_\odot$ models, i.e., model m15 and its more energetic counterpart m15e, range between the previously discussed low-mass models (s9.0 and z9.6) and the more massive $18.88\,M_\odot$ and $20\,M_\odot$ models (s18.88, s20, and s20e; see below). This concerns, in particular, their mass-accretion rates, PNS masses, neutrino luminosities, and explosion energies (see Figures 3.9 – 3.11). After ∼7–8 s, when we stopped the two simulations, the deformed shock front had reached radii of around ∼50,000 km and penetrated the base of the star's helium layer. By this time, the models m15 and m15e had obtained (basically saturated) explosion energies of ∼0.3 B and ∼0.4 B, respectively, with a remaining small overburden of ∼0.04–0.05 B (see Table 3.5).

In Figures 3.14 and 3.15, we show the overall flow dynamics and explosion morphologies of models m15 and m15e for the entire evolution period with the Nemesis neutrino scheme by exemplary snapshots of the specific entropy and the radial fluid velocity (in cross-sectional cuts in the equatorial plane; i.e., perpendicular to the rotation axis of the progenitor). Both models display an overall explosion morphology dominated by one prominent neutrino-heated, high-entropy plume that expands into the hemisphere towards the positive y-direction, pushing and deforming the shock front noticeably. This large-scale plume still carries the imprint of the early-time SASI spiral mode that drove the shock front outwards initially and thus aided the onset of runaway shock expansion (see Figure 3.5 and Summa et al., 2018). At the end of our simulations, the fastest parts of the deformed shock front have entered the helium shell, which causes the crescent-shaped high-entropy features visible in the last snapshots of both models in Figures 3.14 and 3.15.

From the opposite hemisphere (i.e., from the negative y-direction), which features generally slower expansion velocities, massive accretion streams fall into the gravitational well of the central PNS over timescales of several seconds. These accretion downflows fragment into smaller-scale vortices near the PNS, where the gas is heated

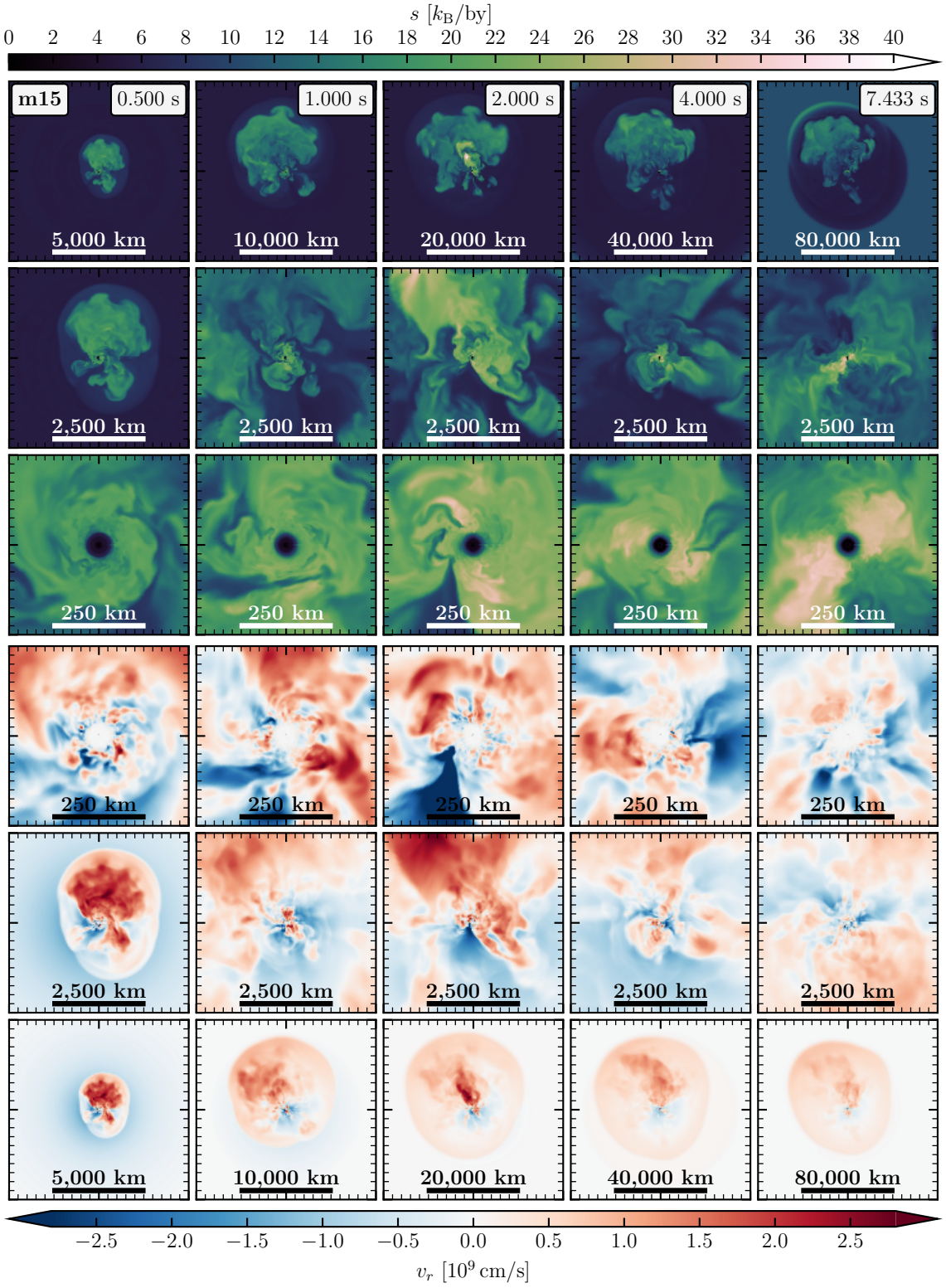

Figure 3.14.: Snapshots of model m15 with the NEMESIS neutrino scheme, showing cross-sectional cuts of the specific entropy (*upper panels*) and the radial velocity (*lower panels*) in the x-y plane. Note the varying length scales. The post-bounce times of the snapshots are indicated in each column's top panel.

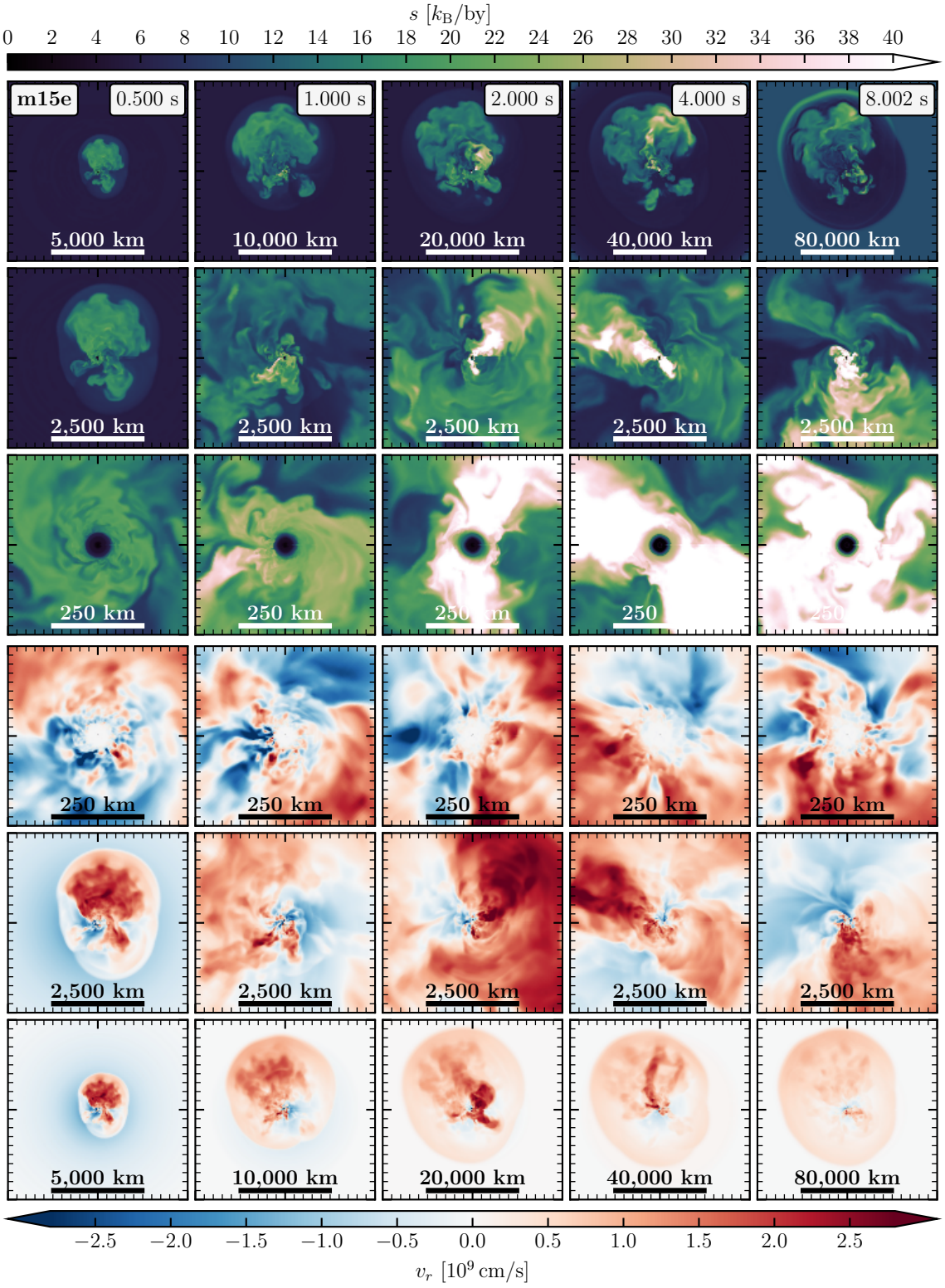

Figure 3.15.: Snapshots of model m15e with the NEMESIS neutrino scheme, showing cross-sectional cuts of the specific entropy (*upper panels*) and the radial velocity (*lower panels*) in the x-y plane. Note the varying length scales. The post-bounce times of the snapshots are indicated in each column's top panel.

by neutrino-energy deposition and gets re-ejected subsequently (in stochastically changing directions). In the model m15e, which features a higher neutrino-heating rate compared to the model m15, the neutrino-driven outflows have generally higher temperatures (i.e., larger values of the entropy) and higher radial velocities (compare, e.g., the snapshots at 2.0 s in Figures 3.14 and 3.15). The strength of the matter downdrafts is, therefore, partly weakened in model m15e (see the lower mass-accretion rate compared to model m15 in Figure 3.10). Nevertheless, none of the two 15 $M_\odot$ models shows any sign of a (spherical) neutrino-driven wind until the end of our simulations.

Interestingly, the early-time rotational flow pattern around the PNS, as inherited from the progenitor rotation, changes during our long-time simulations. For both models, the stellar gas in the PNS's vicinity rotates counter-clockwise in the equatorial plane initially. However, it reverts its direction between ∼1 s and ∼2 s after the bounce as a consequence of the stochastic angular-momentum flux associated with the accretion flows (see Figures 3.30 and 3.31 in Section 3.6; cf. Antoni & Quataert, 2022, 2023). Nevertheless, since only a tiny fraction of this matter settles onto the PNS (see the basically converged PNS mass at ∼1 s in Figure 3.10), the impact on the PNS spin is almost negligible (see Section 3.6.2 for more details).

Model s18.88

The explosion of the model s18.88 has been described previously in the publication by Bollig et al. (2021). Here, we only summarize the model's most essential features and outcomes. It is characterized by a high mass-accretion rate, a correspondingly massive PNS (with a baryonic mass of ∼1.9 $M_\odot$), and thus relatively high neutrino luminosities (i.e., intense neutrino heating), which lead to comparatively violent flow dynamics around the central PNS (see Figure 3.16). Several seconds after the onset of shock expansion, massive accretion streams are still reaching down to the vicinity of the PNS (see, e.g., the snapshot at 4.0 s), where they can gain energy by neutrino heating most efficiently and thus fuel the continuous rise of the explosion energy (Figure 3.11). After ∼5 s, when the neutrino luminosities and mean energies have declined significantly (Figure 3.9), the in- and outflows gradually lose their vigor (see, e.g., the last two snapshots in Figure 3.16), and the growth of the explosion energy levels off visibly. Most remarkably, we could show for the first time that "ab initio," self-consistent 3D simulations of neutrino-powered CCSNe (of non-rotating progenitors) can reach the canonical explosion energy of ∼1 B (Kasen & Woosley, 2009; Pejcha & Prieto, 2015b; Martinez et al., 2022), therefore demonstrating the viability of the delayed neutrino-driven mechanism.

As we have already pointed out in Section 3.2.2, the global explosion asymmetries of model s18.88 are heavily influenced by the presence of pre-collapse progenitor perturbations. The ram-pressure variations associated with convective mass motions in the progenitor's oxygen-burning shell determine the directions of the fastest shock expansion (see Section 3.2 of Bollig et al., 2021). This is why the bulk of the neutrino-heated matter initially expands into the negative y-hemisphere, i.e., around the time

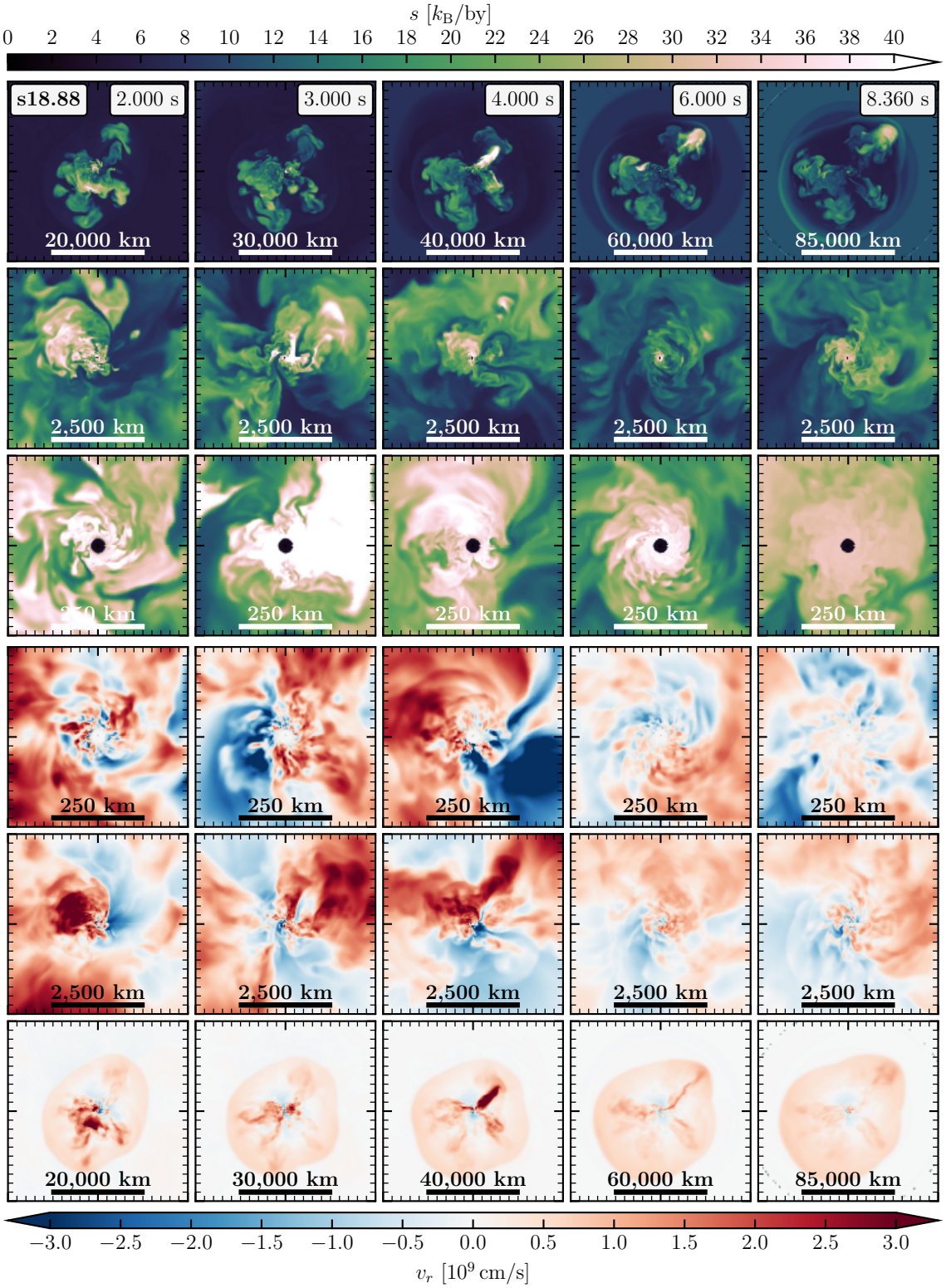

Figure 3.16.: Snapshots of model s18.88 with the NEMESIS neutrino scheme, showing cross-sectional cuts of the specific entropy (*upper panels*) and the radial velocity (*lower panels*) in the x-y plane. Note the varying length scales. The post-bounce times of the snapshots are indicated in each column's top panel.

of shock revival (see Figure 3.6). At later times (roughly one second after bounce), a second large-scale plume develops in another direction of low ram pressure, between the positive x- and y-axes and the negative z-axis, paving the way for subsequent outflows (see, e.g., the collimated high-velocity feature visible in the snapshots at 4.0 s and 6.0 s in Figure 3.16, and the associated Rayleigh-Taylor mushroom head that pushes and deforms the shock front). At the end of our simulation, i.e., at 8.36 s after the core bounce, the shock has reached ∼60,000 km and has penetrated the helium layer. A neutrino-driven wind does not develop until this time.

Models s20 and s20e

Lastly, in Figures 3.17 and 3.18, we show the overall flow dynamics and explosion morphology of model s20 and its more energetic sibling, s20e, respectively. These two models are the most extreme ones among all cases discussed in this work, concerning their high mass-accretion rates, large PNS masses, high neutrino luminosities, and high explosion energies of significantly more than 1 B (i.e., close to the value of ∼1.5 B estimated for SN 1987A; e.g., Arnett et al., 1989; Utrobin et al., 2015, 2021; Jerkstrand et al., 2020). Massive accretion downflows (arriving primarily from the negative z-hemisphere; see, e.g., the first two snapshots in Figure 3.17) are feeding the early and steep rise of the diagnostic explosion energy during the first second after bounce (see Figure 3.11; cf. Melson et al., 2015a). These accretion streams are powerful enough to reach down to small radii, where they (partly) enter the PNS's cooling layer and lose energy through neutrino emission (see, e.g., the radial profiles of the specific neutrino-cooling rate in Figure 2.4). Because the cooling source term is down-regulated for model s20e within a relatively short timescale of ∼100 ms (guided by the corresponding 1D model; see Section 3.3.1), the explosion energy grows even more rapidly than in the case of model s20. However, since the stronger net heating in model s20e leads to generally higher outflow velocities, this also causes a partial weakening of the accretion downdrafts (compare, e.g., the snapshots at 0.8 s in Figures 3.17 and 3.18). The reduced mass-accretion rate then, in turn, leads to a somewhat smaller PNS mass (Figure 3.10), to a diminished accretion component of the neutrino luminosities (Figure 3.9), as well as to a faster contraction of the gain radius (see Equation (2.26)). In the long run, the less energetic s20 model, which maintains a higher mass-accretion rate and shows a slower but steady rise of the diagnostic explosion energy, nearly catches up with the more energetic model s20e. The final, saturated explosion energies without overburden differ by less than 20% (see Table 3.5).

Both models, s20 and s20e, show a high degree of large-scale, nonradial explosion asymmetries. In both cases, the overall flow morphology is shaped early on, around the time of shock revival (with more prominent shock expansion in the positive z-direction and accretion downdrafts arriving primarily from the opposite hemisphere). Nevertheless, differences between the two models arise during the first few seconds after explosion onset as a consequence of the highly non-linear, stochastic interplay of accretion downdrafts and neutrino-driven outflows (see, e.g., the spiral flow pattern

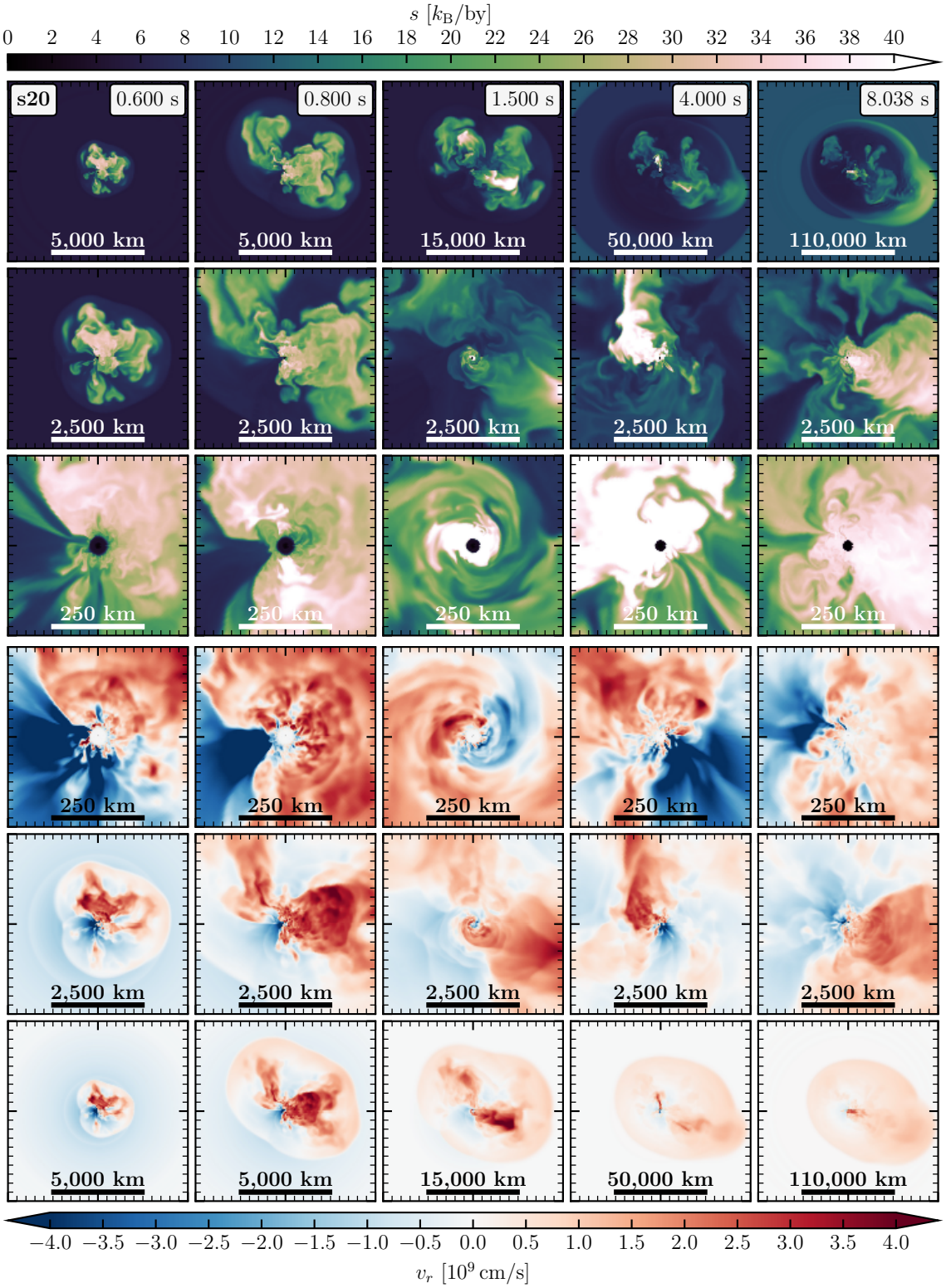

Figure 3.17.: Snapshots of model s20 with the NEMESIS neutrino scheme, showing cross-sectional cuts of the specific entropy (*upper panels*) and the radial velocity (*lower panels*) in the z-y plane. Note the varying length scales. The post-bounce times of the snapshots are indicated in each column's top panel.

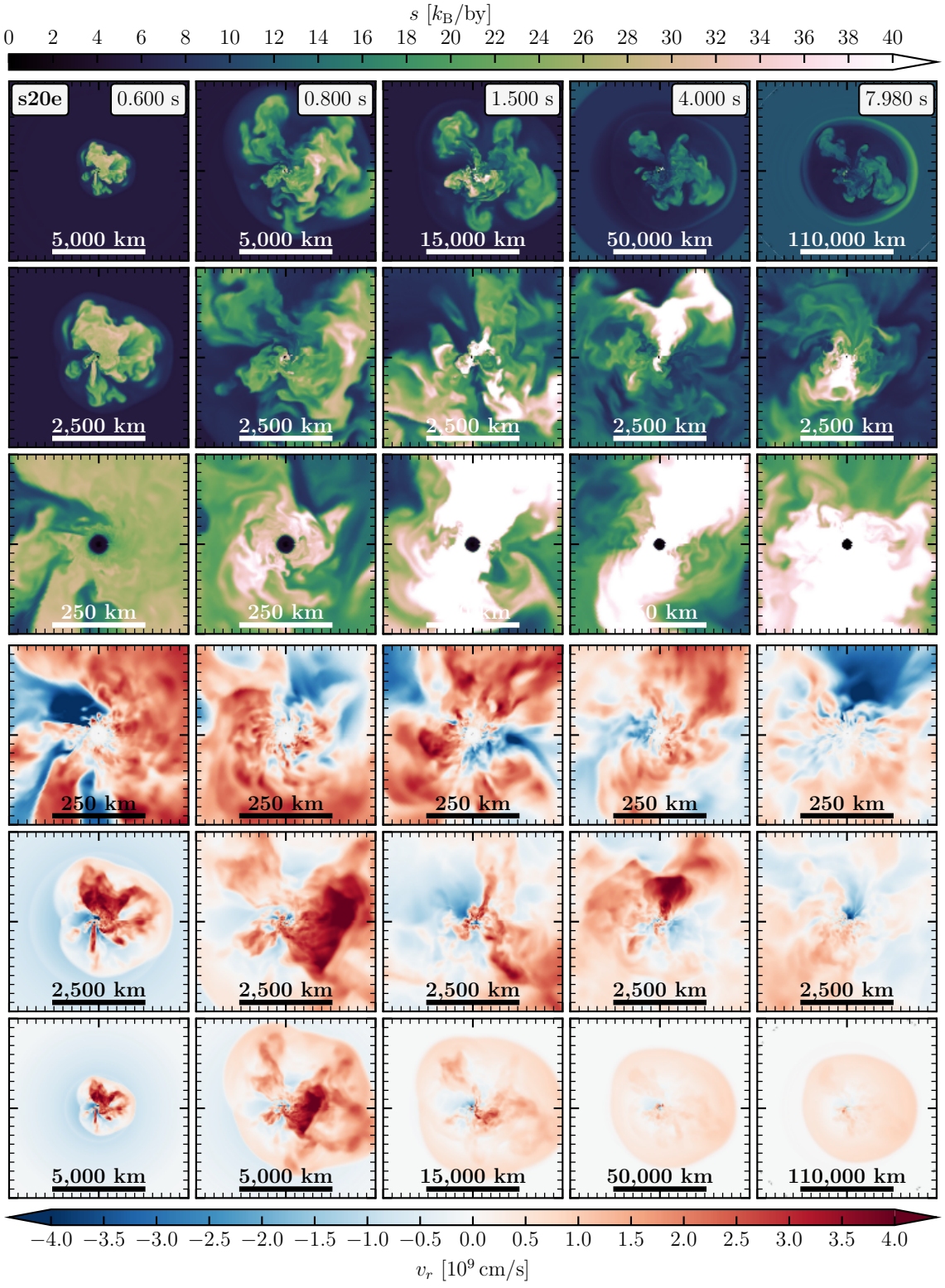

Figure 3.18.: Snapshots of model s20e with the NEMESIS neutrino scheme, showing cross-sectional cuts of the specific entropy (*upper panels*) and the radial velocity (*lower panels*) in the z-y plane. Note the varying length scales. The post-bounce times of the snapshots are indicated in each column's top panel.

in the snapshot at 1.5 s in Figure 3.17, with an accretion stream winding around the central PNS). Notably, the s20 model develops an extremely unipolar (i.e., one-sided) explosion, which results in a strong recoil acceleration of the remnant NS into the negative z-direction (i.e., opposite to the bulk of the ejecta motion), with a final NS kick velocity of more than thousand kilometers per second (see Section 3.6.1 for more details). The model s20e, on the other hand, explodes somewhat more spherically (compare, e.g., the last snapshots in Figures 3.17 and 3.18). This can be understood because of the initially stronger shock expansion and higher outflow velocities of model s20e, which partly counterbalance the massive accretion downflows that cause the strong asphericity of model s20 (see discussion above). Nevertheless, the NS in model s20e still receives a sizable kick of several hundred kilometers per second (see Section 3.6.1). At the end of our simulations (i.e., at ∼8 s after the bounce), the shock has, on average, reached ∼70,000 km in both models and has entered the helium shell with final shock velocities of ∼9,000 km/s (see Table 3.5). Neither of the two models shows indications of a neutrino-driven wind.

3.4. Growth of the Explosion Energy

In this section, we provide more details on the buildup and saturation of the explosion energy in our long-time 3D models presented above. The basic picture of the energy growth in neutrino-driven CCSN explosions has been described in previous works (e.g., Scheck et al., 2006; Marek & Janka, 2009; Müller, 2015; Bruenn et al., 2016; Müller et al., 2017). The stellar matter that is channeled in accretion streams close to the gain radius gets heated by efficient neutrino energy deposition. In response, it is lifted out of the PNS's gravitational well and re-ejected outwards. As this (marginally unbound) neutrino-heated gas, which consists mainly of free protons and neutrons, expands and cools, the free nucleons recombine into α particles and iron-group nuclei. The associated release of recombination energy (which has been lost earlier during infall due to nuclear dissociation and transiently stored in the form of rest-mass energy of the free nucleons) then powers the long-time growth of the explosion energy.

As we have already pointed out in the previous section, the critical quantity determining the dynamical evolution and the energetics of an explosion model during the seconds after successful shock revival is the strength of mass accretion into the layer around the neutrino-emitting PNS. This accretion rate is strongly connected to the outflow rate of expelled neutrino-heated gas. In Figure 3.19, we compare the mass-accretion rate of downflows, $\dot{M}_{\rm down}$ (Equation (3.2)), with the mass-outflow rate, which is defined analogously:

$$\dot{M}_{\rm out}(r) = r^2 \int_{4\pi} \mathrm{d}\Omega\, \rho\, v_r\, \Theta(v_r)\,, \tag{3.11}$$

i.e., as the surface integral of the density ρ times the radial velocity v_r over a sphere of given radius r, where $\Theta(x)$ is the Heaviside step function. Both the mass-accretion

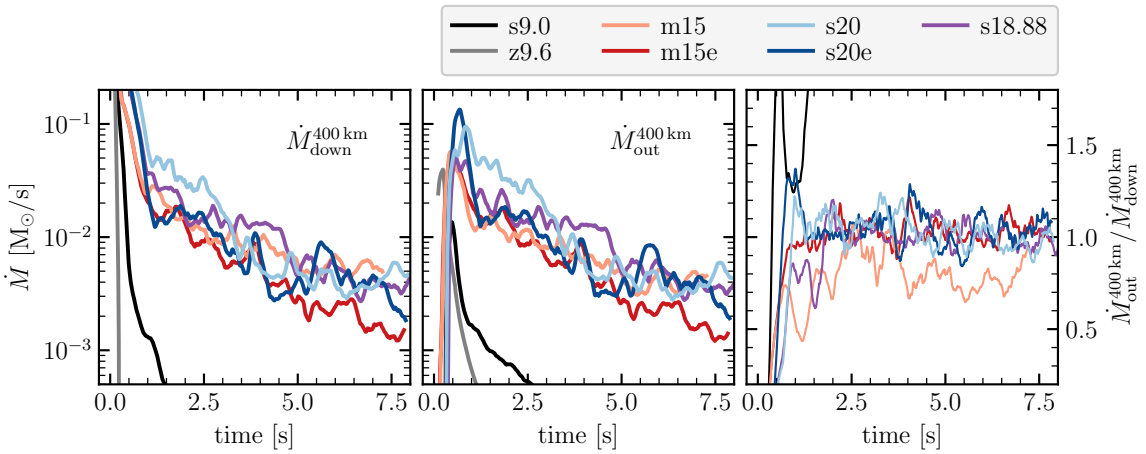

Figure 3.19.: Time evolution of the mass-accretion rate of downflows (i.e., $v_r < 0$; *left*) and the mass-outflow rate (i.e., $v_r > 0$; *center*), both evaluated at a fixed radius of 400 km. *Right*: Ratio of the mass-outflow rate to the accretion rate of downflows for all long-time 3D models considered in this work. The curves are smoothed by running averages of 0.2 s.

rate of downflows and the mass-outflow rate shown in Figure 3.19 are evaluated at a fixed radius of 400 km.

In all models, the mass-outflow rate rises steeply during the first few hundred milliseconds after the shock revival. It quickly reaches a similar magnitude as the mass-accretion rate (or even surpasses it). This is apparent also from the ratio of the two quantities, as shown in the right panel of Figure 3.19. It fluctuates around unity, which indicates that most of the accreted matter gets re-ejected very efficiently. Exceptions arise for the two low-mass models s9.0 and z9.6, which have very small accretion rates and are dominated by low-density outflows early on (see Section 3.3.3). The fact that the model m15 shows an outflow-to-downflow ratio below one during most of its evolution (fluctuating around a value of ∼0.8) is a consequence of the fixed gain radius at a rather large distance of ∼55 km from the center (see Figure 3.10), which leads to a relatively low, probably underestimated, neutrino-heating rate. Hence, not all of the accreted matter gets re-ejected, and a small fraction of the gas settles onto the PNS, as can also be seen by the slightly larger PNS mass of model m15 compared to model m15e (see Table 3.5).

In Figure 3.20, we provide an overview of the energy-growth conditions for all of our long-time 3D models. We compare the growth rates of the diagnostic explosion energy and the explosion energy without overburden (upper panels in Figure 3.20) with the net neutrino-heating rate in the gain layer (center left panel). Moreover, we show the ratio of the explosion energy (diagnostic and without overburden) and the mass-outflow rate (lower panels). The neutrino-heating rate, $\dot{Q}_\nu$, is computed as the integral of the net neutrino energy-deposition rate per volume (i.e., the neutrino-energy source term Q_E appearing on the right-hand side of the hydrodynamic equation

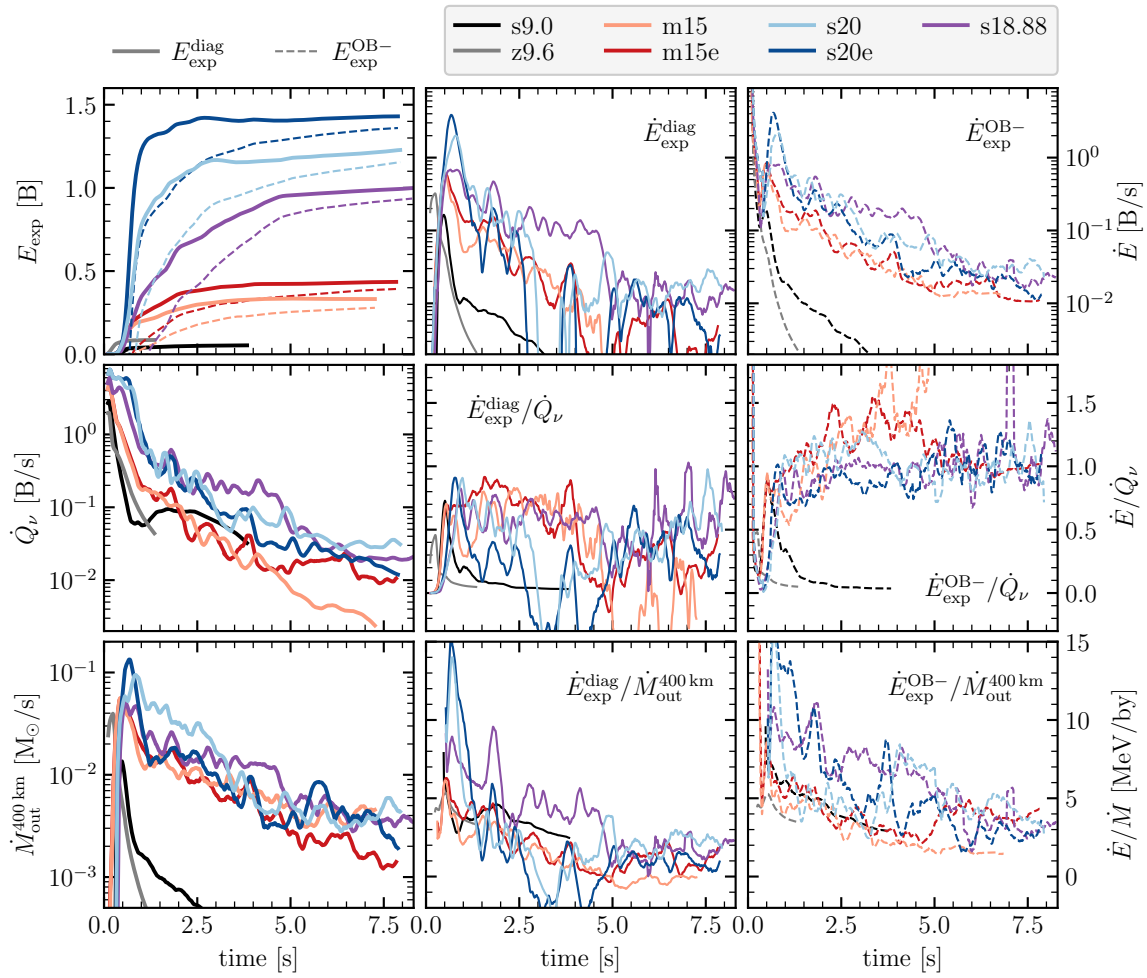

Figure 3.20.: Comparison of the growth rate of the explosion energy (diagnostic and without overburden; *top row*) to the volume-integrated net neutrino-heating rate in the gain layer ($\dot{Q}_\nu$; *middle row*). *Bottom row*: Ratio of the explosion energy (diagnostic and without overburden) and the mass-outflow rate at 400 km (cf. Figure 3.19). The curves are smoothed by running averages of 0.2 s. Appendix A provides a slightly modified version of this figure, which shows only the (dynamically most relevant) first three seconds of the evolution (Figure A.1).

for energy conservation; Equation (2.3)) over the volume of the gain layer,

$$\dot{Q}_\nu = \int_{R_{\rm gain}<r<R_{\rm sh}} Q_{\rm E}\,{\rm d}V\,. \tag{3.12}$$

As described in Sections 2.1.2 and 2.2.1, $Q_{\rm E}$ is either computed self-consistently from the neutrino-transport equations (for the early phase with full VERTEX neutrino transport; Section 3.2) or calculated by means of our NEMESIS neutrino scheme (for the long-time evolution; Section 3.3).

In all of our models, the diagnostic explosion energy has leveled off until the end of the simulations, with final growth rates of around or less than $\sim 10^{-2}\,\mathrm{B\,s^{-1}}$. In some cases, the diagnostic energy even decreases slightly at late times (for models m15, s20, and s20e between $\sim 3\,\mathrm{s}$ and $\sim 7\,\mathrm{s}$) as the SN shock sweeps up the bound matter of the overlying shells. The explosion energy that accounts for the negative overburden (i.e., $E_{\mathrm{exp}}^{\mathrm{OB-}}$; Equation (3.10)), on the other hand, increases until late times, therefore approaching the diagnostic energy. Only the two low-mass models, s9.0 and z9.6, reach their final converged values of the explosion energy ($\sim 0.05\,\mathrm{B}$ and $\sim 0.09\,\mathrm{B}$, respectively) on a relatively short timescale, with $\dot{E}_{\mathrm{exp}}^{\mathrm{OB-}}$ falling below $10^{-2}\,\mathrm{B\,s^{-1}}$ after less than $\sim 1.5\,\mathrm{s}$. For the more massive, $15\,\mathrm{M_\odot}$, $\sim 19\,\mathrm{M_\odot}$, and $20\,\mathrm{M_\odot}$ progenitors with significantly higher mass-accretion (and mass-outflow) rates, it takes several seconds until the energy saturates. Nevertheless, towards the end of our simulations at ~ 7–$8\,\mathrm{s}$ after bounce, the growth rate $\dot{E}_{\mathrm{exp}}^{\mathrm{OB-}}$ has decreased to values of $\mathcal{O}(10^{-2})\,\mathrm{B\,s^{-1}}$ in all models, and the remaining overburden has shrunk to a few percent of the diagnostic explosion energy.

Figure 3.20 clearly demonstrates that the rise of the explosion energy is fueled predominantly by neutrino heating (see middle row of the figure). In good agreement with the previous results by Müller et al. (2017) and Bollig et al. (2021), we find that the approximate relations $\dot{E}_{\mathrm{exp}}^{\mathrm{diag}}/\dot{Q}_\nu \approx 0.5$ and $\dot{E}_{\mathrm{exp}}^{\mathrm{OB-}}/\dot{Q}_\nu \approx 1$ hold for all models with long-lasting mass accretion. However, notice the strong temporal fluctuations, which can be explained by the complex and highly non-linear interplay of ejecta outflows with ongoing and persistent accretion downflows. Neutrino energy is partly deposited and stored also in still bound matter that does not (yet) count into the diagnostic energy (see its definition in Equation (3.9)). Only once this matter has become unbound by continued heating (or through turbulent mixing processes), it can contribute to the energy budget of the explosion (yet with some delay). For the models m15, s20, and s20e, $\dot{E}_{\mathrm{exp}}^{\mathrm{diag}}$ becomes even negative temporarily, as we have noted above. Most prominently, however, the ratio of $\dot{E}_{\mathrm{exp}}^{\mathrm{OB-}}/\dot{Q}_\nu$ remains very close to unity for all models with ongoing mass accretion, from the explosion onset until several seconds after the bounce. This demonstrates nicely that neutrino heating of long-lasting accretion flows is indeed the primary energy source that powers the explosions.[29]

Even though the growth of the explosion energy is primarily fueled by neutrino-energy deposition, it eventually shows up as the release of recombination energy when the free nucleons in the neutrino-heated, expanding SN ejecta reassemble into α particles and iron-group nuclei (i.e., freeze out from NSE). In principle, up to 8.8 MeV can be released per nucleon in the case of complete recombination to the iron group.

[29] The fact that $\dot{E}_{\mathrm{exp}}^{\mathrm{OB-}}/\dot{Q}_\nu$ rises at late times (after ~ 3–$4\,\mathrm{s}$) for model m15 is a consequence of the steep decline of the neutrino-heating rate, which is connected to the afore-mentioned large gain radius. The continued shallow rise of $\dot{E}_{\mathrm{exp}}^{\mathrm{OB-}}$ is caused by the (hydrodynamic) reshuffling of energy between bound and unbound matter. In the model m15e, the large gain radius is partly counterbalanced by an enhanced neutrino-heating rate towards late times (see Section 3.3.1).

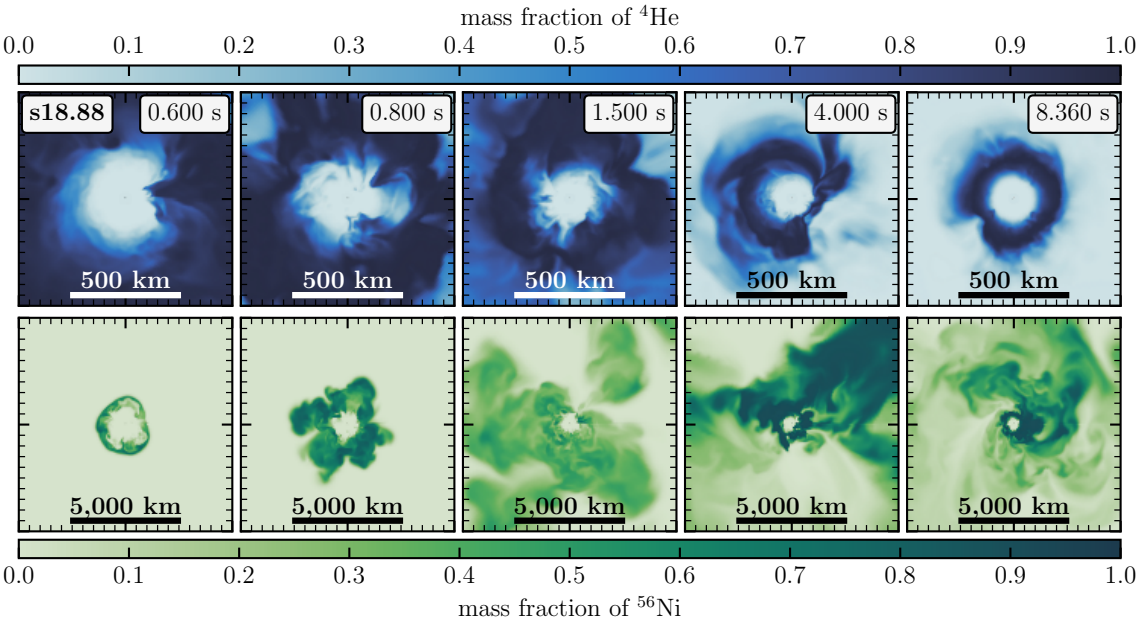

Figure 3.21.: Snapshots of model s18.88 showing cross-sectional cuts of the mass fraction of ^{4}He (*top row*) and ^{56}Ni (*bottom row*) in the *x*-*y* plane. Note the different length scales, as indicated by the scale bars. The post-bounce times of the snapshots are indicated in each column's top panel.

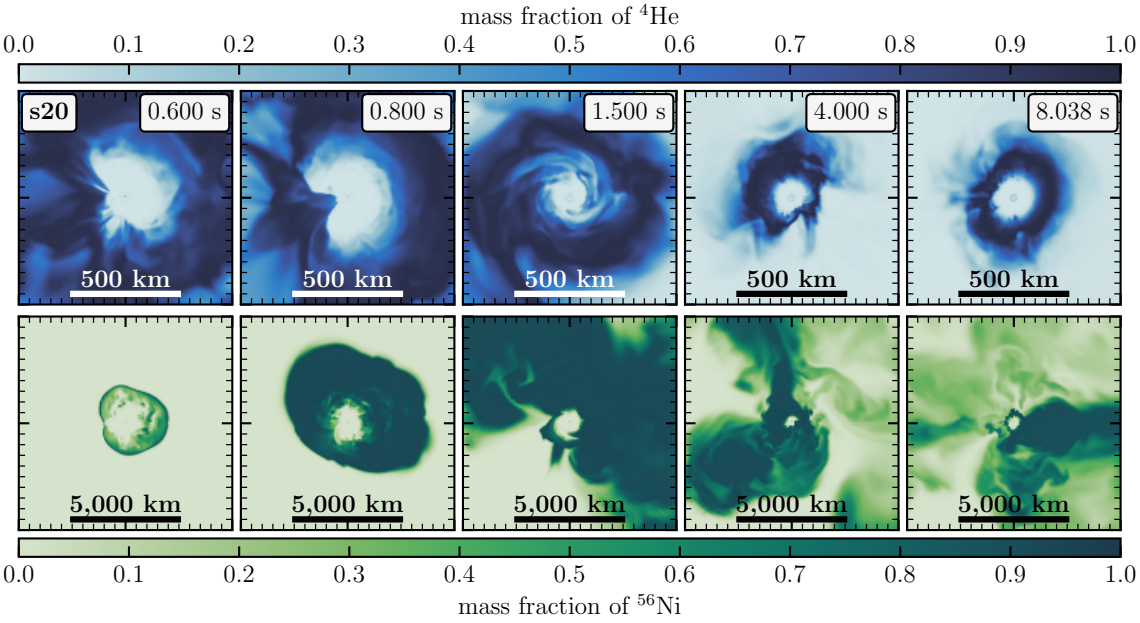

Figure 3.22.: Snapshots of model s20 showing cross-sectional cuts of the mass fraction of ^{4}He (*top row*) and ^{56}Ni (*bottom row*) in the *z*-*y* plane. Note the different length scales, as indicated by the scale bars. The post-bounce times of the snapshots are indicated in each column's top panel.

In practice, though, recombination is often incomplete and hydrodynamic mixing of outflows with downdrafts further reduces the average energy that is released per nucleon to typical values of around ∼5–6 MeV during the first ∼2 s of the explosions (cf. Janka, 2001; Scheck et al., 2006; Marek & Janka, 2009; Müller, 2015; Müller et al., 2017, 2019). However, notice the strong temporal and model-dependent variations in Figure 3.20 (of several MeV in amplitude), reflecting the stochastic and highly non-linear nature of the postshock flow. At later times, the energy growth per nucleon decreases to smaller values because the accretion downflows do not reach close to the gain radius any longer but return outwards at increasingly larger radii (see, e.g., Müller et al., 2017; Bollig et al., 2021).

In Figures 3.21 and 3.22, we show the mass fractions of ^{4}He (i.e., α particles) and radioactive ^{56}Ni for the exemplary cases of the models s18.88 and s20 to illustrate the process of NSE freeze-out in our simulations. The innermost volume within ∼100–200 km around the PNS exhibits temperatures above $\sim 10^{10}$ K (see Figures A.2–A.7 in Appendix A), such that free protons and neutrons dominate the nuclear composition. As the outwards flowing gas expands and cools, the nucleons first recombine to α particles (see upper panels in Figures 3.21 and 3.22) and, once the temperatures drop below $\sim 6 \times 10^9$ K (i.e., $\log_{10}(T/\mathrm{K}) \approx 9.8$; see Figures A.2–A.7) at typical radii of ∼300–500 km, the α particles reassemble further to produce ^{56}Ni (lower panels in Figures 3.21 and 3.22). The efficient formation of α particles and ^{56}Ni requires that the electron fraction, Y_e, remains relatively close to a value of 0.5, which is the case for all of our models, except for the case of model z9.6 (see Figures A.8–A.13 in Appendix A). In addition to the production of ^{56}Ni via freeze-out from NSE, radioactive nickel can also be formed through explosive silicon burning in the shock-heated ejecta. This might explain that almost the entire postshock volume of model s20 is filled with matter consisting mainly of ^{56}Ni in the snapshot at 800 ms in Figure 3.22. This still needs to be investigated further.

A note of caution is indicated here. In our models nuclear reactions are treated in an approximate manner (i.e., via the flashing scheme of Rampp & Janka, 2002, and assuming NSE down to low temperatures; see Sections 2.1.1 and 3.3.1). Our simulations are, therefore, not suited for a reliable description of the chemical composition. The simplified treatment of nuclear reactions in our models is instead meant to roughly capture the overall basic trends. Most certainly, the production of ^{56}Ni is overestimated in our simulations (possibly by up to a factor of ∼2; see Section 3.5). In the near future, we plan to address this uncertainty of our explosion models through a detailed post-processing analysis with tracer particles and an extensive nuclear-reaction network (see, e.g., Sieverding et al., 2020, 2023).

The overproduction of ^{56}Ni in our models may cause a boost of the explosion energy on the order of around ∼10–20%. We speculate that, under more realistic conditions, the average energy release per nucleon in the neutrino-heated freeze-out matter could be reduced by ∼0.5–1 MeV (assuming that some ten percent of the synthesized ^{56}Ni could instead end up in ^{4}He). For a typical freeze-out mass on the order of $\sim 0.1\,\mathrm{M}_\odot$, this translates into an energy boost of ∼0.1–0.2 B. Nevertheless,

we are confident that the overall explosion dynamics of our models are not much affected by our simplified treatment of the nuclear reactions since the energy input through neutrino heating by far dominates over the net release of nuclear energy.

3.5. Nucleosynthesis Yields

CCSNe are major sites of heavy-element formation (i.e., nucleosynthesis) and thus contribute significantly to the chemical enrichment of galaxies (e.g., Kobayashi et al., 2020). Moreover, the nucleosynthesis yields of SN explosions have a direct impact on their observable light curves and spectra (e.g., Pejcha & Prieto, 2015b; Jerkstrand et al., 2012), as well as on the appearance of gaseous SN remnants (e.g., Hwang et al., 2004; Mayer et al., 2022). CCSN nucleosynthesis proceeds mainly via explosive burning in the shock-heated ejecta, as well as through (normal and α-rich) freeze-out from NSE (or quasi-equilibrium; QSE) in neutrino-driven outflows (e.g., Hix & Thielemann, 1999a; Magkotsios et al., 2010). For progenitors at the low-mass end of CCSNe, neutrino-driven winds can further contribute to the chemical yields (possibly, even through a weak r-process; see, e.g., Takahashi et al., 1994; Wanajo et al., 2002). For a dedicated review of SN nucleosynthesis, we refer to the recent article by Janka & Bauswein (2022).

Even though our approximate treatment of the nuclear reactions does not allow us to draw firm conclusions on the detailed nucleosynthetic yields of our CCSN models (see discussion in the previous section), we nevertheless want to provide a brief overview of the ejecta masses for the most abundant nuclear species included in our simulations. In Figure 3.23, we show the time evolution of the total mass of unbound postshock matter, $M_{\rm ej}$, together with the ejecta masses of eight selected isotopes (out of the set of 23 evolved nuclear species; see Section 2.1.1). Around the time of shock revival, when the total mass of unbound postshock matter starts to increase rapidly, most of the ejecta exhibit very high temperatures (around or above $\sim 10^{10}$ K; see Figures A.2–A.7 in Appendix A) and thus consist mainly of free protons and neutrons (not shown in Figure 3.23). Shortly afterward, most of the free nucleons first recombine to α particles and then (at typical radii of $\sim$300–500 km; see Figures 3.21 and 3.22) further to ^{56}Ni. This can be seen clearly in Figure 3.23 as a drop of the ^{4}He ejecta mass during the first few hundred milliseconds in all of our models. The only exception arises for the (ECSN-like) case of model z9.6, whose fast shock expansion does not allow for efficient production of ^{56}Ni, such that the final nickel yield remains slightly below $\sim 5 \times 10^{-4}\,M_\odot$ (see Table 3.6).[30] At early times, when the shock runs through the silicon-rich layers, ^{56}Ni can also be formed through explosive silicon burning in the shock-heated ejecta. Later, as the shock

[30] Model s9.0 shows the same qualitative trend as the high-mass models, i.e., an initial rise of the ^{4}He mass (up to $\sim 7 \times 10^{-4}\,M_\odot$) and a subsequent decline shortly after shock revival. The corresponding line is barely visible in Figure 3.23 because it is covered by the other models.

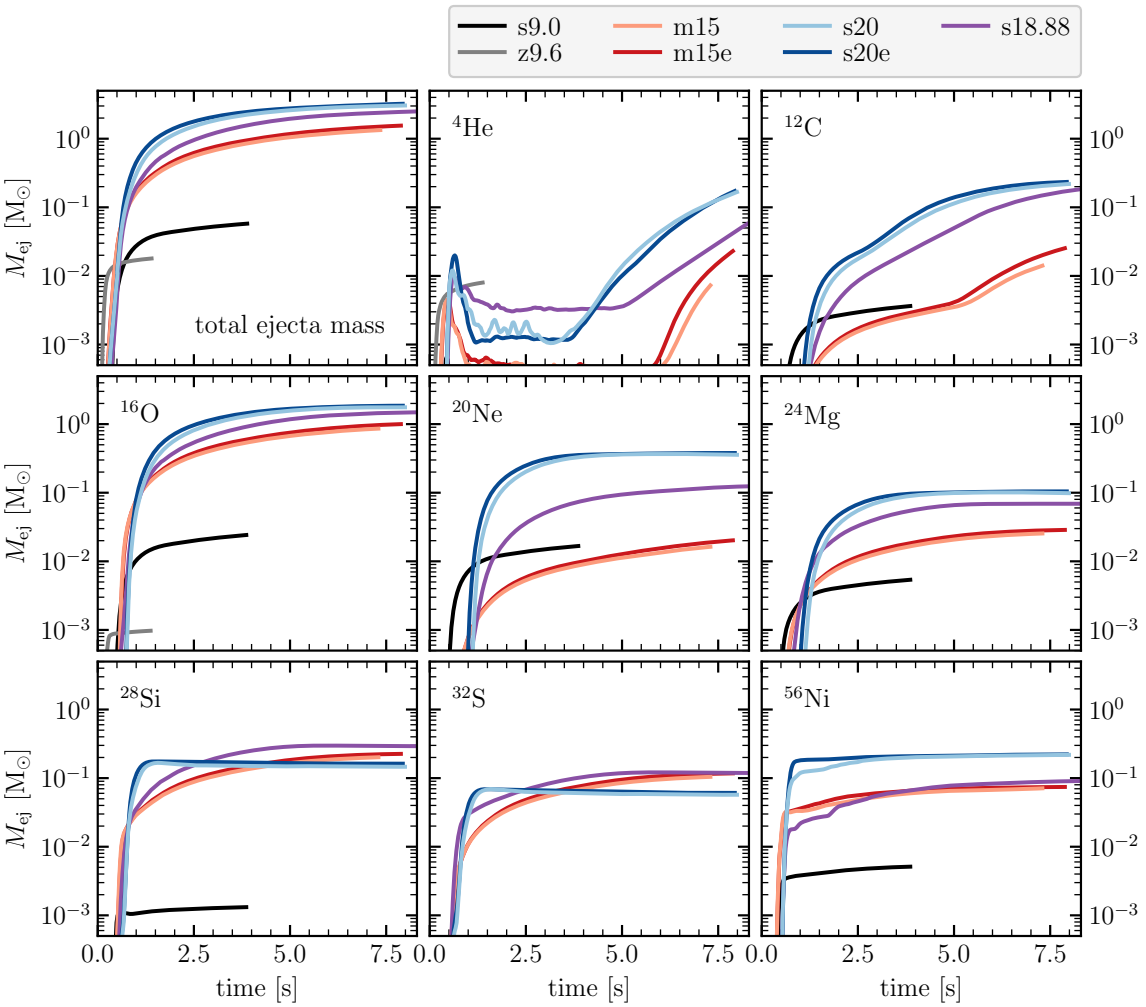

Figure 3.23.: Time evolution of the total mass of unbound postshock ejecta (*top left panel*) and the ejecta masses of the most abundant nuclear species, from ^{4}He (*center top*) to ^{56}Ni (*bottom right*), for all of our long-time CCSN models.

expands to larger radii, it sweeps up matter that consists mainly of intermediate-mass elements (such as carbon, oxygen, neon, and magnesium), i.e., largely reflecting the composition of the stellar progenitor. Most of this matter remains unburned.[31] The

[31] Burning of ^{12}C to ^{24}Mg and burning of ^{16}O, ^{20}Ne, and ^{24}Mg to ^{28}Si can, in principle, occur in the shock-heated ejecta if the temperatures exceed values of $\sim 2.5 \times 10^9$ K and $\sim 3.5 \times 10^9$ K, respectively (Woosley et al., 2002). These reactions are included in our simulations via the flashing scheme of Rampp & Janka (2002, Appendix B). However, at the large radii of relevance, the temperatures are typically too low for these processes to occur significantly. Note that, in the simulations of models s20 and s20e, ^{12}C was erroneously labeled as ^{14}N (and vice versa). Here, we correct this mistake, assuming that the effects of carbon burning can indeed be neglected. A detailed nucleosynthetic post-processing analysis of our explosion models will eventually need to shine a light on the quality of our rough estimates.

Table 3.6.: Ejecta masses of the most abundant nuclear species.

Model	^{4}He [$M_\odot$]	^{12}C [$M_\odot$]	^{16}O [$M_\odot$]	^{20}Ne [$M_\odot$]	^{24}Mg [$M_\odot$]	^{28}Si [$M_\odot$]	^{32}S [$M_\odot$]	^{56}Ni [$M_\odot$]
s9.0	0.00006	0.00368	0.02442	0.01687	0.00543	0.00132	0.00003	0.00514
z9.6	0.00813	0.00045	0.00098	0.00015	0.00001	0.00027	0.00004	0.00048
m15	0.00879	0.01491	0.86720	0.01656	0.02562	0.20266	0.10494	0.07154
m15e	0.02605	0.02651	1.00503	0.02048	0.02876	0.22613	0.11759	0.07449
s18.88	0.06259	0.18589	1.48612	0.12436	0.06903	0.29197	0.11871	0.09104
s20	0.17184	0.21973	1.75865	0.35651	0.09832	0.14635	0.05724	0.21855
s20e	0.17853	0.23503	1.85483	0.37909	0.10448	0.16233	0.06090	0.22206

Note: All masses are evaluated for unbound postshock matter (i.e., for fluid elements with positive total specific energy, $\varepsilon_{\rm tot} > 0$; cf. Equation (3.9)) at the end of our simulations (i.e., at the times $t_{\rm f}$; see Table 3.5). Notice that the yields of ^{56}Ni are most certainly overestimated in some of our models (possibly by up to a factor of $\sim$2; see main text).

steep rise of the ^{4}He ejecta mass several seconds after the explosion onset signals the arrival of the (deformed) SN shock in the helium layer for all of our five massive-star models.

Table 3.6 provides the final ejecta masses at the end of our simulations for the same nuclear isotopes, as shown in Figure 3.23. (Obviously, these values do not include the contribution from elements in the extended stellar envelope ahead of the shock that still needs to get unbound.)[32] Of particular relevance are the final yields of radioactive nickel, as the decay chain $^{56}\mathrm{Ni} \longrightarrow {}^{56}\mathrm{Co} \longrightarrow {}^{56}\mathrm{Fe}$ powers the observable SN light curves. While the yields of the lightest and intermediate-mass elements in the SN ejecta are determined mainly by the composition of the stellar progenitor, the amount of synthesized radioactive nickel is directly connected to the neutrino-heating mechanism. As we have discussed in the previous section, ^{56}Ni acts as a tracer of neutrino-heated freeze-out matter and, thus, correlates strongly with the explosion energy, i.e., in good agreement with the trends observed for Type IIP SNe (e.g., Pejcha & Prieto, 2015b).

However, we need to point out that the yields of ^{56}Ni are, most probably, overestimated in our simulations (possibly by up to a factor of $\sim$2) as a consequence of our simplified treatment of the nuclear reactions (i.e., the assumption of NSE down

[32] Radioactive ^{44}Ti (which can be observed in young SN remnants, e.g., Grefenstette et al., 2014) is not produced abundantly in our simulations (and therefore not shown in Figure 3.23 and Table 3.6). The final yields are on the order of $10^{-5}\,M_\odot$ for all of our models, except for model s18.88, which was simulated with a small, 23-species α-chain reaction network until $\sim$1.7 s after bounce (see Section 3.2.1) and which shows a final ^{44}Ti yield of $\sim$0.014 $M_\odot$. However, as discussed previously (e.g., Wongwathanarat et al., 2013; Harris et al., 2017), using a small α-chain network leads to an overproduction of ^{44}Ti by one or two orders of magnitude.

to low temperatures; see Sections 2.1.1 and 3.3.1). This is also suggested by the sudden increase of the nickel mass at ∼1.7 s after the bounce in model s18.88, which coincides with the time when we replaced the small α-chain reaction network (as employed during the full-transport evolution of this model) by our NSE treatment to low temperatures (see Bollig et al., 2021). Especially, the large ^{56}Ni masses in the models s20 and s20e (of more than 0.2 $M_\odot$; see Table 3.6) are certainly on the high side of the observationally inferred nickel mass distribution of Type IIP SNe (Pejcha & Prieto, 2015b; Martinez et al., 2022) and should rather be considered as an upper bound. Nevertheless, our models demonstrate that nickel masses on the order of 10^{-2}–10^{-1} $M_\odot$ can be reached in neutrino-driven CCSN models, compatible with observations (see, e.g., the value of ∼0.07 $M_\odot$ estimated for SN 1987A; Bouchet et al., 1991; Suntzeff et al., 1992). Our results, thus, do not support earlier claims of a "nickel mass problem" (e.g., Suwa et al., 2019; Sawada & Suwa, 2023).

Detailed nucleosynthetic post-processing of our simulation data, e.g., using tracer particles and an extensive nuclear-reaction network, will eventually need to provide more reliable estimates of the elemental yields in our explosion models (e.g., Wanajo et al., 2018; Sieverding et al., 2020, 2023). Complementary to such a post-processing approach, CCSN simulations can also be run with in-situ nuclear-reaction networks (see, e.g., the 2D models by Kifonidis et al., 2003; Harris et al., 2017; Bruenn et al., 2023; Navó et al., 2023; or the 3D simulations by Wongwathanarat et al., 2013; Sandoval et al., 2021; Bollig et al., 2021). However, computational constraints still limit their application to relatively small networks (typically considering only $\mathcal{O}(10)$, in some cases up to $\mathcal{O}(10^2)$ individual isotopes).

3.6. Neutron Star Properties

The birth properties of NSs, such as their masses, spin periods, and recoil ("kick") velocities, which can be constrained directly from astronomical observations (e.g., Özel & Freire, 2016; Kaspi & Helfand, 2002; Hobbs et al., 2005), are strongly connected to the dynamical evolution of the CCSN explosions that form the compact remnants. This section discusses the NS kick velocities and spin periods obtained in our long-time 3D CCSN simulations. For an overview of the NS masses of our models, we refer to Table 3.4 in Section 3.3.2.

3.6.1. Neutron Star Kick

Nascent NSs can receive sizable kicks from anisotropic neutrino emission as well as through asymmetric ejection of neutrino-heated matter. In the following, we shall discuss both of these mechanisms contributing to the NS recoil acceleration. At this point, we should note that in our simulations, the NS is fixed at the coordinate center of the computational grid (as is often the case in modern 3D finite-volume hydrodynamics simulations of CCSNe). Thus, the NS cannot move and acts as a

momentum sink with "infinite inertial mass."[33] The NS recoil velocity, therefore, needs to be evaluated in a post-processing manner by assuming global (linear) momentum conservation of the NS plus the ejected gas plus the escaping neutrino radiation (i.e., the NS's momentum is given by the negative sum of the net momentum carried away by neutrinos and the net momentum contained in the asymmetric ejecta; see discussion below). For more details on the theoretical framework of neutrino-induced and hydrodynamic NS kicks, we refer the reader to the literature (e.g., Scheck et al., 2004, 2006; Nordhaus et al., 2010a, 2012; Wongwathanarat et al., 2013; Janka, 2017c; Gessner & Janka, 2018; Coleman & Burrows, 2022) and a forthcoming publication (Janka & Kresse, in preparation).

General Considerations

The NS kick can either be estimated directly from linear momentum conservation or, alternatively, via time integration of the instantaneous, net external forces that accelerate it. Because the PNS's inertial (i.e., gravitational) mass changes over time as a consequence of ongoing neutrino emission (see Equation (3.3)), deducing the PNS's kick velocity from its momentum is not as trivial as one might expect. The widely used approach of Scheck et al. (2006, Appendix A), which employs global momentum conservation, cannot capture this time-dependent reduction of the inertial mass. In their approach, the NS kick velocity is instead approximated by

$$\boldsymbol{v}_{\rm NS}(t) \simeq -\frac{\boldsymbol{p}_\nu(t) + \boldsymbol{p}_{\rm gas}(t)}{M_{\rm NS,b}(t)}\,, \tag{3.13}$$

where $\boldsymbol{p}_\nu$ and $\boldsymbol{p}_{\rm gas}$ denote the net momentum associated with the anisotropic neutrino emission and the net momentum of the asymmetric ejecta gas, respectively, and $M_{\rm NS,b}$ is the baryonic PNS mass, which is nearly constant during the time interval when the PNS receives its kick (see, e.g., Figure 3.10). The use of the baryonic (instead of the gravitational) mass is, indeed, more appropriate here because the NS kick velocity should remain constant in the absence of external forces (i.e., in the limit $(\dot{\boldsymbol{p}}_\nu + \dot{\boldsymbol{p}}_{\rm gas}) \to 0$) when the gravitational mass of the PNS decreases due to isotropic neutrino emission in its rest frame. The momentum associated with the PNS's mass reduction is instead carried away by the neutrinos that stream off from the moving PNS since an isotropic emission in the PNS's rest frame translates into a net momentum in the observer frame (Bollig et al., 2021).

[33] In a detailed analysis, Scheck et al. (2006) examined the impact of this approximation (i.e., of a fixed NS) on the explosion dynamics by performing simulations where the NS was allowed to move freely relative to the ejecta, thus investigating possible feedback of the NS's displacement from the explosion center on the gas motions (see their Appendix B for the technical details of their approach). Besides stochastic differences compared to respective models with fixed NS, they did not find any significant effects of the NS movement on the evolution of their explosion models (see their Section 7.2). However, see Janka et al. (2022) for possible (late-time) implications of the NS's displacement from the explosion center.

Nevertheless, using the baryonic mass in Equation (3.13) yields an underestimated value of the kick velocity because, under realistic conditions, anisotropic neutrino emission and asymmetric ejection of matter accelerate the PNS also at times when the neutrino emission has already reduced the PNS's gravitational (i.e., inertial) mass significantly. A more direct estimate of the kick velocity that accounts for the time-dependent reduction of the gravitational PNS mass can be obtained through time integration of the instantaneous recoil acceleration by external forces. We, thus, consider changes in the PNS's momentum,

$$\dot{\boldsymbol{p}}_{\mathrm{NS}} = \underbrace{-\left(\dot{\boldsymbol{p}}_{\nu} + \dot{\boldsymbol{p}}_{\mathrm{gas}}\right)}_{\substack{\text{external forces acting on}\\ \text{the PNS (through aniso-}\\ \text{tropic neutrino emission}\\ \text{and asymmetric ejecta)}}} - \underbrace{c^{-2} L_{\nu}^{\mathrm{tot}}\, \boldsymbol{v}_{\mathrm{NS}}}_{\substack{\text{momentum carried away by}\\ \text{isotropic neutrino emission}\\ \text{in the PNS's rest frame}}} . \tag{3.14}$$

Here, L_{ν}^{tot} is the total neutrino luminosity (i.e., the sum of the luminosities of all six neutrino species), and c is the speed of light. The first term on the right-hand side of Equation (3.14) describes the external forces acting on the PNS (through anisotropic neutrino emission and asymmetric mass ejection), whereas the second term corresponds to the PNS's momentum reduction through isotropic neutrino emission in its rest frame. More generally, the time derivative of the PNS's momentum can be written as

$$\begin{aligned} \dot{\boldsymbol{p}}_{\mathrm{NS}} &= M_{\mathrm{NS,g}}\, \dot{\boldsymbol{v}}_{\mathrm{NS}} + \dot{M}_{\mathrm{NS,g}}\, \boldsymbol{v}_{\mathrm{NS}} \\ &= M_{\mathrm{NS,g}}\, \dot{\boldsymbol{v}}_{\mathrm{NS}} + \left(\dot{M}_{\mathrm{NS,b}} - c^{-2} L_{\nu}^{\mathrm{tot}}\right) \boldsymbol{v}_{\mathrm{NS}} , \end{aligned} \tag{3.15}$$

where we made use of the time-dependent gravitational mass, $M_{\mathrm{NS,g}}$, according to Equation (3.3). Hence, we recover the term $c^{-2} L_{\nu}^{\mathrm{tot}}\, \boldsymbol{v}_{\mathrm{NS}}$ from the right-hand side of Equation (3.14). The time derivative of the baryonic mass, $\dot{M}_{\mathrm{NS,b}}$, accounts for possible mass accretion onto and outflow from the PNS. Combining Equations (3.14) and (3.15) then yields the instantaneous PNS recoil kick acceleration:

$$\dot{\boldsymbol{v}}_{\mathrm{NS}}(t) = -\frac{\dot{\boldsymbol{p}}_{\nu}(t) + \dot{\boldsymbol{p}}_{\mathrm{gas}}(t)}{M_{\mathrm{NS,g}}(t)} - \frac{\dot{M}_{\mathrm{NS,b}}(t)}{M_{\mathrm{NS,g}}(t)}\, \boldsymbol{v}_{\mathrm{NS}}(t) . \tag{3.16}$$

This equation can either be solved numerically for the PNS kick velocity, $\boldsymbol{v}_{\mathrm{NS}}$. Or, alternatively, one can make the simplifying assumption of neglecting the second term on the right-hand side of Equation (3.16). This is well justified because, at early times (during the first few hundred milliseconds after the bounce), when the baryonic PNS mass is growing significantly, the kick velocity is still small (i.e., $v_{\mathrm{NS}} \approx 0$). In contrast, at later times, the baryonic PNS mass is nearly constant (i.e., $\dot{M}_{\mathrm{NS,b}} \approx 0$). The PNS kick velocity can then be computed approximately via time-integration of the recoil acceleration:

$$\boldsymbol{v}_{\mathrm{NS}}(t) = \int_0^t \dot{\boldsymbol{v}}_{\mathrm{NS}}(t')\, \mathrm{d}t' \simeq -\int_0^t \frac{\dot{\boldsymbol{p}}_{\nu}(t') + \dot{\boldsymbol{p}}_{\mathrm{gas}}(t')}{M_{\mathrm{NS,g}}(t')}\, \mathrm{d}t' . \tag{3.17}$$

Neutrino-induced Kick

The enormous amount of energy released during a CCSN from the newborn PNS in the form of neutrinos, $E_\nu^{\mathrm{tot}} \sim 3 \times 10^{53}$ erg, translates into an immense momentum of $E_\nu^{\mathrm{tot}}/c \sim 10^{43}\,\mathrm{g\,cm\,s^{-1}}$. A relatively small global neutrino-emission anisotropy of $\bar{\alpha}_\nu^{\mathrm{tot}} \sim 0.5\%$ is therefore enough to accelerate an NS with a typical mass of $M_{\mathrm{NS}} \sim 1.4\,\mathrm{M}_\odot$ to a kick velocity of (e.g., Gessner & Janka, 2018),

$$v_{\mathrm{NS}}^{\nu} \approx \frac{\bar{\alpha}_\nu^{\mathrm{tot}} E_\nu^{\mathrm{tot}}}{c\, M_{\mathrm{NS}}} \approx 180\,\mathrm{km\,s^{-1}}\, \frac{\bar{\alpha}_\nu^{\mathrm{tot}}}{0.005}\, \frac{E_\nu^{\mathrm{tot}}}{3 \times 10^{53}\,\mathrm{erg}} \left(\frac{M_{\mathrm{NS}}}{1.4\,\mathrm{M}_\odot}\right)^{-1} . \tag{3.18}$$

Anisotropic neutrino emission from the (convective) PNS core can be caused by the LESA phenomenon, which manifests itself as a hemispheric (i.e., dipolar) asymmetry of the neutrino lepton-number flux (e.g., Tamborra et al., 2014a; Glas et al., 2019a). Moreover, neutrino emission and absorption in stochastically varying, asymmetric accretion downflows (see Section 3.3.3) can cause an additional anisotropy of the escaping neutrino radiation. As discussed in this section, time-integrated neutrino anisotropies of around 0.5% seem realistic. A more detailed assessment of the neutrino-induced NS kicks in our explosion models will be presented in a forthcoming paper (Janka & Kresse, in preparation).

The net linear momentum that is carried away per unit of time by neutrinos of a species $\nu_i \in \{\nu_{\mathrm{e}}, \bar{\nu}_{\mathrm{e}}, \nu_x\}$ and by the total neutrino emission of all species is given by the following expressions (corresponding to net force vectors):

$$\dot{\boldsymbol{p}}_{\nu_i}(R,t) = R^2 \oint_{r=R} \frac{F_{\nu_i}(\boldsymbol{r},t)}{c}\, \hat{\boldsymbol{r}}\, \mathrm{d}\Omega\,, \tag{3.19}$$

$$\dot{\boldsymbol{p}}_{\nu}^{\mathrm{tot}}(R,t) = R^2 \oint_{r=R} \sum_{\nu_i} \frac{F_{\nu_i}(\boldsymbol{r},t)}{c}\, \hat{\boldsymbol{r}}\, \mathrm{d}\Omega\,. \tag{3.20}$$

Here, F_{ν_i} denotes the radial component of the neutrino energy flux density of the neutrino species ν_i (see Equation (2.15)), evaluated in the lab frame, c is the speed of light, and $\hat{\boldsymbol{r}}$ is a unit vector pointing in the radial direction. In general, the radial neutrino energy flux density is given by $F_{\nu_i} = \boldsymbol{F}_{\nu_i} \cdot \hat{\boldsymbol{r}}$, where $\boldsymbol{F}_{\nu_i}$ denotes the vector-valued neutrino energy flux. However, for our models, which employ the ray-by-ray approximation, all nonradial flux components are zero (see Section 2.1.2). The sum in Equation (3.20) runs over all six neutrino species (i.e., ν_{e}, $\bar{\nu}_{\mathrm{e}}$, and four times ν_x in the case of three-species neutrino transport as employed for the discussed models). We evaluate the neutrino-momentum emission at a fixed radius of $R = 400$ km, i.e., in the free-streaming regime.

Using these equations, we can define (instantaneous) neutrino-anisotropy parameters for a single neutrino species and the total neutrino emission (e.g., Stockinger et al., 2020; Coleman & Burrows, 2022):

$$\alpha_{\nu_i}(R,t) = c\, \frac{|\dot{\boldsymbol{p}}_{\nu_i}(R,t)|}{L_{\nu_i}(R,t)}\,, \tag{3.21}$$

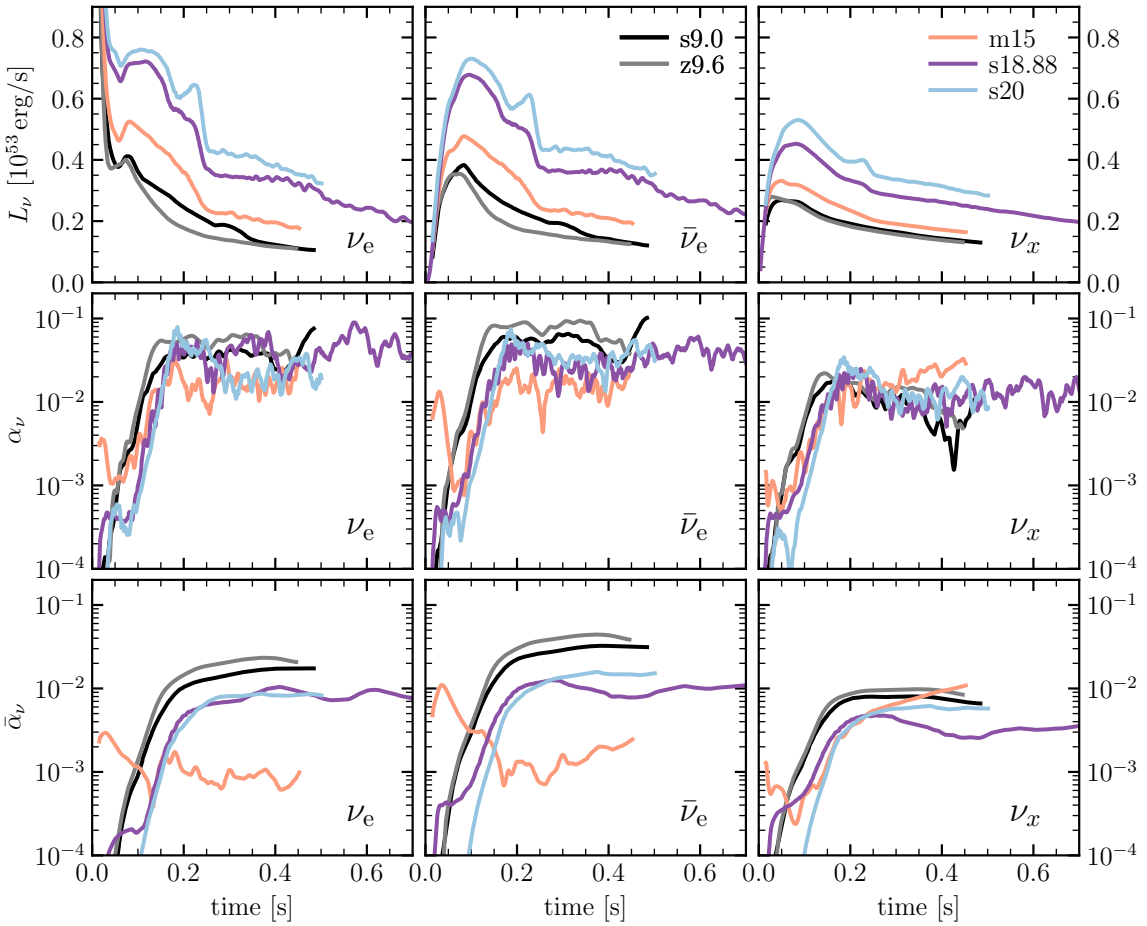

Figure 3.24.: Time evolution of the neutrino luminosity (*top*), instantaneous neutrino-anisotropy parameter (*center*), and time-integrated neutrino-anisotropy parameter (*bottom*) of electron neutrinos, electron antineutrinos, and a representative species of heavy-lepton (anti)neutrinos (from *left* to *right*), evaluated at a radius of 400 km for a lab-frame observer at large distance (i.e., gravitationally redshifted to infinity). Note that we only show the initial 0.7 s of the evolution period with VERTEX neutrino transport, while model s18.88 was computed with full neutrino transport until ∼1.7 s after bounce (see Figure A.14 in Appendix A for the whole evolution).

$$\alpha_\nu^{\mathrm{tot}}(R,t) = c\,\frac{|\dot{\boldsymbol{p}}_\nu^{\mathrm{tot}}(R,t)|}{L_\nu^{\mathrm{tot}}(R,t)}\,, \tag{3.22}$$

where we made use of the (lab-frame) neutrino luminosities, L_{ν_i} and L_ν^{tot}, which are defined as (cf. Equation (2.17) in Section 2.1.2):

$$L_{\nu_i}(R,t) = R^2 \oint_{r=R} F_{\nu_i}(\boldsymbol{r},t)\,\mathrm{d}\Omega\,, \tag{3.23}$$

$$L_\nu^{\mathrm{tot}}(R,t) = \sum_{\nu_i} L_{\nu_i}(R,t)\,. \tag{3.24}$$

Moreover, in an analogous manner, we also define time-integrated neutrino-anisotropy parameters,

$$\bar{\alpha}_{\nu_i}(R,t) = c\,\frac{\left|\int_0^t \dot{\boldsymbol{p}}_{\nu_i}(R,t')\,\mathrm{d}t'\right|}{\int_0^t L_{\nu_i}(R,t')\,\mathrm{d}t'}\,, \tag{3.25}$$

$$\bar{\alpha}_{\nu}^{\mathrm{tot}}(R,t) = c\,\frac{\left|\int_0^t \dot{\boldsymbol{p}}_{\nu}^{\mathrm{tot}}(R,t')\,\mathrm{d}t'\right|}{\int_0^t L_{\nu}^{\mathrm{tot}}(R,t')\,\mathrm{d}t'}\,. \tag{3.26}$$

In Figure 3.24, we show the time-dependent neutrino luminosities, instantaneous anisotropy parameters, and time-integrated anisotropies of the neutrino emission of the individual species for all of our five full-transport models (see Section 3.2). During the first ∼200 ms after the bounce, the instantaneous neutrino-emission anisotropies quickly ramp up to values of a few percent in all of our models. For ν_e and $\bar{\nu}_\mathrm{e}$, the instantaneous α parameter fluctuates around typical values of ∼3%–5% (reaching up to ∼10% in peaks), whereas the heavy-lepton neutrinos display distinctly smaller anisotropies of around 0.5%–3%. This can be understood based on the facts that, firstly, the dipolar asymmetry caused by the LESA is much less pronounced for ν_x (see, e.g., Tamborra et al., 2014a) and, secondly, heavy-lepton neutrinos are less sensitive to (asymmetric) accretion effects because of their smaller interaction cross-sections with matter (notice also their lower accretion luminosities; see Section 3.3.2).

In the two low-mass models, s9.0 and z9.6, the neutrino-emission anisotropy is primarily driven by the LESA, whose dipole direction remains fairly constant and drifts only slowly over time (cf. Tamborra et al., 2014a; Glas et al., 2019a). This is why these two models feature relatively large values of $\bar{\alpha}_{\nu_\mathrm{e}}$ and $\bar{\alpha}_{\bar{\nu}_\mathrm{e}}$ (of around ∼2%–4%). In the more massive models, the neutrino anisotropy is instead dominated by emission and absorption effects in asymmetric accretion flows (see Janka & Kresse, in preparation). The stochastic nature of these matter downdrafts leads to substantial cancellations of the net neutrino-momentum emission vectors $\dot{\boldsymbol{p}}_{\nu_i}$ over time and, thus, to significantly smaller values of the time-integrated neutrino anisotropy (typically around or less than ∼1%).

As a consequence of the anisotropic neutrino emission, the nascent PNS experiences an instantaneous recoil acceleration in the direction opposite to the strongest neutrino-momentum flux, i.e., employing Equation (3.16),

$$\dot{\boldsymbol{v}}_{\mathrm{NS}}^{\nu}(t) = -\frac{\dot{\boldsymbol{p}}_{\nu}^{\mathrm{tot}}(t)}{M_{\mathrm{NS,g}}(t)} - \frac{\dot{M}_{\mathrm{NS,b}}(t)}{M_{\mathrm{NS,g}}(t)}\,\boldsymbol{v}_{\mathrm{NS}}^{\nu}(t) \simeq -\frac{\dot{\boldsymbol{p}}_{\nu}^{\mathrm{tot}}(t)}{M_{\mathrm{NS,g}}(t)}\,. \tag{3.27}$$

Here, we again made use of the simplifying assumption that the term proportional to the time derivative of the PNS's baryonic mass, $\dot{M}_{\mathrm{NS,b}}$, can be neglected (see discussion on page 98). This is justified because the PNS's kick velocity is still small during the time when $M_{\mathrm{NS,b}}$ grows significantly by mass accretion (see Figures 3.2 and 3.10). Time integration of the PNS's recoil acceleration eventually yields the

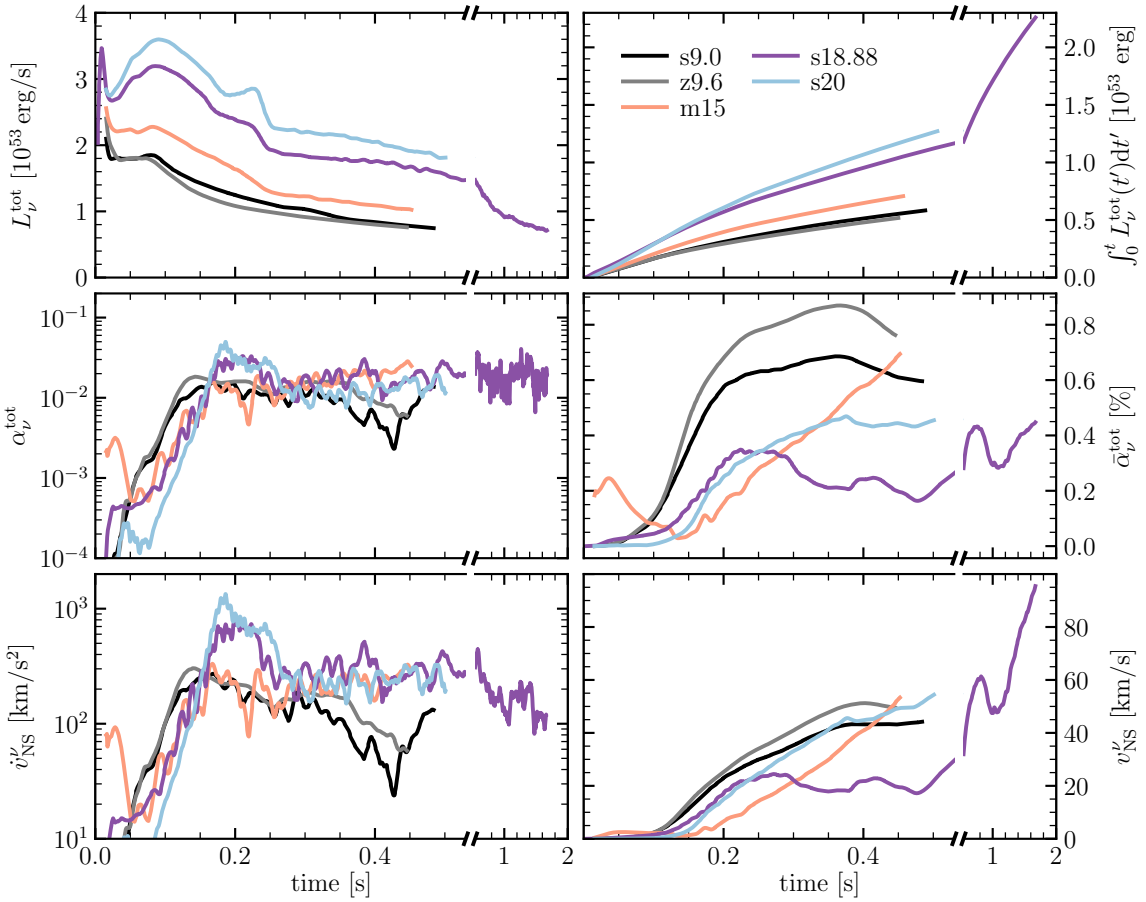

Figure 3.25.: Time evolution of the total neutrino luminosity (i.e., the sum of the luminosities of all six neutrino species; *top left*), the time-integrated total neutrino luminosity (*top right*), the instantaneous neutrino-anisotropy parameter of the total neutrino emission (*center left*), the time-integrated total neutrino-anisotropy parameter (*center right*), the magnitude of the instantaneous neutrino-induced NS recoil acceleration (*bottom left*), and the magnitude of the neutrino-induced NS kick velocity (*bottom right*). Note that model s18.88 was simulated with VERTEX neutrino transport until ∼1.7 s after bounce, whereas the full-transport calculations of all other models were stopped at ∼0.5 s (see Section 3.2). The time axes are split into two parts with differing scales for optimal visibility.

neutrino-induced NS kick velocity:

$$\boldsymbol{v}^{\nu}_{\mathrm{NS}}(t) = \int_0^t \dot{\boldsymbol{v}}^{\nu}_{\mathrm{NS}}(t')\,\mathrm{d}t' \simeq -\int_0^t \frac{\dot{\boldsymbol{p}}^{\mathrm{tot}}_{\nu}(t')}{M_{\mathrm{NS,g}}(t')}\,\mathrm{d}t'\,. \tag{3.28}$$

In Figure 3.25, we provide an overview of the total (instantaneous and time-integrated) neutrino luminosities, the corresponding neutrino-anisotropy parameters, and the magnitudes of the neutrino-induced NS recoil acceleration and kick velocity,

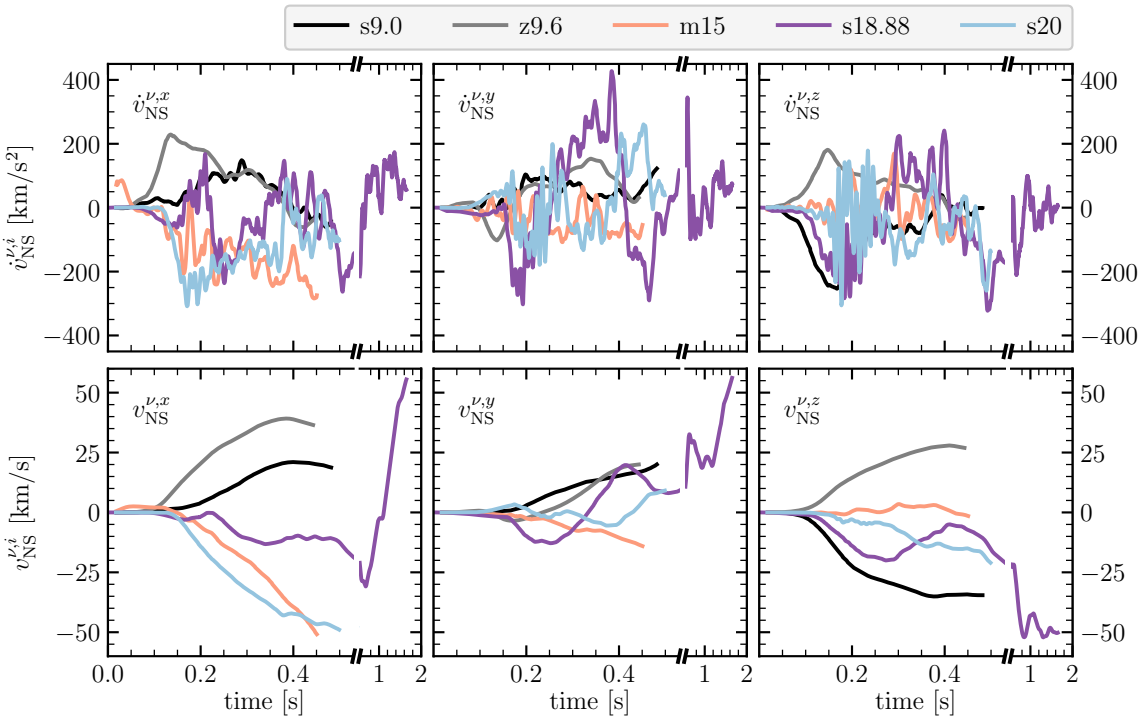

Figure 3.26.: Time evolution of the instantaneous neutrino-induced NS recoil acceleration (*top*) and the neutrino-induced NS kick velocity (*bottom*) in terms of their Cartesian (i.e., x, y, and z) vector components (from *left* to *right*). Note that model s18.88 was simulated with VERTEX neutrino transport until ∼1.7 s after bounce, whereas the full-transport calculations of all other models were stopped at ∼0.5 s (see Section 3.2). The time axes are split into two parts with differing scales for optimal visibility.

$\dot{v}^{\nu}_{\rm NS} = |\dot{\boldsymbol{v}}^{\nu}_{\rm NS}|$ and $v^{\nu}_{\rm NS} = |\boldsymbol{v}^{\nu}_{\rm NS}|$, respectively. The Cartesian vector components of $\dot{\boldsymbol{v}}^{\nu}_{\rm NS}$ and $\boldsymbol{v}^{\nu}_{\rm NS}$ are shown in Figure 3.26. Table 3.7 provides the final neutrino-kick velocities and time-integrated neutrino-anisotropy parameters at the end of the evolution with full neutrino transport. As noted above, the two low-mass models, s9.0 and z9.6, are characterized by a clear LESA dipole (which is evident also from large angles of close to 180° between the directions of the $\nu_{\rm e}$ momentum flux and the ones of $\bar{\nu}_{\rm e}$ and ν_x in these models). Because the net neutrino-momentum emission of $\bar{\nu}_{\rm e}$ and ν_x, which points in the anti-LESA direction, dominates over the emission of $\nu_{\rm e}$, the resultant neutrino-induced kick direction is roughly aligned with the LESA direction in both models (though less prominently for the case of s9.0; see the detailed discussion in Section 4.3 of Stockinger et al., 2020).[34]

[34] The hemispheric asymmetry of the neutrino-lepton number flux due to the LESA phenomenon also leaves a considerable imprint in the spatial distribution of the electron fraction (i.e., proton-to-baryon ration; $Y_{\rm e}$) of the neutrino-processed ejecta, as clearly visible in Figure A.8 for the model z9.6; see the detailed discussion in Section 4.4 of Stockinger et al. (2020).

Table 3.7.: Neutrino-induced NS kicks and neutrino anisotropies.

Model	v_{NS}^{ν} [km/s]	$v_{\mathrm{NS}}^{\nu,x}$ [km/s]	$v_{\mathrm{NS}}^{\nu,y}$ [km/s]	$v_{\mathrm{NS}}^{\nu,z}$ [km/s]	$\bar{\alpha}_{\nu_\mathrm{e}}$ [%]	$\bar{\alpha}_{\bar{\nu}_\mathrm{e}}$ [%]	$\bar{\alpha}_{\nu_x}$ [%]	$\bar{\alpha}_{\nu}^{\mathrm{tot}}$ [%]	$\tilde{v}_{\mathrm{NS}}^{\nu,\infty}$ [km/s]
s9.0	44.39	+18.49	+20.87	−34.55	1.73	3.12	0.66	0.60	156.6
z9.6	49.40	+36.26	+20.25	+26.74	2.06	3.81	0.84	0.76	194.2
m15	54.45	−52.50	−14.25	−2.21	0.11	0.25	1.10	0.70	264.3
s18.88	95.69	+57.15	+58.16	−50.08	0.56	0.57	0.47	0.45	173.6
s20	55.01	−49.56	+9.47	−21.93	0.82	1.53	0.57	0.46	197.8

Note: $v_{\mathrm{NS}}^{\nu} = |\boldsymbol{v}_{\mathrm{NS}}^{\nu}|$ is the magnitude of the neutrino-induced NS kick velocity at the end of the evolution with full neutrino transport (i.e., at the time t_0; Table 3.5); $v_{\mathrm{NS}}^{\nu,x}$, $v_{\mathrm{NS}}^{\nu,y}$, and $v_{\mathrm{NS}}^{\nu,z}$ are its Cartesian components; $\bar{\alpha}_{\nu_\mathrm{e}}$, $\bar{\alpha}_{\bar{\nu}_\mathrm{e}}$, $\bar{\alpha}_{\nu_x}$, and $\bar{\alpha}_{\nu}^{\mathrm{tot}}$ are the time-integrated neutrino-anisotropy parameters of ν_e, $\bar{\nu}_\mathrm{e}$, ν_x, and of the total neutrino emission at the time t_0; $\tilde{v}_{\mathrm{NS}}^{\nu,\infty}$ is the approximate upper bound of the final, neutrino-induced kick velocity (for $t \to \infty$), according to Equation (3.29).

The situation is more entangled in the models m15, s18.88, and s20, which feature long-lasting and significant mass accretion into the partially neutrino-opaque layers around the PNS. Even though the models show, at least to some extent, signs of the LESA, the neutrino-induced NS kicks are instead dominated by anisotropic neutrino emission and absorption in asymmetric accretion downflows. In the models m15 and s20, the directions of the neutrino kicks are roughly aligned with the most massive accretion downdrafts at the end of the full-transport evolution (i.e., pointing approximately towards the negative x-direction for model m15 and a direction between the $-x$-axis and the $-z$-axis for model s20; see Figures 3.8, 3.14, and 3.17). This might indicate that neutrino absorption in the accretion downflows acts as a "shield" for some of the neutrino emission, resulting in an excess neutrino-momentum flux in the opposite direction. A more thorough assessment of this hypothesis will be provided in the forthcoming paper by Janka & Kresse (in preparation). In model s18.88, which was evolved with full Vertex neutrino transport for significantly longer times compared to the other models, a considerable migration of the neutrino-kick direction can be observed (see Figure 3.26 and the discussion in Section 3.5.2 of Bollig et al., 2021). This migration could have manifold reasons, such as the above-mentioned shielding effects of neutrino absorption (or boosting effects due to enhanced neutrino emission) in the stochastically fluctuating accretion downdrafts, a drift of the LESA dipole direction, or the complex interplay of different effects of relevance. This still needs to be investigated in more detail.

At the end of the evolution period with full Vertex neutrino transport, the neutrino-induced NS kick velocities still grow steeply in the models m15, s18.88, and s20. The relatively short timescales of ∼0.5 s (and even the significantly longer evolution time of ∼1.7 s in the case of model s18.88) are certainly too short to make conclusive statements on the final neutrino-induced kick velocities. For this reason,

we want to provide, at least, an order-of-magnitude estimate of the neutrino-induced NS acceleration that is to be expected at times after the detailed neutrino transport is switched off (i.e., for $t > t_0$; see Table 3.5 for the exact values). Based on the long-time neutrino signals as employed in our NEMESIS models (see Section 3.3.2), we compute

$$\tilde{v}_{\mathrm{NS}}^{\nu,\infty} = \frac{\bar{\alpha}_{\nu}^{\mathrm{tot}}}{c} \int_0^{\infty} \frac{L_{\nu}^{\mathrm{tot}}(t')}{M_{\mathrm{NS,g}}(t')} \,\mathrm{d}t' \,, \tag{3.29}$$

as an approximate upper bound of the final neutrino-induced kick velocity (i.e., for $t \to \infty$). Here, we employ the time-dependent gravitational PNS mass, $M_{\mathrm{NS,g}}(t)$, according to Equation (3.3) and, as in Equations (3.27) and (3.28), neglect the term $\propto \dot{M}_{\mathrm{NS,b}} \boldsymbol{v}_{\mathrm{NS}}^{\nu}$. Moreover, this estimate employs the time-integrated neutrino-anisotropy parameter $\bar{\alpha}_{\nu}^{\mathrm{tot}}$ at the time t_0 (see Table 3.7), assuming its value does not change significantly at later times. Of course, this is only a crude estimate because the magnitude and direction of the net neutrino-momentum emission can vary over time. Nevertheless, Equation (3.29) can serve as a rough upper bound for the neutrino kick velocities that could be expected for our explosion models if they were evolved with full neutrino transport until several seconds after the bounce. We find typical values of ∼150–250 $\mathrm{km\,s^{-1}}$ (see Table 3.7), which is considerably below the most extreme value reported in the recent paper by Coleman & Burrows (2022) of more than 400 $\mathrm{km\,s^{-1}}$, which they obtained for a 19 $\mathrm{M_{\odot}}$ model after an evolution period of only less than one second.

Hydrodynamic Kick

In addition to the recoil acceleration by anisotropic neutrino emission, the asymmetric ejection of (neutrino-heated) matter can impart a sizable kick to the remnant NS. As has been discussed in much detail by, e.g., Scheck et al. (2004, 2006); Nordhaus et al. (2010a, 2012); Wongwathanarat et al. (2010b, 2013); Janka (2017c); Gessner & Janka (2018), the NS receives a recoil acceleration into the direction opposite to the strongest ejecta expansion, mainly by the gravitational pull of more slowly expanding gas (therefore coined "gravitational tug-boat mechanism;" Wongwathanarat et al., 2013; Janka, 2017c).[35]

Following Scheck et al. (2006, Appendix A), the hydrodynamic NS kick velocity can, approximately, be computed directly from linear momentum conservation. Assuming

[35] The NS is subject to momentum transfer not only by gravitational forces but also through hydrodynamic pressure forces and momentum advection. However, as has been demonstrated in previous works (e.g., Scheck et al., 2006; Nordhaus et al., 2012; Wongwathanarat et al., 2013; Müller et al., 2017; Gessner & Janka, 2018; Coleman & Burrows, 2022), the effects of momentum advection, pressure forces, and gravitational forces cancel partially, such that the NS's net (hydrodynamic) acceleration is mainly determined by the long-range gravitational pull of the asymmetric ejecta (see also Janka & Kresse, in preparation). The net effect of all hydrodynamic forces is captured to good precision by the conservation of the total linear momentum of the NS plus the surrounding gas.

that the entire system (of the NS plus the surrounding gas) has a vanishing total momentum,[36] the NS kick velocity is given by

$$\boldsymbol{v}_{\rm NS}^{\rm hyd,mc}(t) = -\frac{\boldsymbol{p}_{\rm gas}(t)}{M_{\rm NS,b}(t)}\,, \tag{3.30}$$

where the net linear momentum of the surrounding gas is computed by integrating the density ρ times the local gas velocity $\boldsymbol{v}$ over the entire volume outside of the NS, i.e.,

$$\boldsymbol{p}_{\rm gas}(t) = \int_{r>R_{\rm NS}} \rho\,\boldsymbol{v}\,{\rm d}V\,. \tag{3.31}$$

Note that the baryonic (instead of the gravitational) NS mass is employed in Equation (3.30) to account for the fact that a reduction of the PNS's gravitational mass by isotropic neutrino emission in its rest frame (at late times, in the limit of vanishing external forces) should not change the PNS's kick velocity (see the detailed discussion on page 97 ff.). Since this approach yields a lower limit of the hydrodynamic kick velocity, we also compute the hydrodynamic PNS kick via time integration of the instantaneous recoil acceleration (as done for the neutrino-induced kick), i.e., via

$$\boldsymbol{v}_{\rm NS}^{\rm hyd}(t) = -\int_0^t \frac{\dot{\boldsymbol{p}}_{\rm gas}(t')}{M_{\rm NS,g}(t')}\,{\rm d}t'\,. \tag{3.32}$$

This accounts for the fact that asymmetric gas flows also exert a gravitational pull on the PNS when its inertial mass is already reduced significantly (compared to its baryonic mass). As before, we have neglected the term $\propto \dot{M}_{\rm NS,b}\boldsymbol{v}_{\rm NS}$ (see Equation (3.17)), which is well justified considering that the baryonic PNS mass remains essentially constant (i.e., $\dot{M}_{\rm NS,b} \approx 0$) at late times when the PNS receives its hydrodynamic acceleration through asymmetric ejecta.[37]

Figure 3.27 shows the time-dependent hydrodynamic NS kick velocities for our long-time 3D CCSN models computed according to the two approaches described above. The dashed lines correspond to the kicks obtained from Equation (3.30), whereas the solid lines show the results based on Equation (3.32). In all massive-star models (i.e., except for the two low-mass models s9.0 and z9.6), the kick velocities grow over the

[36] For model s18.88, whose final evolution before core collapse has been simulated in 3D (Yadav et al., 2020), the total gas momentum at the time of core bounce (i.e., at $t = 0$) is not exactly zero. For the evaluation of the hydrodynamic NS kick velocity of this model via Equation (3.30), we hence subtract this (small) momentum contribution at the time $t = 0$ from the gas momentum during later times, $t > 0$.

[37] From a technical point of view, a minor shortcoming arises in the case of using Equation (3.32) compared to Equation (3.30) since the computation of the time derivative of the linear gas momentum, $\dot{\boldsymbol{p}}_{\rm gas}(t)$, and its subsequent time integration introduce minor numerical inaccuracies. In practice, however, this is not a big problem because the total linear gas-momentum vector changes only slowly compared to the time sampling of our simulation outputs (of typically $\Delta t \sim 0.5\,{\rm ms}$) once the hydrodynamic kick has developed a preferred direction.

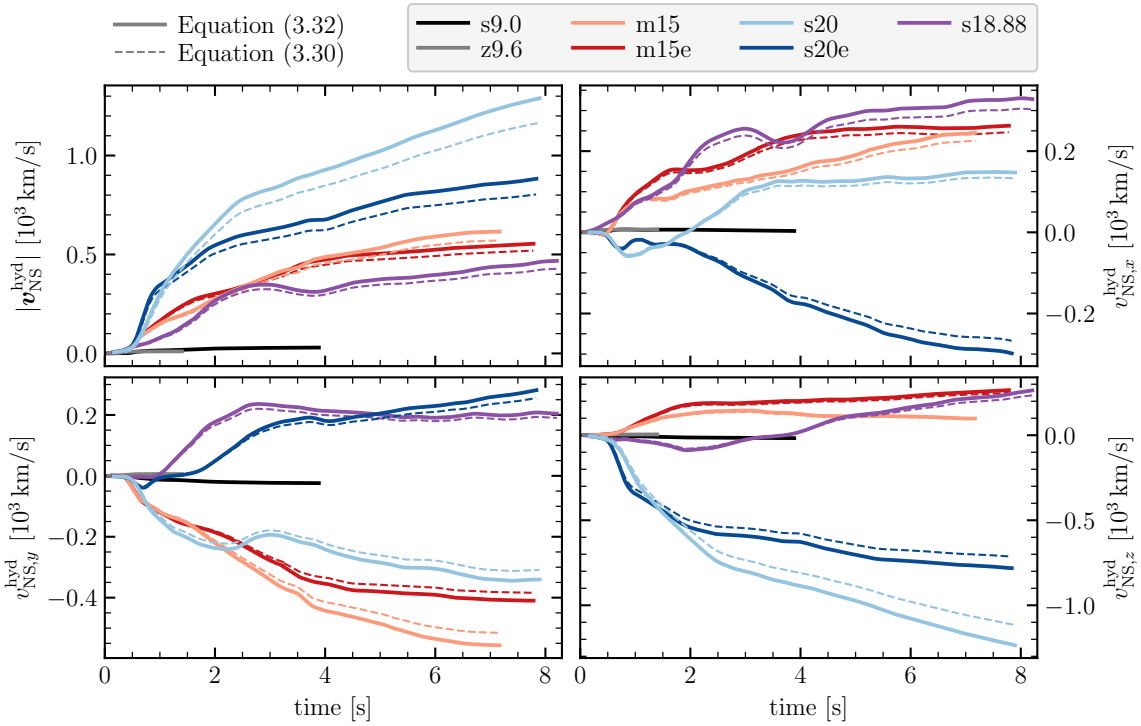

Figure 3.27.: Time evolution of the hydrodynamic NS kick velocity, showing its magnitude and Cartesian (i.e., x, y, and z) vector components (from *top left* to *bottom right*) for all of our long-time CCSN models. The solid lines correspond to the kick velocities obtained from Equation (3.32), i.e., via time integration of the instantaneous recoil acceleration, whereas the dashed lines show the results obtained with Equation (3.30), i.e., assuming linear momentum conservation (which does not capture the time-dependent reduction of the gravitational PNS mass by neutrino emission). Note that the hydrodynamic kick velocities of the models s9.0 and z9.6 are only $\sim$30 km s^{-1} and $\sim$10 km s^{-1}, respectively (see Table 3.8), and are thus barely visible in the figure.

entire evolution period of several seconds as a consequence of long-lasting, massive accretion downflows and the highly asymmetric ejection of neutrino-heated outflows (as discussed in Section 3.3.3). All of these models easily reach kick velocities of several hundred kilometers per second. Most remarkably, the highly asymmetric, unipolar explosion of the s20 model (see Figure 3.17) yields a hydrodynamic NS kick velocity of significantly more than 1,000 km s^{-1}, which is still rising at the end of our simulation. As noted above, the calculation according to Equation (3.30) neglects the time-dependent reduction of the PNS mass through ongoing neutrino emission, which is why the final hydrodynamic kick velocities are smaller by around $\sim$10% compared to results obtained from Equation (3.32), i.e., via time integration of the instantaneous recoil acceleration.

The directions of the hydrodynamic NS kick velocities, as shown by their Cartesian vector components in Figure 3.27, are roughly aligned with the directions of the most

massive accretion downflows (e.g., approximately in the negative y-direction for the models m15 and m15e and pointing in the negative z-direction for the models s20 and s20e; cf. Figures 3.14–3.18). In agreement with previous works (e.g., Scheck et al., 2006; Nordhaus et al., 2010a; Wongwathanarat et al., 2013), and as intuitively expected based on arguments of total momentum conservation, we find that the hydrodynamic NS kick points into the hemisphere opposite to the strongest ejecta expansion. This also agrees well with astronomical observations of young SN remnants (e.g., Katsuda et al., 2018).

To better quantify the explosion asymmetry that drives the hydrodynamic NS kick acceleration, we also define an ejecta-anisotropy parameter (e.g., Janka & Müller, 1994; Scheck et al., 2006; Gessner & Janka, 2018; Janka et al., 2022),

$$\bar{\alpha}_{\mathrm{ej}} = \frac{|\boldsymbol{p}_{\mathrm{gas}}|}{p_{\mathrm{ej}}}\,, \tag{3.33}$$

where $\boldsymbol{p}_{\mathrm{gas}}$ is the net linear gas momentum, computed according to the vector-valued integral of Equation (3.31), and

$$p_{\mathrm{ej}}(t) = \int_{R_{\mathrm{NS}}<r<R_{\mathrm{sh}}} \rho\,|\boldsymbol{v}|\,\mathrm{d}V \tag{3.34}$$

denotes the total momentum stored in the ejecta. In Table 3.8, we provide the final hydrodynamic NS kick velocities (magnitudes and vector components) for all of our explosion models, together with the final values of $\bar{\alpha}_{\mathrm{ej}}$. We find ejecta asymmetries of ∼4%–20%, in good overall agreement with the values presented by, e.g., Scheck et al. (2006) and Janka et al. (2022).

Total Kick

In Figure 3.28, we show the time evolution of the total (i.e., hydrodynamic plus neutrino-induced) NS kick velocity, $\boldsymbol{v}_{\mathrm{NS}}^{\mathrm{tot}}(t) = \boldsymbol{v}_{\mathrm{NS}}^{\mathrm{hyd}}(t) + \boldsymbol{v}_{\mathrm{NS}}^{\nu}(t)$, together with the angle between the hydrodynamic and neutrino-induced NS kick vectors, as well as the angles between the NS spin vector (see Section 3.6.2) and the total and hydrodynamic NS kick vectors. As we have discussed above, the neutrino-induced NS kick velocities of our models (as shown in Figures 3.25 and 3.26) were computed self-consistently only until the times t_0 when we switched off the neutrino transport in our simulations and replaced it by the Nemesis scheme. At these times, the neutrino-induced kick velocities have not yet reached their final saturated values. Nevertheless, our approximate upper bounds $\tilde{v}_{\mathrm{NS}}^{\nu,\infty}$ of up to ∼150–250 km s^{-1} (Equation (3.29) and Table 3.7) suggest that, for massive-star explosions with asymmetric mass ejection (such as our models m15, m15e, s18.88, s20, and s20e), the final NS kicks are dominated by hydrodynamic effects (in marked contrast to the conclusions drawn recently by Coleman & Burrows, 2022). Only for our two low-mass models, s9.0 and z9.6, we find total NS kick velocities with a significant or even dominant contribution from anisotropic neutrino emission (see Table 3.8). Altogether, we find NS kick

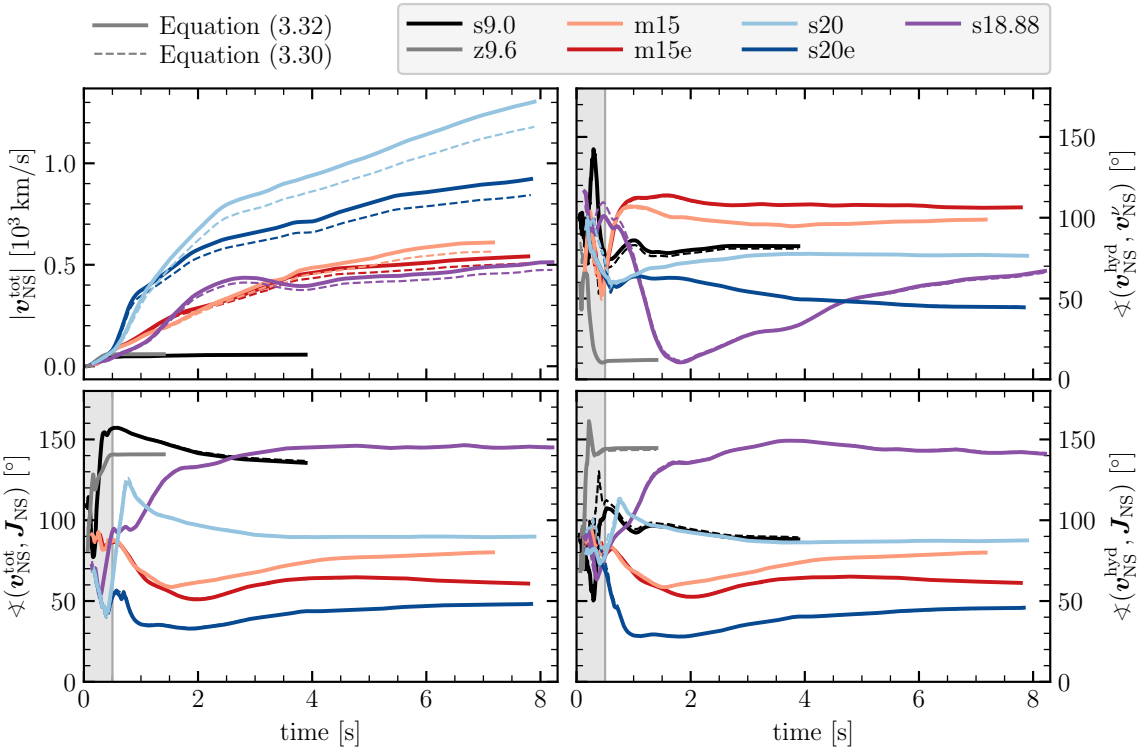

Figure 3.28.: Time evolution of the total NS kick velocity ($v_{\rm NS}^{\rm tot} = |\boldsymbol{v}_{\rm NS}^{\rm tot}| = |\boldsymbol{v}_{\rm NS}^{\rm hyd} + \boldsymbol{v}_{\rm NS}^{\nu}|$; *top left*), the angle between the hydrodynamic and neutrino-induced NS kick vectors (*top right*), the angle between the total NS kick and the NS's angular momentum (i.e., spin) vector (*bottom left*), and the angle between the hydrodynamic NS kick and the NS spin (*bottom right*) for all of our long-time CCSN models. The solid lines correspond to results where the hydrodynamic NS kick velocity is obtained from Equation (3.32), i.e., via time integration of the instantaneous recoil acceleration, whereas the dashed lines show results that employ Equation (3.30), i.e., assuming linear momentum conservation for the computation of the hydrodynamic kick (which does not capture the time-dependent reduction of the gravitational PNS mass by neutrino emission). The gray vertical bands indicate the time span during which the hydrodynamic NS kick velocity still fluctuates strongly (around small values) and during which a reliable computation of the different angles is, therefore, limited by numerical inaccuracies.

velocities over a broad range of values, ranging from below 100 km s^{-1} to more than 1000 km s^{-1}, in good agreement with the kick distribution as inferred from astronomical observations (e.g., Hobbs et al., 2005; Faucher-Giguère & Kaspi, 2006), and significantly above the typical velocities that can be explained solely from the disruption of stellar binary systems (Blaauw, 1961).

Finally, we want to comment briefly on the angles between the hydrodynamic and the neutrino-induced kick vectors (as shown in Figure 3.28 and Table 3.8). In model z9.6, the neutrino-induced and hydrodynamic kick directions are nearly aligned

Table 3.8.: Hydrodynamic NS kicks and ejecta anisotropies.

Model	$v_{\rm NS}^{\rm hyd,mc}$	$v_{\rm NS}^{\rm hyd}$	$v_{{\rm NS},x}^{\rm hyd}$	$v_{{\rm NS},y}^{\rm hyd}$	$v_{{\rm NS},z}^{\rm hyd}$	$v_{\rm NS}^{\rm tot}$	$\bar{\alpha}_{\rm ej}$	$\theta_{\rm hyd}^{\nu,0}$	$\theta_{\rm hyd}^{\nu,{\rm f}}$
			$[10^3$ km/s]					[°]	[°]
s9.0	0.029	0.030	+0.004	−0.024	−0.018	0.057	0.095	76.7	82.4
z9.6	0.010	0.010	+0.007	+0.006	+0.005	0.060	0.039	9.8	12.1
m15	0.575	0.627	+0.249	−0.567	+0.097	0.621	0.196	48.9	98.8
m15e	0.522	0.562	+0.263	−0.417	+0.268	0.549	0.147	48.9	106.1
s18.88	0.432	0.462	+0.322	+0.201	+0.264	0.507	0.074	10.1	67.7
s20	1.176	1.291	+0.146	−0.341	−1.237	1.306	0.167	60.3	76.4
s20e	0.808	0.879	−0.302	+0.288	−0.773	0.919	0.100	60.3	44.2

Note: $v_{\rm NS}^{\rm hyd,mc}$ and $v_{\rm NS}^{\rm hyd}$ are the magnitudes of the hydrodynamic NS kick velocity at the end of our long-time NEMESIS simulations (i.e., at the time $t_{\rm f}$; see Table 3.5) according to Equations (3.30) and (3.32), respectively; $v_{{\rm NS},i}^{\rm hyd}$ $(i = x, y, z)$ are the Cartesian vector components of $\boldsymbol{v}_{\rm NS}^{\rm hyd}$; $v_{\rm NS}^{\rm tot}$ is the magnitude of the total (i.e., hydrodynamic plus neutrino-induced) NS kick velocity at $t = t_{\rm f}$ (with the neutrino kick evaluated at $t = t_0$); $\bar{\alpha}_{\rm ej}$ is the ejecta-anisotropy parameter (Equation (3.33)) at $t = t_{\rm f}$; $\theta_{\rm hyd}^{\nu,0} = \sphericalangle[\boldsymbol{v}_{\rm NS}^{\rm hyd}(t_0), \boldsymbol{v}_{\rm NS}^{\nu}(t_0)]$ and $\theta_{\rm hyd}^{\nu,{\rm f}} = \sphericalangle[\boldsymbol{v}_{\rm NS}^{\rm hyd}(t_{\rm f}), \boldsymbol{v}_{\rm NS}^{\nu}(t_0)]$ are the angles between the hydrodynamic and neutrino-induced NS kick vectors at the end of the full-transport evolution (i.e., at the time t_0; see Table 3.5) and at the time $t_{\rm f}$, respectively. Note that the neutrino-induced kick is not evolved at times $t > t_0$.

because the LESA greatly influences both the anisotropic neutrino emission and the gas dynamics in this model. The total neutrino energy (and thus momentum) flux summed over all six neutrino species, which determines the neutrino-induced NS kick, is strongest in the anti-LESA direction. The same is true also for the summed energy flux of $\nu_{\rm e}$ plus $\bar{\nu}_{\rm e}$, which defines the direction of the most powerful neutrino heating and, thus, the strongest mass ejection. Consequently, the neutrino-induced kick and the hydrodynamic kick point roughly in the direction of the LESA dipole (see Stockinger et al., 2020, Figures 6 and 8).

The situation is less clear in the other models, whose dynamics are heavily influenced by stochastic (i.e., randomly directed) accretion flows. Hence, these models do not show an evident correlation between the neutrino-induced and hydrodynamic kick velocities. Nevertheless, in model s18.88 (which was evolved with full neutrino transport until ∼1.7 s after the bounce), we witness a transient period (from around 1 s until 2 s post bounce) during which the angle between the hydrodynamic kick and the neutrino-induced kick shrinks to relatively small values (of ∼10° in the minimum). Both kick contributions show an acceleration towards the positive x and y directions during this time interval (see Figures 3.26 and 3.27), which may be explained by the arrival of a massive accretion stream around that time, approaching the PNS from a direction between the positive x and y axes (see snapshots at 1.675 s and 2.0 s in Figures 3.6 and 3.16, respectively). On the one hand, this accretion downflow exerts

a gravitational pull on PNS and, on the other hand, it can also block some of the neutrino emission and, thus, could be responsible for the excess neutrino-momentum flux in the opposite direction (see Janka & Kresse, in preparation). Similarly, in the models m15 and s20, we see, at least very roughly, an alignment of the neutrino-induced kicks (at the end of the simulations with full neutrino transport) with the directions of the most massive accretion downflows at these times (see discussion on page 104). However, as the accretion streams can wind around the neutrino-emitting PNS, the flow pattern on the largest spatial scales (which determines the long-range gravitational pull and hence the hydrodynamic kick acceleration) does not need to be aligned with the flow pattern in the immediate surrounding of the PNS (where anisotropic neutrino emission and absorption effects are relevant).

We want to point out once again that we have no solid information on the evolution of the neutrino-induced kick at times later than t_0 (i.e., after the VERTEX transport module was switched off and replaced by our NEMESIS scheme). The question of the final saturated neutrino kicks can be addressed conclusively only through long-time 3D simulations, including full, detailed neutrino-transport calculations over several seconds. This is currently out of reach because of the enormous computational costs of full-physics 3D simulations.

3.6.2. Neutron Star Spin

Even in the case of non-rotating progenitor stars, the remnant NSs can be spun up to high angular velocities during the first seconds of the explosion by the accretion of stochastic angular momentum associated with matter downdrafts that strike the PNS slightly off-center (e.g., Spruit & Phinney, 1998). In this section, we briefly discuss the NS spin periods that we obtain in our models. Because, in general, finite-volume schemes, as employed in our numerical code, do not guarantee to preserve angular momentum (see, e.g., Müller, 2020, and our discussion below), we decided to evaluate the PNS spin via time integration of the net angular-momentum flux onto the PNS. Following previous works (e.g., Wongwathanarat et al., 2010b, 2013; Müller et al., 2017, 2019; Stockinger et al., 2020), we thus compute the PNS's angular momentum at the time t according to

$$\boldsymbol{J}_{\rm NS}(t) = \boldsymbol{J}^0_{\rm NS} + \int_0^t \dot{\boldsymbol{J}}_{\rm NS}(t')\,{\rm d}t'\,, \tag{3.35}$$

where $\boldsymbol{J}^0_{\rm NS} = \boldsymbol{J}_{\rm NS}(t=0)$ is the PNS's angular momentum at the time of core bounce (computed as the integral of the density, ρ, times the specific angular momentum, $\boldsymbol{r}\times\boldsymbol{v}$, over the volume of the PNS, i.e., for $r < R_{\rm NS}$), which is non-zero only for the case of rotating progenitor models (i.e., for our models m15 and m15e). The time-dependent net flux of angular momentum onto the PNS, $\dot{\boldsymbol{J}}_{\rm NS}$, through a sphere of radius R is given by

$$\dot{\boldsymbol{J}}_{\rm NS}(R,t) = -R^2 \oint_{r=R} \rho v_r\, \boldsymbol{r}\times\boldsymbol{v}\,{\rm d}\Omega\,, \tag{3.36}$$

which we evaluate at the time-dependent PNS radius, $R = R_{\rm NS}(t)$. From the magnitude of the PNS's angular-momentum vector at the end of our simulations, we can moreover estimate the NS's birth spin period, assuming rigid rotation, via

$$P_{\rm NS} = 2\pi \frac{I_{\rm NS}}{|\boldsymbol{J}_{\rm NS}|} \,. \tag{3.37}$$

Here, $I_{\rm NS}$ denotes the (cold) NS's moment of inertia, which we estimate through the fit formula of Lattimer & Schutz (2005, their Equation (12)),

$$I_{\rm NS} \simeq 0.237\, M_{\rm NS,g}\, R_{\rm NS}^2 \left[1 + 4.2\, \frac{M_{\rm NS,g}}{\rm M_\odot} \frac{\rm km}{R_{\rm NS}} + 90 \left(\frac{M_{\rm NS,g}}{\rm M_\odot} \frac{\rm km}{R_{\rm NS}} \right)^4 \right] . \tag{3.38}$$

In this formula, we employ the final gravitational NS mass, $M_{\rm NS,g} = M_{\rm NS,g}^{12}$, according to Lattimer & Prakash (2001; see our Equation (3.8)) using a final NS radius of $R_{\rm NS} = 12\,\rm km$ (see Table 3.4).

Figure 3.29 shows the PNS's angular momentum evolution, computed according to Equation (3.35), for our seven long-time 3D explosion models. The corresponding values at the end of our simulations are provided in Table 3.9, where we also list the angles between the NS spin and kick vectors and our estimates of the NS (birth) spin periods. The $15\,\rm M_\odot$ models, m15 and m15e, which were started from a fairly rapidly rotating pre-SN model (see Summa et al., 2018, and our discussion in Section 3.1), are dominated by the angular momentum inherited from the stellar progenitor. After around $\sim$0.5 s, when mass accretion onto the PNS has subsided, and the baryonic mass has essentially saturated to its final value, the PNS's angular momentum has reached a value of $\sim 4.4 \times 10^{48}\,\rm g\,cm^2\,s^{-1}$. This corresponds to a spin period of only $\sim$2 ms, which is certainly at the low end of the spin-period distribution observed for young pulsars (e.g., Kaspi & Helfand, 2002; Faucher-Giguère & Kaspi, 2006; Popov & Turolla, 2012).

As expected, the angular-momentum vector points almost precisely in the positive z-direction in the models m15 and m15e, which coincides with the rotation axis of the progenitor model. Interestingly, however, the flow pattern in the PNS's vicinity changes its orientation after $\sim$1 s in both models. During early times, the gas in the innermost volume within a few hundred kilometers from the PNS rotates counterclockwise in the equatorial (i.e., x-y) plane (Figures 3.30 and 3.31), i.e., concordant with the progenitor's rotation. In contrast, the direction of rotation reverts between 1 s and 2 s after bounce for both models, which is a consequence of the (stochastic) angular-momentum transport through postshock matter that falls back from relatively large radii into the gravitational well of the PNS (cf. Antoni & Quataert, 2022, 2023). Nevertheless, since only a negligible amount of this gas settles onto the PNS (see Figure 3.19), the change in the PNS's angular momentum through fallback accretion during this time window is far below 1%. For the m15 model, $J_{\rm NS}^z$ decreases slightly from $4.445 \times 10^{48}\,\rm g\,cm^2\,s^{-1}$ at $\sim$1.3 s after bounce to a value of $4.432 \times 10^{48}\,\rm g\,cm^2\,s^{-1}$ at $\sim$2.3 s, which is not visible in Figure 3.29 due to

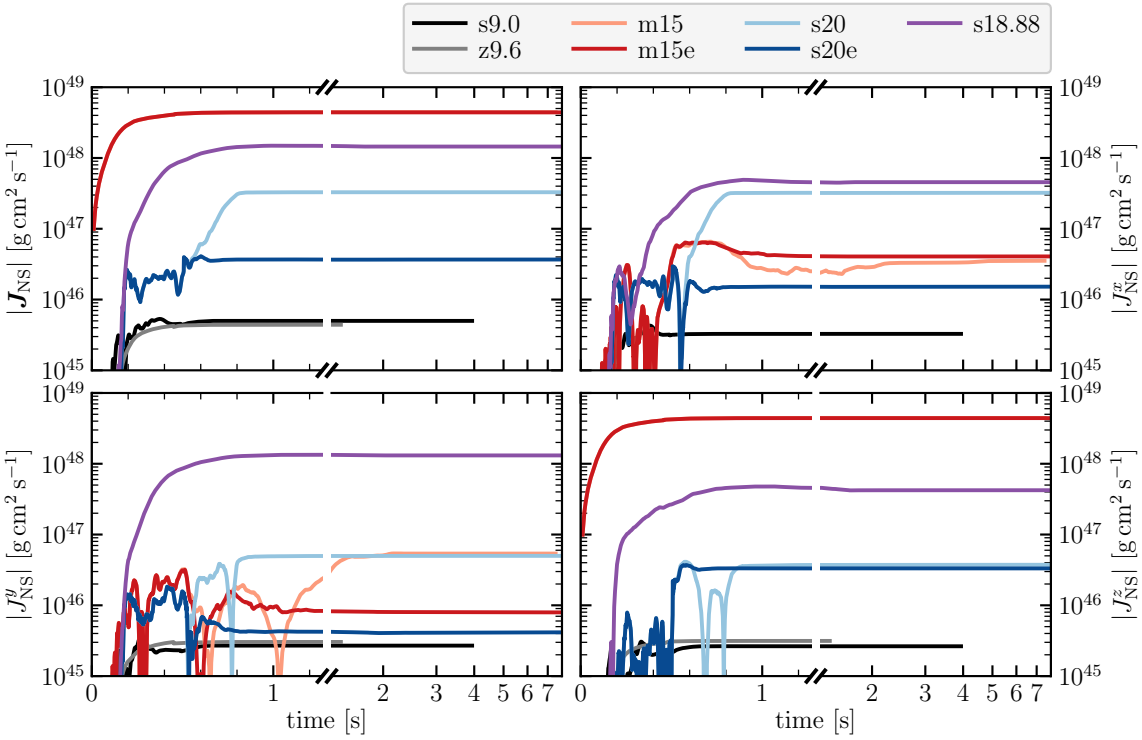

Figure 3.29.: Time evolution of the NS spin. From *top left* to *bottom right*, we show the magnitude of the NS's angular momentum vector, computed according to Equation (3.35), and the absolute values of its Cartesian (i.e., x, y, and z) components for all of our long-time CCSN models. Note that the time axes are split into two parts for better visibility, with a linear scale until ∼1.3 s and a logarithmic scale until ∼8 s.

the logarithmic scale. For model m15e, the reduction of $J^z_{\rm NS}$ (at approximately 1.2 s, i.e., associated with the changing flow morphology in Figure 3.31) is only around 1×10^{45} g cm^2 s^{-1} since almost no additional mass accumulates on the PNS in this model at such late times.

Quite remarkably, the models s18.88 and s20, which are both based on non-rotating progenitor models, still accomplish relatively short NS spin periods of ∼8 ms and ∼36 ms, respectively, solely by the spin-up through asymmetric accretion flows. In the case of model s18.88, this is connected to the accretion of matter with high specific angular momentum originating from the perturbed oxygen-burning shell of the pre-SN star (Yadav et al., 2020; Bollig et al., 2021; see also Müller et al., 2017). But also the model s20, which is based on a spherically symmetric progenitor, shows a substantial increase of the PNS's accreted angular momentum during the time interval between ∼0.5 s and ∼0.8 s after the bounce (even though to less extreme values than in model s18.88). During this time window, a massive accretion downdraft approaches the PNS in the s20 model from a direction between the negative y- and z-axes (Figure 3.17), hits the PNS not exactly head-on but slightly off-center (i.e., with a finite impact parameter), and thus causes a noticeable spin-up roughly around the

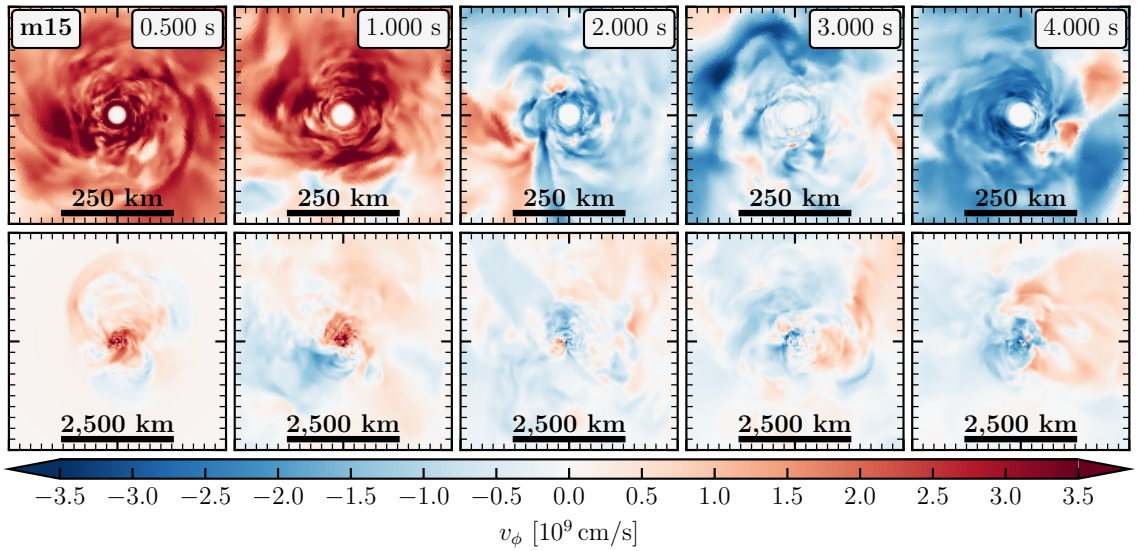

Figure 3.30.: Snapshots of model m15 showing the azimuthal fluid velocity in the equatorial plane (i.e., perpendicular to the rotation axis of the progenitor model) for length scales of 250 km (*top row*) and 2,500 km (*bottom row*). Blue (red) shading indicates clockwise (counterclockwise) rotation in the equatorial plane. The post-bounce times of the snapshots are displayed in each column's top panel.

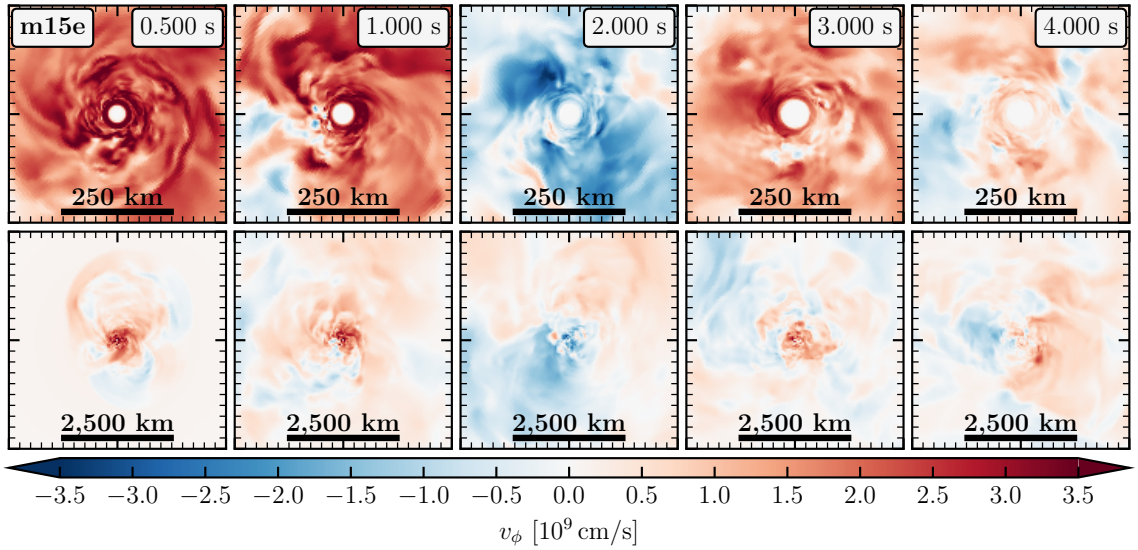

Figure 3.31.: Snapshots of model m15e showing the azimuthal fluid velocity in the equatorial plane (i.e., perpendicular to the rotation axis of the progenitor model) for scales of 250 km (*top row*) and 2,500 km (*bottom row*). Blue (red) shading indicates clockwise (counterclockwise) rotation in the equatorial plane. The post-bounce times of the snapshots are displayed in each column's top panel.

Table 3.9.: NS spins.

Model	$\lvert\boldsymbol{J}_{\rm NS}\rvert$	$J^x_{\rm NS}$	$J^y_{\rm NS}$	$J^z_{\rm NS}$	$\sphericalangle(\boldsymbol{J}_{\rm NS}, \boldsymbol{v}_{\rm NS})$	$M^{12}_{\rm NS,g}$	$I^{12}_{\rm NS}$	$P_{\rm NS}$
		$[10^{48}\,{\rm g\,cm^2\,s^{-1}}]$			[°]	[$\rm M_\odot$]	[$\rm M_\odot\,km^2$]	[ms]
s9.0	0.005	−0.003	−0.003	+0.003	135.4	1.233	60.67	1,518.3
z9.6	0.004	−0.001	−0.003	−0.003	140.7	1.230	60.43	1,714.6
m15	4.433	+0.035	−0.054	+4.432	80.4	1.437	74.64	2.1
m15e	4.414	+0.041	+0.008	+4.414	60.9	1.420	73.42	2.1
s18.88	1.451	−0.455	−1.311	−0.423	145.1	1.653	90.88	7.8
s20	0.328	+0.322	−0.050	+0.037	89.9	1.708	95.31	36.3
s20e	0.037	+0.015	+0.004	−0.033	48.7	1.680	93.02	316.1

Note: $\lvert\boldsymbol{J}_{\rm NS}\rvert$ is the magnitude of NS angular-momentum vector (Equation (3.35)); $J^i_{\rm NS}$ ($i = x, y, z$) are its Cartesian vector components; $\sphericalangle(\boldsymbol{J}_{\rm NS}, \boldsymbol{v}_{\rm NS})$ is the angle between the NS spin and kick vectors; $M^{12}_{\rm NS,g}$ and $I^{12}_{\rm NS}$ are the NS's gravitational mass and moment of inertia according to Equations (3.8) and (3.38), respectively, assuming a final NS radius of 12 km; $P_{\rm NS}$ is the NS spin period (Equation (3.37)). All quantities are evaluated at the end of our long-time simulations (i.e., at the times $t_{\rm f}$; see Table 3.5).

x-axis (see the steep rise of $J^x_{\rm NS}$ in Figure 3.29). The arrival of this accretion downflow coincides with an increase of the baryonic PNS mass in model s20 (compared to its more energetic counterpart s20e; Figure 3.10). Hence, the same asymmetric gas flow that causes the considerable hydrodynamic PNS kick acceleration in model s20 (Section 3.6.1) is responsible for the torques that spin up the PNS to high angular velocities. For this reason, the PNS's spin and kick vectors are nearly orthogonal in this model (see Spruit & Phinney, 1998). In contrast, model s20e yields a PNS with a spin period of more than 300 ms (i.e., almost a factor of ten longer than in the s20 model; Table 3.9) because the stronger neutrino heating in this model leads to higher initial expansion velocities and thus to less powerful matter downdrafts (see Section 3.3.3).

For the two low-mass models, s9.0 and z9.6, we find relatively long NS spin periods of more than 1.5 s at the end of our simulations (Table 3.9), in accordance with the small (hydrodynamic) kick velocities of these models. However, as has been discussed by, e.g., Stockinger et al. (2020) and Janka et al. (2022), late-time fallback can lead to a significant spin-up of the NSs, even for relatively small fallback masses of $\mathcal{O}(10^{-3})\,\rm M_\odot$, provided this matter gets accreted onto the NS and does not get re-ejected. Aside from such late-time accretion effects, the broad range of spin periods obtained in our models (between ∼2 ms and 1.7 s) agrees reasonably well with the spin-period distribution of observed young pulsars (e.g., Kaspi & Helfand, 2002; Faucher-Giguère & Kaspi, 2006; Popov & Turolla, 2012), although our sample of models is too small to draw statistically significant conclusions. On the other hand, all of our models exhibit fairly large angles of ∼49–145° between the NS's spin and kick vectors (see Table 3.9), in contrast to the (seemingly generic) spin-kick

alignment observed for young pulsars (e.g., Spruit & Phinney, 1998; Lai et al., 2001; Johnston et al., 2005; Ng & Romani, 2007; Noutsos et al., 2013). Such an alignment of the NS's spin and kick directions may instead be explained by (selective) late-time fallback accretion (Janka et al., 2022).

As we have mentioned briefly at the beginning of this section, angular-momentum conservation cannot be guaranteed in our numerical code for different reasons, which is why we evaluated the PNS's angular-momentum evolution via time-integration of the net angular-momentum flux onto the PNS (Equations (3.35) and (3.36)), instead of computing it through a volume integral of $\rho \boldsymbol{r} \times \boldsymbol{v}$. Firstly, standard finite-volume methods, as employed in Prometheus-Vertex (as well as in other modern CCSN codes), do generally not preserve angular momentum to machine precision (see, e.g., the discussion in Müller, 2020, Section 2.1.1). Secondly, we cannot exclude that the use of the Yin-Yang grid (Section 2.1.3) leads to some loss of angular momentum due to the numerical treatment of fluxes across the Yin-Yang grid interfaces (see the detailed discussion in Bollig et al., 2021, Appendix B). Lastly, using a spherically symmetric inner core, which is enlarged to radii of more than 10 km in our long-time Nemesis simulations (see Table 3.3), prevents us from following the transport of angular momentum inside the PNS.

Nevertheless, Bollig et al. (2021) pointed out that, from a more physical point of view, neutrino emission could extract angular momentum from the cooling PNS. Because neutrinos are strongly coupled to the stellar medium and thus advected with the gas flow at sufficiently high densities, some angular momentum can be transferred to neutrinos before they leak out. Future simulations with detailed multi-dimensional neutrino transport will need to investigate this possibility of a neutrino-mediated PNS spin-down more quantitatively. We should further note that the spin period of a remnant NS is affected by the (possibly significant) pre-collapse rotation of the stellar progenitor (e.g., Heger et al., 2005); see our models m15 and m15e (which are, admittedly, quite extreme cases with artificially enhanced rotation rates). Progenitor rotation could, for example, be important for stars in tight binary systems (see, e.g., Podsiadlowski et al., 2004; Langer, 2012). Nevertheless, numerous uncertainties in stellar evolution models, such as the angular-momentum transport by magnetic fields, are still complicating reliable predictions of pre-collapse core rotation rates. In the end, post-explosion spin-up by fallback accretion might dominate the measurable spin periods of young NSs (e.g., Chan et al., 2020; Stockinger et al., 2020; Janka et al., 2022).

4
Conclusions and Outlook

After decades of intense research, the neutrino-driven explosion mechanism (Colgate & White, 1966; Arnett, 1966; Bethe & Wilson, 1985) has meanwhile been established as the most promising and widely accepted paradigm for CCSNe. Modern 3D neutrino-hydrodynamics simulations by different groups have demonstrated successfully that CCSN explosions can be launched by neutrino-energy deposition, assisted by large-scale hydrodynamic instabilities. Nevertheless, most of these simulations were carried out only until *shortly after the onset of runaway shock expansion* (i.e., typically until less than a second after the core bounce) because of the high computational demands of detailed neutrino transport calculations. Such timescales are, however, much too short to achieve convergence of the characteristic explosion properties — such as the explosion energies, nucleosynthesis yields, and NS kick velocities and spin periods — that can be probed by astronomical observations. As we have shown, these explosion properties develop only over typical timescales of *several seconds* due to ongoing neutrino-energy deposition in persistent accretion downflows.

The main goal of this thesis was to close this gap between the early phase of shock revival and the fully developed explosion stage of neutrino-driven CCSN models. For this purpose, we developed a computationally efficient scheme (termed Nemesis) that accounts for the most crucial neutrino effects — namely, the exchange of energy and electron-lepton number with the stellar medium — in an approximate manner, thus replacing the expensive neutrino-transport calculations at late times when the explosion is well on its way, but the neutrino emission from the cooling PNS still has a significant dynamical impact. This novel approach allowed us, for the first time, to continue the explosion development for a set of fully self-consistent 3D CCSN models over timescales of many seconds until energy saturation was reached asymptotically.

In total, we carried out seven long-time 3D hydrodynamics simulations with our newly developed Nemesis scheme. These simulations smoothly extend the evolution of five previously computed, fully self-consistent explosion models that have all been run with the Prometheus-Vertex code (Rampp & Janka, 2002; Buras et al., 2006b), including full-fledged, energy-dependent neutrino transport: namely, two models around the low-mass end of CCSN progenitors with initial masses of ∼9–10 $M_\odot$ (s9.0 and z9.6; Melson et al., 2020, 2015b); one rotating, intermediate-mass 15 $M_\odot$ model (m15; Summa et al., 2018); and two rather massive models with ZAMS masses of ∼19–20 $M_\odot$ (s18.88 and s20; Bollig et al., 2021; Melson et al., 2015a).

The long-time evolution of the 15 $M_\odot$ and 20 $M_\odot$ models was simulated each in two slightly different realizations (models m15, m15e, s20, and s20e) to investigate the impact of the neutrino-heating effects on the explosion dynamics in a well-controlled setup. Our most important results, which have already been published partly in the papers by Stockinger et al. (2020) and Bollig et al. (2021), can be summarized as follows:

- **Explosion properties.** For the first time, we demonstrated that "ab initio" self-consistent 3D models of neutrino-driven CCSNe can reach explosion energies in the range of observed values. While our two low-mass models, s9.0 and z9.6, explode with energies below 0.1 B, in good agreement with, e.g., the Crab SN (Yang & Chevalier, 2015) or recently observed low-luminosity Type IIP SNe (e.g., Valerin et al., 2022; Kozyreva et al., 2022), our more massive 15–20 $M_\odot$ models obtain saturated explosion energies of ∼0.3–1.4 B, very well matching the broad distribution of values inferred from SN light-curve measurements (e.g., Kasen & Woosley, 2009; Pejcha & Prieto, 2015b; Martinez et al., 2022). Our results, therefore, provide strong support for the neutrino-driven explosion mechanism of CCSNe, alleviating earlier concerns that numerical models of neutrino-powered explosions might generally be under-energetic compared to observations (e.g., Papish et al., 2015; Murphy et al., 2019).

- We found that, in our massive-star models with high mass-accretion rates, the gradual rise of the explosion energy is fueled by the continuous neutrino heating and re-ejection of matter downdrafts that reach close to the neutrino-emitting PNS, even several seconds after the explosion onset. In contrast, our two low-mass models show a comparatively early saturation of the explosion energy (at relatively low values) due to the steeply declining density structures outside their iron cores and the correspondingly low mass-accretion rates.

- None of our long-time 3D models, apart from the fast-exploding low-mass model z9.6, develops a spherically symmetric neutrino-driven wind. In contrast to long-standing conjectures based on 1D explosion models, we thus conclude that (spherically symmetric) neutrino-driven winds do not seem to be generic features of CCSNe, except for the explosions of stars with sharply dropping density profiles near the very low-mass end of CCSN progenitors (also see, e.g., the 2D simulation results by Witt et al., 2021).

- **Nucleosynthesis properties.** Even though nuclear reactions are treated in a rather approximate manner in our simulations (see Sections 2.1.1 and 3.3.1) and we thus cannot yet draw firm conclusions, our models suggest that ejecta masses of radioactive ^{56}Ni on the order of $\sim 10^{-2}$–10^{-1} $M_\odot$ can be reached in neutrino-driven CCSN models, compatible with the typical values inferred from observations (e.g., Pejcha & Prieto, 2015b; Martinez et al., 2022). Our results, hence, do not support earlier claims of a "nickel mass problem" (e.g., Suwa et al., 2019; Sawada & Suwa, 2023).

- The electron fraction (i.e., the proton-to-baryon ratio) in the neutrino-driven outflows remains fairly close to a value of ∼0.5 in all of our models, except for the case of model z9.6 (see Figures A.8–A.13 in Appendix A).

- **Neutron-star properties.** Our CCSN explosion models yield NSs with baryonic masses ranging between ∼1.35 $M_\odot$ and ∼1.95 $M_\odot$, which corresponds to final gravitating masses of ∼1.24 $M_\odot$ to ∼1.69 $M_\odot$ (Table 3.4), roughly sampling the NS mass distribution as inferred from observations (e.g., Özel & Freire, 2016).

- During the explosions, the newborn NSs can receive sizable recoil kicks from anisotropic neutrino emission and through asymmetric ejection of matter. For our readily exploding low-mass models (s9.0 and z9.6), we find relatively moderate NS kick velocities below ∼100–200 $\mathrm{km\,s^{-1}}$, with a significant or even dominant contribution from anisotropic neutrino emission. In our massive-star models (m15, m15e, s18.88, s20, and s20e), which develop highly asymmetric explosions, the NS kicks are instead dominated by hydrodynamic effects (acting over timescales of several seconds). This is in marked contrast to the conclusions drawn recently by Coleman & Burrows (2022). Overall, we find NS kick velocities over a broad range of values, from below 100 $\mathrm{km\,s^{-1}}$ to more than 1000 $\mathrm{km\,s^{-1}}$, in very good agreement with the kick distribution as inferred from observations (e.g., Hobbs et al., 2005; Faucher-Giguère & Kaspi, 2006).

- The remnant NSs not only get imparted a recoil kick but they can also be spun up to high angular velocities during the explosion. Our models m15 and m15e leave behind NSs with short spin periods of only ∼2 ms, which is not astonishing considering that these models were started from a fast-rotating pre-SN star (Summa et al., 2018). Quite remarkably, however, the models s18.88 and s20, which are both based on non-rotating progenitors, nonetheless yield relatively short NS spin periods of ∼8 ms and ∼36 ms, respectively, which is a consequence of the (stochastic) accretion of angular momentum associated with asymmetric matter downdrafts (e.g., Spruit & Phinney, 1998; Antoni & Quataert, 2022). In cases with less violent accretion flows, this spin-up mechanism is inefficient, such that much longer spin periods of several hundred milliseconds up to more than a second are obtained. The broad range of NS spin periods found in our models (between ∼2 ms and 1.7 s) agrees well with the spin-period distribution of observed young pulsars (e.g., Kaspi & Helfand, 2002; Faucher-Giguère & Kaspi, 2006; Popov & Turolla, 2012). Nevertheless, none of our models reproduces the seemingly generic spin-kick alignment of observed NSs (e.g., Johnston et al., 2005; Ng & Romani, 2007; albeit see Janka et al., 2022).

Our set of long-time 3D CCSN models presented in this thesis marks only one step forward towards an increasingly more complete theoretical picture of neutrino-driven explosions. Undoubtedly, full-physics long-time 3D simulations with detailed energy-dependent neutrino transport and a more sophisticated treatment of nuclear

burning are desirable and will be needed to crosscheck our findings, eventually. With the increasing power of next-generation supercomputers, such fully self-consistent long-time 3D simulations (over timescales of several seconds) may become feasible in the years to come. In a first step towards more realism, addressing our approximate treatment of nuclear burning, we plan to re-evaluate the nucleosynthesis yields of our explosion models using a detailed post-processing analysis with tracer particles and an extensive nuclear-reaction network (see, e.g., Wanajo et al., 2018; Sieverding et al., 2020, 2023). Moreover, to better account for the diversity of pre-SN stellar structures (see Section 3.1), we plan to enlarge our set of self-consistent 3D CCSN models in the future, also considering stellar binary progenitors (e.g., Podsiadlowski et al., 2004; Schneider et al., 2015, 2021; Woosley, 2019; Laplace et al., 2020, 2021).

While the focus of this thesis was on the phase of energy saturation *during the first seconds* of a CCSN explosion (when the neutrino emission from the cooling PNS still plays a dynamically important role), in a follow-up project, we plan to continue the evolution of our models until and beyond shock breakout from the stellar surface, *hours to even days after the explosion onset* (as already done for our two low-mass models, s9.0 and z9.6; see Stockinger et al., 2020). Full-3D hydrodynamics simulations over such long evolution times can be achieved when the central volume containing the NS is excised from the computational domain and replaced by an inner grid boundary (see, e.g., Wongwathanarat et al., 2015; Müller et al., 2018; Stockinger et al., 2020; Sandoval et al., 2021). Only at such late times, the SN ejecta approach homologous (i.e., self-similar) expansion and the explosion is beginning to develop its shape that can be probed directly through SN light-curve and spectral diagnostics (e.g., Dessart & Hillier, 2011; Jerkstrand et al., 2014; Utrobin et al., 2019; Kozyreva et al., 2022; Barker et al., 2022). Such very-long-time models will further allow us to investigate the effects of late-time fallback accretion, which can have significant implications for the measurable properties of the remnant NSs (see, e.g., Stockinger et al., 2020; Janka et al., 2022). Moreover, our models can then serve as starting points for continuation runs to even later times, into the SN remnant stage (e.g., Gabler et al., 2021).

A

Supplementary Figures

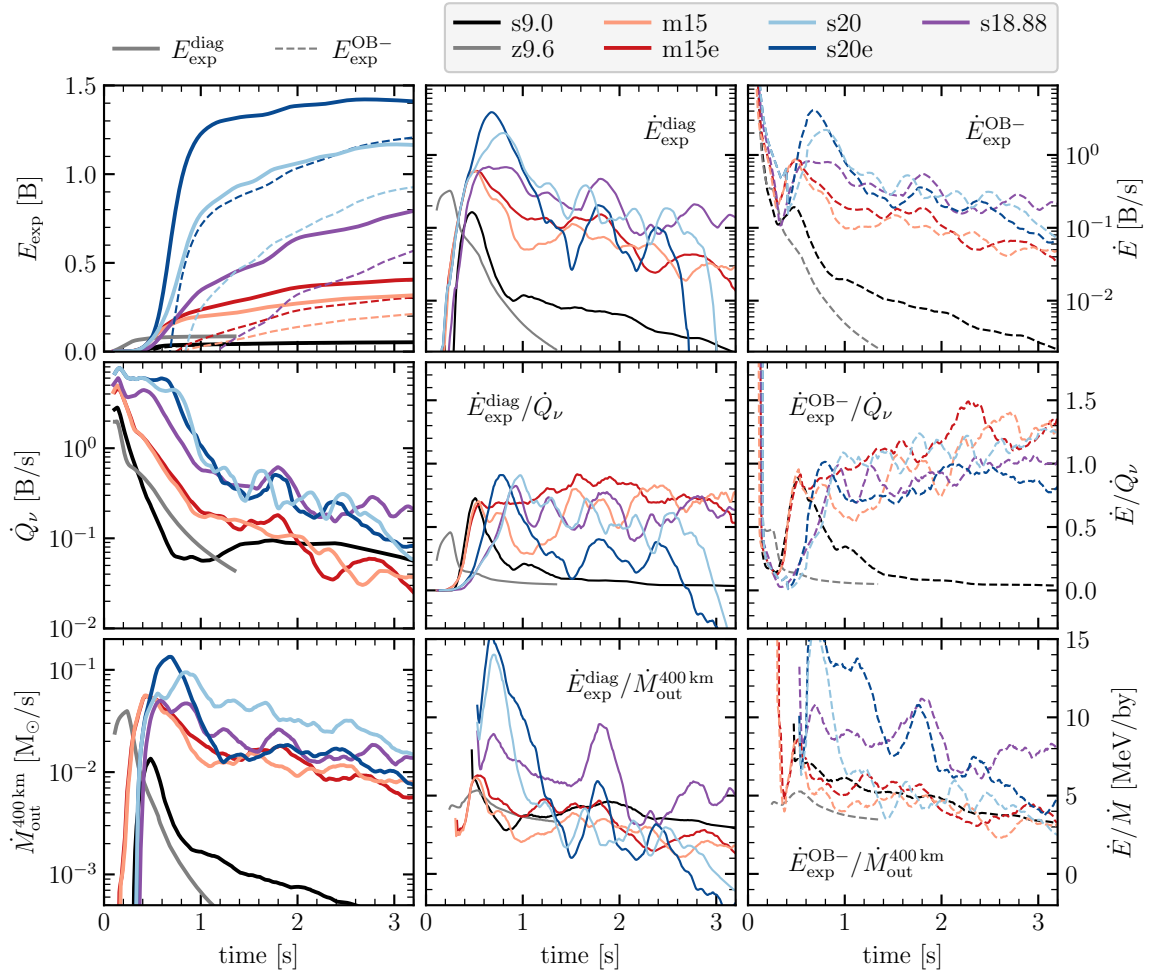

Figure A.1.: Comparison of the growth rate of the explosion energy (diagnostic and without overburden; *top row*) to the volume-integrated net neutrino-heating rate in the gain layer ($\dot{Q}_\nu$; *middle row*). *Bottom row*: Ratio of the explosion energy (diagnostic and without overburden) and the mass-outflow rate at 400 km (cf. Figure 3.19). The curves are smoothed by running averages of 0.2 s. The whole long-time evolution of the models (until the end of our simulations) is shown in Figure 3.20.

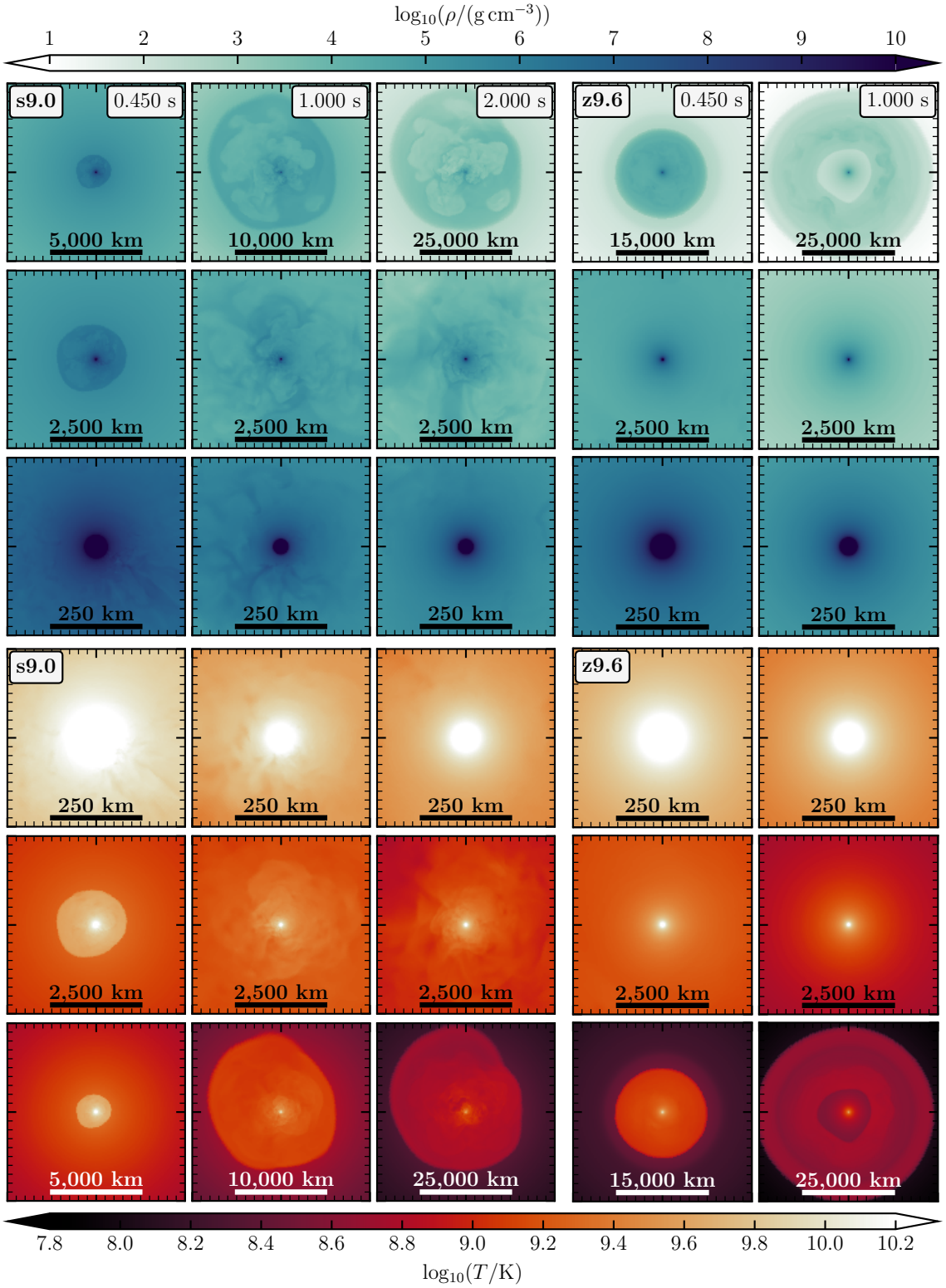

Figure A.2.: Exemplary snapshots of the models s9.0 (*left*) and z9.6 (*right*), showing cross-sectional cuts of the logarithmic density (*upper panels*) and the logarithmic temperature (*lower panels*) in the x-z plane. Note the varying length scales. The post-bounce times of the snapshots are indicated in each column's top panel.

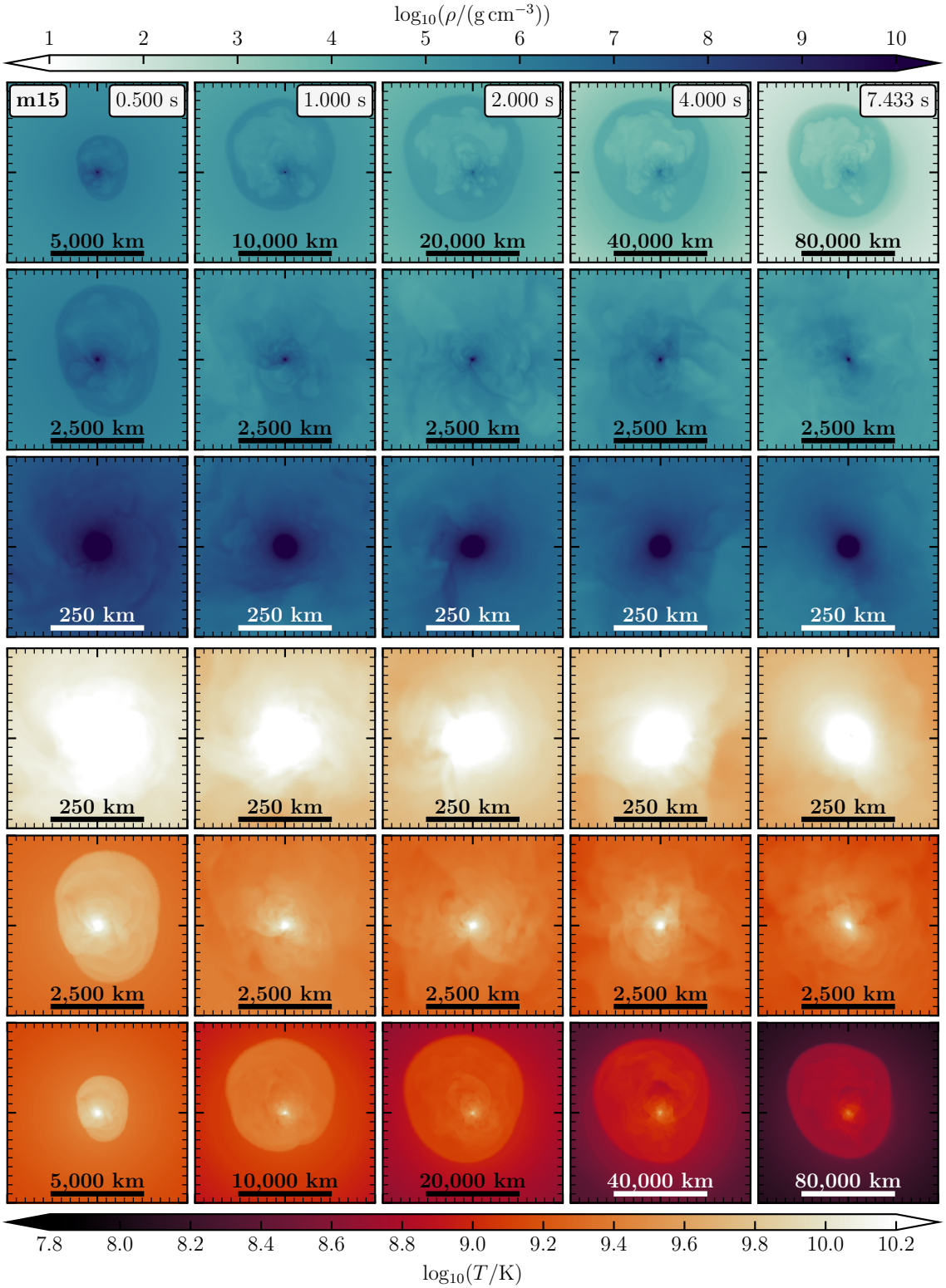

Figure A.3.: Snapshots of model m15 showing cross-sectional cuts of the logarithmic density (*upper panels*) and the logarithmic temperature (*lower panels*) in the x-y plane. Note the varying length scales. The post-bounce times of the snapshots are indicated in each column's top panel.

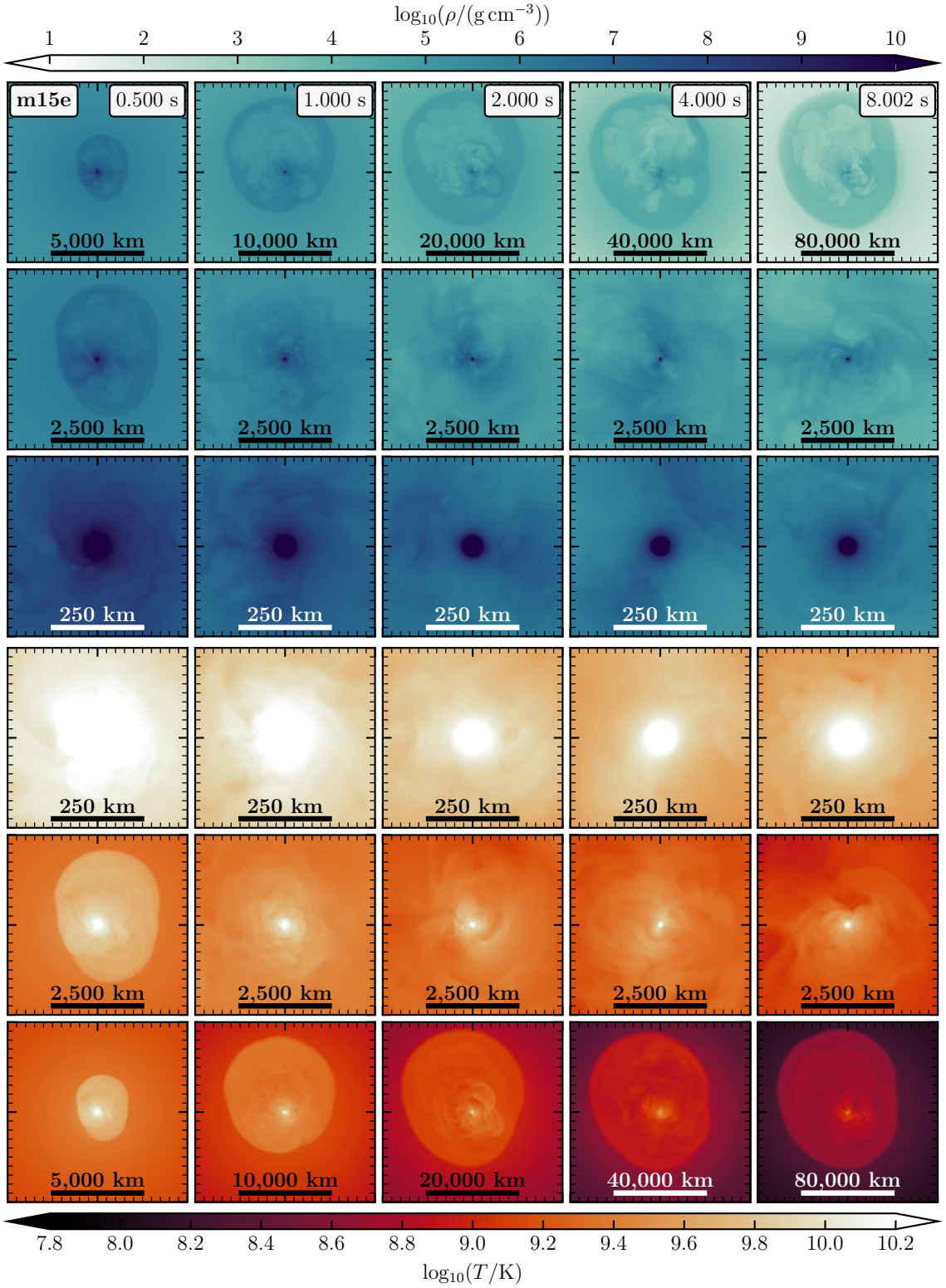

Figure A.4.: Snapshots of model m15e showing cross-sectional cuts of the logarithmic density (*upper panels*) and the logarithmic temperature (*lower panels*) in the x-y plane. Note the varying length scales. The post-bounce times of the snapshots are indicated in each column's top panel.

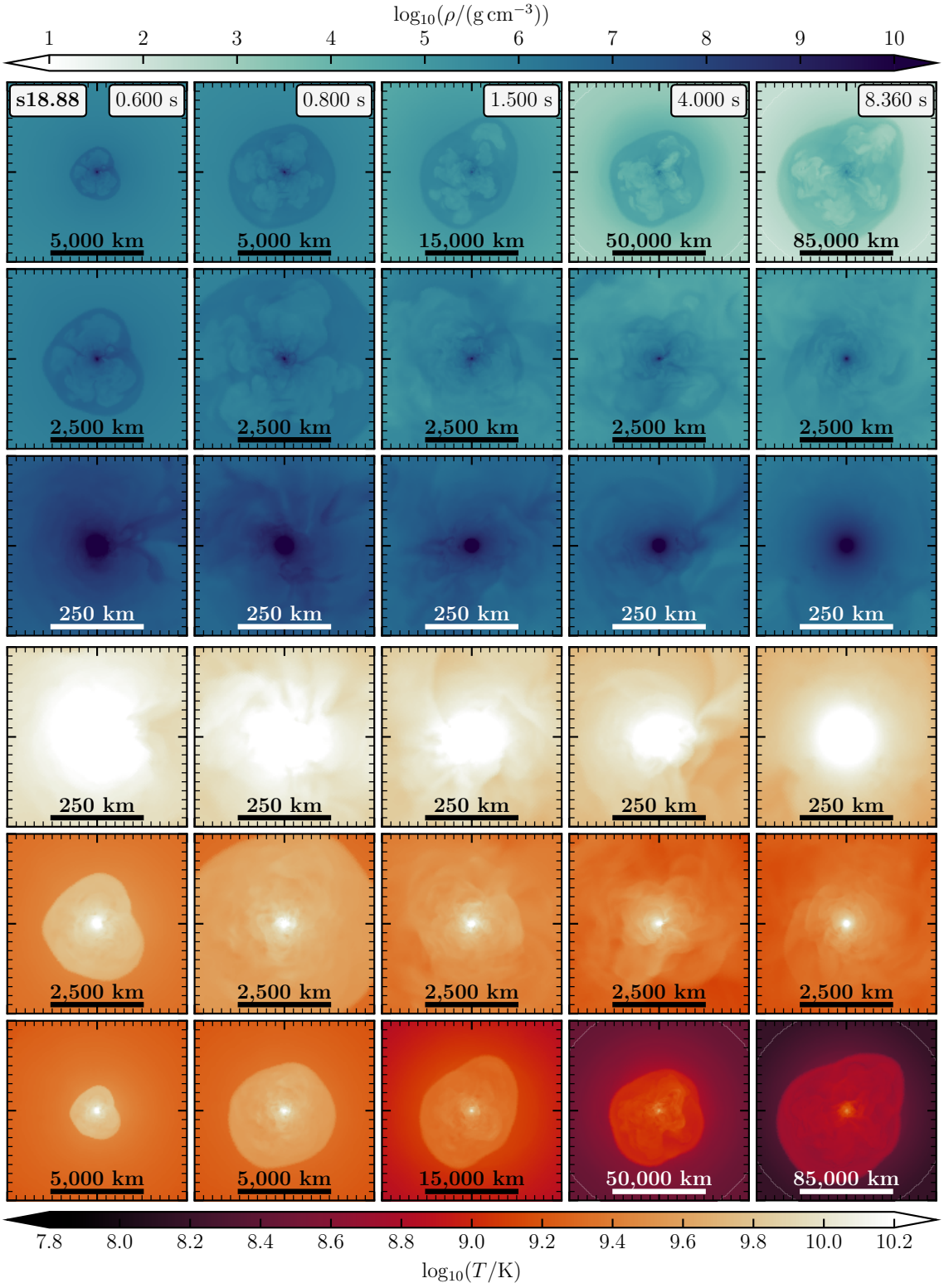

Figure A.5.: Snapshots of model s18.88 showing cross-sectional cuts of the logarithmic density (*upper panels*) and the logarithmic temperature (*lower panels*) in the x-y plane. Note the varying length scales. The post-bounce times of the snapshots are indicated in each column's top panel.

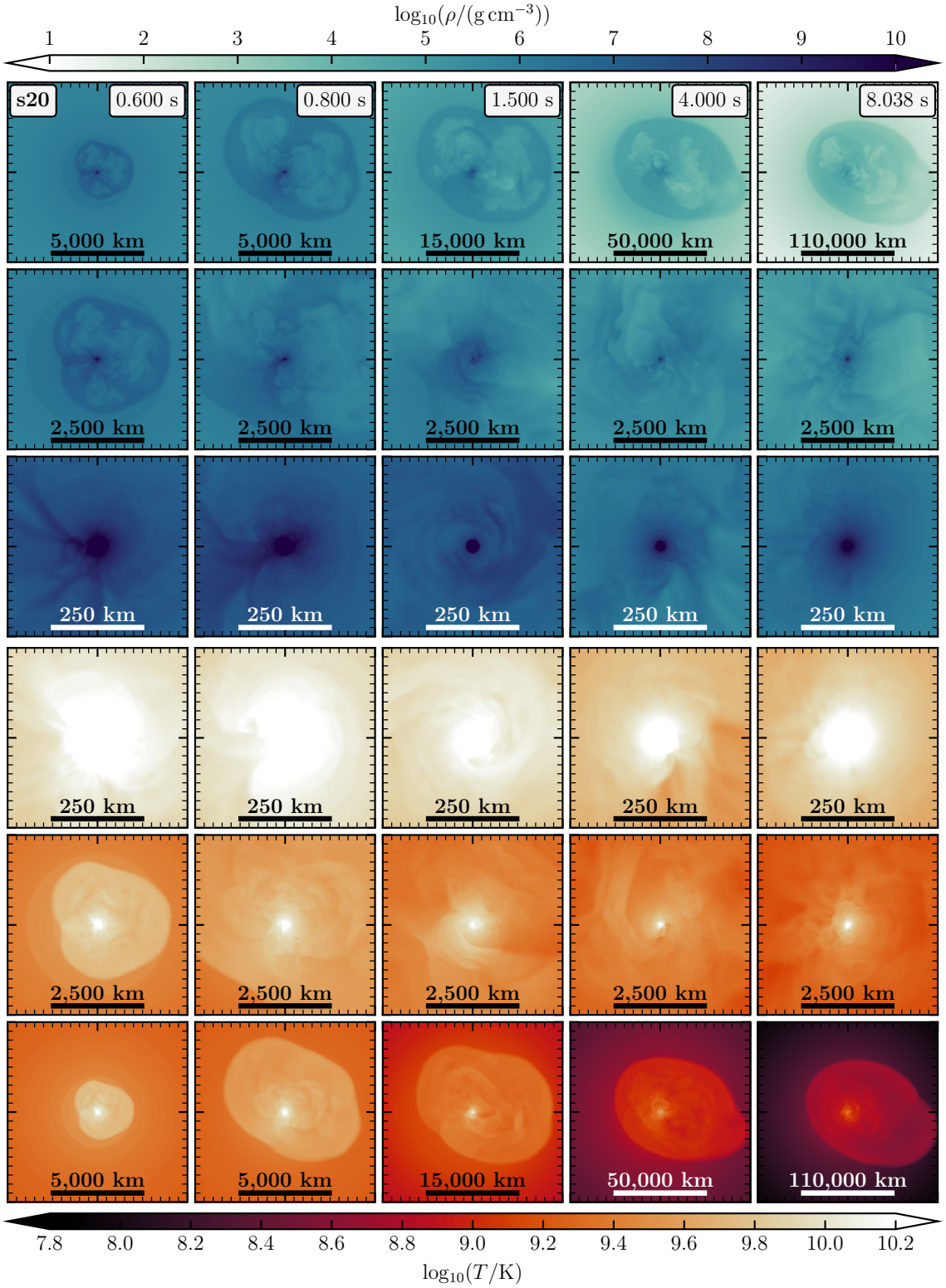

Figure A.6.: Snapshots of model s20 showing cross-sectional cuts of the logarithmic density (*upper panels*) and the logarithmic temperature (*lower panels*) in the z-y plane. Note the varying length scales. The post-bounce times of the snapshots are indicated in each column's top panel.

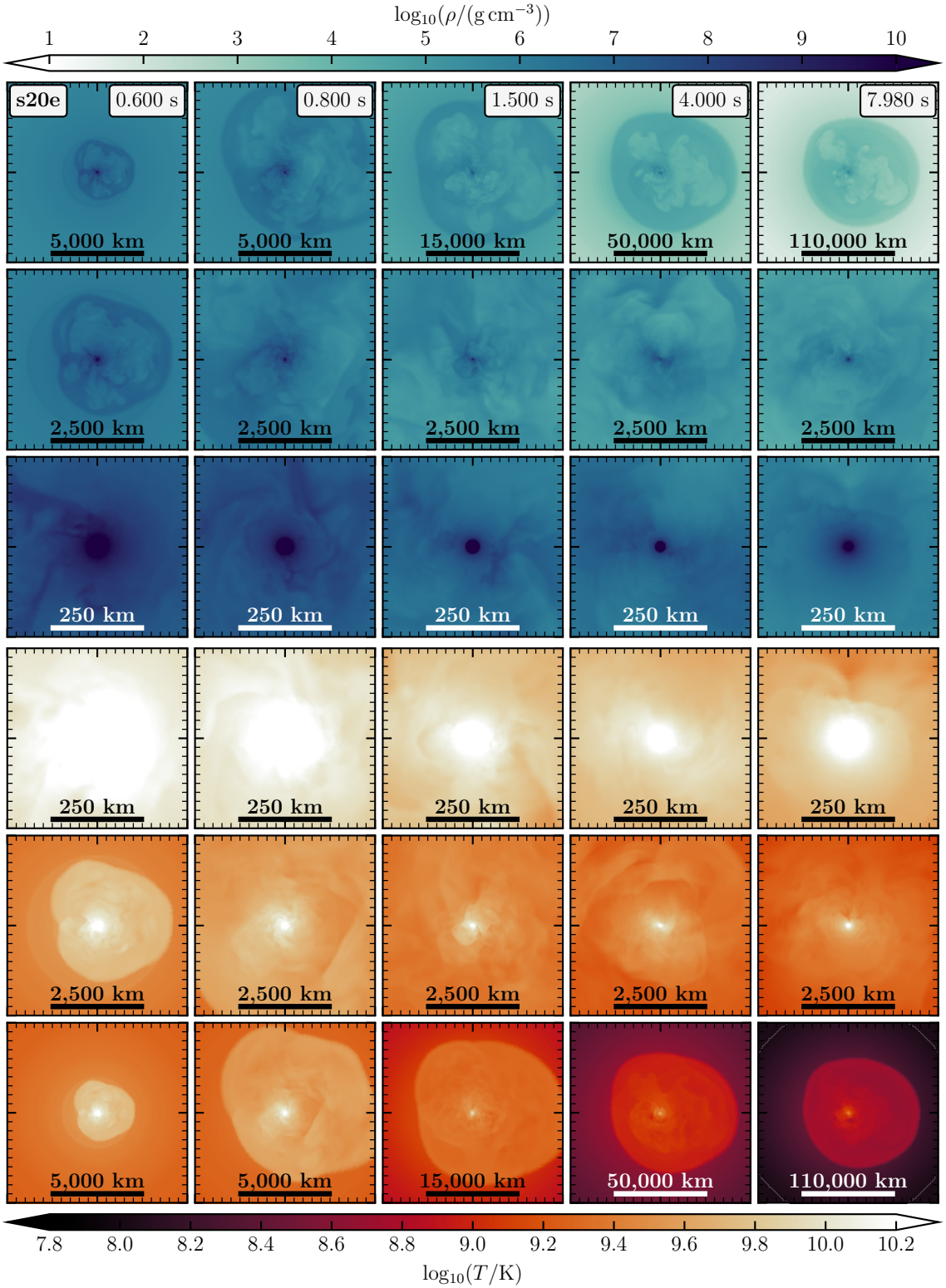

Figure A.7.: Snapshots of model s20e showing cross-sectional cuts of the logarithmic density (*upper panels*) and the logarithmic temperature (*lower panels*) in the z-y plane. Note the varying length scales. The post-bounce times of the snapshots are indicated in each column's top panel.

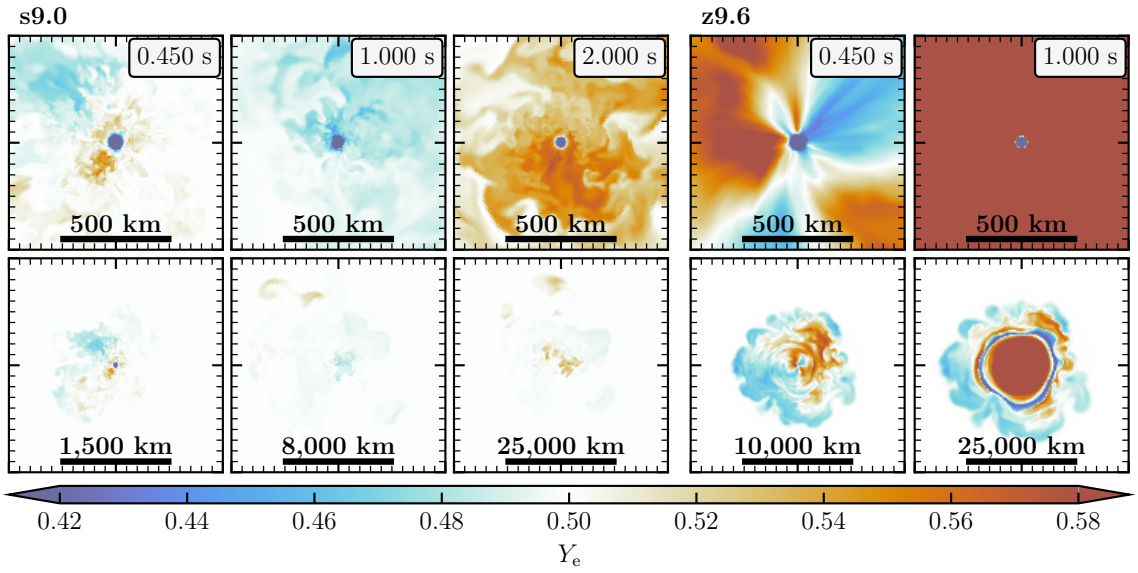

Figure A.8.: Exemplary snapshots of the models s9.0 (*left*) and z9.6 (*right*), showing cross-sectional cuts of the electron fraction Y_e (i.e., the proton-to-baryon ratio) in the x-z plane. The length scales are indicated by scale bars; the post-bounce times of the snapshots are given in each column's top panel. Notice the prominent hemispheric asymmetry of the Y_e distribution in the model z9.6 at 0.45 s, which is an imprint of the LESA, developing during the evolution with full neutrino transport (for more detail, see Section 4.4 of Stockinger et al., 2020). The neutron-rich conditions ($Y_e < 0.5$) in the fastest neutrino-driven outflows of this model are a consequence of the short time span for neutrino-processing (i.e., ν_e absorption) related to the high expansion velocities (see Section 4.4 and Figure 9 of Stockinger et al., 2020). In the s9.0 model, Y_e stays considerably closer to values around 0.5 due to slower expansion velocities and, thus, longer neutrino-processing timescales. The high values of $Y_e \gtrsim 0.6$ in the neutrino-driven wind of model z9.6 are probably an artifact of the too simplistic treatment of the Y_e source term in the old version of our Nemesis scheme used for this model (version v1.1.0; see Section 3.3.1). Nevertheless, the densities (and thus ejecta masses) in this region are already quite low (see Figure A.2).

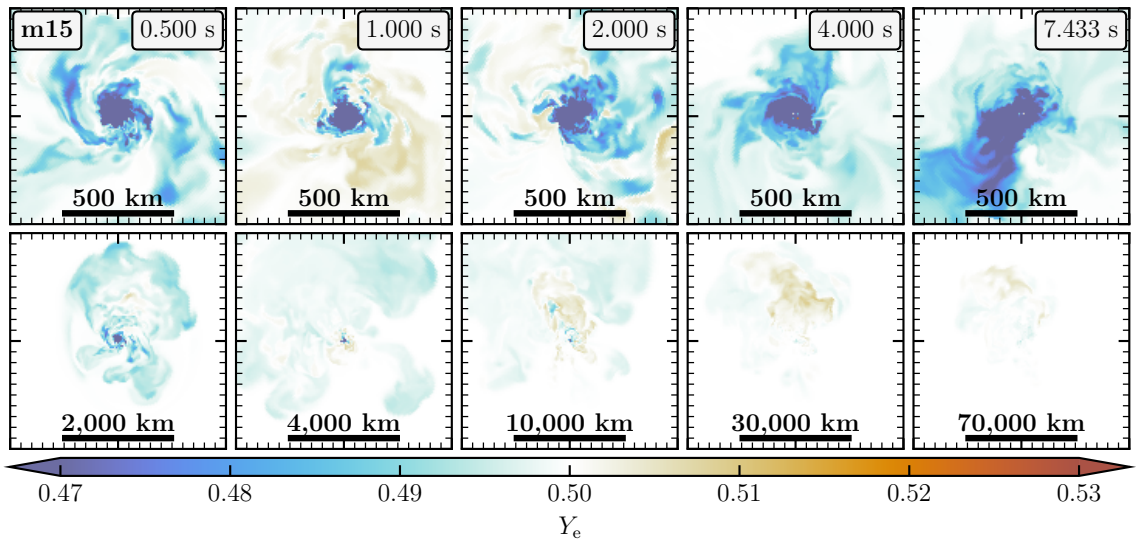

Figure A.9.: Snapshots of model m15 showing cross-sectional cuts of the electron fraction Y_e (i.e., the proton-to-baryon ratio) in the x-y plane. Note the varying length scales. The post-bounce times of the snapshots are indicated in each column's top panel. The slightly neutron-rich conditions ($Y_e \lesssim 0.5$) in the fast-moving ejecta at early times are probably a consequence of the short timescales for neutrino processing (i.e., ν_e absorption) related to the early shock revival in this model (aided by the spiral SASI; see Section 3.2.2), i.e., similarly as in the case of model z9.6 (though less extreme; cf. Figure A.8). The low values of Y_e at late times are possibly an artifact related to the halted contraction of the gain radius in the earliest version of our NEMESIS scheme as used for this model as well as for the slightly more energetic model m15e (version v1.0; see Section 3.3.1 and Figure 3.10), which goes hand in hand with a probably underestimated net neutrino-heating rate (see Section 3.4).

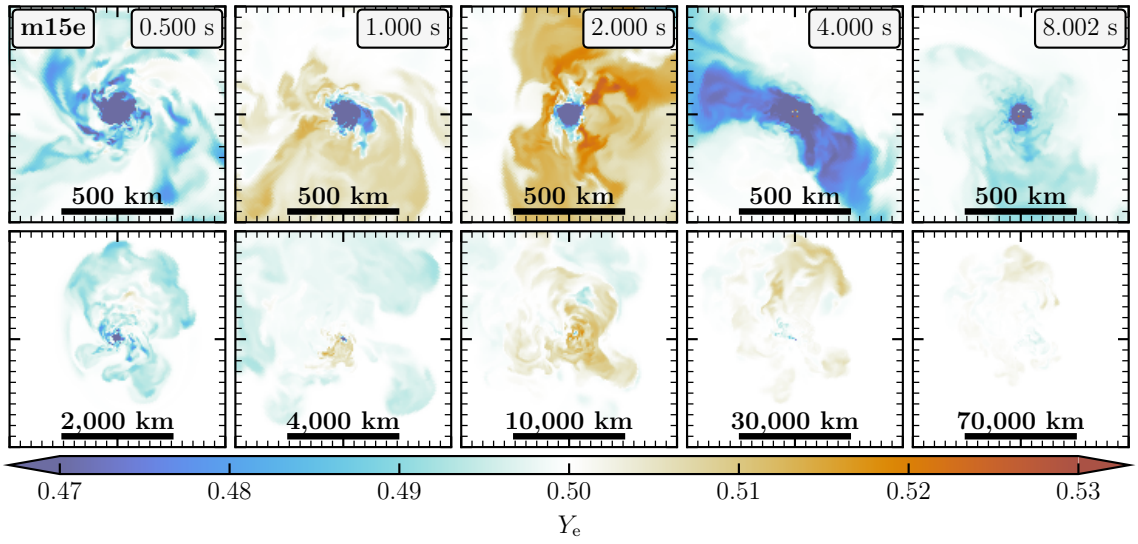

Figure A.10.: Snapshots of model m15e showing cross-sectional cuts of the electron fraction Y_e (i.e., the proton-to-baryon ratio) in the x-y plane. Note the varying length scales. The post-bounce times of the snapshots are indicated in each column's top panel. For a brief discussion of the slightly neutron-rich conditions, shortly after explosion onset (first snapshot) and at late times (last two snapshots), we refer to the caption of Figure A.9.

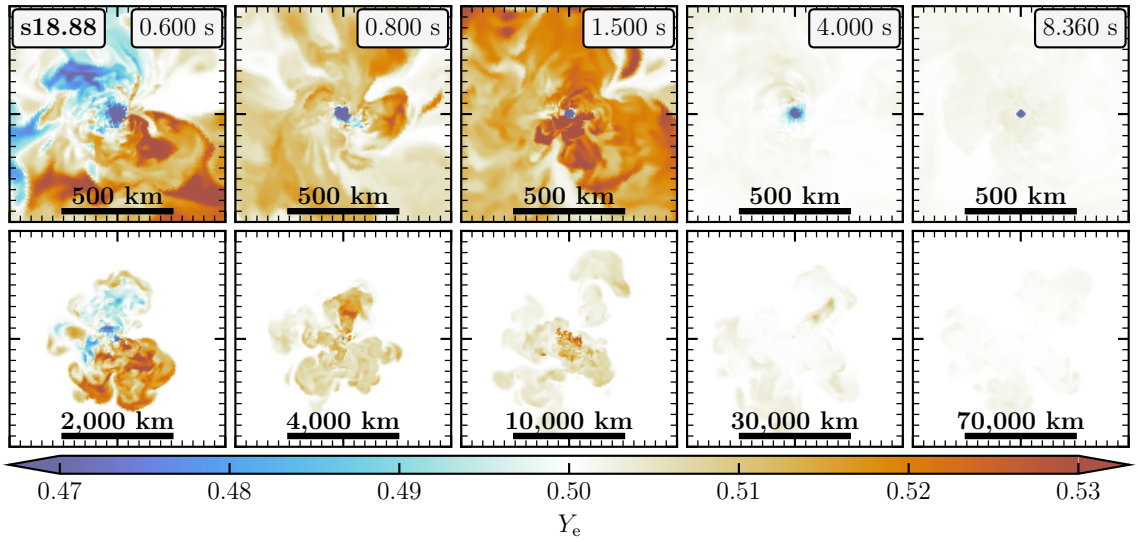

Figure A.11.: Snapshots of model s18.88 showing cross-sectional cuts of the electron fraction Y_e (i.e., the proton-to-baryon ratio) in the x-y plane. Note the varying length scales. The post-bounce times of the snapshots are indicated in each column's top panel. The snapshot at 0.6 s shows a hemispheric asymmetry of the Y_e distribution, which is most likely an imprint of the LESA (see Bollig et al., 2021, Appendix C).

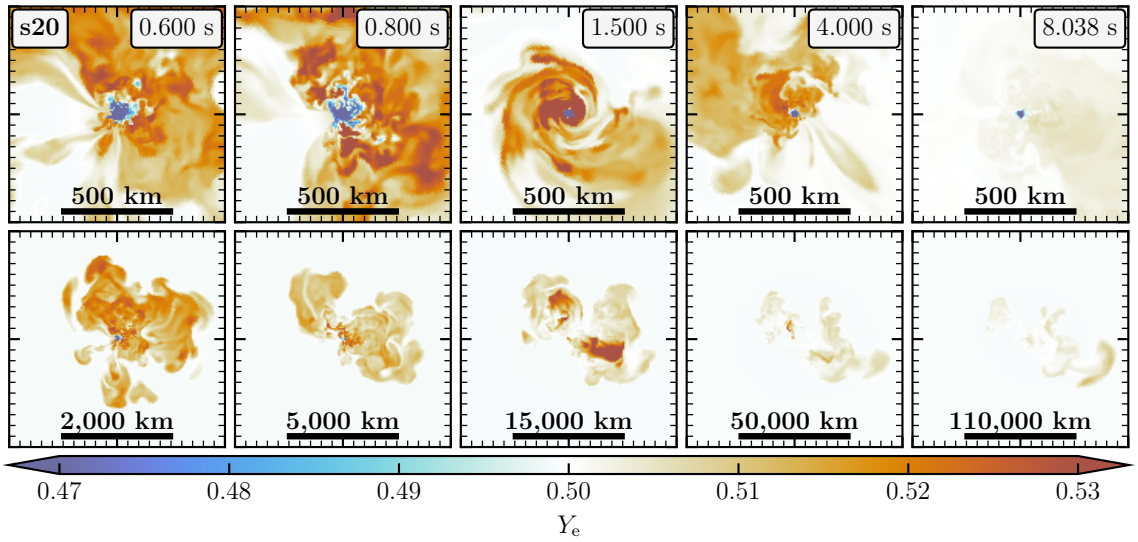

Figure A.12.: Snapshots of model s20 showing cross-sectional cuts of the electron fraction Y_e (i.e., the proton-to-baryon ratio) in the z-y plane. Note the varying length scales. The post-bounce times of the snapshots are indicated in each column's top panel. The neutrino-driven outflows exhibit slightly proton-rich (i.e., $Y_e \gtrsim 0.5$) conditions during the entire long-time evolution of this model, similarly as in the model s18.88.

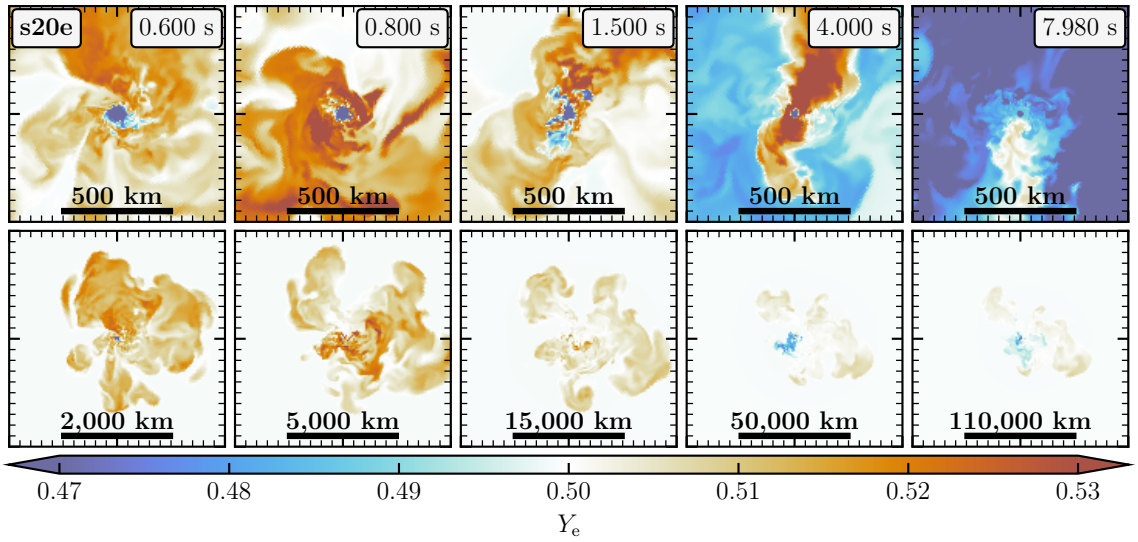

Figure A.13.: Snapshots of model s20e showing cross-sectional cuts of the electron fraction Y_e (i.e., the proton-to-baryon ratio) in the z-y plane. Note the varying length scales. The post-bounce times of the snapshots are indicated in each column's top panel. As in the models s18.88 and s20, Y_e remains relatively close to (or slightly above) a value of 0.5 during most of the long-time evolution. Yet, some of the neutrino-driven outflows at late times show a weak neutron excess (i.e., $Y_e \lesssim 0.5$).

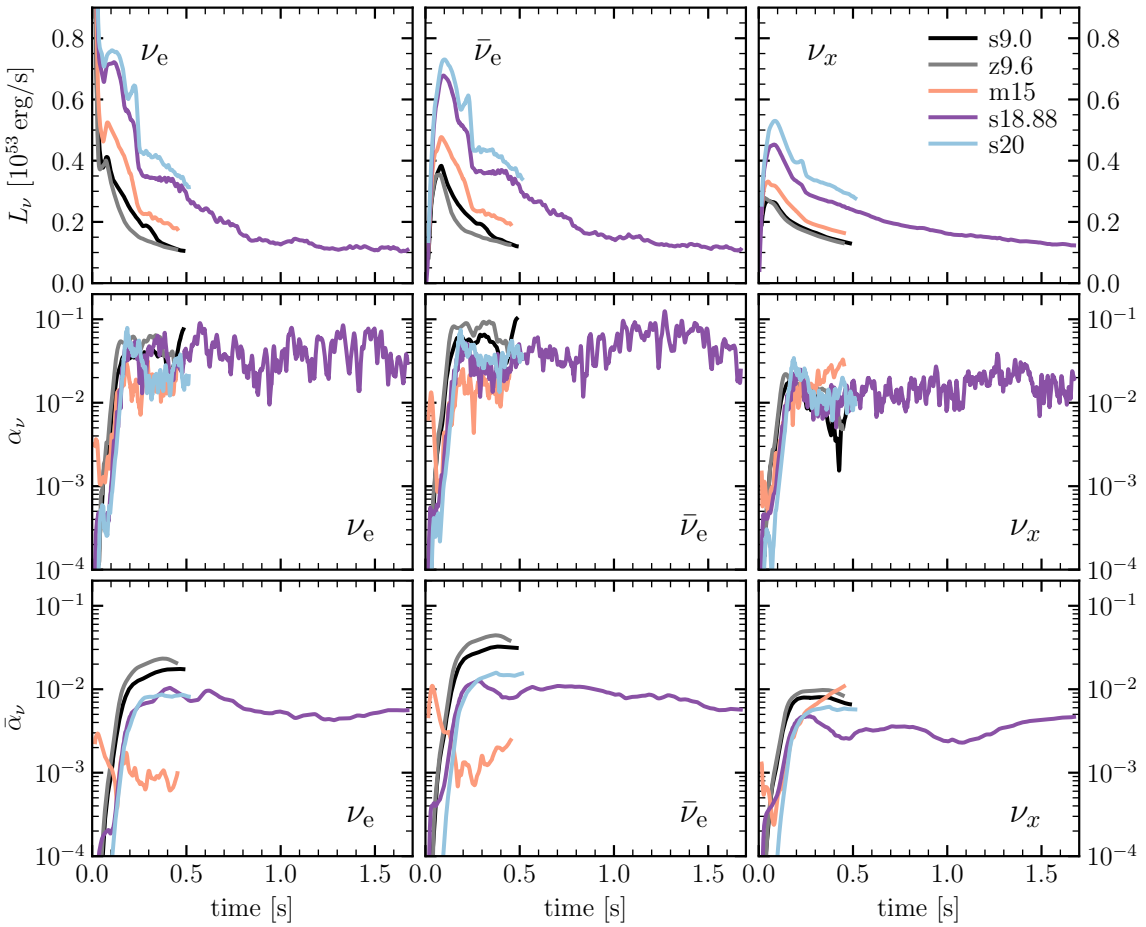

Figure A.14.: Time evolution of the neutrino luminosity (*top*), instantaneous neutrino-anisotropy parameter (*center*), and time-integrated neutrino-anisotropy parameter (*bottom*) of electron neutrinos, electron antineutrinos, and a representative species of heavy-lepton (anti)neutrinos (from *left* to *right*), evaluated at a radius of 400 km for a lab-frame observer at large distance (i.e., gravitationally redshifted to infinity). This figure shows the same quantities as Figure 3.24 but for the entire evolution period with full neutrino transport.

B
List of Abbreviations

1D	one-dimensional (spherically symmetric)
2D	two-dimensional (axisymmetric)
3D	three-dimensional
CCSN(e)	core-collapse supernova(e)
CFL	Courant-Friedrichs-Lewy
CMA	consistent multifluid advection
DSNB	diffuse supernova neutrino background
ECSN(e)	electron-capture supernova(e)
EoS(s)	equation(s) of state
HPC	high-performance computing
LESA	lepton-number emission self-sustained asymmetry
LRZ	Leibniz Supercomputing Centre
LS220	high-density EoS by Lattimer & Swesty (1991) with incompressibility modulus of $K = 220\,\mathrm{MeV}$
MPI	Message Passing Interface
NICER	Neutron star Interior Composition Explorer
NS(s)	neutron star(s)
NSE	nuclear statistical equilibrium
OpenMP	Open Multi-Processing
PNS(s)	proto-neutron star(s)
PPM	piecewise parabolic method
SASI	standing accretion shock instability
SMR	static mesh refinement
SN(e)	supernova(e)
SP	spherical polar
SPH	smoothed-particle hydrodynamics
TOV	Tolman-Oppenheimer-Volkoff
WD(s)	white dwarf(s)
YY	Yin-Yang
ZAMS	zero-age main sequence

C
List of Publications

2020/03 Melson, T., **Kresse, D.**, & Janka, H.-T.: Resolution Study for Three-dimensional Supernova Simulations with the Prometheus-Vertex Code; ApJ, 891, 27 (Melson et al., 2020)

2020/06 Walk, L., Tamborra, I., Janka, H.-T., Summa, A., & **Kresse, D.**: Neutrino Emission Characteristics of Black Hole Formation in Three-dimensional Simulations of Stellar Collapse; PRD, 101, 123013 (Walk et al., 2020)

2020/08 Stockinger, G., Janka, H.-T., **Kresse, D.**, Melson, T., et al.: Three-dimensional Models of Core-collapse Supernovae from Low-mass Progenitors with Implications for Crab; MNRAS, 496, 2039 (Stockinger et al., 2020)

2021/01 Sawatzki, J., Wurm, M., & **Kresse, D.**: Detecting the Diffuse Supernova Neutrino Background in the Future Water-based Liquid Scintillator Detector Theia; PRD, 103, 023021 (Sawatzki et al., 2021)

2021/03 **Kresse, D.**, Ertl, T., & Janka, H.-T.: Stellar Collapse Diversity and the Diffuse Supernova Neutrino Background; ApJ, 909, 169 (Kresse et al., 2021)

2021/07 Bollig, R., Yadav, N., **Kresse, D.**, Janka, H.-T., et al.: Self-consistent 3D Supernova Models From -7 Minutes to +7 Seconds: A 1-bethe Explosion of a 19 $M_\odot$ Progenitor; ApJ, 915, 28 (Bollig et al., 2021)

2022/08 Kozyreva, A., Janka, H.-T., **Kresse, D.**, Taubenberger, S., & Baklanov, P.: Low-luminosity Type IIP Supernovae: SN 2005cs and SN 2020cxd as Very Low-energy Iron Core-collapse Explosions; MNRAS, 514, 4173 (Kozyreva et al., 2022)

Software

- Prometheus-Vertex (Fryxell et al., 1989; Keil, 1997; Kifonidis et al., 2003; Rampp & Janka, 2002; Buras et al., 2006b; Marek et al., 2006; Müller et al., 2010; Hanke, 2014; Hüdepohl, 2014; Melson, 2016; Bollig, 2018)
- `NumPy` (Harris et al., 2020); `SciPy` (Virtanen et al., 2020); `IPython` (Perez & Granger, 2007); `Matplotlib` (Hunter, 2007); `CMasher` (van der Velden, 2020); `cubehelix` (Green, 2011)[38]
- `VisIt` (Childs et al., 2012)
- `bibmanager` (Cubillos, 2020)[39]

[38] https://github.com/jradavenport/cubehelix
[39] https://bibmanager.readthedocs.io/en/latest/index.html

Bibliography

Abbasi, R., Abdou, Y., Abu-Zayyad, T., Ackermann, M., et al., 2011. IceCube sensitivity for low-energy neutrinos from nearby supernovae. *A&A*, 535:A109, doi: 10.1051/0004-6361/201117810.

Abbott, B. P., Abbott, R., Abbott, T. D., Acernese, F., et al., 2017. GW170817: Observation of Gravitational Waves from a Binary Neutron Star Inspiral. *Phys. Rev. Lett.*, 119 (16):161101, doi: 10.1103/PhysRevLett.119.161101.

Abbott, B. P., Abbott, R., Abbott, T. D., Abraham, S., et al., 2020. Prospects for observing and localizing gravitational-wave transients with Advanced LIGO, Advanced Virgo and KAGRA. *Living Reviews in Relativity*, 23(1):3, doi: 10.1007/s41114-020-00026-9.

Abdikamalov, E., Ott, C. D., Radice, D., Roberts, L. F., et al., 2015. Neutrino-driven Turbulent Convection and Standing Accretion Shock Instability in Three-dimensional Core-collapse Supernovae. *ApJ*, 808(1):70, doi: 10.1088/0004-637X/808/1/70.

Agafonova, N. Y., Aglietta, M., Antonioli, P., Ashikhmin, V. V., et al., 2015. Implication for the Core-collapse Supernova Rate from 21 Years of Data of the Large Volume Detector. *ApJ*, 802(1):47, doi: 10.1088/0004-637X/802/1/47.

Airapetian, A., Akopov, N., Akopov, Z., Andrus, A., et al., 2007. Precise determination of the spin structure function g_1 of the proton, deuteron, and neutron. *Phys. Rev. D*, 75 (1):012007, doi: 10.1103/PhysRevD.75.012007.

Aker, M., Altenmüller, K., Arenz, M., Babutzka, M., et al., 2019. Improved Upper Limit on the Neutrino Mass from a Direct Kinematic Method by KATRIN. *Phys. Rev. Lett.*, 123(22):221802, doi: 10.1103/PhysRevLett.123.221802.

Alexeyev, E. N., Alexeyeva, L. N., Krivosheina, I. V., & Volchenko, V. I., 1988. Detection of the neutrino signal from SN 1987A in the LMC using the INR Baksan underground scintillation telescope. *Physics Letters B*, 205(2-3):209–214, doi: 10.1016/0370-2693(88)91651-6.

Almanstötter, M., Melson, T., Janka, H.-T., & Müller, E., 2018. Parallelized Solution Method of the Three-dimensional Gravitational Potential on the Yin-Yang Grid. *ApJ*, 863(2):142, doi: 10.3847/1538-4357/aad33a.

An, F., An, G., An, Q., Antonelli, V., et al., 2016. Neutrino physics with JUNO. *Journal of Physics G Nuclear Physics*, 43(3):030401, doi: 10.1088/0954-3899/43/3/030401.

Andresen, H., Müller, B., Müller, E., & Janka, H. T., 2017. Gravitational wave signals from 3D neutrino hydrodynamics simulations of core-collapse supernovae. *MNRAS*, 468 (2):2032–2051, doi: 10.1093/mnras/stx618.

Andresen, H., Glas, R., & Janka, H. T., 2021. Gravitational-wave signals from 3D supernova simulations with different neutrino-transport methods. *MNRAS*, 503(3): 3552–3567, doi: 10.1093/mnras/stab675.

Antoni, A. & Quataert, E., 2022. Numerical simulations of the random angular momentum in convection: Implications for supergiant collapse to form black holes. *MNRAS*, 511(1): 176–197, doi: 10.1093/mnras/stab3776.

Antoni, A. & Quataert, E., 2023. Numerical simulations of the random angular momentum in convection - II. Delayed explosions of red supergiants following 'failed' supernovae. *MNRAS*, 525(1):1229–1245, doi: 10.1093/mnras/stad2328.

Antoniadis, J., Freire, P. C. C., Wex, N., Tauris, T. M., et al., 2013. A Massive Pulsar in a Compact Relativistic Binary. *Science*, 340(6131):448, doi: 10.1126/science.1233232.

Arcones, A. & Janka, H. T., 2011. Nucleosynthesis-relevant conditions in neutrino-driven supernova outflows. II. The reverse shock in two-dimensional simulations. *A&A*, 526: A160, doi: 10.1051/0004-6361/201015530.

Arcones, A., Janka, H.-T., & Scheck, L., 2007. Nucleosynthesis-relevant conditions in neutrino-driven supernova outflows. I. Spherically symmetric hydrodynamic simulations. *A&A*, 467(3):1227–1248, doi: 10.1051/0004-6361:20066983.

Arcones, A., Martínez-Pinedo, G., O'Connor, E., Schwenk, A., et al., 2008. Influence of light nuclei on neutrino-driven supernova outflows. *Phys. Rev. C*, 78(1):015806, doi: 10.1103/PhysRevC.78.015806.

Arnett, W. D., 1966. Gravitational collapse and weak interactions. *Canadian Journal of Physics*, 44:2553–2594, doi: 10.1139/p66-210.

Arnett, W. D., 1977. Neutrino trapping during gravitational collapse of stars. *ApJ*, 218: 815–833, doi: 10.1086/155738.

Arnett, W. D., 1980. Analytic solutions for light curves of supernovae of Type II. *ApJ*, 237:541–549, doi: 10.1086/157898.

Arnett, W. D. & Meakin, C., 2011. Toward Realistic Progenitors of Core-collapse Supernovae. *ApJ*, 733:78, doi: 10.1088/0004-637X/733/2/78.

Arnett, W. D., Bahcall, J. N., Kirshner, R. P., & Woosley, S. E., 1989. Supernova 1987A. *ARA&A*, 27:629–700, doi: 10.1146/annurev.aa.27.090189.003213.

Asplund, M., Grevesse, N., Sauval, A. J., & Scott, P., 2009. The Chemical Composition of the Sun. *ARA&A*, 47(1):481–522, doi: 10.1146/annurev.astro.46.060407.145222.

Baade, W. & Zwicky, F., 1934a. On Super-novae. *PNAS*, 20:254–259, doi: 10.1073/pnas.20.5.254.

Baade, W. & Zwicky, F., 1934b. Cosmic Rays from Super-novae. *Proceedings of the National Academy of Science*, 20(5):259–263, doi: 10.1073/pnas.20.5.259.

Baade, W. & Zwicky, F., 1934c. Remarks on Super-Novae and Cosmic Rays. *Physical Review*, 46(1):76–77, doi: 10.1103/PhysRev.46.76.2.

Balbus, S. A. & Hawley, J. F., 1991. A Powerful Local Shear Instability in Weakly Magnetized Disks. I. Linear Analysis. *ApJ*, 376:214, doi: 10.1086/170270.

Barker, B. L., Harris, C. E., Warren, M. L., O'Connor, E. P., & Couch, S. M., 2022. Connecting the Light Curves of Type IIP Supernovae to the Properties of Their Progenitors. *ApJ*, 934(1):67, doi: 10.3847/1538-4357/ac77f3.

Bauswein, A., Just, O., Janka, H.-T., & Stergioulas, N., 2017. Neutron-star Radius Constraints from GW170817 and Future Detections. *ApJ*, 850(2):L34, doi: 10.3847/2041-8213/aa9994.

Bethe, H. A., 1990. Supernova mechanisms. *RvMP*, 62:801–866, doi: 10.1103/RevModPhys.62.801.

Bethe, H. A. & Wilson, J. R., 1985. Revival of a stalled supernova shock by neutrino heating. *ApJ*, 295:14–23, doi: 10.1086/163343.

Bethe, H. A., Brown, G. E., Applegate, J., & Lattimer, J. M., 1979. Equation of state in the gravitational collapse of stars. *Nucl. Phys. A*, 324(2-3):487–533, doi: 10.1016/0375-9474(79)90596-7.

Bionta, R. M., Blewitt, G., Bratton, C. B., Casper, D., et al., 1987. Observation of a neutrino burst in coincidence with supernova 1987A in the Large Magellanic Cloud. *Phys. Rev. Lett.*, 58(14):1494–1496, doi: 10.1103/PhysRevLett.58.1494.

Blaauw, A., 1961. On the origin of the O- and B-type stars with high velocities (the "run-away" stars), and some related problems. *Bull. Astron. Inst. Netherlands*, 15:265.

Blondin, J. M. & Mezzacappa, A., 2007. Pulsar spins from an instability in the accretion shock of supernovae. *Nature*, 445(7123):58–60, doi: 10.1038/nature05428.

Blondin, J. M., Mezzacappa, A., & DeMarino, C., 2003. Stability of Standing Accretion Shocks, with an Eye toward Core-Collapse Supernovae. *ApJ*, 584:971–980, doi: 10.1086/345812.

Bludman, S. A. & van Riper, K. A., 1978. Diffusion approximation to neutrino transport in dense matter. *ApJ*, 224:631–642, doi: 10.1086/156412.

Bollig, R., 2018. *Muon Creation and Effects in Supernovae.* PhD thesis, Technische Universität München.

Bollig, R., 2022. Private communication.

Bollig, R., Janka, H.-T., Lohs, A., Martínez-Pinedo, G., et al., 2017. Muon Creation in Supernova Matter Facilitates Neutrino-Driven Explosions. *Phys. Rev. Lett.*, 119(24):242702, doi: 10.1103/PhysRevLett.119.242702.

Bollig, R., Yadav, N., Kresse, D., Janka, H.-T., et al., 2021. Self-consistent 3D Supernova Models From -7 Minutes to +7 s: A 1-bethe Explosion of a 19 $M_\odot$ Progenitor. *ApJ*, 915(1):28, doi: 10.3847/1538-4357/abf82e.

Bouchet, P., Phillips, M. M., Suntzeff, N. B., Gouiffes, G., et al., 1991. The bolometric light curve of SN 1987A. II. Results from visible and infrared spectrophotometry. *A&A*, 245:490.

Bruenn, S. W., 1985. Stellar core collapse - Numerical model and infall epoch. *ApJS*, 58: 771–841, doi: 10.1086/191056.

Bruenn, S. W., 1986. A Comparison of Recent Numerical Calculations of Stellar Core Collapse. *ApJS*, 62:331, doi: 10.1086/191143.

Bruenn, S. W. & Mezzacappa, A., 1997. Ion screening effects and stellar collapse. *PhRvD*, 56:7529–7547, doi: 10.1103/PhysRevD.56.7529.

Bruenn, S. W., Mezzacappa, A., Hix, W. R., Lentz, E. J., et al., 2013. Axisymmetric Ab Initio Core-collapse Supernova Simulations of 12-25 M &sun; Stars. *ApJL*, 767:L6, doi: 10.1088/2041-8205/767/1/L6.

Bruenn, S. W., Lentz, E. J., Hix, W. R., Mezzacappa, A., et al., 2016. The Development of Explosions in Axisymmetric Ab Initio Core-collapse Supernova Simulations of 12-25 M Stars. *ApJ*, 818:123, doi: 10.3847/0004-637X/818/2/123.

Bruenn, S. W., Blondin, J. M., Hix, W. R., Lentz, E. J., et al., 2020. CHIMERA: A Massively Parallel Code for Core-collapse Supernova Simulations. *ApJS*, 248(1):11, doi: 10.3847/1538-4365/ab7aff.

Bruenn, S. W., Sieverding, A., Lentz, E. J., Sukhbold, T., et al., 2023. Comparison of the Core-collapse Evolution of Two Nearly Equal-mass Progenitors. *ApJ*, 947(1):35, doi: 10.3847/1538-4357/acbb65.

Bugli, M., Guilet, J., & Obergaulinger, M., 2021. Three-dimensional core-collapse supernovae with complex magnetic structures - I. Explosion dynamics. *MNRAS*, 507(1): 443–454, doi: 10.1093/mnras/stab2161.

Buras, R., Janka, H.-T., Keil, M. T., Raffelt, G. G., & Rampp, M., 2003. Electron Neutrino Pair Annihilation: A New Source for Muon and Tau Neutrinos in Supernovae. *ApJ*, 587: 320–326, doi: 10.1086/368015.

Buras, R., Janka, H.-T., Rampp, M., & Kifonidis, K., 2006a. Two-dimensional hydrodynamic core-collapse supernova simulations with spectral neutrino transport. II. Models for different progenitor stars. *A&A*, 457:281–308, doi: 10.1051/0004-6361:20054654.

Buras, R., Rampp, M., Janka, H.-T., & Kifonidis, K., 2006b. Two-dimensional hydrodynamic core-collapse supernova simulations with spectral neutrino transport. I. Numerical method and results for a 15 M⊙ star. *A&A*, 447(3):1049–1092, doi: 10.1051/0004-6361: 20053783.

Burrows, A., 1987. Convection and the mechanism of type II supernovae. *ApJL*, 318: L57–L61, doi: 10.1086/184937.

Burrows, A., 2013. Colloquium: Perspectives on core-collapse supernova theory. *Reviews of Modern Physics*, 85(1):245–261, doi: 10.1103/RevModPhys.85.245.

Burrows, A. & Goshy, J., 1993. A Theory of Supernova Explosions. *ApJL*, 416:L75, doi: 10.1086/187074.

Burrows, A. & Lattimer, J. M., 1986. The Birth of Neutron Stars. *ApJ*, 307:178, doi: 10.1086/164405.

Burrows, A. & Lattimer, J. M., 1988. Convection, Type II supernovae, and the early evolution of neutron stars. *Phys. Rep.*, 163(1):51–62, doi: 10.1016/0370-1573(88)90035-X.

Burrows, A. & Sawyer, R. F., 1998. Effects of correlations on neutrino opacities in nuclear matter. *PhRvC*, 58:554–571, doi: 10.1103/PhysRevC.58.554.

Burrows, A. & Sawyer, R. F., 1999. Many-body corrections to charged-current neutrino absorption rates in nuclear matter. *PhRvC*, 59:510–514, doi: 10.1103/PhysRevC.59.510.

Burrows, A. & Vartanyan, D., 2021. Core-collapse supernova explosion theory. *Nature*, 589(7840):29–39, doi: 10.1038/s41586-020-03059-w.

Burrows, A., Hayes, J., & Fryxell, B. A., 1995. On the Nature of Core-Collapse Supernova Explosions. *ApJ*, 450:830, doi: 10.1086/176188.

Burrows, A., Dolence, J. C., & Murphy, J. W., 2012. An Investigation into the Character of Pre-explosion Core-collapse Supernova Shock Motion. *ApJ*, 759:5, doi: 10.1088/0004-637X/759/1/5.

Burrows, A., Radice, D., & Vartanyan, D., 2019. Three-dimensional supernova explosion simulations of 9-, 10-, 11-, 12-, and 13-$M_\odot$ stars. *MNRAS*, 485(3):3153–3168, doi: 10.1093/mnras/stz543.

Burrows, A., Radice, D., Vartanyan, D., Nagakura, H., et al., 2020. The overarching framework of core-collapse supernova explosions as revealed by 3D FORNAX simulations. *MNRAS*, 491(2):2715–2735, doi: 10.1093/mnras/stz3223.

Cantiello, M., Mankovich, C., Bildsten, L., Christensen-Dalsgaard, J., & Paxton, B., 2014. Angular Momentum Transport within Evolved Low-mass Stars. *ApJ*, 788(1):93, doi: 10.1088/0004-637X/788/1/93.

Cernohorsky, J., 1994. Symmetries in neutrino-electron scattering. *ApJ*, 433:247–249, doi: 10.1086/174639.

Chadwick, J., 1932. The Existence of a Neutron. *Proceedings of the Royal Society of London Series A*, 136(830):692–708, doi: 10.1098/rspa.1932.0112.

Chan, C., Müller, B., & Heger, A., 2020. The impact of fallback on the compact remnants and chemical yields of core-collapse supernovae. *MNRAS*, 495(4):3751–3762, doi: 10.1093/mnras/staa1431.

Chandrasekhar, S., 1931. The Maximum Mass of Ideal White Dwarfs. *ApJ*, 74:81, doi: 10.1086/143324.

Chandrasekhar, S., 1935. The highly collapsed configurations of a stellar mass (Second paper). *MNRAS*, 95:207–225, doi: 10.1093/mnras/95.3.207.

Childs, H., Brugger, E., Whitlock, B., Meredith, J., et al., 2012. *VisIt: An End-User Tool For Visualizing and Analyzing Very Large Data*. Boca Raton, FL: CRC Press.

Cigan, P., Matsuura, M., Gomez, H. L., Indebetouw, R., et al., 2019. High Angular Resolution ALMA Images of Dust and Molecules in the SN 1987A Ejecta. *ApJ*, 886(1): 51, doi: 10.3847/1538-4357/ab4b46.

Clark, D. H. & Stephenson, F. R., 1977. *The historical supernovae*.

Colella, P. & Woodward, P. R., 1984. The Piecewise Parabolic Method (PPM) for Gas-Dynamical Simulations. *Journal of Computational Physics*, 54:174–201, doi: 10.1016/0021-9991(84)90143-8.

Coleman, M. S. B. & Burrows, A., 2022. Kicks and induced spins of neutron stars at birth. *MNRAS*, 517(3):3938–3961, doi: 10.1093/mnras/stac2573.

Colgate, S. A. & White, R. H., 1966. The Hydrodynamic Behavior of Supernovae Explosions. *ApJ*, 143:626, doi: 10.1086/148549.

COMPASS Collaboration, Alexakhin, V. Y., Alexandrov, Y., Alexeev, G. D., et al., 2007. The deuteron spin-dependent structure function g1d and its first moment. *Physics Letters B*, 647(1):8–17, doi: 10.1016/j.physletb.2006.12.076.

Couch, S. M., 2013. On the Impact of Three Dimensions in Simulations of Neutrino-driven Core-collapse Supernova Explosions. *ApJ*, 775:35, doi: 10.1088/0004-637X/775/1/35.

Couch, S. M. & O'Connor, E. P., 2014. High-resolution Three-dimensional Simulations of Core-collapse Supernovae in Multiple Progenitors. *ApJ*, 785:123, doi: 10.1088/0004-637X/785/2/123.

Couch, S. M. & Ott, C. D., 2013. Revival of the Stalled Core-collapse Supernova Shock Triggered by Precollapse Asphericity in the Progenitor Star. *ApJL*, 778:L7, doi: 10.1088/2041-8205/778/1/L7.

Couch, S. M. & Ott, C. D., 2015. The Role of Turbulence in Neutrino-driven Core-collapse Supernova Explosions. *ApJ*, 799:5, doi: 10.1088/0004-637X/799/1/5.

Couch, S. M., Graziani, C., & Flocke, N., 2013. An Improved Multipole Approximation for Self-gravity and Its Importance for Core-collapse Supernova Simulations. *ApJ*, 778(2): 181, doi: 10.1088/0004-637X/778/2/181.

Couch, S. M., Chatzopoulos, E., Arnett, W. D., & Timmes, F. X., 2015. The Three-dimensional Evolution to Core Collapse of a Massive Star. *ApJL*, 808:L21, doi: 10.1088/2041-8205/808/1/L21.

Courant, R., Friedrichs, K., & Lewy, H., 1928. Über die partiellen Differenzengleichungen der mathematischen Physik. *MatAn*, 100(1):32. ISSN 1432-1807, doi: 10.1007/BF01448839. URL http://dx.doi.org/10.1007/BF01448839.

Cromartie, H. T., Fonseca, E., Ransom, S. M., Demorest, P. B., et al., 2020. Relativistic Shapiro delay measurements of an extremely massive millisecond pulsar. *Nature Astronomy*, 4:72–76, doi: 10.1038/s41550-019-0880-2.

Cubillos, P. E., 2020. bibmanager: A BibTeX manager for LaTeX projects. Zenodo.

da Silva Schneider, A., O'Connor, E., Granqvist, E., Betranhandy, A., & Couch, S. M., 2020. Equation of State and Progenitor Dependence of Stellar-mass Black Hole Formation. *ApJ*, 894(1):4, doi: 10.3847/1538-4357/ab8308.

Demorest, P. B., Pennucci, T., Ransom, S. M., Roberts, M. S. E., & Hessels, J. W. T., 2010. A two-solar-mass neutron star measured using Shapiro delay. *Nature*, 467(7319): 1081–1083, doi: 10.1038/nature09466.

Dessart, L. & Hillier, D. J., 2005. Distance determinations using type II supernovae and the expanding photosphere method. *A&A*, 439(2):671–685, doi: 10.1051/0004-6361:20053217.

Dessart, L. & Hillier, D. J., 2011. Non-LTE time-dependent spectroscopic modelling of Type II-plateau supernovae from the photospheric to the nebular phase: case study for 15 and 25 $M_\odot$ progenitor stars. *MNRAS*, 410(3):1739–1760, doi: 10.1111/j.1365-2966.2010.17557.x.

Dessart, L. & Hillier, D. J., 2019. The difficulty of inferring progenitor masses from type-II-Plateau supernova light curves. *A&A*, 625:A9, doi: 10.1051/0004-6361/201834732.

Dessart, L., Burrows, A., Livne, E., & Ott, C. D., 2006. Multidimensional Radiation/Hydrodynamic Simulations of Proto-Neutron Star Convection. *ApJ*, 645:534–550, doi: 10.1086/504068.

Dessart, L., Livne, E., & Waldman, R., 2010. Determining the main-sequence mass of Type II supernova progenitors. *MNRAS*, 408(2):827–840, doi: 10.1111/j.1365-2966.2010.17190.x.

Diehl, R., Halloin, H., Kretschmer, K., Lichti, G. G., et al., 2006. Radioactive ^{26}Al from massive stars in the Galaxy. *Nature*, 439(7072):45–47, doi: 10.1038/nature04364.

Dolence, J. C., Burrows, A., Murphy, J. W., & Nordhaus, J., 2013. Dimensional Dependence of the Hydrodynamics of Core-collapse Supernovae. *ApJ*, 765:110, doi: 10.1088/0004-637X/765/2/110.

Dolence, J. C., Burrows, A., & Zhang, W., 2015. Two-dimensional Core-collapse Supernova Models with Multi-dimensional Transport. *ApJ*, 800(1):10, doi: 10.1088/0004-637X/800/1/10.

Duncan, R. C., Shapiro, S. L., & Wasserman, I., 1986. Neutrino-driven Winds from Young, Hot Neutron Stars. *ApJ*, 309:141, doi: 10.1086/164587.

Einfeldt, B., 1988. On Godunov type methods for the Euler equations with a general equation of state. In Groenig, H., editor, *Shock Tubes and Waves*, page 671.

Ellis, J. & Karliner, M., 1996. The Strange Spin of the Nucleon. *arXiv e-prints*, art. hep-ph/9601280.

Faucher-Giguère, C.-A. & Kaspi, V. M., 2006. Birth and Evolution of Isolated Radio Pulsars. *ApJ*, 643(1):332–355, doi: 10.1086/501516.

Fernández, R., 2015. Three-dimensional simulations of SASI- and convection-dominated core-collapse supernovae. *MNRAS*, 452:2071–2086, doi: 10.1093/mnras/stv1463.

Fields, C. E., 2022. The Three-dimensional Collapse of a Rapidly Rotating 16 M $_\odot$ Star. *ApJ*, 924(1):L15, doi: 10.3847/2041-8213/ac460c.

Fields, C. E. & Couch, S. M., 2021. Three-dimensional Hydrodynamic Simulations of Convective Nuclear Burning in Massive Stars Near Iron Core Collapse. *ApJ*, 921(1):28, doi: 10.3847/1538-4357/ac24fb.

Fischer, T., Whitehouse, S. C., Mezzacappa, A., Thielemann, F. K., & Liebendörfer, M., 2009. The neutrino signal from protoneutron star accretion and black hole formation. *A&A*, 499(1):1–15, doi: 10.1051/0004-6361/200811055.

Fischer, T., Whitehouse, S. C., Mezzacappa, A., Thielemann, F. K., & Liebendörfer, M., 2010. Protoneutron star evolution and the neutrino-driven wind in general relativistic neutrino radiation hydrodynamics simulations. *A&A*, 517:A80, doi: 10.1051/0004-6361/200913106.

Fischer, T., Guo, G., Martínez-Pinedo, G., Liebendörfer, M., & Mezzacappa, A., 2020. Muonization of supernova matter. *Phys. Rev. D*, 102(12):123001, doi: 10.1103/PhysRevD.102.123001.

Foglizzo, T., Scheck, L., & Janka, H.-T., 2006. Neutrino-driven Convection versus Advection in Core-Collapse Supernovae. *ApJ*, 652:1436–1450, doi: 10.1086/508443.

Foglizzo, T., Galletti, P., Scheck, L., & Janka, H.-T., 2007. Instability of a Stalled Accretion Shock: Evidence for the Advective-Acoustic Cycle. *ApJ*, 654:1006–1021, doi: 10.1086/509612.

Foglizzo, T., Kazeroni, R., Guilet, J., Masset, F., et al., 2015. The Explosion Mechanism of Core-Collapse Supernovae: Progress in Supernova Theory and Experiments. *PASA*, 32:e009, doi: 10.1017/pasa.2015.9.

Foucart, F., 2018. Monte Carlo closure for moment-based transport schemes in general relativistic radiation hydrodynamic simulations. *MNRAS*, 475(3):4186–4207, doi: 10.1093/mnras/sty108.

Foucart, F., O'Connor, E., Roberts, L., Duez, M. D., et al., 2015. Post-merger evolution of a neutron star-black hole binary with neutrino transport. *Phys. Rev. D*, 91(12):124021, doi: 10.1103/PhysRevD.91.124021.

Fryer, C. L. & Warren, M. S., 2002. Modeling Core-Collapse Supernovae in Three Dimensions. *ApJL*, 574:L65–L68, doi: 10.1086/342258.

Fryer, C. L. & Warren, M. S., 2004. The Collapse of Rotating Massive Stars in Three Dimensions. *ApJ*, 601:391–404, doi: 10.1086/380193.

Fryxell, B., Müller, E., & Arnett, D., 1989. Computation of multi-dimensional flows with non-uniform composition. In Hillebrandt, W. & Müller, E., editors, *Proceedings of the 5$^{\text{th}}$ Workshop on Nuclear Astrophysics*, page 100.

Gabler, M., Wongwathanarat, A., & Janka, H.-T., 2021. The infancy of core-collapse supernova remnants. *MNRAS*, 502(3):3264–3293, doi: 10.1093/mnras/stab116.

Gessner, A. & Janka, H.-T., 2018. Hydrodynamical Neutron-star Kicks in Electron-capture Supernovae and Implications for the CRAB Supernova. *ApJ*, 865(1):61, doi: 10.3847/1538-4357/aadbae.

Glas, R., Janka, H. T., Melson, T., Stockinger, G., & Just, O., 2019a. Effects of LESA in Three-dimensional Supernova Simulations with Multidimensional and Ray-by-ray-plus Neutrino Transport. *ApJ*, 881(1):36, doi: 10.3847/1538-4357/ab275c.

Glas, R., Just, O., Janka, H.-T., & Obergaulinger, M., 2019b. Three-dimensional Core-collapse Supernova Simulations with Multidimensional Neutrino Transport Compared to the Ray-by-ray-plus Approximation. *ApJ*, 873(1):45, doi: 10.3847/1538-4357/ab0423.

Goldberg, J. A. & Bildsten, L., 2020. The Value of Progenitor Radius Measurements for Explosion Modeling of Type II-Plateau Supernovae. *ApJ*, 895(2):L45, doi: 10.3847/2041-8213/ab9300.

Goldberg, J. A., Bildsten, L., & Paxton, B., 2019. Inferring Explosion Properties from Type II-Plateau Supernova Light Curves. *ApJ*, 879(1):3, doi: 10.3847/1538-4357/ab22b6.

Green, D. A., 2011. A colour scheme for the display of astronomical intensity images. *Bulletin of the Astronomical Society of India*, 39:289–295, doi: 10.48550/arXiv.1108.5083.

Grefenstette, B. W., Harrison, F. A., Boggs, S. E., Reynolds, S. P., et al., 2014. Asymmetries in core-collapse supernovae from maps of radioactive ^{44}Ti in CassiopeiaA. *Nature*, 506:339–342, doi: 10.1038/nature12997.

Guilet, J. & Foglizzo, T., 2012. On the linear growth mechanism driving the standing accretion shock instability. *MNRAS*, 421:546–560, doi: 10.1111/j.1365-2966.2012.20333.x.

Guilet, J., Sato, J., & Foglizzo, T., 2010. The Saturation of SASI by Parasitic Instabilities. *ApJ*, 713:1350–1362, doi: 10.1088/0004-637X/713/2/1350.

Guilet, J., Müller, E., & Janka, H.-T., 2015. Neutrino viscosity and drag: impact on the magnetorotational instability in protoneutron stars. *MNRAS*, 447:3992–4003, doi: 10.1093/mnras/stu2550.

Haas, M. R., Colgan, S. W. J., Erickson, E. F., Lord, S. D., et al., 1990. Velocity-resolved Far-Infrared Spectra of Fe ii: Evidence for Mixing and Clumping in SN 1987A. *ApJ*, 360:257, doi: 10.1086/169115.

Hamuy, M., 2003. Observed and Physical Properties of Core-Collapse Supernovae. *ApJ*, 582(2):905–914, doi: 10.1086/344689.

Hanke, F., 2014. *Two- and Three-Dimensional Simulations of Core-Collapse Supernova Explosions of Massive Stars Applying Neutrino Hydrodynamics*. PhD thesis, Technische Universität München.

Hanke, F., Marek, A., Müller, B., & Janka, H.-T., 2012. Is Strong SASI Activity the Key to Successful Neutrino-driven Supernova Explosions? *ApJ*, 755:138, doi: 10.1088/0004-637X/755/2/138.

Hanke, F., Müller, B., Wongwathanarat, A., Marek, A., & Janka, H.-T., 2013. SASI Activity in Three-dimensional Neutrino-hydrodynamics Simulations of Supernova Cores. *ApJ*, 770:66, doi: 10.1088/0004-637X/770/1/66.

Hannestad, S. & Raffelt, G., 1998. Supernova Neutrino Opacity from Nucleon-Nucleon Bremsstrahlung and Related Processes. *ApJ*, 507:339–352, doi: 10.1086/306303.

Harris, C. R., Millman, K. J., van der Walt, S. J., Gommers, R., et al., 2020. Array programming with NumPy. *Nature*, 585(7825):357–362, doi: 10.1038/s41586-020-2649-2.

Harris, J. A., Hix, W. R., Chertkow, M. A., Lee, C. T., et al., 2017. Implications for Post-processing Nucleosynthesis of Core-collapse Supernova Models with Lagrangian Particles. *ApJ*, 843(1):2, doi: 10.3847/1538-4357/aa76de.

Heger, A., 2012. Private communication.

Heger, A. & Woosley, S. E., 2010. Nucleosynthesis and Evolution of Massive Metal-free Stars. *ApJ*, 724:341–373, doi: 10.1088/0004-637X/724/1/341.

Heger, A., Woosley, S. E., & Spruit, H. C., 2005. Presupernova Evolution of Differentially Rotating Massive Stars Including Magnetic Fields. *ApJ*, 626:350–363, doi: 10.1086/429868.

Hempel, M. & Schaffner-Bielich, J., 2010. A statistical model for a complete supernova equation of state. *Nucl. Phys. A*, 837(3-4):210–254, doi: 10.1016/j.nuclphysa.2010.02.010.

Herant, M., Benz, W., Hix, W. R., Fryer, C. L., & Colgate, S. A., 1994. Inside the supernova: A powerful convective engine. *ApJ*, 435:339–361, doi: 10.1086/174817.

Hester, J. J., 2008. The Crab Nebula : an astrophysical chimera. *ARA&A*, 46:127–155, doi: 10.1146/annurev.astro.45.051806.110608.

Hillebrandt, W. & Müller, E., 1981. Computer simulations of stellar collapse and shock wave propagation. *A&A*, 103(1):147–153.

Hillebrandt, W. & Niemeyer, J. C., 2000. Type IA Supernova Explosion Models. *ARA&A*, 38:191–230, doi: 10.1146/annurev.astro.38.1.191.

Hillebrandt, W., Kromer, M., Röpke, F. K., & Ruiter, A. J., 2013. Towards an understanding of Type Ia supernovae from a synthesis of theory and observations. *Frontiers of Physics*, 8(2):116–143, doi: 10.1007/s11467-013-0303-2.

Hirata, K., Kajita, T., Koshiba, M., Nakahata, M., et al., 1987. Observation of a neutrino burst from the supernova SN1987A. *Phys. Rev. Lett.*, 58(14):1490–1493, doi: 10.1103/PhysRevLett.58.1490.

Hix, W. R. & Thielemann, F.-K., 1999a. Silicon Burning. II. Quasi-Equilibrium and Explosive Burning. *ApJ*, 511(2):862–875, doi: 10.1086/306692.

Hix, W. R. & Thielemann, F. K., 1999b. Computational methods for nucleosynthesis and nuclear energy generation. *Journal of Computational and Applied Mathematics*, 109(1): 321–351.

Hobbs, G., Lorimer, D. R., Lyne, A. G., & Kramer, M., 2005. A statistical study of 233 pulsar proper motions. *MNRAS*, 360(3):974–992, doi: 10.1111/j.1365-2966.2005.09087.x.

Horowitz, C. J., 1997. Neutrino trapping in a supernova and the screening of weak neutral currents. *PhRvD*, 55:4577–4581, doi: 10.1103/PhysRevD.55.4577.

Horowitz, C. J., 2002. Weak magnetism for antineutrinos in supernovae. *Phys. Rev. D*, 65 (4):043001, doi: 10.1103/PhysRevD.65.043001.

Horowitz, C. J. & Li, G., 1999. Nucleosynthesis in Supernovae. *Phys. Rev. Lett.*, 82(26): 5198–5201, doi: 10.1103/PhysRevLett.82.5198.

Horowitz, C. J., Caballero, O. L., Lin, Z., O'Connor, E., & Schwenk, A., 2017. Neutrino-nucleon scattering in supernova matter from the virial expansion. *Phys. Rev. C*, 95(2): 025801, doi: 10.1103/PhysRevC.95.025801.

Hüdepohl, L., 2014. *Neutrinos from the Formation, Cooling and Black Hole Collapse of Neutron Stars*. PhD thesis, Technische Universität München.

Hunter, J. D., 2007. Matplotlib: A 2d graphics environment. *Computing in Science & Engineering*, 9(3):90–95, doi: 10.1109/MCSE.2007.55.

Hwang, U., Laming, J. M., Badenes, C., Berendse, F., et al., 2004. A Million Second Chandra View of Cassiopeia A. *ApJ*, 615(2):L117–L120, doi: 10.1086/426186.

Ikeda, M., Takeda, A., Fukuda, Y., Vagins, M. R., et al., 2007. Search for Supernova Neutrino Bursts at Super-Kamiokande. *ApJ*, 669(1):519–524, doi: 10.1086/521547.

Iwakami, W., Kotake, K., Ohnishi, N., Yamada, S., & Sawada, K., 2008. Three-Dimensional Simulations of Standing Accretion Shock Instability in Core-Collapse Supernovae. *ApJ*, 678:1207-1222, doi: 10.1086/533582.

Janka, H.-T., 1999. Unpublished.

Janka, H.-T., 2001. Conditions for shock revival by neutrino heating in core-collapse supernovae. *A&A*, 368:527–560, doi: 10.1051/0004-6361:20010012.

Janka, H.-T., 2012. Explosion Mechanisms of Core-Collapse Supernovae. *Annual Review of Nuclear and Particle Science*, 62(1):407–451, doi: 10.1146/annurev-nucl-102711-094901.

Janka, H.-T., 2017a. Neutrino-Driven Explosions. In Alsabti, A. W. & Murdin, P., editors, *Handbook of Supernovae*, page 1095. doi: 10.1007/978-3-319-21846-5_109.

Janka, H.-T., 2017b. Neutrino Emission from Supernovae. In Alsabti, A. W. & Murdin, P., editors, *Handbook of Supernovae*, page 1575. doi: 10.1007/978-3-319-21846-5_4.

Janka, H.-T., 2017c. Neutron Star Kicks by the Gravitational Tug-boat Mechanism in Asymmetric Supernova Explosions: Progenitor and Explosion Dependence. *ApJ*, 837(1): 84, doi: 10.3847/1538-4357/aa618e.

Janka, H. T. & Bauswein, A., 2022. Dynamics and Equation of State Dependencies of Relevance for Nucleosynthesis in Supernovae and Neutron Star Mergers. *arXiv e-prints*, art. arXiv:2212.07498, doi: 10.48550/arXiv.2212.07498.

Janka, H. T. & Müller, E., 1994. Neutron star recoils from anisotropic supernovae. *A&A*, 290:496–502.

Janka, H.-T. & Müller, E., 1996. Neutrino heating, convection, and the mechanism of Type-II supernova explosions. *A&A*, 306:167.

Janka, H.-T., Müller, B., Kitaura, F. S., & Buras, R., 2008. Dynamics of shock propagation and nucleosynthesis conditions in O-Ne-Mg core supernovae. *A&A*, 485(1):199–208, doi: 10.1051/0004-6361:20079334.

Janka, H.-T., Hanke, F., Hüdepohl, L., Marek, A., et al., 2012. Core-collapse supernovae: Reflections and directions. *Progress of Theoretical and Experimental Physics*, 2012(1): 01A309, doi: 10.1093/ptep/pts067.

Janka, H.-T., Melson, T., & Summa, A., 2016. Physics of Core-Collapse Supernovae in Three Dimensions: A Sneak Preview. *ARNPS*, 66:341–375, doi: 10.1146/annurev-nucl-102115-044747.

Janka, H.-T., Summa, A., & Melson, T., 2017. Unpublished.

Janka, H.-T., Wongwathanarat, A., & Kramer, M., 2022. Supernova Fallback as Origin of Neutron Star Spins and Spin-kick Alignment. *ApJ*, 926(1):9, doi: 10.3847/1538-4357/ac403c.

Jerkstrand, A., Fransson, C., Maguire, K., Smartt, S., et al., 2012. The progenitor mass of the Type IIP supernova SN 2004et from late-time spectral modeling. *A&A*, 546:A28, doi: 10.1051/0004-6361/201219528.

Jerkstrand, A., Smartt, S. J., Fraser, M., Fransson, C., et al., 2014. The nebular spectra of SN 2012aw and constraints on stellar nucleosynthesis from oxygen emission lines. *MNRAS*, 439(4):3694–3703, doi: 10.1093/mnras/stu221.

Jerkstrand, A., Ertl, T., Janka, H. T., Müller, E., et al., 2018. Emission line models for the lowest mass core-collapse supernovae - I. Case study of a 9 $M_\odot$ one-dimensional neutrino-driven explosion. *MNRAS*, 475(1):277–305, doi: 10.1093/mnras/stx2877.

Jerkstrand, A., Wongwathanarat, A., Janka, H. T., Gabler, M., et al., 2020. Properties of gamma-ray decay lines in 3D core-collapse supernova models, with application to SN 1987A and Cas A. *MNRAS*, 494(2):2471–2497, doi: 10.1093/mnras/staa736.

Johnston, S., Hobbs, G., Vigeland, S., Kramer, M., et al., 2005. Evidence for alignment of the rotation and velocity vectors in pulsars. *MNRAS*, 364(4):1397–1412, doi: 10.1111/j.1365-2966.2005.09669.x.

Just, O., Obergaulinger, M., & Janka, H. T., 2015. A new multidimensional, energy-dependent two-moment transport code for neutrino-hydrodynamics. *MNRAS*, 453(4):3386–3413, doi: 10.1093/mnras/stv1892.

Just, O., Bollig, R., Janka, H. T., Obergaulinger, M., et al., 2018. Core-collapse supernova simulations in one and two dimensions: comparison of codes and approximations. *MNRAS*, 481(4):4786–4814, doi: 10.1093/mnras/sty2578.

Kageyama, A. & Sato, T., 2004. "Yin-Yang grid": An overset grid in spherical geometry. *GGG*, 5:Q09005, doi: 10.1029/2004GC000734.

Kane, J., Arnett, D., Remington, B. A., Glendinning, S. G., et al., 2000. Two-dimensional versus Three-dimensional Supernova Hydrodynamic Instability Growth. *ApJ*, 528(2):989–994, doi: 10.1086/308220.

Kasen, D. & Woosley, S. E., 2009. Type II Supernovae: Model Light Curves and Standard Candle Relationships. *ApJ*, 703(2):2205–2216, doi: 10.1088/0004-637X/703/2/2205.

Kaspi, V. M. & Helfand, D. J., 2002. Constraining the Birth Events of Neutron Stars. In Slane, P. O. & Gaensler, B. M., editors, *Neutron Stars in Supernova Remnants*, volume 271 of *Astronomical Society of the Pacific Conference Series*, page 3, doi: 10.48550/arXiv.astro-ph/0201183.

Katsuda, S., Morii, M., Janka, H.-T., Wongwathanarat, A., et al., 2018. Intermediate-mass Elements in Young Supernova Remnants Reveal Neutron Star Kicks by Asymmetric Explosions. *ApJ*, 856(1):18, doi: 10.3847/1538-4357/aab092.

Kazeroni, R., Guilet, J., & Foglizzo, T., 2016. New insights on the spin-up of a neutron star during core collapse. *MNRAS*, 456:126–135, doi: 10.1093/mnras/stv2666.

Kazeroni, R., Guilet, J., & Foglizzo, T., 2017. Are pulsars spun up or down by SASI spiral modes? *MNRAS*, 471(1):914–925, doi: 10.1093/mnras/stx1566.

Keil, W., 1997. *Konvektive Instabilitäten in entstehenden Neutronensternen*. PhD thesis, Technische Universität München.

Keil, W., Janka, H.-T., & Müller, E., 1996. Ledoux Convection in Protoneutron Stars—A Clue to Supernova Nucleosynthesis? *ApJL*, 473:L111, doi: 10.1086/310404.

Kifonidis, K., Plewa, T., Janka, H.-T., & Müller, E., 2003. Non-spherical core collapse supernovae. I. Neutrino-driven convection, Rayleigh-Taylor instabilities, and the formation and propagation of metal clumps. *A&A*, 408:621–649, doi: 10.1051/0004-6361:20030863.

Kitaura, F. S., Janka, H.-T., & Hillebrandt, W., 2006. Explosions of O-Ne-Mg cores, the Crab supernova, and subluminous type II-P supernovae. *A&A*, 450(1):345–350, doi: 10.1051/0004-6361:20054703.

Kiziltan, B., Kottas, A., De Yoreo, M., & Thorsett, S. E., 2013. The Neutron Star Mass Distribution. *ApJ*, 778(1):66, doi: 10.1088/0004-637X/778/1/66.

Kobayashi, C., Karakas, A. I., & Lugaro, M., 2020. The Origin of Elements from Carbon to Uranium. *ApJ*, 900(2):179, doi: 10.3847/1538-4357/abae65.

Kolmogorov, A., 1941. The Local Structure of Turbulence in Incompressible Viscous Fluid for Very Large Reynolds' Numbers. *DoSSR*, 30:301–305.

Kotake, K., Sato, K., & Takahashi, K., 2006. Explosion mechanism, neutrino burst and gravitational wave in core-collapse supernovae. *Reports on Progress in Physics*, 69(4): 971–1143, doi: 10.1088/0034-4885/69/4/R03.

Kotake, K., Takiwaki, T., Fischer, T., Nakamura, K., & Martínez-Pinedo, G., 2018. Impact of Neutrino Opacities on Core-collapse Supernova Simulations. *ApJ*, 853(2):170, doi: 10.3847/1538-4357/aaa716.

Kozyreva, A., Janka, H.-T., Kresse, D., Taubenberger, S., & Baklanov, P., 2022. Low-luminosity type IIP supermnovae: SN 2005cs and SN 2020cxd as very low-energy iron core-collapse explosions. *MNRAS*, 514(3):4173–4189, doi: 10.1093/mnras/stac1518.

Kraichnan, R. H., 1967. Inertial Ranges in Two-Dimensional Turbulence. *PhFl*, 10: 1417–1423, doi: 10.1063/1.1762301.

Kresse, D., Ertl, T., & Janka, H.-T., 2021. Stellar Collapse Diversity and the Diffuse Supernova Neutrino Background. *ApJ*, 909(2):169, doi: 10.3847/1538-4357/abd54e.

Kuroda, T., Takiwaki, T., & Kotake, K., 2014. Gravitational wave signatures from low-mode spiral instabilities in rapidly rotating supernova cores. *Phys. Rev. D*, 89(4):044011, doi: 10.1103/PhysRevD.89.044011.

Kuroda, T., Kotake, K., & Takiwaki, T., 2016a. A New Gravitational-wave Signature from Standing Accretion Shock Instability in Supernovae. *ApJ*, 829(1):L14, doi: 10.3847/2041-8205/829/1/L14.

Kuroda, T., Takiwaki, T., & Kotake, K., 2016b. A New Multi-energy Neutrino Radiation-Hydrodynamics Code in Full General Relativity and Its Application to the Gravitational Collapse of Massive Stars. *ApJS*, 222:20, doi: 10.3847/0067-0049/222/2/20.

Kuroda, T., Arcones, A., Takiwaki, T., & Kotake, K., 2020. Magnetorotational Explosion of a Massive Star Supported by Neutrino Heating in General Relativistic Three-dimensional Simulations. *ApJ*, 896(2):102, doi: 10.3847/1538-4357/ab9308.

Lai, D., Chernoff, D. F., & Cordes, J. M., 2001. Pulsar Jets: Implications for Neutron Star Kicks and Initial Spins. *ApJ*, 549(2):1111–1118, doi: 10.1086/319455.

Langanke, K., Martínez-Pinedo, G., Sampaio, J. M., Dean, D. J., et al., 2003. Electron Capture Rates on Nuclei and Implications for Stellar Core Collapse. *Phys. Rev. Lett.*, 90(24):241102, doi: 10.1103/PhysRevLett.90.241102.

Langanke, K., Martínez-Pinedo, G., Müller, B., Janka, H.-T., et al., 2008. Effects of Inelastic Neutrino-Nucleus Scattering on Supernova Dynamics and Radiated Neutrino Spectra. *Phys. Rev. Lett.*, 100(1):011101, doi: 10.1103/PhysRevLett.100.011101.

Langer, N., 2012. Presupernova Evolution of Massive Single and Binary Stars. *ARA&A*, 50:107–164, doi: 10.1146/annurev-astro-081811-125534.

Laplace, E., Götberg, Y., de Mink, S. E., Justham, S., & Farmer, R., 2020. The expansion of stripped-envelope stars: Consequences for supernovae and gravitational-wave progenitors. *A&A*, 637:A6, doi: 10.1051/0004-6361/201937300.

Laplace, E., Justham, S., Renzo, M., Götberg, Y., et al., 2021. Different to the core: The pre-supernova structures of massive single and binary-stripped stars. *A&A*, 656:A58, doi: 10.1051/0004-6361/202140506.

Lattimer, J. M. & Prakash, M., 2001. Neutron Star Structure and the Equation of State. *ApJ*, 550(1):426–442, doi: 10.1086/319702.

Lattimer, J. M. & Schutz, B. F., 2005. Constraining the Equation of State with Moment of Inertia Measurements. *ApJ*, 629(2):979–984, doi: 10.1086/431543.

Lattimer, J. M. & Swesty, D. F., 1991. A generalized equation of state for hot, dense matter. *Nucl. Phys. A*, 535(2):331–376, doi: 10.1016/0375-9474(91)90452-C.

Lentz, E. J., Bruenn, S. W., Hix, W. R., Mezzacappa, A., et al., 2015. Three-dimensional Core-collapse Supernova Simulated Using a 15 M $_\odot$ Progenitor. *ApJ*, 807(2):L31, doi: 10.1088/2041-8205/807/2/L31.

Liebendörfer, M., Messer, O. E. B., Mezzacappa, A., Bruenn, S. W., et al., 2004. A Finite Difference Representation of Neutrino Radiation Hydrodynamics in Spherically Symmetric General Relativistic Spacetime. *ApJS*, 150(1):263–316, doi: 10.1086/380191.

Liebendörfer, M., Rampp, M., Janka, H.-T., & Mezzacappa, A., 2005. Supernova Simulations with Boltzmann Neutrino Transport: A Comparison of Methods. *ApJ*, 620: 840–860, doi: 10.1086/427203.

Lodders, K., 2003. Solar System Abundances and Condensation Temperatures of the Elements. *ApJ*, 591(2):1220–1247, doi: 10.1086/375492.

Mabanta, Q. A. & Murphy, J. W., 2018. How Turbulence Enables Core-collapse Supernova Explosions. *ApJ*, 856:22, doi: 10.3847/1538-4357/aaaec7.

Magkotsios, G., Timmes, F. X., Hungerford, A. L., Fryer, C. L., et al., 2010. Trends in ^{44}Ti and ^{56}Ni from Core-collapse Supernovae. *ApJS*, 191(1):66–95, doi: 10.1088/0067-0049/191/1/66.

Marek, A. & Janka, H.-T., 2009. Delayed Neutrino-Driven Supernova Explosions Aided by the Standing Accretion-Shock Instability. *ApJ*, 694:664–696, doi: 10.1088/0004-637X/694/1/664.

Marek, A., Dimmelmeier, H., Janka, H.-T., Müller, E., & Buras, R., 2006. Exploring the relativistic regime with Newtonian hydrodynamics: an improved effective gravitational potential for supernova simulations. *A&A*, 445:273–289, doi: 10.1051/0004-6361:20052840.

Marek, A., Rampp, M., Hanke, F., & Janka, H.-T., 2014. Towards Petaflops Capability of the VERTEX Supernova Code. *arXiv:1404.1719*.

Martinez, L., Bersten, M. C., Anderson, J. P., González-Gaitán, S., et al., 2020. Progenitor properties of type II supernovae: fitting to hydrodynamical models using Markov chain Monte Carlo methods. *A&A*, 642:A143, doi: 10.1051/0004-6361/202038393.

Martinez, L., Bersten, M. C., Anderson, J. P., Hamuy, M., et al., 2022. Type II supernovae from the Carnegie Supernova Project-I. II. Physical parameter distributions from hydrodynamical modelling. *A&A*, 660:A41, doi: 10.1051/0004-6361/202142076.

Matsumoto, J., Asahina, Y., Takiwaki, T., Kotake, K., & Takahashi, H. R., 2022. Magnetic support for neutrino-driven explosion of 3D non-rotating core-collapse supernova models. *MNRAS*, 516(2):1752–1767, doi: 10.1093/mnras/stac2335.

Mayer, M., Becker, W., Patnaude, D., Winkler, P. F., & Kraft, R., 2020. The Proper Motion of the Central Compact Object RX J0822-4300 in the Supernova Remnant Puppis A, Revisited. *ApJ*, 899(2):138, doi: 10.3847/1538-4357/aba121.

Mayer, M. G. F., Becker, W., Predehl, P., Sasaki, M., & Freyberg, M., 2022. A global view of shocked plasma in the supernova remnant Puppis A provided by SRG/eROSITA. *A&A*, 661:A31, doi: 10.1051/0004-6361/202142517.

McCray, R., 1993. Supernova 1987A revisited. *ARA&A*, 31:175–216, doi: 10.1146/annurev.aa.31.090193.001135.

McLaughlin, G. C., Fuller, G. M., & Wilson, J. R., 1996. The Influence of Nuclear Composition on the Electron Fraction in the Post–Core Bounce Supernova Environment. *ApJ*, 472:440, doi: 10.1086/178077.

McNeill, L. O. & Müller, B., 2022. Differential rotation in a 3D simulation of oxygen shell burning. *MNRAS*, 509(1):818–830, doi: 10.1093/mnras/stab3076.

Melson, T., 2016. *Modeling neutrino-driven core-collapse supernova explosions in three dimensions*. PhD thesis, Technische Universität München.

Melson, T., Janka, H.-T., Bollig, R., Hanke, F., et al., 2015a. Neutrino-driven Explosion of a 20 Solar-mass Star in Three Dimensions Enabled by Strange-quark Contributions to Neutrino-Nucleon Scattering. *ApJL*, 808:L42, doi: 10.1088/2041-8205/808/2/L42.

Melson, T., Janka, H.-T., & Marek, A., 2015b. Neutrino-driven Supernova of a Low-mass Iron-core Progenitor Boosted by Three-dimensional Turbulent Convection. *ApJ*, 801(2): L24, doi: 10.1088/2041-8205/801/2/L24.

Melson, T., Kresse, D., & Janka, H.-T., 2020. Resolution Study for Three-dimensional Supernova Simulations with the Prometheus-Vertex Code. *ApJ*, 891(1):27, doi: 10.3847/1538-4357/ab72a7.

Mezzacappa, A., 2005. ASCERTAINING THE CORE COLLAPSE SUPERNOVA MECHANISM: The State of the Art and the Road Ahead. *Annual Review of Nuclear and Particle Science*, 55(1):467–515, doi: 10.1146/annurev.nucl.55.090704.151608.

Mezzacappa, A. & Bruenn, S. W., 1993a. Stellar core collapse - A Boltzmann treatment of neutrino-electron scattering. *ApJ*, 410:740–760, doi: 10.1086/172791.

Mezzacappa, A. & Bruenn, S. W., 1993b. Type II supernovae and Boltzmann neutrino transport - The infall phase. *ApJ*, 405:637–668, doi: 10.1086/172394.

Mezzacappa, A., Liebendörfer, M., Messer, O. E., Hix, W. R., et al., 2001. Simulation of the Spherically Symmetric Stellar Core Collapse, Bounce, and Postbounce Evolution of a Star of 13 Solar Masses with Boltzmann Neutrino Transport, and Its Implications for the Supernova Mechanism. *PhRvL*, 86:1935–1938, doi: 10.1103/PhysRevLett.86.1935.

Mihalas, D. & Mihalas, B. W., 1984. *Foundations of radiation hydrodynamics*. Oxford University Press.

Miller, M. C., Lamb, F. K., Dittmann, A. J., Bogdanov, S., et al., 2019. PSR J0030+0451 Mass and Radius from NICER Data and Implications for the Properties of Neutron Star Matter. *ApJ*, 887(1):L24, doi: 10.3847/2041-8213/ab50c5.

Mirizzi, A., Tamborra, I., Janka, H.-T., Saviano, N., et al., 2016. Supernova neutrinos: production, oscillations and detection. *Nuovo Cimento Rivista Serie*, 39(1-2):1–112, doi: 10.1393/ncr/i2016-10120-8.

Mösta, P., Richers, S., Ott, C. D., Haas, R., et al., 2014. Magnetorotational Core-collapse Supernovae in Three Dimensions. *ApJ*, 785(2):L29, doi: 10.1088/2041-8205/785/2/L29.

Müller, B., 2015. The dynamics of neutrino-driven supernova explosions after shock revival in 2D and 3D. *MNRAS*, 453:287–310, doi: 10.1093/mnras/stv1611.

Müller, B., 2016. The Status of Multi-Dimensional Core-Collapse Supernova Models. *PASA*, 33:e048, doi: 10.1017/pasa.2016.40.

Müller, B., 2020. Hydrodynamics of core-collapse supernovae and their progenitors. *Living Reviews in Computational Astrophysics*, 6(1):3, doi: 10.1007/s41115-020-0008-5.

Müller, B. & Chan, C., 2019. An FFT-based Solution Method for the Poisson Equation on 3D Spherical Polar Grids. *ApJ*, 870(1):43, doi: 10.3847/1538-4357/aaf100.

Müller, B. & Janka, H.-T., 2014. A New Multi-dimensional General Relativistic Neutrino Hydrodynamics Code for Core-collapse Supernovae. IV. The Neutrino Signal. *ApJ*, 788 (1):82, doi: 10.1088/0004-637X/788/1/82.

Müller, B. & Janka, H.-T., 2015. Non-radial instabilities and progenitor asphericities in core-collapse supernovae. *MNRAS*, 448:2141–2174, doi: 10.1093/mnras/stv101.

Müller, B. & Varma, V., 2020. A 3D simulation of a neutrino-driven supernova explosion aided by convection and magnetic fields. *MNRAS*, 498(1):L109–L113, doi: 10.1093/mnrasl/slaa137.

Müller, B., Janka, H.-T., & Dimmelmeier, H., 2010. A New Multi-dimensional General Relativistic Neutrino Hydrodynamic Code for Core-collapse Supernovae. I. Method and Code Tests in Spherical Symmetry. *ApJS*, 189:104–133, doi: 10.1088/0067-0049/189/1/104.

Müller, B., Janka, H.-T., & Marek, A., 2013. A New Multi-dimensional General Relativistic Neutrino Hydrodynamics Code of Core-collapse Supernovae. III. Gravitational Wave Signals from Supernova Explosion Models. *ApJ*, 766:43, doi: 10.1088/0004-637X/766/1/43.

Müller, B., Viallet, M., Heger, A., & Janka, H.-T., 2016. The Last Minutes of Oxygen Shell Burning in a Massive Star. *ApJ*, 833:124, doi: 10.3847/1538-4357/833/1/124.

Müller, B., Melson, T., Heger, A., & Janka, H.-T., 2017. Supernova simulations from a 3D progenitor model - Impact of perturbations and evolution of explosion properties. *MNRAS*, 472(1):491–513, doi: 10.1093/mnras/stx1962.

Müller, B., Gay, D. W., Heger, A., Tauris, T. M., & Sim, S. A., 2018. Multidimensional simulations of ultrastripped supernovae to shock breakout. *MNRAS*, 479(3):3675–3689, doi: 10.1093/mnras/sty1683.

Müller, B., Tauris, T. M., Heger, A., Banerjee, P., et al., 2019. Three-dimensional simulations of neutrino-driven core-collapse supernovae from low-mass single and binary star progenitors. *MNRAS*, 484:3307–3324, doi: 10.1093/mnras/stz216.

Müller, E., 1998. Simulation of Astrophysical Fluid Flow. In Steiner, O. & Gautschy, A., editors, *Saas-Fee Advanced Course 27: Computational Methods for Astrophysical Fluid Flow.*, page 343.

Müller, E. & Steinmetz, M., 1995. Simulating self-gravitating hydrodynamic flows. *CoPhC*, 89:45–58, doi: 10.1016/0010-4655(94)00185-5.

Müller, E., Rampp, M., Buras, R., Janka, H. T., & Shoemaker, D. H., 2004. Toward Gravitational Wave Signals from Realistic Core-Collapse Supernova Models. *ApJ*, 603 (1):221–230, doi: 10.1086/381360.

Murphy, J. W., Dolence, J. C., & Burrows, A., 2013. The Dominance of Neutrino-driven Convection in Core-collapse Supernovae. *ApJ*, 771:52, doi: 10.1088/0004-637X/771/1/52.

Murphy, J. W., Mabanta, Q., & Dolence, J. C., 2019. A comparison of explosion energies for simulated and observed core-collapse supernovae. *MNRAS*, 489(1):641–652, doi: 10.1093/mnras/stz2123.

Nadyozhin, D. K., 1994. The Properties of NI CO Fe Decay. *ApJS*, 92:527, doi: 10.1086/192008.

Nagakura, H., Burrows, A., Radice, D., & Vartanyan, D., 2019. Towards an understanding of the resolution dependence of Core-Collapse Supernova simulations. *MNRAS*, 490(4):4622–4637, doi: 10.1093/mnras/stz2730.

Nagakura, H., Burrows, A., Radice, D., & Vartanyan, D., 2020. A systematic study of proto-neutron star convection in three-dimensional core-collapse supernova simulations. *MNRAS*, 492(4):5764–5779, doi: 10.1093/mnras/staa261.

Nagao, T., Cikota, A., Patat, F., Taubenberger, S., et al., 2019. The aspherical explosion of the Type IIP SN 2017gmr$^{\breve{D}}$. *MNRAS*, 489(1):L69–L74, doi: 10.1093/mnrasl/slz119.

Nagao, T., Patat, F., Taubenberger, S., Baade, D., et al., 2021. Evidence for multiple origins of fast declining Type II supernovae from spectropolarimetry of SN 2013ej and SN 2017ahn. *MNRAS*, 505(3):3664–3680, doi: 10.1093/mnras/stab1582.

Nakamura, K., Kuroda, T., Takiwaki, T., & Kotake, K., 2014. Impacts of Rotation on Three-dimensional Hydrodynamics of Core-collapse Supernovae. *ApJ*, 793:45, doi: 10.1088/0004-637X/793/1/45.

Nakamura, K., Takiwaki, T., & Kotake, K., 2019. Long-term simulations of multi-dimensional core-collapse supernovae: Implications for neutron star kicks. *PASJ*, 71(5):98, doi: 10.1093/pasj/psz080.

Nakar, E., Poznanski, D., & Katz, B., 2016. The Importance of ^{56}Ni in Shaping the Light Curves of Type II Supernovae. *ApJ*, 823(2):127, doi: 10.3847/0004-637X/823/2/127.

Navó, G., Reichert, M., Obergaulinger, M., & Arcones, A., 2023. Core-collapse Supernova Simulations with Reduced Nucleosynthesis Networks. *ApJ*, 951(2):112, doi: 10.3847/1538-4357/acd640.

Nevins, B. & Roberts, L. F., 2023. Proto-Neutron Star Convection and the Neutrino-Driven Wind: Implications for the r-Process. *MNRAS*, doi: 10.1093/mnras/stad372.

Ng, C. Y. & Romani, R. W., 2007. Birth Kick Distributions and the Spin-Kick Correlation of Young Pulsars. *ApJ*, 660(2):1357–1374, doi: 10.1086/513597.

Nordhaus, J., Brandt, T. D., Burrows, A., Livne, E., & Ott, C. D., 2010a. Theoretical support for the hydrodynamic mechanism of pulsar kicks. *Phys. Rev. D*, 82(10):103016, doi: 10.1103/PhysRevD.82.103016.

Nordhaus, J., Burrows, A., Almgren, A., & Bell, J., 2010b. Dimension as a Key to the Neutrino Mechanism of Core-collapse Supernova Explosions. *ApJ*, 720:694–703, doi: 10.1088/0004-637X/720/1/694.

Nordhaus, J., Brandt, T. D., Burrows, A., & Almgren, A., 2012. The hydrodynamic origin of neutron star kicks. *MNRAS*, 423(2):1805–1812, doi: 10.1111/j.1365-2966.2012.21002.x.

Noutsos, A., Schnitzeler, D. H. F. M., Keane, E. F., Kramer, M., & Johnston, S., 2013. Pulsar spin-velocity alignment: kinematic ages, birth periods and braking indices. *MNRAS*, 430(3):2281–2301, doi: 10.1093/mnras/stt047.

Obergaulinger, M. & Aloy, M. Á., 2021. Magnetorotational core collapse of possible GRB progenitors - III. Three-dimensional models. *MNRAS*, 503(4):4942–4963, doi: 10.1093/mnras/stab295.

Obergaulinger, M., Cerdá-Durán, P., Müller, E., & Aloy, M. A., 2009. Semi-global simulations of the magneto-rotational instability in core collapse supernovae. *A&A*, 498 (1):241–271, doi: 10.1051/0004-6361/200811323.

O'Connor, E., 2015. An Open-source Neutrino Radiation Hydrodynamics Code for Core-collapse Supernovae. *ApJS*, 219(2):24, doi: 10.1088/0067-0049/219/2/24.

O'Connor, E. & Ott, C. D., 2011. Black Hole Formation in Failing Core-Collapse Supernovae. *ApJ*, 730(2):70, doi: 10.1088/0004-637X/730/2/70.

O'Connor, E. P. & Couch, S. M., 2018a. Exploring Fundamentally Three-dimensional Phenomena in High-fidelity Simulations of Core-collapse Supernovae. *ApJ*, 865(2):81, doi: 10.3847/1538-4357/aadcf7.

O'Connor, E. P. & Couch, S. M., 2018b. Two-dimensional Core-collapse Supernova Explosions Aided by General Relativity with Multidimensional Neutrino Transport. *ApJ*, 854(1):63, doi: 10.3847/1538-4357/aaa893.

Oertel, M., Hempel, M., Klähn, T., & Typel, S., 2017. Equations of state for supernovae and compact stars. *Reviews of Modern Physics*, 89(1):015007, doi: 10.1103/RevModPhys.89.015007.

Otsuki, K., Tagoshi, H., Kajino, T., & Wanajo, S.-y., 2000. General Relativistic Effects on Neutrino-driven Winds from Young, Hot Neutron Stars and r-Process Nucleosynthesis. *ApJ*, 533(1):424–439, doi: 10.1086/308632.

Ott, C. D., Burrows, A., Thompson, T. A., Livne, E., & Walder, R., 2006. The Spin Periods and Rotational Profiles of Neutron Stars at Birth. *ApJS*, 164(1):130–155, doi: 10.1086/500832.

Ott, C. D., Abdikamalov, E., Mösta, P., Haas, R., et al., 2013. General-relativistic Simulations of Three-dimensional Core-collapse Supernovae. *ApJ*, 768:115, doi: 10.1088/0004-637X/768/2/115.

Ott, C. D., Roberts, L. F., da Silva Schneider, A., Fedrow, J. M., et al., 2018. The Progenitor Dependence of Core-collapse Supernovae from Three-dimensional Simulations with Progenitor Models of 12-40 M $_\odot$. *ApJ*, 855(1):L3, doi: 10.3847/2041-8213/aaa967.

Özel, F. & Freire, P., 2016. Masses, Radii, and the Equation of State of Neutron Stars. *ARA&A*, 54:401–440, doi: 10.1146/annurev-astro-081915-023322.

Page, D., Beznogov, M. V., Garibay, I., Lattimer, J. M., et al., 2020. NS 1987A in SN 1987A. *ApJ*, 898(2):125, doi: 10.3847/1538-4357/ab93c2.

Pan, K.-C., Liebendörfer, M., Hempel, M., & Thielemann, F.-K., 2016. Two-dimensional Core-collapse Supernova Simulations with the Isotropic Diffusion Source Approximation for Neutrino Transport. *ApJ*, 817(1):72, doi: 10.3847/0004-637X/817/1/72.

Papish, O., Nordhaus, J., & Soker, N., 2015. A call for a paradigm shift from neutrino-driven to jet-driven core-collapse supernova mechanisms. *MNRAS*, 448(3):2362–2367, doi: 10.1093/mnras/stv131.

Pastorello, A., Zampieri, L., Turatto, M., Cappellaro, E., et al., 2004. Low-luminosity Type II supernovae: spectroscopic and photometric evolution. *MNRAS*, 347(1):74–94, doi: 10.1111/j.1365-2966.2004.07173.x.

Pejcha, O. & Prieto, J. L., 2015a. A Global Model of The Light Curves and Expansion Velocities of Type II-plateau Supernovae. *ApJ*, 799(2):215, doi: 10.1088/0004-637X/799/2/215.

Pejcha, O. & Prieto, J. L., 2015b. On the Intrinsic Diversity of Type II-Plateau Supernovae. *ApJ*, 806(2):225, doi: 10.1088/0004-637X/806/2/225.

Peng, X., Xiao, F., & Takahashi, K., 2006. Conservative constraint for a quasi-uniform overset grid on the sphere. *QJRMS*, 132:979–996, doi: 10.1256/qj.05.18.

Perez, F. & Granger, B. E., 2007. IPython: A System for Interactive Scientific Computing. *Computing in Science and Engineering*, 9(3):21–29, doi: 10.1109/MCSE.2007.53.

Petre, R., Becker, C. M., & Winkler, P. F., 1996. A Central Stellar Remnant in Puppis A. *ApJ*, 465:L43, doi: 10.1086/310141.

Plewa, T. & Müller, E., 1999. The consistent multi-fluid advection method. *A&A*, 342: 179–191.

Pllumbi, E., Tamborra, I., Wanajo, S., Janka, H.-T., & Hüdepohl, L., 2015. Impact of Neutrino Flavor Oscillations on the Neutrino-driven Wind Nucleosynthesis of an Electron-capture Supernova. *ApJ*, 808(2):188, doi: 10.1088/0004-637X/808/2/188.

Podsiadlowski, P., Langer, N., Poelarends, A. J. T., Rappaport, S., et al., 2004. The Effects of Binary Evolution on the Dynamics of Core Collapse and Neutron Star Kicks. *ApJ*, 612(2):1044–1051, doi: 10.1086/421713.

Pons, J. A., Miralles, J. A., & Ibanez, J. M. A., 1998. Legendre expansion of the $\nu\bar{\nu} \rightleftharpoons e^+e^-$ kernel: Influence of high order terms. *A&AS*, 129:343–351, doi: 10.1051/aas:1998189.

Popov, D. V., 1993. An Analytical Model for the Plateau Stage of Type II Supernovae. *ApJ*, 414:712, doi: 10.1086/173117.

Popov, S. B. & Turolla, R., 2012. Initial spin periods of neutron stars in supernova remnants. *Ap&SS*, 341(2):457–464, doi: 10.1007/s10509-012-1100-z.

Powell, J. & Müller, B., 2019. Gravitational wave emission from 3D explosion models of core-collapse supernovae with low and normal explosion energies. *MNRAS*, 487(1): 1178–1190, doi: 10.1093/mnras/stz1304.

Powell, J. & Müller, B., 2020. Three-dimensional core-collapse supernova simulations of massive and rotating progenitors. *MNRAS*, 494(4):4665–4675, doi: 10.1093/mnras/staa1048.

Powell, J. & Müller, B., 2022. Inferring astrophysical parameters of core-collapse supernovae from their gravitational-wave emission. *Phys. Rev. D*, 105(6):063018, doi: 10.1103/PhysRevD.105.063018.

Qian, Y. Z. & Woosley, S. E., 1996. Nucleosynthesis in Neutrino-driven Winds. I. The Physical Conditions. *ApJ*, 471:331, doi: 10.1086/177973.

Quirk, J. J., 1994. A contribution to the great Riemann solver debate. *IJNMF*, 18:555–574, doi: 10.1002/fld.1650180603.

Raaijmakers, G., Greif, S. K., Hebeler, K., Hinderer, T., et al., 2021. Constraints on the Dense Matter Equation of State and Neutron Star Properties from NICER's Mass-Radius Estimate of PSR J0740+6620 and Multimessenger Observations. *ApJ*, 918(2): L29, doi: 10.3847/2041-8213/ac089a.

Radice, D., Couch, S. M., & Ott, C. D., 2015. Implicit large eddy simulations of anisotropic weakly compressible turbulence with application to core-collapse supernovae. *ComAC*, 2: 7, doi: 10.1186/s40668-015-0011-0.

Radice, D., Ott, C. D., Abdikamalov, E., Couch, S. M., et al., 2016. Neutrino-driven Convection in Core-collapse Supernovae: High-resolution Simulations. *ApJ*, 820:76, doi: 10.3847/0004-637X/820/1/76.

Radice, D., Burrows, A., Vartanyan, D., Skinner, M. A., & Dolence, J. C., 2017. Electron-capture and Low-mass Iron-core-collapse Supernovae: New Neutrino-radiation-hydrodynamics Simulations. *ApJ*, 850(1):43, doi: 10.3847/1538-4357/aa92c5.

Rampp, M., 2000. *Radiation Hydrodynamics with Neutrinos: Stellar Core Collapse and the Explosion Mechanism of Type II Supernovae*. PhD thesis, Technische Universität München.

Rampp, M. & Janka, H.-T., 2002. Radiation hydrodynamics with neutrinos. Variable Eddington factor method for core-collapse supernova simulations. *A&A*, 396:361–392, doi: 10.1051/0004-6361:20021398.

Riley, T. E., Watts, A. L., Bogdanov, S., Ray, P. S., et al., 2019. A NICER View of PSR J0030+0451: Millisecond Pulsar Parameter Estimation. *ApJ*, 887(1):L21, doi: 10.3847/2041-8213/ab481c.

Riley, T. E., Watts, A. L., Ray, P. S., Bogdanov, S., et al., 2021. A NICER View of the Massive Pulsar PSR J0740+6620 Informed by Radio Timing and XMM-Newton Spectroscopy. *ApJ*, 918(2):L27, doi: 10.3847/2041-8213/ac0a81.

Roberts, L. F., Ott, C. D., Haas, R., O'Connor, E. P., et al., 2016. General-Relativistic Three-Dimensional Multi-group Neutrino Radiation-Hydrodynamics Simulations of Core-Collapse Supernovae. *ApJ*, 831:98, doi: 10.3847/0004-637X/831/1/98.

Romani, R. W., Kandel, D., Filippenko, A. V., Brink, T. G., & Zheng, W., 2021. PSR J1810+1744: Companion Darkening and a Precise High Neutron Star Mass. *ApJ*, 908 (2):L46, doi: 10.3847/2041-8213/abe2b4.

Romani, R. W., Kandel, D., Filippenko, A. V., Brink, T. G., & Zheng, W., 2022. PSR J0952-0607: The Fastest and Heaviest Known Galactic Neutron Star. *ApJ*, 934(2):L17, doi: 10.3847/2041-8213/ac8007.

Ronchi, C., Iacono, R., & Paolucci, P. S., 1996. The "Cubed Sphere": A New Method for the Solution of Partial Differential Equations in Spherical Geometry. *JCoPh*, 124: 93–114, doi: 10.1006/jcph.1996.0047.

Sandoval, M. A., Hix, W. R., Messer, O. E. B., Lentz, E. J., & Harris, J. A., 2021. Three-dimensional Core-collapse Supernova Simulations with 160 Isotopic Species Evolved to Shock Breakout. *ApJ*, 921(2):113, doi: 10.3847/1538-4357/ac1d49.

Sawada, R. & Suwa, Y., 2023. Updating the ^{56}Ni Problem in Core-collapse Supernova Explosion. *arXiv e-prints*, art. arXiv:2301.03610, doi: 10.48550/arXiv.2301.03610.

Sawatzki, J., Wurm, M., & Kresse, D., 2021. Detecting the diffuse supernova neutrino background in the future water-based liquid scintillator detector Theia. *Phys. Rev. D*, 103(2):023021, doi: 10.1103/PhysRevD.103.023021.

Scheck, L., Plewa, T., Janka, H. T., Kifonidis, K., & Müller, E., 2004. Pulsar Recoil by Large-Scale Anisotropies in Supernova Explosions. *Phys. Rev. Lett.*, 92(1):011103, doi: 10.1103/PhysRevLett.92.011103.

Scheck, L., Kifonidis, K., Janka, H.-T., & Müller, E., 2006. Multidimensional supernova simulations with approximative neutrino transport. I. Neutron star kicks and the anisotropy of neutrino-driven explosions in two spatial dimensions. *A&A*, 457(3):963–986, doi: 10.1051/0004-6361:20064855.

Scheck, L., Janka, H.-T., Foglizzo, T., & Kifonidis, K., 2008. Multidimensional supernova simulations with approximative neutrino transport. II. Convection and the advective-acoustic cycle in the supernova core. *A&A*, 477:931–952, doi: 10.1051/0004-6361: 20077701.

Schneider, A. S., Constantinou, C., Muccioli, B., & Prakash, M., 2019. Akmal-Pandharipande-Ravenhall equation of state for simulations of supernovae, neutron stars, and binary mergers. *Phys. Rev. C*, 100(2):025803, doi: 10.1103/PhysRevC.100.025803.

Schneider, F. R. N., Izzard, R. G., Langer, N., & de Mink, S. E., 2015. Evolution of Mass Functions of Coeval Stars through Wind Mass Loss and Binary Interactions. *ApJ*, 805 (1):20, doi: 10.1088/0004-637X/805/1/20.

Schneider, F. R. N., Podsiadlowski, P., & Müller, B., 2021. Pre-supernova evolution, compact-object masses, and explosion properties of stripped binary stars. *A&A*, 645:A5, doi: 10.1051/0004-6361/202039219.

Sedov, L. I., 1959. *Similarity and Dimensional Methods in Mechanics*. Infosearch.

Shapiro, S. L. & Teukolsky, S. A., 1983. *Black Holes, White Dwarfs and Neutron Stars*. WILEY-VCH.

Sieverding, A., Müller, B., & Qian, Y. Z., 2020. Nucleosynthesis of an 11.8 $M_\odot$ Supernova with 3D Simulation of the Inner Ejecta: Overall Yields and Implications for Short-lived Radionuclides in the Early Solar System. *ApJ*, 904(2):163, doi: 10.3847/1538-4357/abc61b.

Sieverding, A., Waldrop, P. G., Harris, J. A., Hix, W. R., et al., 2023. Tracer Particles for Core-collapse Supernova Nucleosynthesis: The Advantages of Moving Backward. *ApJ*, 950(1):34, doi: 10.3847/1538-4357/acc8d1.

Skinner, M. A., Burrows, A., & Dolence, J. C., 2016. Should One Use the Ray-by-Ray Approximation in Core-collapse Supernova Simulations? *ApJ*, 831(1):81, doi: 10.3847/0004-637X/831/1/81.

Skinner, M. A., Dolence, J. C., Burrows, A., Radice, D., & Vartanyan, D., 2019. FORNAX: A Flexible Code for Multiphysics Astrophysical Simulations. *ApJS*, 241:7, doi: 10.3847/1538-4365/ab007f.

Smartt, S. J., Valenti, S., Fraser, M., Inserra, C., et al., 2015. PESSTO: survey description and products from the first data release by the Public ESO Spectroscopic Survey of Transient Objects. *A&A*, 579:A40, doi: 10.1051/0004-6361/201425237.

Smith, N., 2013. The Crab nebula and the class of Type IIn-P supernovae caused by sub-energetic electron-capture explosions. *MNRAS*, 434(1):102–113, doi: 10.1093/mnras/stt1004.

Spiro, S., Pastorello, A., Pumo, M. L., Zampieri, L., et al., 2014. Low luminosity Type II supernovae - II. Pointing towards moderate mass precursors. *MNRAS*, 439(3):2873–2892, doi: 10.1093/mnras/stu156.

Spruit, H. & Phinney, E. S., 1998. Birth kicks as the origin of pulsar rotation. *Nature*, 393 (6681):139–141, doi: 10.1038/30168.

Steiner, A. W., Hempel, M., & Fischer, T., 2013. Core-collapse Supernova Equations of State Based on Neutron Star Observations. *ApJ*, 774(1):17, doi: 10.1088/0004-637X/774/1/17.

Stockinger, G., Janka, H.-T., Kresse, D., Melson, T., et al., 2020. Three-dimensional models of core-collapse supernovae from low-mass progenitors with implications for Crab. *MNRAS*, 496(2):2039–2084, doi: 10.1093/mnras/staa1691.

Sukhbold, T., Ertl, T., Woosley, S. E., Brown, J. M., & Janka, H.-T., 2016. Core-collapse Supernovae from 9 to 120 Solar Masses Based on Neutrino-powered Explosions. *ApJ*, 821(1):38, doi: 10.3847/0004-637X/821/1/38.

Summa, A., Hanke, F., Janka, H.-T., Melson, T., et al., 2016. Progenitor-dependent Explosion Dynamics in Self-consistent, Axisymmetric Simulations of Neutrino-driven Core-collapse Supernovae. *ApJ*, 825:6. URL http://stacks.iop.org/0004-637X/825/i=1/a=6.

Summa, A., Janka, H.-T., Melson, T., & Marek, A., 2018. Rotation-supported Neutrino-driven Supernova Explosions in Three Dimensions and the Critical Luminosity Condition. *ApJ*, 852(1):28, doi: 10.3847/1538-4357/aa9ce8.

Suntzeff, N. B., Phillips, M. M., Elias, J. H., Depoy, D. L., & Walker, A. R., 1992. The Energy Sources Powering the Late-Time Bolometric Evolution of SN 1987A. *ApJ*, 384: L33, doi: 10.1086/186256.

Suwa, Y., Takiwaki, T., Kotake, K., Fischer, T., et al., 2013. On the Importance of the Equation of State for the Neutrino-driven Supernova Explosion Mechanism. *ApJ*, 764: 99, doi: 10.1088/0004-637X/764/1/99.

Suwa, Y., Yamada, S., Takiwaki, T., & Kotake, K., 2016. The Criterion of Supernova Explosion Revisited: The Mass Accretion History. *ApJ*, 816:43, doi: 10.3847/0004-637X/816/1/43.

Suwa, Y., Tominaga, N., & Maeda, K., 2019. Importance of ^{56}Ni production on diagnosing explosion mechanism of core-collapse supernova. *MNRAS*, 483(3):3607–3617, doi: 10.1093/mnras/sty3309.

Takahashi, K., Witti, J., & Janka, H. T., 1994. Nucleosynthesis in neutrino-driven winds from protoneutron stars II. The r-process. *A&A*, 286:857–869.

Takiwaki, T. & Kotake, K., 2018. Anisotropic emission of neutrino and gravitational-wave signals from rapidly rotating core-collapse supernovae. *MNRAS*, 475(1):L91–L95, doi: 10.1093/mnrasl/sly008.

Takiwaki, T., Kotake, K., & Suwa, Y., 2012. Three-dimensional Hydrodynamic Core-collapse Supernova Simulations for an 11.2 $M_\odot$ Star with Spectral Neutrino Transport. *ApJ*, 749:98, doi: 10.1088/0004-637X/749/2/98.

Takiwaki, T., Kotake, K., & Suwa, Y., 2014. A Comparison of Two- and Three-dimensional Neutrino-hydrodynamics Simulations of Core-collapse Supernovae. *ApJ*, 786(2):83, doi: 10.1088/0004-637X/786/2/83.

Takiwaki, T., Kotake, K., & Suwa, Y., 2016. Three-dimensional simulations of rapidly rotating core-collapse supernovae: finding a neutrino-powered explosion aided by non-axisymmetric flows. *MNRAS*, 461:L112–L116, doi: 10.1093/mnrasl/slw105.

Tamborra, I., Hanke, F., Müller, B., Janka, H.-T., & Raffelt, G., 2013. Neutrino Signature of Supernova Hydrodynamical Instabilities in Three Dimensions. *PhRvL*, 111(12):121104, doi: 10.1103/PhysRevLett.111.121104.

Tamborra, I., Hanke, F., Janka, H.-T., Müller, B., et al., 2014a. Self-sustained Asymmetry of Lepton-number Emission: A New Phenomenon during the Supernova Shock-accretion Phase in Three Dimensions. *ApJ*, 792:96, doi: 10.1088/0004-637X/792/2/96.

Tamborra, I., Raffelt, G., Hanke, F., Janka, H.-T., & Müller, B., 2014b. Neutrino emission characteristics and detection opportunities based on three-dimensional supernova simulations. *Phys. Rev. D*, 90(4):045032, doi: 10.1103/PhysRevD.90.045032.

Thorsett, S. E. & Chakrabarty, D., 1999. Neutron Star Mass Measurements. I. Radio Pulsars. *ApJ*, 512(1):288–299, doi: 10.1086/306742.

Tominaga, N., Blinnikov, S. I., & Nomoto, K., 2013. Supernova Explosions of Super-asymptotic Giant Branch Stars: Multicolor Light Curves of Electron-capture Supernovae. *ApJ*, 771(1):L12, doi: 10.1088/2041-8205/771/1/L12.

Typel, S., Röpke, G., Klähn, T., Blaschke, D., & Wolter, H. H., 2010. Composition and thermodynamics of nuclear matter with light clusters. *PhRvC*, 81(1):015803, doi: 10.1103/PhysRevC.81.015803.

Utrobin, V. P., Wongwathanarat, A., Janka, H.-T., & Müller, E., 2015. Supernova 1987A: neutrino-driven explosions in three dimensions and light curves. *A&A*, 581:A40, doi: 10.1051/0004-6361/201425513.

Utrobin, V. P., Wongwathanarat, A., Janka, H. T., Müller, E., et al., 2019. Three-dimensional mixing and light curves: constraints on the progenitor of supernova 1987A. *A&A*, 624:A116, doi: 10.1051/0004-6361/201834976.

Utrobin, V. P., Wongwathanarat, A., Janka, H. T., Müller, E., et al., 2021. Supernova 1987A: 3D Mixing and Light Curves for Explosion Models Based on Binary-merger Progenitors. *ApJ*, 914(1):4, doi: 10.3847/1538-4357/abf4c5.

Valerin, G., Pumo, M. L., Pastorello, A., Reguitti, A., et al., 2022. Low luminosity Type II supernovae - IV. SN 2020cxd and SN 2021aai, at the edges of the sub-luminous supernovae class. *MNRAS*, 513(4):4983–4999, doi: 10.1093/mnras/stac1182.

van den Horn, L. J. & van Weert, C. G., 1984. Transport properties of neutrinos in stellar collapse. II - Shear viscosity, heat conduction, and diffusion. *A&A*, 136(1):74–80.

van der Velden, E., 2020. CMasher: Scientific colormaps for making accessible, informative and 'cmashing' plots. *The Journal of Open Source Software*, 5(46):2004, doi: 10.21105/joss.02004.

Van Halen, P. & Pulfrey, D. L., 1985. Accurate, short series approximations to Fermi-Dirac integrals of order -1/2, 1/2, 1, 3/2, 2, 5/2, 3, and 7/2. *Journal of Applied Physics*, 57 (12):5271–5274, doi: 10.1063/1.335269.

Varma, V. & Müller, B., 2021. 3D simulations of oxygen shell burning with and without magnetic fields. *MNRAS*, 504(1):636–647, doi: 10.1093/mnras/stab883.

Varma, V., Müller, B., & Schneider, F. R. N., 2023. 3D simulations of strongly magnetized non-rotating supernovae: explosion dynamics and remnant properties. *MNRAS*, 518(3): 3622–3636, doi: 10.1093/mnras/stac3247.

Vartanyan, D. & Burrows, A., 2020. Gravitational Waves from Neutrino Emission Asymmetries in Core-collapse Supernovae. *ApJ*, 901(2):108, doi: 10.3847/1538-4357/abafac.

Vartanyan, D., Burrows, A., Radice, D., Skinner, M. A., & Dolence, J., 2018. Revival of the fittest: exploding core-collapse supernovae from 12 to 25 $M_\odot$. *MNRAS*, 477(3): 3091–3108, doi: 10.1093/mnras/sty809.

Vartanyan, D., Burrows, A., & Radice, D., 2019a. Temporal and angular variations of 3D core-collapse supernova emissions and their physical correlations. *MNRAS*, 489(2): 2227–2246, doi: 10.1093/mnras/stz2307.

Vartanyan, D., Burrows, A., Radice, D., Skinner, M. A., & Dolence, J., 2019b. A successful 3D core-collapse supernova explosion model. *MNRAS*, 482(1):351–369, doi: 10.1093/mnras/sty2585.

Vartanyan, D., Coleman, M. S. B., & Burrows, A., 2022. The collapse and three-dimensional explosion of three-dimensional massive-star supernova progenitor models. *MNRAS*, 510 (4):4689–4705, doi: 10.1093/mnras/stab3702.

Vasylyev, S. S., Yang, Y., Patra, K. C., Filippenko, A. V., et al., 2023. Spectropolarimetry of the type IIP supernova 2021yja: an unusually high continuum polarization during the photospheric phase. *arXiv e-prints*, art. arXiv:2303.06497.

Virtanen, P., Gommers, R., Oliphant, T. E., Haberland, M., et al., 2020. SciPy 1.0: fundamental algorithms for scientific computing in Python. *Nature Methods*, 17:261–272, doi: 10.1038/s41592-019-0686-2.

Walborn, N. R., Lasker, B. M., Laidler, V. G., & Chu, Y.-H., 1987. The Composite Image of Sanduleak -69 degrees 202, Candidate Precursor to Supernova 1978A in the Large Magellanic Cloud. *ApJ*, 321:L41, doi: 10.1086/185002.

Walk, L., Tamborra, I., Janka, H.-T., & Summa, A., 2019. Effects of the standing accretion-shock instability and the lepton-emission self-sustained asymmetry in the neutrino emission of rotating supernovae. *Phys. Rev. D*, 100(6):063018, doi: 10.1103/PhysRevD.100.063018.

Walk, L., Tamborra, I., Janka, H.-T., Summa, A., & Kresse, D., 2020. Neutrino emission characteristics of black hole formation in three-dimensional simulations of stellar collapse. *Phys. Rev. D*, 101(12):123013, doi: 10.1103/PhysRevD.101.123013.

Wanajo, S., 2007. Cold r-Process in Neutrino-driven Winds. *ApJ*, 666(2):L77–L80, doi: 10.1086/521724.

Wanajo, S., Itoh, N., Ishimaru, Y., Nozawa, S., & Beers, T. C., 2002. The r-Process in the Neutrino Winds of Core-Collapse Supernovae and U-Th Cosmochronology. *ApJ*, 577(2): 853–865, doi: 10.1086/342230.

Wanajo, S., Müller, B., Janka, H.-T., & Heger, A., 2018. Nucleosynthesis in the Innermost Ejecta of Neutrino-driven Supernova Explosions in Two Dimensions. *ApJ*, 852(1):40, doi: 10.3847/1538-4357/aa9d97.

Wang, L. & Wheeler, J. C., 2008. Spectropolarimetry of Supernovae. *ARA&A*, 46:433–474, doi: 10.1146/annurev.astro.46.060407.145139.

Weaver, T. A., Zimmerman, G. B., & Woosley, S. E., 1978. Presupernova evolution of massive stars. *ApJ*, 225:1021–1029, doi: 10.1086/156569.

Wilson, J. R., 1985. Supernovae and Post-Collapse Behavior. In Centrella, J. M., Leblanc, J. M., & Bowers, R. L., editors, *Numerical Astrophysics*, page 422.

Winkler, P. F. & Kirshner, R. P., 1985. Discovery of fast-moving oxygen filaments in Puppis A. *ApJ*, 299:981–986, doi: 10.1086/163764.

Witt, M., Psaltis, A., Yasin, H., Horn, C., et al., 2021. Post-explosion Evolution of Core-collapse Supernovae. *ApJ*, 921(1):19, doi: 10.3847/1538-4357/ac1a6d.

Wongwathanarat, A., Hammer, N. J., & Müller, E., 2010a. An axis-free overset grid in spherical polar coordinates for simulating 3D self-gravitating flows. *A&A*, 514:A48, doi: 10.1051/0004-6361/200913435.

Wongwathanarat, A., Janka, H.-T., & Müller, E., 2010b. Hydrodynamical Neutron Star Kicks in Three Dimensions. *ApJL*, 725:L106–L110, doi: 10.1088/2041-8205/725/1/L106.

Wongwathanarat, A., Janka, H.-T., & Müller, E., 2013. Three-dimensional neutrino-driven supernovae: Neutron star kicks, spins, and asymmetric ejection of nucleosynthesis products. *A&A*, 552:A126, doi: 10.1051/0004-6361/201220636.

Wongwathanarat, A., Müller, E., & Janka, H. T., 2015. Three-dimensional simulations of core-collapse supernovae: from shock revival to shock breakout. *A&A*, 577:A48, doi: 10.1051/0004-6361/201425025.

Woosley, S. E., 2019. The Evolution of Massive Helium Stars, Including Mass Loss. *ApJ*, 878(1):49, doi: 10.3847/1538-4357/ab1b41.

Woosley, S. E. & Heger, A., 2007. Nucleosynthesis and remnants in massive stars of solar metallicity. *Phys. Rep.*, 442(1-6):269–283, doi: 10.1016/j.physrep.2007.02.009.

Woosley, S. E. & Heger, A., 2015. The Remarkable Deaths of 9-11 Solar Mass Stars. *ApJ*, 810(1):34, doi: 10.1088/0004-637X/810/1/34.

Woosley, S. E., Pinto, P. A., & Ensman, L., 1988. Supernova 1987A: Six Weeks Later. *ApJ*, 324:466, doi: 10.1086/165908.

Woosley, S. E., Heger, A., & Weaver, T. A., 2002. The evolution and explosion of massive stars. *Reviews of Modern Physics*, 74(4):1015–1071, doi: 10.1103/RevModPhys.74.1015.

Yadav, N., Müller, B., Janka, H. T., Melson, T., & Heger, A., 2020. Large-scale Mixing in a Violent Oxygen-Neon Shell Merger Prior to a Core-collapse Supernova. *ApJ*, 890(2): 94, doi: 10.3847/1538-4357/ab66bb.

Yang, H. & Chevalier, R. A., 2015. Evolution of the Crab Nebula in a Low Energy Supernova. *ApJ*, 806(2):153, doi: 10.1088/0004-637X/806/2/153.

Yasin, H., Schäfer, S., Arcones, A., & Schwenk, A., 2020. Equation of State Effects in Core-Collapse Supernovae. *Phys. Rev. Lett.*, 124(9):092701, doi: 10.1103/PhysRevLett.124.092701.

Yoshida, T., Takiwaki, T., Kotake, K., Takahashi, K., et al., 2019. One-, Two-, and Three-dimensional Simulations of Oxygen-shell Burning Just before the Core Collapse of Massive Stars. *ApJ*, 881(1):16, doi: 10.3847/1538-4357/ab2b9d.

Danksagung

Allen voran danke ich besonders meinem Doktorvater und Mentor Thomas Janka für seine uneingeschränkte Unterstützung während der gesamten Zeit meiner Doktorarbeit, für stets wertvolle und konstruktive Kritik, für seinen Vertrauensvorschuss und dafür, dass er sich immer Zeit genommen hat, wenn es nötig war. Seine zahlreichen Denkanstöße, Anregungen und Ideen waren essenziell für das Zustandekommen dieser Dissertation.

Mein Dank gilt außerdem meinen vielen netten und hilfsbereiten Kolleginnen und Kollegen, die nicht unwesentlich zum Gelingen dieser Arbeit beigetragen haben. Ich bedanke mich insbesondere bei Tobias Melson für seine Einführungen in PROMETHEUS-VERTEX *und die zugehörige Auswertungssoftware (*`vertexpython` *bzw.* `snappy`*) sowie für die Bereitstellung seiner Simulationsergebnisse, auf denen die Rechnungen dieser Arbeit aufbauen. Im Weiteren möchte ich mich bei Robert Bollig für seine Hilfe bei technischen Fragen (rund um* PROMETHEUS-VERTEX *und Hochleistungsrechnen) bedanken sowie für die Bereitstellung seiner 1D- und 3D-Simulationsdaten, die als wichtiger Input für die Simulationen dieser Dissertation gedient haben. Außerdem bedanke ich mich bei Alexander Summa für das Überlassen seiner Simulationsergebnisse und seine Implementierung einer frühen Version des "Neutrino-Schemas", das im Rahmen dieser Arbeit weiterentwickelt wurde (siehe Abschnitt 2.2). Ein besonderer Dank gilt zudem Robert Glas für seine allzeit hilfsbereite und aufgeschlossene Art, seine vielen Tipps rund um* `Python` *und* `git`*, das Gegenlesen von Teilen dieser Arbeit sowie die gute Zusammenarbeit bei der Weiterentwicklung von* `snappy`. Many thanks also to Naveen Yadav for providing his 3D progenitor model, for his help regarding 3D data visualization, and for many joyful discussions. *Vielen herzlichen Dank auch an André Sieverding für das gründliche Gegenlesen weiter Teile dieser Dissertation sowie für viele hilfreiche Kommentare.*

Moreover, I also thank all my other former and current colleagues for numerous inspiring (scientific and non-scientific) discussions and the generally very pleasant working environment at the institute. Thanks to my PhD fellows Eirini Batziou, Jakob Ehring, Jakob Hein, Malte Heinlein, Liliya Imasheva, Katlego Ramalatswa, and Johannes Ringler; to my former colleagues Ricard Ardevol Pulpillo, Thomas Ertl, Michael Gabler, Anders Jerkstrand, Rémi Kazeroni, Sasha Kozyreva, Georg Stockinger, Ninoy Rahman, Annop Wongwathanarat; and especially to my (former and current) office mates Robert Glas, Ninoy Rahman, Jakob Hein, and Katlego Ramalatswa for the enjoyable working atmosphere in room 008. Furthermore, I thank Benedetta Ciardi and Achim Weiß for their valuable feedback during my PhD committee meetings. Thanks also to the entire IT group of the Max Planck Institute for Astrophysics for their technical support. Moreover, I want to thank our collaborators Petr Baklanov, Alexandra Gessner, Alexander Heger, Shing Chi Leung,

Bernhard Müller, Ewald Müller, Ken'ichi Nomoto, Julia Sawatzki, Irene Tamborra, Stefan Taubenberger, Alexey Tolstov, Laurie Walk, and Michael Wurm. And thanks to all the others who are not mentioned explicitly.

Mein Dank gebührt ferner der Deutschen Forschungsgemeinschaft (DFG) für die Förderung dieser Doktorarbeit unter Sonderforschungsbereich SFB-1258 ("Neutrinos and Dark Matter in Astro- and Particle Physics"). Darüber hinaus bedanke ich mich für Unterstützung durch das Max-Planck-Institut für Astrophysik (MPA), die Max Planck Computing and Data Facility (MPCDF) sowie die Technische Universität München (TUM). The author gratefully acknowledges the Gauss Centre for Supercomputing e.V. (GCS; www.gauss-centre.eu) for funding this project by providing computing time on the GCS Supercomputers SuperMUC and SuperMUC-NG at the Leibniz Supercomputing Centre (LRZ; www.lrz.de) under project IDs pr53yi, pn69ho, pn25su, and pn25me.

Zu guter Letzt: Vielen Dank, Jasmin, und danke an meine Familie und Freunde, die mich in den vergangenen Monaten nur viel zu selten zu Gesicht bekommen haben und mich dennoch stets unterstützt und mir den Rücken gestärkt haben. Ihr seid das Fundament, das mich bis hierhin getragen hat. Danke vielmals an euch alle!! Many thanks to all of you!!